https://theses.gla.ac.uk/

Theses Digitisation:

https://www.gla.ac.uk/myglasgow/research/enlighten/theses/digitisation/

This is a digitised version of the original print thesis.

Copyright and moral rights for this work are retained by the author

A copy can be downloaded for personal non-commercial research or study, without prior permission or charge

This work cannot be reproduced or quoted extensively from without first obtaining permission in writing from the author

The content must not be changed in any way or sold commercially in any format or medium without the formal permission of the author

When referring to this work, full bibliographic details including the author, title, awarding institution and date of the thesis must be given

Enlighten: Theses
https://theses.gla.ac.uk/
research-enlighten@glasgow.ac.uk

RADIATION DAMAGE OF TiC AND TiN DURING MICROANALYSIS IN THE ELECTRON MICROSCOPE

by Mary M Cluckie

submitted for the degree of Doctor of Philosophy in the University of Glasgow September 1990

© 1990. M.M.Cluckie

ProQuest Number: 11007535

All rights reserved

INFORMATION TO ALL USERS
The quality of this reproduction is dependent upon the quality of the copy submitted.

In the unlikely event that the author did not send a complete manuscript
and there are missing pages, these will be noted. Also, if material had to be removed,
a note will indicate the deletion.

ProQuest 11007535

Published by ProQuest LLC (2018). Copyright of the Dissertation is held by the Author.

All rights reserved.
This work is protected against unauthorized copying under Title 17, United States Code
Microform Edition © ProQuest LLC.

ProQuest LLC.
789 East Eisenhower Parkway
P.O. Box 1346
Ann Arbor, MI 48106 – 1346

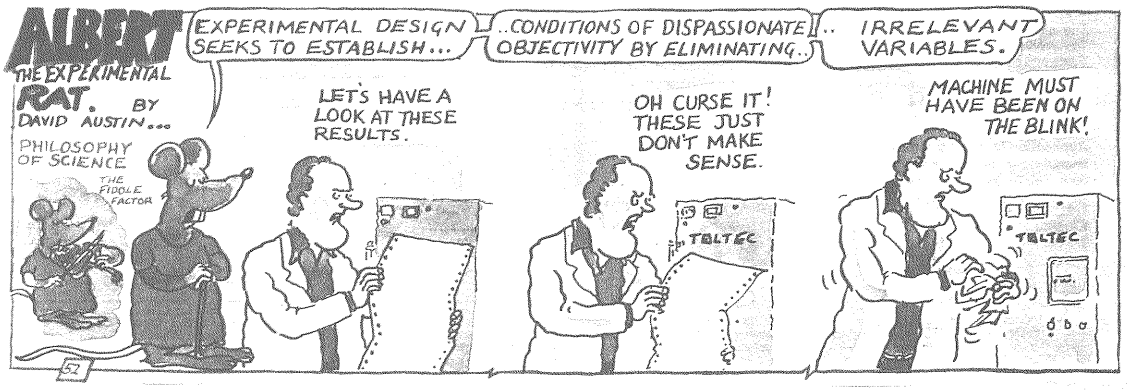

New Scientist, 15 April 1989

DECLARATION

This thesis has been written solely by myself and details the research which I have carried out in the Department of Physics and Astronomy at the University of Glasgow. The work described is my own, except where otherwise stated. Some of the results from this work have been presented in the following papers:-

"High spatial resolution EELS; the problem of quantification in the presence of radiation damage", A.J.Craven, M.M.Cluckie, S.P.Duckworth and T.N.Baker (1988), in EUREM 1988 (Inst.Phys.Conf.Ser.No.93), p179

"Analysis of small VC precipitates using Electron Energy Loss Spectroscopy", A.J.Craven, M.M.Cluckie, S.P.Duckworth and T.N.Baker (1989), Ultramicroscopy, **28**, p330

"Low-energy displacement damage and the effect on the AEM of ceramics", D.G.Howitt, D.L.Medlin and M.M.Cluckie (1990), in proceedings of the XIIth International Congress for Electron Microscopy (San Francisco Press 1990), **4**, p822

This thesis has not been presented in any previous application for a degree.

CONTENTS

ACKNOWLEDGEMENTS

SUMMARY

ACKNOWLEDGEMENTS

I would like to thank all those who have helped me to carry out the work presented in this thesis. First of all, I must thank my supervisor Dr. A.J.Craven for his guidance in all aspects of this work. My thanks also to Professors R.P Ferrier and J.N.Chapman for their encouragement and for the provision of research facilities within the Solid State Physics group in the department of Physics and Astronomy at Glasgow University. I am also indebted to Dr W.A.P.Nicholson for the maintenance of the HB5 microscope facilities at Glasgow University and for his many long and sometimes relevant discussions. My thanks also to the other members of the Solid State Physics Group for their help and constructive abuse, which kept me on my toes. I would particularly like to thank Professor J.Hough for many useful discussions and above all for his constant encouragement throughout the writing of this thesis.

I would also like to thank Mr A.Young for technical support during specimen preparation, Mrs M.Waterson for stenciling a number of the diagrams in this thesis and Mr I.McVicar for assistance in producing the photographic prints.

Above all I would like to thank my family for their support and encouragement and especially for putting up with me over the last 5 years. My special thanks to Alastair for his invaluable help and support and in particular for his faith in me.

SUMMARY

The work presented in this thesis is concerned with the preferential mass loss observed during high spatial resolution micro-analysis of ceramic materials such as TiC and TiN. Electron energy loss spectroscopy (EELS) was used to investigate the preferential loss of the light elements as a function of dose incident upon the specimen. This thesis is primarily concerned with the characterisation of the knock-on displacement damage mechanism thought to be responsible for the mass loss. Chapter 1 gives a general introduction to these knock-on damage processes with particular emphasis on radiation damage observed in the electron microscope.

To perform quantitative EELS microanalysis without the use of standard specimens it is necessary to have an accurate knowledge of the cross-sections relevant to the inelastic scattering of electrons. Chapter 2 outlines the development of partial cross-sections required for EELS analysis and discusses other processes which may contribute to the EELS spectrum. Chapter 3 develops two radiation damage mechanisms as possible explanations for the depletion of the light elements in TiC and TiN during electron irradiation: a forward knock-on displacement model and an isotropic radiation induced diffusion model.

In chapter 4 a brief description is given of the scanning transmission electron microscope (STEM) used to carry out the high current density radiation damage experiments described in this thesis. The discussion includes a

description of two specimen preparation techniques developed to provide electron transparent samples with a plentiful supply of uniform thin areas, suitable for radiation damage experiments.

The reduced dose rate incident upon the specimen during radiation damage experiments results in statistically poor EEL spectra. Often, the accuracy with which quantitative data can be extracted from these "noisy" spectra is limited by the accuracy of the background stripping routines. Chapter 5 compares and contrast three such background fitting routines using both experimental and theoretically generated spectra in an attempt to assess which, if any, is more reliable in the presence of noise.

The experimental results are presented in chapter 6 and 7 for the TiC and TiN materials. Comparison of the rate of loss of C and N with respect to dose at various specimen thicknesses is carried out to establish which, if either, of the two radiation damage mechanisms considered in chapter 3 is applicable to the data. Other considerations such as dose rate effects, channeling effects and the loss of Ti from the sample are considered in more detail in chapter 7 and their effect on the measured rate of loss of N is established. Some high angle ADF images are presented in chapter 6 as a possible method of following the radiation damage process and to highlight the inhomogeneous nature of the damage processes in TiC and TiN.

CHAPTER 1 RADIATION DAMAGE IN THE ELECTRON MICROSCOPE

1.1 INTRODUCTION

Electron microscopy (EM) has played an important role in the microstructural characterisation of many materials. Many such applications today involve the analysis of light elements such as those in the second phase transition metal carbides and nitrides precipitates that are used in the hardening of steels. However, at the high current densities that are required to investigate such materials using EM, the preferential loss of the light element on irradiation by the electron beam can hinder accurate quantitative analysis of elemental concentrations.

One such area of interest, of particular importance to this thesis, is vanadium carbide precipitates in steel, where high spatial resolution microanalysis techniques were required to examine the precipitates close to nucleation. This results in the rapid loss of carbon from the precipitates (Duckworth 1985). In a previous study of vanadium carbide in the electron microscope, Venables (1969) attributed the disordering of the diffraction patterns to the preferential loss of carbon atoms through a knock-on displacement damage process.

The main aim of this project is to characterise the knock-on damage process thought to be responsible for the loss of C in vanadium carbide with a view to extrapolating the C content to zero dose. This involves defocussing the electron probe over relatively large areas of the specimen in order to decrease the incident electron dose. In the absence of a supply of bulk vanadium carbide, titanium

carbides and nitrides, which have similar properties, were used in the experimental work considered in this thesis. Because of their exceptional technical performance in metal cutting applications and for hard wear components, microanalysis of titanium carbides and nitrides in the electron microscope has been widely reported in the literature (eg Sarian 1983, Vuorinen 1983), and so a further benefit of the work described in this thesis is that it can be used to supplement information gathered on such important materials.

We begin this chapter by giving a general outline of radiation damage work, which covers a wide variety of materials and applications. Particular emphasis is given to describing the way in which the study of knock-on damage in these materials has led to the study of preferential mass loss in transition metal carbides and nitrides.

1.2 A GENERAL OUTLINE OF RADIATION DAMAGE

In the 1960s, in an attempt to gain an understanding of the interactions that can occur in materials inside nuclear reactors, the nuclear power industry initiated a number of radiation damage experiments that were used to investigate knock-on displacement damage mechanisms. Knock-on displacement damage is defined to be the direct transfer of momentum between the incident electron and the atomic nucleus. The materials used in the construction of reactors had to be suitable for operation at high temperatures whilst being continuously bombarded with both fast and thermal neutrons and γ rays. The first studies that were used to characterise the knock-on damage of materials were

carried out using neutron irradiation and high energy electron accelerators and involved the study of the change in the electrical resistivity of the materials resulting from the production of defects. (Vajda 1977, Morillo 1981, 1983).

Subsequently, in-situ irradiation experiments in the high voltage electron microscope (HVEM) were applied to this field of study. The build up of defects into clusters, observed as "black spots" on electron microscope images, allowed direct observations to be made of the microscopic behaviour of these materials under electron irradiation. (For a review of these experiments see Makin 1971 and Norris 1975). Extensive work was carried out on the displacement damage mechanisms in the HVEM for various metals (eg Karim 1978, Phillip 1979). It was found that, for the knock-on displacement damage mechanism, the energy required to displace an atom from its lattice site was dependent on the crystal orientation. An extensive review of the displacement energies and their orientation dependence for most commonly used metals is given by Vajda (1977).

More recently, again in connection with the nuclear industry, but on a slightly different theme, radiation damage analysis has been carried out in the electron microscope on sodium silicate glasses with a view to using them to store radioactive waste (DeNatale 1984). It should be noted that this is a different damage mechanism to that discussed above, as it is thought to involve local cation diffusion.

Radiation damage considerations are important in many other aspects of solid state physics. For example the

development of ion implantation as a method of doping semiconductors has heightened the need for a greater understanding of the damage structures which result from bombardment with energetic ions (eg Nelson 1975).

With an electron microscope operating at accelerating voltages of 100kV, the situation is different from that of high energy neutron and high energy electron irradiation considered above. At such energies, the incident electrons are more likely to interact with the atomic electrons, due to the equivalence in masses, than with the heavier atomic nucleus. Therefore, although knock-on interactions occur in all materials, radiation damage by ionisation processes will be dominant in the analysis of biological and organic materials for which there is an efficient mechanism to convert the excitations of the electrons into atomic displacements (Cosslett 1978, Hobbs 1979 and Egerton 1987).

More recently, attention has focussed on the practical aspects of radiation damage such as the ability to burn holes and lines with the dimensions of a few nanometres using a high brightness field emission gun at 100kV in a STEM. Such nanolithography techniques were originally reported for ionic insulators such as Al_2O_3 (eg Berger 1987a) and were shown to occur by an ionisation damage process which involved the separation and displacement of the ionic-species (Humphreys 1985). More recently, however, Berger (1987b) has reported a similar ionisation damage process in the three forms of titanium oxide, which have conductivities ranging from that corresponding to an insulator to that of a conductor. Materials which are susceptible to this drilling process include NaCl (Isaacson 1981), β Al_2O_3 (Mochel 1983), CaF_2 and MgO (Salisbury

1984), AlF_3 (Murray 1984), MgO and ZnO (Devenish 1989). Initial experiments have suggested that different hole drilling mechanisms may be operating in different materials and much work is being carried out in this field to understand the possible damage mechanisms (eg Allen 1989).

However, for materials such as TiC and TiN, which are good conductors (with conductances of $\sim 10^6\ \Omega^{-1}/m$ at room temperature - CRC handbook 1988) ionisation damage is likely to be ineffective because of the rapid response of the conduction electrons to shield the interactions. Therefore, the dominant damage mechanism in titanium carbides and nitrides is likely to be that of knock-on displacement, as considered above for high energy electron and neutron bombardment of metals. It should be noted, however, that the energy transferred to the nucleus from the incident electron is inversely proportional to the mass of the atom. Therefore, light elements such as C and N can be displaced at 100keV whereas metals such as Ti will be relatively undamaged at these incident electron energies. For a general review of radiation damage mechanisms the reader is referred to Hobbs (1984) and Howitt (1988).

1.3 RADIATION DAMAGE OF TiC AND TiN IN THE ELECTRON MICROSCOPE

Even at the lower doses that are available in the conventional transmission electron microscope, radiation damage has been observed in many of the transition metal carbides for a range of accelerating voltages (100kV to 2MV). Venables (1969) used the rate of disordering of the superlattice diffraction pattern to measure the

cross-section for C displacement in VC at incident electron energies ranging between 33 and 100keV. By comparison with theoretical displacement cross-sections (Seitz and Koehler 1956), he calculated the energy required to displace a C atom in the <110> direction in VC to be 5.4eV. Similar disordering has been observed in VO (Bell and Lewis 1974), in TiC (Das 1981) and in Ti(Mo)C (Murata 1988). As mentioned previously, the imaging capability of the TEM at high and intermediate voltages has been utilised to observe the onset of defects in the specimen, visible as "black spots", in many metallic compounds (eg Norris 1975, Karim 1978) and in materials related to those studied in this thesis, such as TaC (Allison 1988). By measuring the threshold voltage at which damage is observed, it is possible to calculate the threshold displacement energy of, for example C in TaC.

In a scanning transmission electron microscope (STEM) which possesses a field emission source, sufficient current can be made available in the probe (~20Å diameter) to allow statistically meaningful information to be obtained in relatively short times. The small probe sizes allow composition measurements to be made with high spatial resolution, as required for the study of VC precipitates close to nucleation. However, unlike the TEM, where the radiation damage is observed by monitoring the production of specimen defects and the loss of order in the electron diffraction pattern, the high current densities within the electron probe can result in a significant mass loss from the specimen. Therefore, at high spatial resolution, the high current densities required for statistically significant data can result in misleading compositional

information due to mass loss. This leads to a situation that is not dissimilar to the uncertainty principle, where the more precisely defined the information is on the specimen composition the less likely the material is to still have that form. Loss of the light elements during microanalysis has been reported in the literature for TiC, Cr_3C_2, Cr_2N and Fe_2O_3 (Thomas 1984, 1985) and NiO (Crozier 1984a, Liu 1987). Preferential loss of the light element may also explain the lower than expected C/V ratios obtained by Allison (1984).

Therefore, STEM presents us with an ideal opportunity for a qualitative study of radiation damage effects in TiC and TiN in the form of loss of the light elements. The two techniques most commonly used in STEM for quantitative analysis are energy dispersive X-ray (EDX) microanalysis and electron energy loss spectroscopy (EELS). The main disadvantage of EDX for light element analysis is the protective Be window that separates the microscope column and the detector, and strongly absorbs X-rays of energies $\leq$2keV . In recent years, ultra thin window and windowless EDX detectors have greatly improved the efficiency of detection of the lower energy X-rays. However, Paterson (1988) indicated that the uncertainty involved in the absorption of low energy photons in the windowless detectors hinders accurate quantitative analysis of C or N (see also Thomas 1984). No windowless detector was available on the extended VG HB5 STEM at Glasgow at the time of this work and therefore EELS analysis was used to quantify the radiation damage processes in TiC and TiN. EELS analysis allows the quantification of light elements C and N routinely and provides information on structure that

is not available in the EDX spectra.

The complexity of the EEL spectrum precludes the use of standard specimens such as those used for EDX microanalysis and so the standardless approach, using theoretical cross-sections, is followed by most workers. Consequently, theoretical considerations of electron-specimen interactions are discussed in chapter 2 with particular emphasis given to the development of partial ionisation cross-sections for EELS analysis. Chapter 3 compares and contrasts two knock-on damage mechanisms. Both models assume that the initial atomic displacement occurs as a result of a direct transfer of momentum from the incident electron to the atomic nucleus. However, the displacement of the ejected atom within the crystal lattice is considered in two extreme cases; a forward knock-on displacement model where the atom is displaced in a forward direction through the sample as a result of the forward bias of the energy transfer and a radiation induced diffusion mechanism where the displacements are isotropic due to the presence of the crystal structure.

To enable the accurate measurement of elemental compositions, many aspects involved with the development of experimental procedures and the correct interpretation of the data must be carefully considered. A detailed discussion of such considerations is given in chapters 4 and 5. This involves a description of the instrumentation used and the specimen preparation techniques developed to ensure that specimens are suitable for analysis in the STEM. Preparation of specimens that are electron transparent at 100keV and possess a plentiful supply of uniform thin areas that are suitable for radiation damage

experiments formed a major part of this project since TiC and TiN are exceptionally brittle (Williams 1983). Several data analysis techniques for the extraction of quantitative information from the EEL spectra are considered in chapter 5 because of the noisy data recorded, which is inherent to low dose radiation damage experiments.

The experimental results are presented in chapters 6 and 7 for the TiC and TiN materials respectively. Comparison of the C and N depletion curves at various specimen thicknesses were carried out to establish whether either of the two possible damage mechanisms considered in chapter 3 applied to these specimens. Other factors such as dose rate effects, orientation and loss of Ti from the sample are considered in chapter 7 and their effect on the observed rate of loss of material is estimated. Some high angle annular dark field images are presented in chapter 6 as a possible method of following the damage process and highlight the inhomogeneous nature of the radiation damage mechanism.

CHAPTER 2 THEORETICAL CONSIDERATIONS FOR EELS

2.1 INTRODUCTION

In this thesis, we are interested in the extraction of quantitative information from EEL spectra. Due to the lack of suitable standard specimens, it is necessary to calculate the probabilities of scattering events theoretically. The probability of a scattering event is expressed as a cross-section

$$\sigma = \frac{N}{nI_e} \qquad 2.1$$

where N is the number of scattering events

n is the number of scatterers per unit area

and I_e is the number of incident electrons.

This chapter outlines the development of theoretical cross-sections that are used in EELS analysis. The discussion is mainly concerned with signals resulting from the interaction of a monoenergetic beam of electrons with a thin specimen. The incident electron is assumed to interact only once with the specimen and to lose a negligible fraction of its energy. However, plural inelastic scattering can be important since it limits the practical application of EELS. This effect will be discussed in section 2.5.

The most frequently used method of calculating cross-sections for microanalysis is based on the Bethe theory for inelastic scattering of fast electrons as reviewed by Inokuti (1971). The Bethe theory is based upon

the Born approximation, which is valid for incident electron energies that are very much greater than the ionisation energy of the atomic electron, and it assumes that the atom can be regarded as a sudden and small perturbation to the incident electron. Application of the Bethe theory to the current work is valid for incident energies of 100keV because the electrons can be considered "fast" relative to the mean orbital velocity of the inner shell atomic electrons for light and medium atomic numbers. It should be noted that no account is taken of exchange effects resulting from the indistinguishability of the incident and atomic electron. However, experimental results (Massey 1931) suggest that exchange effects are only important if the incident electron loses a large fraction of its energy which would invalidate the Born approximation. This leads to the Bethe differential cross-section for an electron scattered into solid angle $d\omega$ and losing energy E. Evaluation of the cross-section requires a knowledge of the relevant initial and final quantum mechanical wave functions. The semi-analytical hydrogenic model (Egerton 1979) and the numerical Hartree-Slater model (Leapman, Rez and Mayers 1980) are described in section 2.4.

It should be noted that other phenomena, such as solid state effects, plural inelastic scattering by valence electrons and plasmon excitations also contribute to the energy loss spectrum. These effects are discussed in section 2.5.

2.2 FAST ELECTRON SCATTERING FROM ATOMIC INNER SHELLS

Consider an incident electron of rest mass m_o and charge (-e) colliding with a stationary atom with atomic number Z in an initial energy state E_o. The electron is scattered into a small solid angle $d\omega$ centred about a direction (θ,ϕ) with respect to its incident direction, and loses energy E = E_o-E_n, where E_n is the energy of the excited state of the atom. The momentum of the electron before and after the collision is given by $\hbar\underline{k}$ and $\hbar\underline{k}_n$ respectively as shown in figure 2.1. The momentum transferred to the atom is given by $\hbar\underline{K}$, where $\underline{K} = \underline{k}_n - \underline{k}$. $d\sigma_n$ is generally independent of the azimuthal angle, ϕ, either because the initial state is spatially symmetric or because the atoms are randomly oriented. Therefore, there are many transitions to energy state E_n corresponding to different directions for $\underline{K}$, and so $d\sigma_n$ is redefined for a momentum transfer $\hbar K$ and the cross-section becomes a function of the scalar variable K instead of θ. For fast but non-relativistic electrons the cross-section, $d\sigma_n$, may be written within the first Born approximation as (Inokuti 1971):-

$$d\sigma_n = 4\pi Z_n \left(\frac{m_o e^2}{2\hbar^2} \right)^2 \frac{1}{k^2 K^4} \left| \varepsilon_n(iKr_j) \right|^2 d(k^2) \qquad 2.2$$

where Z_n is the number of electrons in the n^{th} shell and $\varepsilon_n(K)$ is the inelastic scattering form factor given by

$$\varepsilon_n(K) = \langle n \left| \sum_j \exp(iK.r_j) \right| o \rangle \qquad 2.3$$

where o,n are the initial and final states of the atomic

$$d\Omega = 2\pi \sin\theta d\theta$$

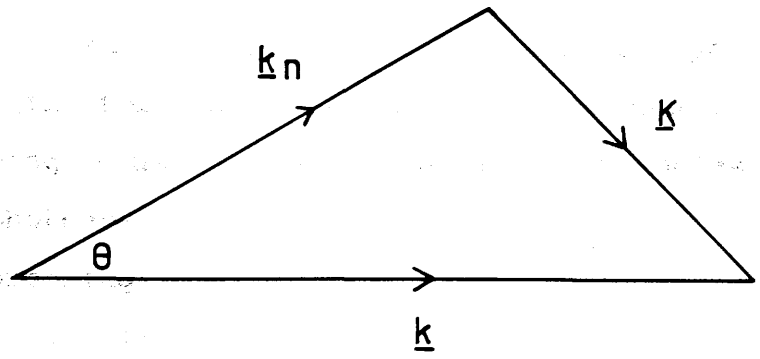

from the cosine rule $K^2 = k^2 + k_n^2 - 2kk_n\cos\theta$

$$\therefore 2KdK = 2kk_n \sin\theta d\theta$$

$$\Rightarrow \quad d\Omega = \pi d(K^2)/kk_n$$

Figure 2.1 Scattering geometry and the relationship between $d\Omega$, the scattering vector and the electron wave vectors for cylindrically symmetric scattering which is independent of the azimuthal angle, ϕ.

electrons and r_j is the coordinate of j^{th} atomic electron.

Following atomic physics, a useful way to describe the interaction of interest here, is to define a generalised oscillator strength (GOS) for a transition to all energy states E_n involving an exchange of momentum $\hbar K$ and energy loss E as

$$f_n(K) = \frac{E}{R(Ka_o)^2} |\varepsilon_n(K)|^2 \qquad 2.4$$

where R is the Rydberg energy and a_o is the Bohr radius. As $K \rightarrow 0$ the GOS tends to the dipole optical oscillator strength for the absorption of a photon of energy E allowing a useful comparison between inelastic scattering and photoabsorption data.

Expressing the cross-section in terms of the GOS and making a convenient change of variables, the cross-section can be expressed as

$$d\sigma_n = \frac{4\pi a_o^2 \, Z_n \, f_n(K) d(\ln(Ka_o)^2)}{T/R \quad E/R} \qquad 2.5$$

where $T = {}^1/_2 \, m_o v^2$, which is the kinetic energy of the incident electron for the non-relativistic case. This expression for the cross-section factorises into two terms; Firstly the generalised oscillator strength, $f_n(K)$, is related to the probability that the atom will make a transition to an excited state n after receiving momentum transfer $\hbar K$ and reflects the internal dynamics of the atom. Secondly, the remaining terms deal with the properties of the incident electron and are equivalent to the Rutherford cross-section for scattering of a particle with charge Z_n

by a free electron.

2.3 PARTIAL CROSS-SECTIONS FOR EELS

For EELS analysis it is necessary to know the cross-section for an electron losing energy E and being scattered through all angles θ from zero degrees to the spectrometer collection angle, β. The relationship between (Ka_o^2) and θ is derived from conservation of energy and momentum as applied to the collision shown in figure 2.1 and is given by :-

$$(Ka_o)^2 = \frac{2T}{R}\left(1 - \frac{E}{2T} - \sqrt{(1 - \frac{E}{T})}\cos\theta\right) \qquad 2.6$$

where θ=0 corresponds to $(Ka_o)^2_{min}$ and θ=β to $(Ka_o)^2_{max}$. Therefore the cross-section for an electron losing energy E and being scattered into a cone of half angle β is given by integrating equation 2.5 over all kinematically allowed momentum transfers. This is known as the energy differential cross section and is given by

$$d\sigma_n(\beta) = \frac{4\pi a_o^2 Z_n}{T/R} \int_{(Ka_o)^2_{min}}^{(Ka_o)^2_{max}} \frac{df_n(K,E)}{d(E)} \frac{R}{E} d(\ln(Ka_o)^2) \qquad 2.7$$

In this discussion, the contribution to the cross-section from transitions to discrete states above the fermi level is neglected ie. the atomic electron is assumed to make a transition into the continuum. In many cases the contribution from the discrete states is small compared to

that from the continuum. However, for the transition metals V and Ti, of interest in this thesis, there is a dominant, optically favourable, transition between discrete states which leads to an underestimation of the cross-section by the continuum model. The effect of these inaccuracies are discussed briefly in section 2.5.1 and more fully in chapter 5.

The partial ionisation cross-section, for an electron being scattered into a cone of half angle β and losing energy in the range E to E+δE is given by:-

$$\sigma(\delta,\beta) = \int_{E}^{E+\delta E} \frac{d\sigma_n(\beta)}{d(E)}\, d(E) \qquad 2.8$$

In order to calculate partial cross-sections, it is necessary to know the form of the GOS which involves knowledge of the atomic wave functions.

2.4 EVALUATION OF THE GOS FUNCTION

The semi-analytical hydrogenic model of Egerton (1979, 1981b) proposes wave functions for the initial and final states of the electron which are solutions of Schrödinger's equation in the presence of a Coulombic potential. Although this gives accurate results for hydrogen, where the wave functions are known exactly, a screening correction is necessary for all other elements to account for the reduced nuclear charge experienced by an atomic electron due to the presence of the other electrons orbiting the atom (Zener 1930). For the K shell, the interaction takes place close

to the nucleus, and so the inner shell wave functions are not greatly distorted by the outer shell electrons. However, the hydrogenic model will give less accurate results for the L and higher order shells. Egerton (1984c) modified the original hydrogenic programs to take some account of relativistic effects resulting in a 5% correction to the cross-section at incident energies of 100keV. These modified programs, known here as SIGMAKR and SIGMALR, were used for the initial experimental data presented in chapter 5 of this thesis. More recently, Egerton (1985) proposed a more accurate version of the L shell cross-section in the fortran program SIGMAL2 where approximate allowance has been made for the "white lines" present in many transition metals. The energy dependent correction factor has also been modified in view of the experimental EELS results of Malis and Titchmarsh (1985) and to give better agreement with photoabsorption data.

The GOS has also been calculated numerically using the Hartree-Slater model (Leapman et al 1980, Rez 1984), where the atomic wave functions are solutions to Schrödinger's equation in the presence of a self-consistent central field. Leapman et al have compiled tables of the GOS, as a function of K and E, for a limited range of elements (Crozier 1984b). The energy differential cross-section can then be calculated by integrating the GOS over all kinematically allowed momentum transfers as discussed in section 2.3. An expression for the partial cross-section required for quantitative EELS analysis can be obtained by integrating the differential cross-section over the energy range applicable to the experimental conditions.

Both the Hydrogenic and the Hartree Slater models

correctly predict the shape of the energy-differential cross-section for the K shell, and agree in their predictions to within 10% (Egerton 1984c, Rez 1984). However, the differences in the predictions for the L-shell cross-sections are generally greater, particularly for small energy ranges. The differences introduced into the analysis of VC and TiN samples with the use of each of the above mentioned cross-sections will be discussed further in chapter 5.6.

2.5 ADDITIONAL CONTRIBUTIONS TO EEL SPECTRA

2.5.1 Solid State Effects

The hydrogenic and Hartree-Slater cross sections are based on the assumption of single scattering by an isolated atom. As such they cannot explain the aspects of an EEL spectrum which arise due to solid state effects in real specimens. The energy levels of the atoms within a solid become broadened into bands. For the inner shell this does not significantly alter the form of the wave function. However, for outer electrons and those in the continuum, the broadening of energy levels into bands can lead to a considerable distortion of the final state wave functions. This produces fine structure within the first 50eV of the ionisation edge, known as Energy Loss Near Edge Structure (ELNES) which can yield information on the density of states above the Fermi level (Egerton 1985). Thus a carbon edge recorded from a crystalline specimen such as TiC will have a different edge shape than that resulting from an amorphous carbon layer produced by beam induced

contamination. This effect can be used to monitor the level of contamination during an experiment on a sample containing C.

The white line transitions, seen in the Ti and V characteristic L-edges, represent an optically favorable transition between a p and a d state, not normally allowed for in continuum cross-section models. Egerton (1985), however, has made approximate allowance for these white lines in the SIGMAL2 program by using the full hydrogenic oscillator strength within the first 20eV of the edge.

Back-scattering of the ejected electron by neighbouring atoms can produce interference with the outgoing wave causing a redistribution of the GOS. This leads to an oscillatory structure extending for many hundreds of eV beyond the edge onset known as extended energy loss fine structure (EXELFS). Measurement and analysis of EXELFS allows the interatomic distances, principally of the first nearest neighbours, to be calculated (Egerton 1985).

2.5.2 Valence Electron Excitation and Plural Scattering

To this point, we have only considered the interaction between the incident electrons and inner shell electrons. However, the interaction between incident electrons and valence electrons can also contribute to the EEL spectrum. In substances such as TiC and TiN, where the valence electrons can be considered as a nearly free electron gas, the electric field of the incident electrons induces a longitudinal charge density oscillation or volume plasmon resulting in a broad peak in the EEL spectra at the plasmon energy E_p~25eV. The interaction is characterised by a

plasmon mean free path, λ_p, which for light and medium atomic numbers is typically between 500 and 1500Å for 100keV incident electrons (Egerton 1984a). Therefore, for specimen thicknesses exceeding λ_p, plural inelastic scattering by valence electrons becomes important, reducing the peak to background ratio of the characteristic edges at higher energies. For thicker samples there will be a second plasmon at $2E_p$ but in the TiC and TiN materials this energy region is dominated by a characteristic M edge for the transition elements such as Ti.

The assumption of a single scattering event in the Bethe theory becomes increasingly invalid in thicker specimens due to multiple scattering effects. This multiple scattering of one or more inelastic collision with the outer shell electrons in addition to the core level ionisation can drastically alter the observed shape of the ionisation edge redistributing the counts within the edge. Therefore, quantitative EELS analysis using the cross-sections predicted by the Bethe theory is limited to specimens of thicknesses that are less than the plasmon mean free path unless a deconvolution process (Egerton 1985) is used to remove the multiple scattering effects from the ionisation edge before analysis.

Assuming the scattering events are independent, the probability of an electron being scattered n times is given by Poisson statistics as

$$P_n = \frac{I_n}{I} = {}^1/_{n!} \left({}^t/_{\lambda}\right)^n \exp\left({}^{-t}/_{\lambda}\right) \qquad 2.9$$

where t is the specimen thickness and λ is the total mean free path summed over all energy losses, i, and is given by

$$ {}^{1}/_{\lambda} = \sum_{i} {}^{1}/_{\lambda_i} \qquad 2.10 $$

However, the valence electron excitations which correspond to the shorter mean free path lengths tend to dominate this summation.

Substituting for n=0 in equation 2.9, we obtain an expression for the relative thickness of the specimen

$$ {}^{t}/_{\lambda} = \ln\left(\frac{I_{tot}}{I_o}\right) \qquad 2.11 $$

where I_o is the current intensity in the zero loss peak and I_{tot} is the total intensity in the spectrum (up to typically 100eV).

Measurements made on several elements and inorganic compounds suggest that the total mean free path, λ, is given by

$$ \lambda = \frac{0.106\ T}{E_M \ln\left(\frac{2\beta E_o}{E_M}\right)} \quad (nm) \qquad 2.12 $$

to an accuracy of 20% (Egerton 1989).

where $E_M = 7.6\ Z^{0.36}$ and Z is the mean atomic number of the specimen

E_o is the incident electron energy in eV.

β is the spectrometer collection angle.

T is the relativistically corrected incident energy in eV defined by

$$ T = \frac{E_o(1+E_o/2m_oc^2)}{(1+E_o/m_oc^2)^2} $$

In conclusion, quantitative EELS analysis is limited to specimens with $t<<\lambda$ if the theoretical cross-sections evaluated from the single scattering theory outlined in section 2.2 are to remain valid. In practice however, a simple first order correction for the multiple scattering is made to the experimental edges allowing quantitative data to be extracted from samples up to $t/\lambda \sim 0.5$ (Egerton 1978). As mentioned previously, the range of specimen thicknesses examined by EELS analysis can be extended still further by deconvoluting the spectrum although this approach was not used in the work presented here. The difficulties of preparing specimens to match these strict criteria (t<500Å) will be discussed in chapter 4.

CHAPTER 3 RADIATION DAMAGE MECHANISMS

3.1 INTRODUCTION

In "close packed" solids, such as TiC and TiN, the direct transfer of momentum between the incident electron and the nucleus can result in the displacement of atoms from their lattice sites. However, for mass loss to be observed, atoms must be displaced either to the specimen surface from which they can escape or into an unirradiated region of the specimen. It follows, therefore, that transport mechanisms are an important feature of the radiation damage process.

In this chapter we consider two transport mechanisms which may be responsible for the depletion of C and N observed in TiC and TiN; direct knock-on displacement and radiation induced diffusion. The first of these was suggested by Howitt et al (1988) to explain the observed loss of C from a TiC sample that was irradiated by an electron beam. This model assumes that the large difference in masses between the C atom and the incident electron results in the atom being displaced in a direction close to that of the electron. This model may not be a good description because, although the initial displacements are forward biased, the presence of nearest neighbours in the "close packed" structure of TiC suggests that the atom may then vibrate in the crystal lattice, dissipating energy as phonons in the crystal structure or recoiling in directions other than that of the incident electron. To take this effect into consideration a second model based on radiation induced diffusion is proposed.

The final section of this chapter considers a 1-dimensional numerical solution to the diffusion equation and in particular examines the importance of the approximate boundary conditions assumed in the analytical solution.

3.2. KNOCK-ON DISPLACEMENT DAMAGE

3.2.1 A Damage Mechanism for TiC

Assuming a forward bias in the displaced atoms, the depletion of C can occur as a shuffling process whereby the atoms move through the lattice in short displacements until they are sputtered from the electron exit surface. Assuming that the rate of loss of material knocked forward out of a layer is proportional to the amount of material in that layer then, from the definition of the displacement cross-section, the loss of material, ds_j, from the j^{th} layer of the sample can be expressed as (Howitt 1988)

$$\frac{ds_j}{s_j} = - \sigma_D idt \qquad 3.1$$

where s_j is the initial concentration of C atoms in the j^{th} layer

σ_D is the displacement cross-section

idt is the electron dose incident upon the sample.

The j^{th} layer of the sample is defined to be the layer where the atoms require j knock-on collisions to be completely removed from the sample. Therefore j=1 corresponds to the electron exit surface of the specimen as

shown schematically in figure 3.1. Assuming that each displacement is independent of all others, the probability that a fraction $P(\sigma_D it)$ of the atoms will be displaced k times is given by the Poisson distribution as

$$P(\sigma_D it) = \frac{\exp(-\sigma_D it)\ (\sigma_D it)^k}{k!} \qquad 3.2$$

where $(\sigma_D it)$ is the fraction of atoms undergoing one displacement interaction (equation 3.1).

The fraction of atoms which are displaced from the j^{th} layer but do not receive enough displacements to leave the sample is then given by summing this probability over j-1 displacement as

$$S_j = \sum_{m=0}^{j-1} \frac{\exp(-\sigma_D it)\ (\sigma_D it)^m}{m!} \qquad 3.3$$

where m=0 corresponds to the atoms which are not displaced from the j^{th} layer.

The total fraction of displaced atoms, S, remaining within the sample is given by summing the fraction S_j over the sample thickness

$$S = {}^1/_n \sum_{j=1}^{n} S_j = \sum_{j=0}^{n-1} \frac{(n-j)}{n} \frac{\exp(-\sigma_D it)\ (\sigma_D it)^j}{j!} \qquad 3.4$$

where n is the number of hits necessary to knock an atom all the way through the specimen ie. the specimen thickness

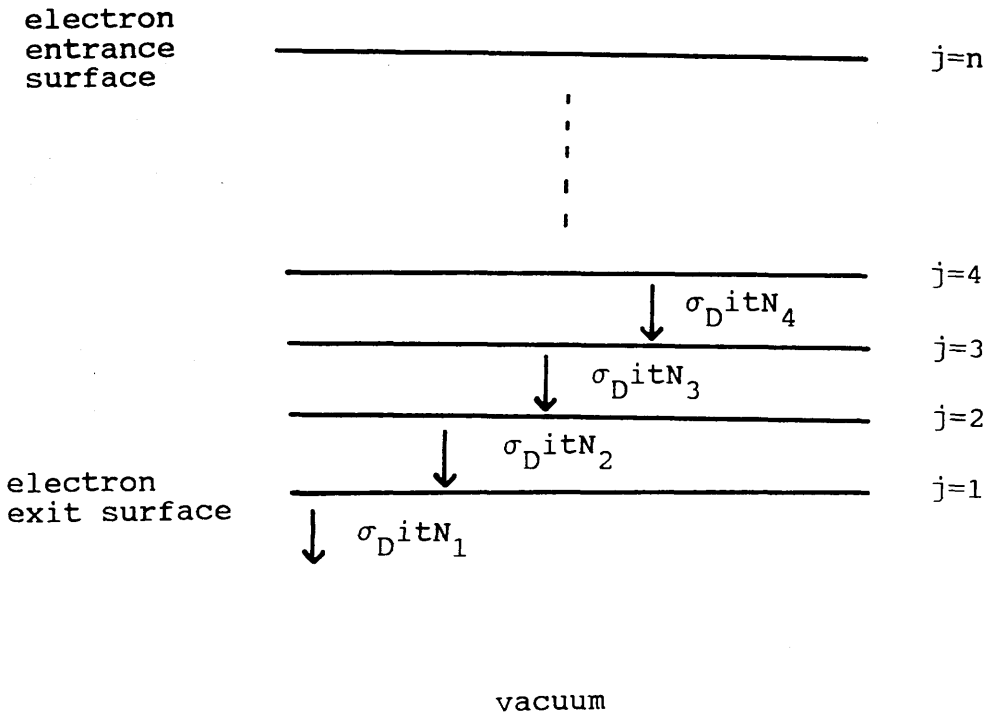

Figure 3.1 Schematic representation of the forward knock-on displacement model. The number of atoms displaced from the j^{th} layer is dependent on the displacement cross-section (σ_D), the electron dose (it) and the number of atoms in the layer (N_j).

expressed in terms of the displacement distance, a. It should be noted that the fraction of atoms displaced from a given layer in the sample is dependent only on the cross-section and the electron dose (equation 3.1). Therefore, the model does not take into account the ability of the next layer to accommodate the displaced atoms ie. the vacancy fraction.

3.2.2 Knock On Displacement Damage Cross-Sections

The energy differential cross-section, which determines the energy transferred from the electron to the nucleus via the Coulomb interaction, is given by the McKinley-Feshbach approximation to the original Mott solution (reviewed by Seitz and Koehler 1956). The displacement cross-section is obtained by integrating this differential cross-section over energies ranging from E_d, the energy required to displace an atom from its position in the lattice to E_m, the maximum energy transferred in a head on collision. In the notation of Seitz and Koehler the displacement cross-section is given by

$$\sigma_D = \frac{\pi b'^2}{4}\left(\left(\frac{E_m}{E_d} - 1\right) - \beta^2 \log\left(\frac{E_m}{E_d}\right) + \pi\alpha\beta\left(2\left(\sqrt{\frac{E_m}{E_d}} - 1\right) - \log\left(\frac{E_m}{E_d}\right)\right)\right) \qquad 3.5$$

where $\frac{\pi b'^2}{4} = \frac{2.495\times10^{-25}\ Z^2(cm^2)}{\beta^4\ \gamma^2}$, $\beta = {}^{v}/_{c}$, $\alpha = \frac{Z}{137}$

and $E_m = 2.148E_o\left(\frac{\frac{E_o}{1000} + 1.022}{A}\right)$ eV $\qquad 3.6$

In equation 3.6, which is relativistic, A is the atomic weight and E_o is the incident electron energy in keV.

The energy differential cross-section, which involves only the initial electron-nucleus interaction, is valid for all collisions of free or constrained atoms because the electron passes through the material, transferring its energy, in a time in which the displacement of the excited atom is negligible. However, integration of this differential cross-section over the energy range E_d to E_m may overestimate the displacement cross-section for an atom constrained in a crystal structure. The reason for this is that, in a crystal, the threshold energy is dependent on the orientation (Vajda 1977 in crystalline metals) and the C atoms will only be displaced if they receive enough energy to overcome the binding energy of the direction into which they have been scattered. Therefore, the C atoms in TiC will only be displaced if the direction of the energy transfer allows the atoms to pass over the saddle points in the atomic potential well ie. between the Ti atoms. If the threshold displacement energy is not exceeded, the transferred energy may be dissipated as phonons in the crystal structure as the excited atom vibrates in the cage of surrounding Ti atoms. Thus, while the cross-section for excitation is the same for both the free atom and an atom constrained in a crystal lattice the displacement cross-section is unlikely to be the same for both cases.

Figure 3.2 shows the displacement cross-section for C as a function of the incident electron energy for a range of threshold displacement energies, E_d (3ev to 7ev). It can be clearly seen that the displacement cross-section is

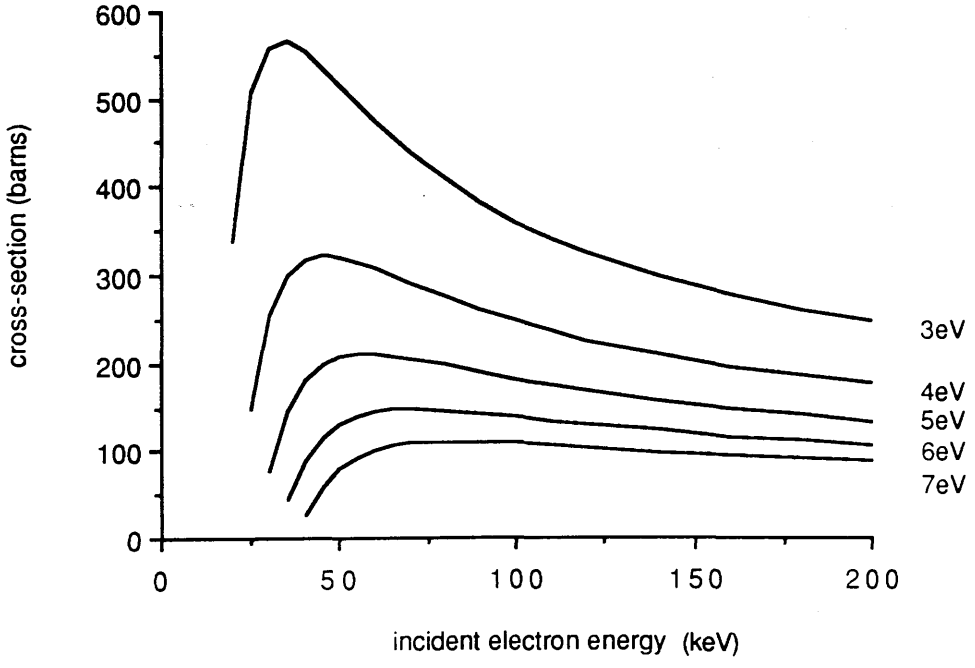

Figure 3.2 A plot of the displacement cross-section for C as a function of incident electron energy, evaluated using equation 3.5.

strongly dependent on the threshold displacement energy which, however, is not accurately known for the refractory carbides. Self diffusion energies for C in TiC (Sarian 1968) and experimental data from vanadium carbide (Venables 1969) suggest that E_d is approximately 5eV for C in TiC. Therefore, for a displacement threshold energy in the range 3 to 7eV figure 3.2 predicts a displacement cross-section for C in TiC between 360 and 110 barns for 100keV incident electron energies.

It should be noted that, although the McKinley-Feshbach approximation works well for the lighter elements ($Z \leq 30$) which are of interest in this thesis, a numerical calculation of the full Mott series is required for heavier elements. These have been calculated and tabulated by Oen (1973) and more recently by Bradley (1988).

3.2.3 Application of the Model

Theoretical depletion rates for C as a function of dose were calculated for the knock-on displacement model from equation 3.4 using a superBASIC computer program on a QL microcomputer. The dose was normalised in units of $\sigma_D it$ and the specimen thickness was calculated as a multiple, n, of the displacement distance, a.

The output from the above program is illustrated in figure 3.3(a) for the absolute and (b) for the relative loss of material over specimen thicknesses ranging between n=10 and n=200. There is a linear region on the depletion curves corresponding to the initial depletion of C atoms, where the j^{th} layer is only depleted of C atoms once the

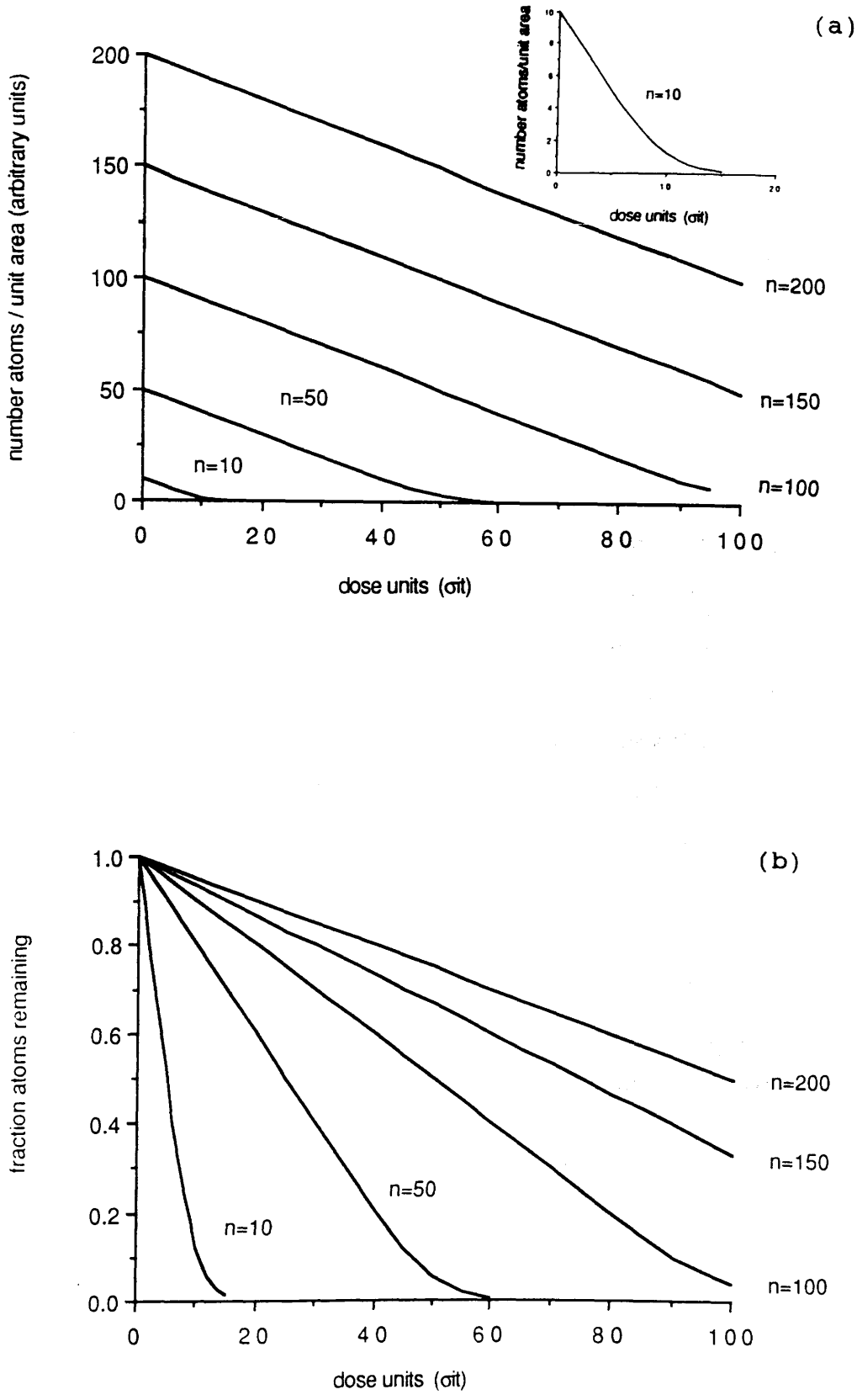

Figure 3.3 Theoretical depletion curves evaluated from the knock-on displacement model of equation 3.4 at various specimen thicknesses (n) for (a) the absolute loss of atoms/unit area and (b) the fractional loss of atoms. (Insert: n=10)

$(j+1)^{th}$ layer has begun to deplete (figure 3.1). The C atoms are lost from the sample via a shuffling process which is only dependent on the rate of loss of material from the exit surface of the specimen (ie $\sigma_D$it). Therefore, the gradients of the lines in figure 3.3(a) are independent of the specimen thickness. However, the extent of this linear depletion region is dependent on the specimen thickness as it relies on the time required for the depleted region to be swept through the sample. The deviation from linearity is more clear for n=10 shown inserted in figure 3.3(a). It should be noted that, since the initial rate of loss is surface controlled the initial gradients of the fractional loss curves (figure 3.3(b)) are inversely proportional to the specimen thickness. This model does not take into account the crystal structure of the material or the fact that the C atoms are less likely to be displaced if there is no vacancy in the layer immediately preceding it.

A comparison of the theoretical depletion curves shown in figure 3.3 (which are measured in dose units of $\sigma_D$it) with that of the experimental depletion curves (measured in dose units of it) can yield a value for the displacement cross-section from the experimental data. The best way to achieve this is to use the simple relationship between the gradient of the fractional loss curves (figure 3.3b) and the specimen thickness in units of displacement distances, n, so that the displacement cross-section is given as

$$\sigma_D = n.G \qquad 3.7$$

where G is the gradient of the experimental depletion curves. For easier comparison between the theoretical and experimental depletion curves the fractional loss of material was used. Therefore, provided the specimen thickness is known and assuming a displacement distance equal to the interatomic spacing it is possible to estimate σ_D. A more detailed discussion of the extraction of the displacement cross-section from experimental data is given in chapters 6 and 7.

3.3 RADIATION INDUCED DIFFUSION

In the knock-on displacement model we have examined one extreme case for the transport and subsequent loss of C atoms from TiC. The knock-on displacement theory assumed that, on receiving energy from the incident electron which exceeds the value of the displacement energy, the C atom moves in a forward direction through the sample. However, the other extreme occurs if, on receiving energy from the electron in a knock-on collision, the direction of displacement is isotropic. This is possible because the atom can recoil in any direction from the surrounding Ti atoms in the crystal lattice. These essentially random displacements of the atom are analogous to diffusion and a diffusion coefficient can be defined as

$$D = f \nu a^2 \qquad 3.8$$

where f is a geometric factor related to the fraction of jumps in a particular direction.

ν is the jump frequency and is equal to the cross-section multiplied by the electron flux

a is the jump distance

The following section develops a radiation induced diffusion model as a possible explanation for the depletion of C in TiC.

3.3.1 A Three Dimensional Diffusion Model

The solution for diffusion in 3 dimensions can be simplified by noting that if $c_1(z,t)$ is a solution of the 1-dimensional linear equation and $c_2(r,t)$ is a solution of the 2-dimensional radial equation then $c=c_1c_2$ is a solution of the 3-dimensional diffusion equation (Pipes 1958). In this way, a solution for 3-dimensional diffusion was evaluated by combining two well known diffusion solutions, namely diffusion from a thin slab in 1-dimension and diffusion from a cylindrical volume in 2-dimensions along the radial direction.

Following Shewmon (1963) the solution for diffusion from a slab in 1-dimension is given by

$$c_1(z,t)=\frac{4C_{01}}{\pi}\sum_{j=0}^{\infty}\frac{1}{(2j+1)}\sin\left(\frac{(2j+1)\pi z}{h}\right)\exp\left(-\left(\frac{(2j+1)\pi}{h}\right)^2 Dt\right) \qquad 3.9$$

where C_{01} is the initial concentration level and is independent of position in the specimen.

h is the specimen thickness and

D is the diffusion coefficient of equation 3.8

for boundary conditions

$$c=C_{01} \text{ for } 0<z<h \text{ at } t=0$$

$$\text{and} \quad c=0 \text{ for } z=h \text{ and } z=0 \text{ at } t>0$$

For the purpose of this calculation we assume that the C and N atoms are lost from both the entrance and exit surfaces of the specimen.

By integrating the above concentration over the specimen thickness, an expression for the fraction of atoms remaining within the sample as a function of time is given by

$$\frac{C_1(t)}{C_1'} = \frac{8}{\pi^2} \sum_{j=0}^{\infty} \frac{1}{(2j+1)^2} \exp\left(-\left(\frac{(2j+1)\pi}{h}\right)^2 Dt\right) \qquad 3.10$$

where C_1' is the initial number of atoms in the specimen and is equal to the constant C_{01} integrated over the specimen thickness.

Diffusion in 2-dimensions from a cylinder expressed in cylindrical coordinates is given by Crank (1975) as

$$c_2(r,t) = \frac{2C_{02}}{b^2} \sum_{n=1}^{\infty} \exp\left(-D\alpha_n^2 t\right) \frac{J_0(r\alpha_n)}{J_1^2(b\alpha_n)} \int_0^b rJ_0(r\alpha_n)dr \qquad 3.11$$

where b is the probe radius

D is the diffusion coefficient of equation 3.8

$b\alpha_n$ are the roots of the zero order Bessel function

$J_0(b\alpha_n) = 0$

and J_1 is the first order Bessel function

for the boundary conditions

$$c = 0 \text{ at } r = b,\ t>0$$

and $$c = C_{02} \text{ for } 0 < r < b \text{ at } t=0,$$

where C_{02} is the initial concentration , assumed constant at t=0.

Integrating the concentration over the cross-sectional area of the cylinder, an expression for the fraction of C atoms remaining as a function of time can be calculated and is given by

$$\frac{C_2(t)}{C_2'} = 4 \sum_{n=1}^{\infty} \frac{1}{(b\alpha_n)^2} \exp\left(-D\alpha_n^2 t\right) \qquad 3.12$$

where C_2' is the initial concentration integrated over the cross-sectional area of the cylinder and is equal to the total number of atoms in the cylinder at t=0.

Note that the above boundary conditions of free-flow from the edge of the irradiated region are only an approximation where the irradiated volume is bounded by the specimen. The possible means of dispersion of the C atoms outwith the irradiated area (such as thermal diffusion and billiard ball type collisions which transfer energy through the crystal lattice) are not as efficient as the radiation induced diffusion process. Consequently, the concentration of C atoms at the periphery increases with time as more C atoms leave the irradiated area due to radiation induced diffusion than are dispersed from the peripheral region by other means. The effects of these approximations are examined in more detail in section 3.5.

Thus the fraction of C atoms remaining within the irradiated volume can be calculated by multiplying the 1 and 2-dimensional solutions and is expressed as

$$\frac{C(t)}{C'} = \frac{C_1(t)}{C_1'} \times \frac{C_2(t)}{C_2'} \qquad 3.13$$

where C′ is the initial concentration integrated over the cylindrical volume and is equal to the initial number of atoms in the irradiated volume.

3.3.2 Application of the Model

As part of this project, a superBASIC program was written for the QL microcomputer to calculate the relative concentration as a function of dose from equation 3.13. The dose dependency was introduced via the diffusion coefficient defined in equation 3.8. As in the case of the knock-on model, the units of dose were normalised, this time in units of $f\sigma_D it$. The specimen thickness and the radius of the cylinder were assumed to be integral multiples of the displacement distance, a, denoted n and n_r respectively. Therefore, by substituting a range of values for n and n_r, the program can evaluate the theoretical depletion rate for various specimen geometries.

Figure 3.4 illustrates the output of the above computer program for two extreme geometries; a thin slab of material with thickness equal to 10 displacement distances (n=10) and a probe diameter of 100 displacement distances (n_r=100), and a thick but narrow cylinder with n=100 and probe diameter n_r=10. As expected for the thin slab, where

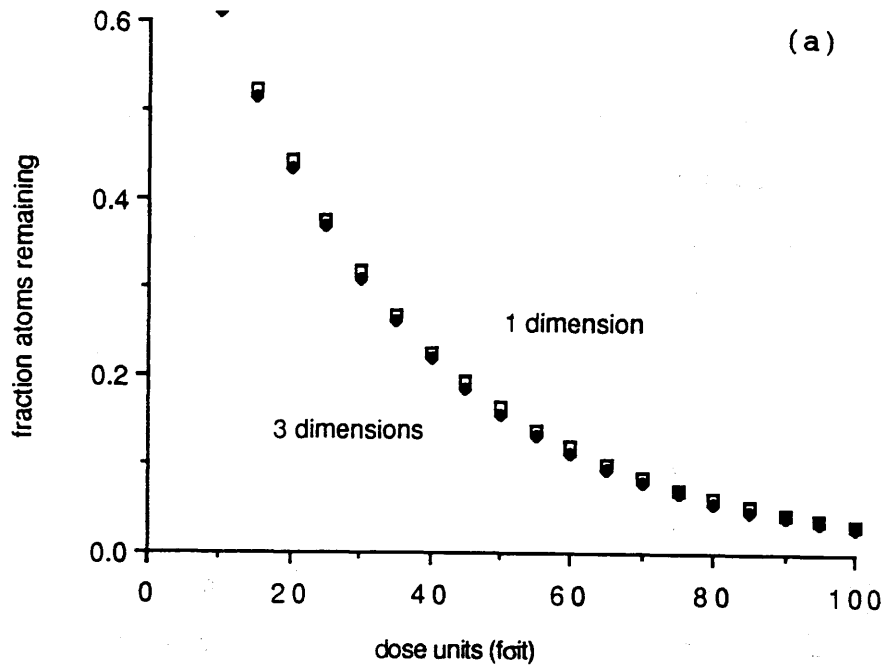

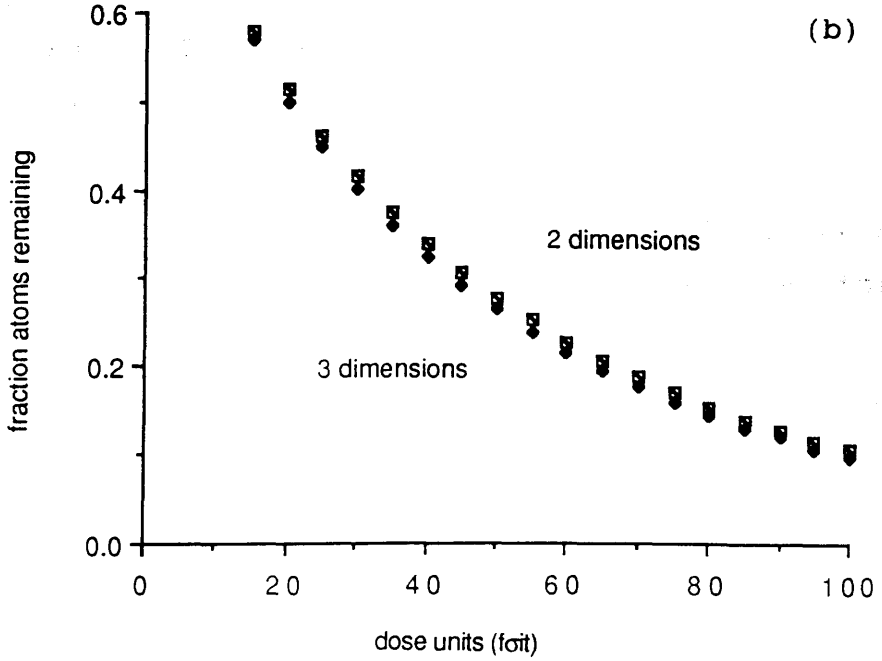

Figure 3.4 Theoretical depletion curves evaluated by the radiation enhanced diffusion model of equation 3.13 for (a) a thin slab of material of thickness n=10 and radius n_r=100 and (b) a thick but narrow cylinder of thickness n=100 and radius n_r=10. In both cases the geometric factor, f, in the definition of the diffusion coefficient was taken to be 1/3.

the loss of atoms occurs predominantly at the specimen surface, the 1-dimensional diffusion model of equation 3.10 (also shown in figure 3.4a) is a good approximation for the 3-dimensional diffusion process. However, for a much thicker sample with a very small surface area, the atoms are predominantly lost from the edge of the cylindrically irradiated volume and the 2-dimensional diffusion model of equation 3.12 is a good approximation for the damage process, as shown in figure 3.4(b). Where the area at the specimen surfaces and the surface area of the cylindrically irradiated volume are equal in magnitude (ie. $\pi n_r^2 x2 = 2\pi n_r n \Rightarrow n=n_r$) the total loss by the diffusion process has similar contributions from loss at the specimen surface and loss from the edge of the irradiated volume (figure 3.5).

To compare the theoretically predicted depletion curves with experimental results for various specimen thicknesses, the radius of the irradiated cylindrical volume was assumed to equal 65Å corresponding to a probe diameter of 130Å. Assuming a displacement distance equal to the interatomic spacing of 3Å in TiC and TiN (CRC handbook 1988) this gives a radius, in displacement distances, of n_r=22. Figure 3.6 shows the resulting depletion graphs for (a) the absolute number of atoms/unit area and (b) the fraction of atoms remaining for a range of specimen thicknesses from n=10 to n=200 at a constant probe diameter of n_r=22. As expected, figure 3.6(b) shows that the fractional rate of loss of material at larger specimen thicknesses tends towards a constant rate of loss as the loss of material from the edge of the irradiated volume becomes dominant. This behaviour can be most clearly seen for $n \geq 150$

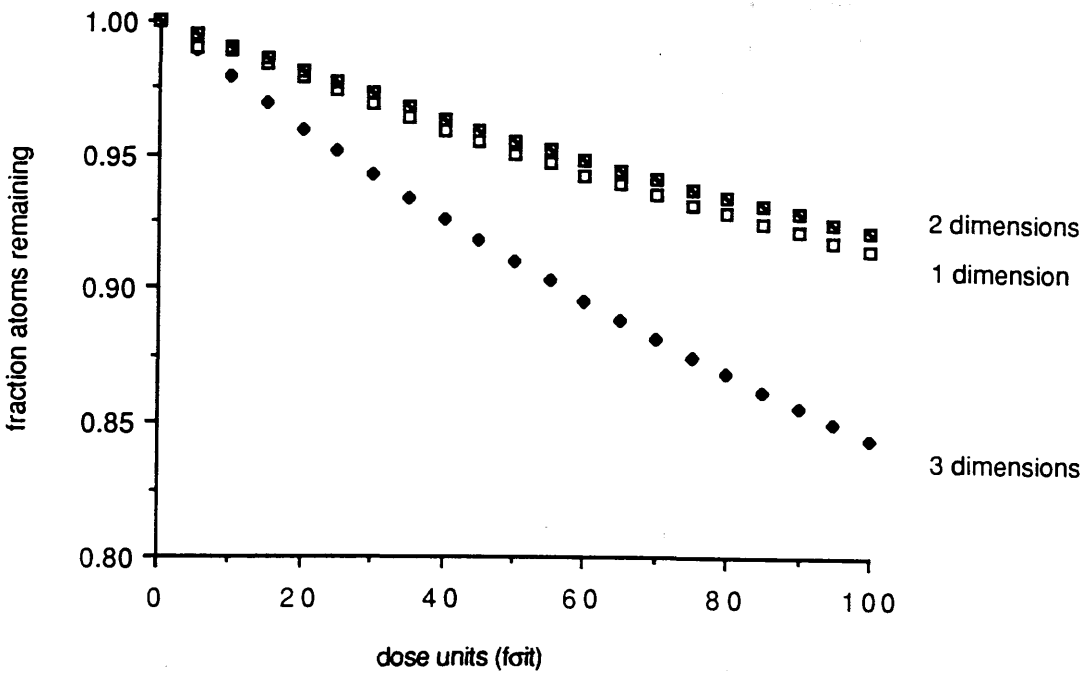

Figure 3.5 The relative contributions of the 1 dimensional and 2 dimensional loss mechanisms to the total depletion predicted by the radiation induced diffusion model for specimen thickness (n) = radius(n_r) = 100. The geometric factor, f, in the definition of the diffusion coefficient was taken to be 1/3.

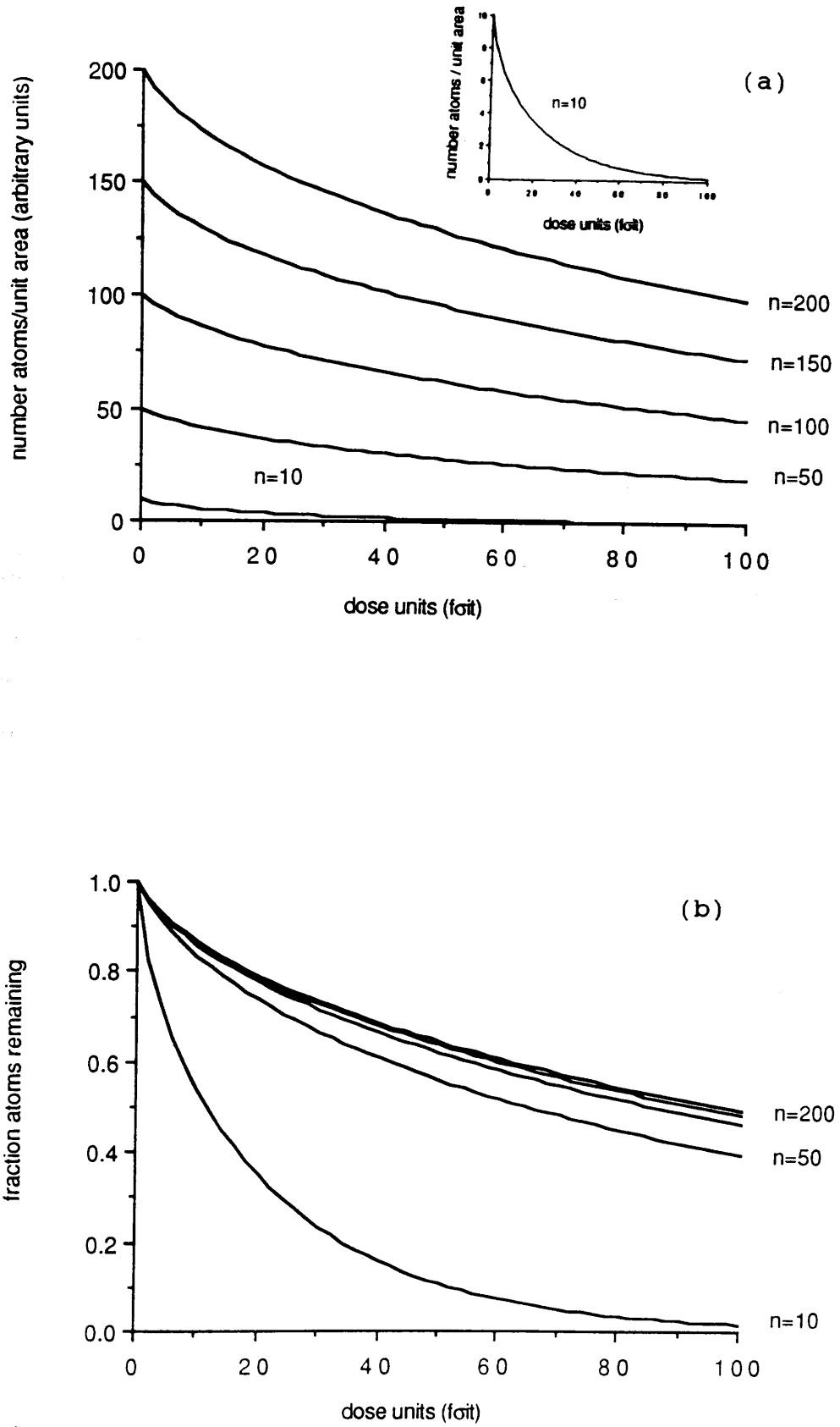

Figure 3.6 Theoretical depletion curves evaluated from the radiation induced diffusion model of equation 3.13 at various specimen thicknesses (n) for (a) the absolute loss of atoms /unit area and (b) the fractional loss of atoms. The geometric factor, f, in the definition of the diffusion coefficient was taken to be 1/3. (Insert: n=10)

In the presence of noise, which is inherent to the experimental data, it would be very difficult to observe the curvature in these depletion graphs. In particular the experimental data points might not show the initial rapid decrease in concentration observed in figure 3.6. Consequently, it would be very difficult to decide from the depletion curves alone if either the radiation induced diffusion process (figure 3.6) or the forward knock-on process (figure 3.3) was responsible for the observed experimental depletion of C and N. Further discussion of this point is given in the following section. It should be noted, however, that in reality the damage mechanism is likely to lie somewhere between the two extreme models considered here since the momentum transfer is forward biased.

3.4 COMPARISON OF THE DAMAGE MODELS

One possible method that can be used to gauge the relative effect of the two damage mechanisms is to investigate the rate of loss of material with respect to dose as a function of the specimen thickness. The knock-on displacement model predicted a constant rate of loss of C or N with increasing specimen thickness as observed in the constant gradients of figure 3.3(a). To calculate a similar rate of loss from the diffusion-based depletion curves of figure 3.6(a) an average "gradient" (as would be fitted to the experimental data in the presence of noise) was extracted using a linear least squares fit computer program. It should be noted that the initial rapid

depletion at small n (shown inserted in figure 3.6a) would still be obvious in the presence of noise and in the experimental data the linear fit would be applied to the initial depletion regions only. Therefore, to remain consistent with experimental procedures and to ensure the comparison of similar initial depletion regions as a function of specimen thickness, the gradients were calculated over a dose which resulted in a 30% loss of material. Imposing this condition on the extraction of an "average gradient" from the depletion curves of figure 3.6a will have very little effect on the gradient extracted from thicker specimens ($n \geq 50$) but has a significant effect at smaller values of n. The choice of a 30% loss was arbitrary and will only change the relative size of the gradients and not the relationship between them. The results are shown in figure 3.7 for both the knock-on displacement and radiation induced diffusion models. As expected, the knock-on displacement model predicts a constant gradient, which is a measure of the rate of loss of C atoms per unit dose. The gradient of unity is not significant and only occurs as a result of the chosen normalisation constant between the specimen thickness and the number of atoms in the specimen. For the diffusion model, at values of thickness corresponding to $n \leq 10$ the gradients are likely to be unrealistic because at such thicknesses neither the atomic distribution nor the jump lengths are effectively continuous variables as assumed in the summation of equation 3.9. Figure 3.7 shows that as the specimen thickness increases, diffusion from the edge of the cylindrically irradiated area becomes dominant resulting in

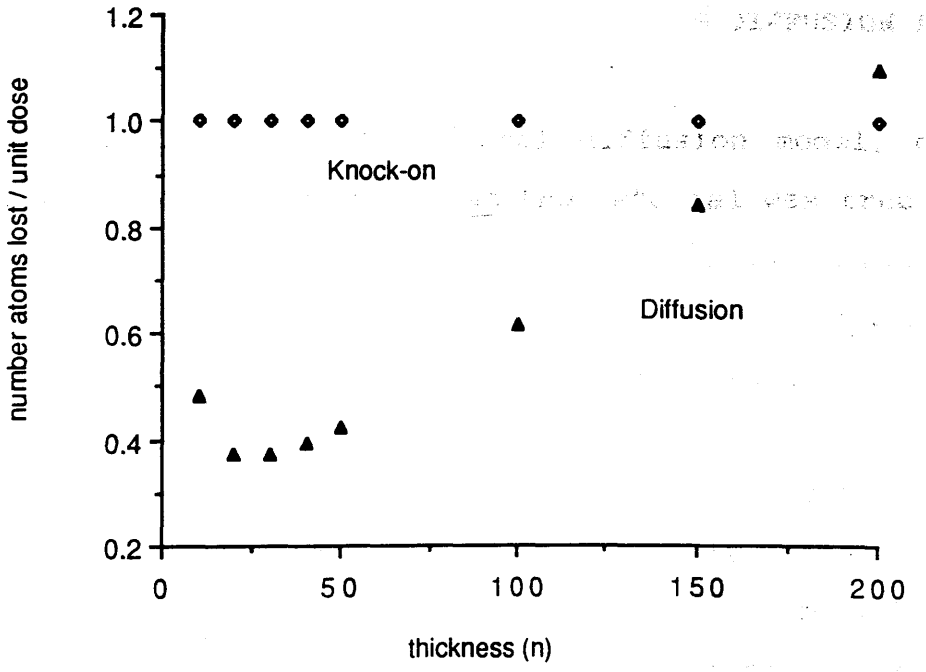

Figure 3.7 The gradients extracted from the theoretical depletion curves predicted by the knock-on displacement model (figure 3.2a) and the radiation induced diffusion model (figure 3.5a) as a function of specimen thickness (n). The gradients are a measure of the rate of loss of material per unit dose.

an increase in the rate of loss of material with specimen thickness.

In conclusion, by examining the relationship between the rate of loss of material as a function of specimen thickness, over a suitably wide range of specimen thicknesses (as in figure 3.7), it should be possible to determine which model best describes the radiation damage process in TiC or TiN.

3.5 A ONE DIMENSIONAL NUMERICAL SOLUTION TO THE DIFFUSION EQUATION

The analytical 3-dimensional diffusion model, discussed in section 3.3, assumed that the material was free to leave the sample on exiting the irradiated volume. Although this applies to the top or bottom surfaces of the sample, the atoms displaced from the edge of the irradiated cylindrical volume will build up in the peripheral regions unless there are mechanisms which can disperse them (such as thermal diffusion). To investigate the likely effect of more realistic boundary conditions, a numerical solution to the 1-dimensional diffusion model was developed by E.Kohl (1990). The program used to evaluate this solution establishes a difference equation for diffusion in a 1-dimensional array given by

$$\frac{U_j^{t+1} - U_j^t}{\Delta t} = \frac{D}{\Delta x^2}\left(U_{j-1}^t + 2U_j^t + U_{j+1}^t \right) \qquad 3.14$$

where U_j^t is the concentration of the j^{th} element in the array at time t, Δx is the jump distance and D is the

effective diffusion coefficient (related to the dose rate in the irradiated region). From equation 3.14 it can be seen that the magnitude of the parameter $\alpha = D\Delta t/\Delta x^2$ determines the time difference (Δt) between successive steps of the program since D and Δx are physically determined. The diffusion coefficients are held in an array where, D_{rad} is the radiation induced diffusion coefficient applicable in the irradiated region and D_{th} is the thermal diffusion coefficient applicable outside the irradiated region. Since the edge of the electron probe is not well defined, the transition between the diffusion coefficients in the irradiated and un-irradiated region is graded over a number of channels. Kohl developed the solution as a tri-diagonal matrix for which there is a rapid solution but found that the algorithm was unstable for large values of α. Consequently, he used a solution which combined the present and previous steps of the difference equations and this was found to produce extra stability.

Although Kohl examined the program extensively, a few simple checks were carried out on the validity of the output from the program before proceeding further with the work described here. Firstly, it was established that an initial delta function concentration distribution spread as a gaussian function of the form $\exp(-x^2/2Dt)$. A second check verified that under conditions which simulated free flow of material from the edge of the specimen, the distribution followed the standard analytical 1-dimensional solution of equation 3.9, where, the concentration distribution eventually tends towards a fundamental sinusoidal term which decays exponentially with time.

As part of this project, the output from the program was modified to produce results in two forms; as a time sequence showing the concentration profiles of material within the sample or as the relative concentration of material within the irradiated region as a function of time (measured in the number of steps through the program). As in the case of the analytical solution of section 3.3, the program was executed for a probe diameter of 44 displacement distances. Figures 3.8, 3.9 and 3.10 show the theoretical depletion curves and the corresponding concentration profiles for a selection of values of the ratio α_{rad}/α_{th} (where $\alpha_{rad}=D_{rad}\Delta t/\Delta x^2$ and $\alpha_{th}=D_{th}\Delta t/\Delta x^2$). The points at which the concentration profiles were extracted are indicated on the depletion curves. From these depletion curves it can be observed that the initial rate of loss of material increases as the value of α_{rad}/α_{th} increases.

As the concentration builds up in the peripheral regions, the loss of material due to radiation induced diffusion is compensated by the gain of material from the surrounding regions due to thermal diffusion which can become considerable in the presence of such high concentration gradients. Consequently, a quasi-equilibrium concentration is achieved beyond which further loss is controlled by thermal diffusion outside the irradiated region. The relative concentration at which this quasi-equilibrium level is attained is dependent on the ratio of the parameters α_{rad} and α_{th} for the radiation induced and thermal diffusion processes respectively. This is consistent with figures 3.8, 3.9 and 3.10 where the

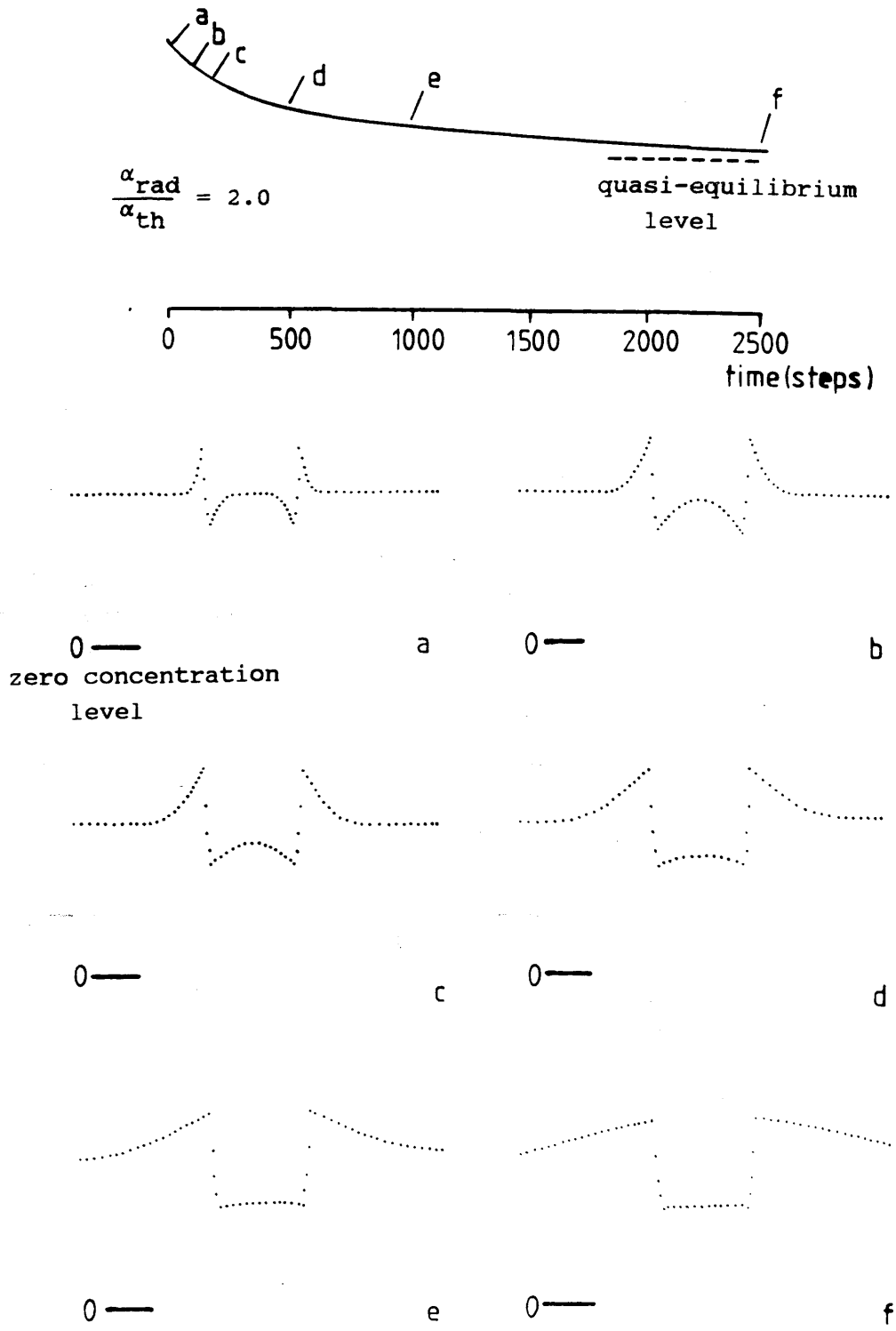

Figure 3.8 Theoretical depletion of material within the irradiated region of the specimen as a function of time for the one dimensional numerical solution to the diffusion equation (equation 3.14). The concentration profiles (a) to (f) show the spatial distribution of material within the sample. The points at which these profiles were calculated is indicated on the depletion curve above.

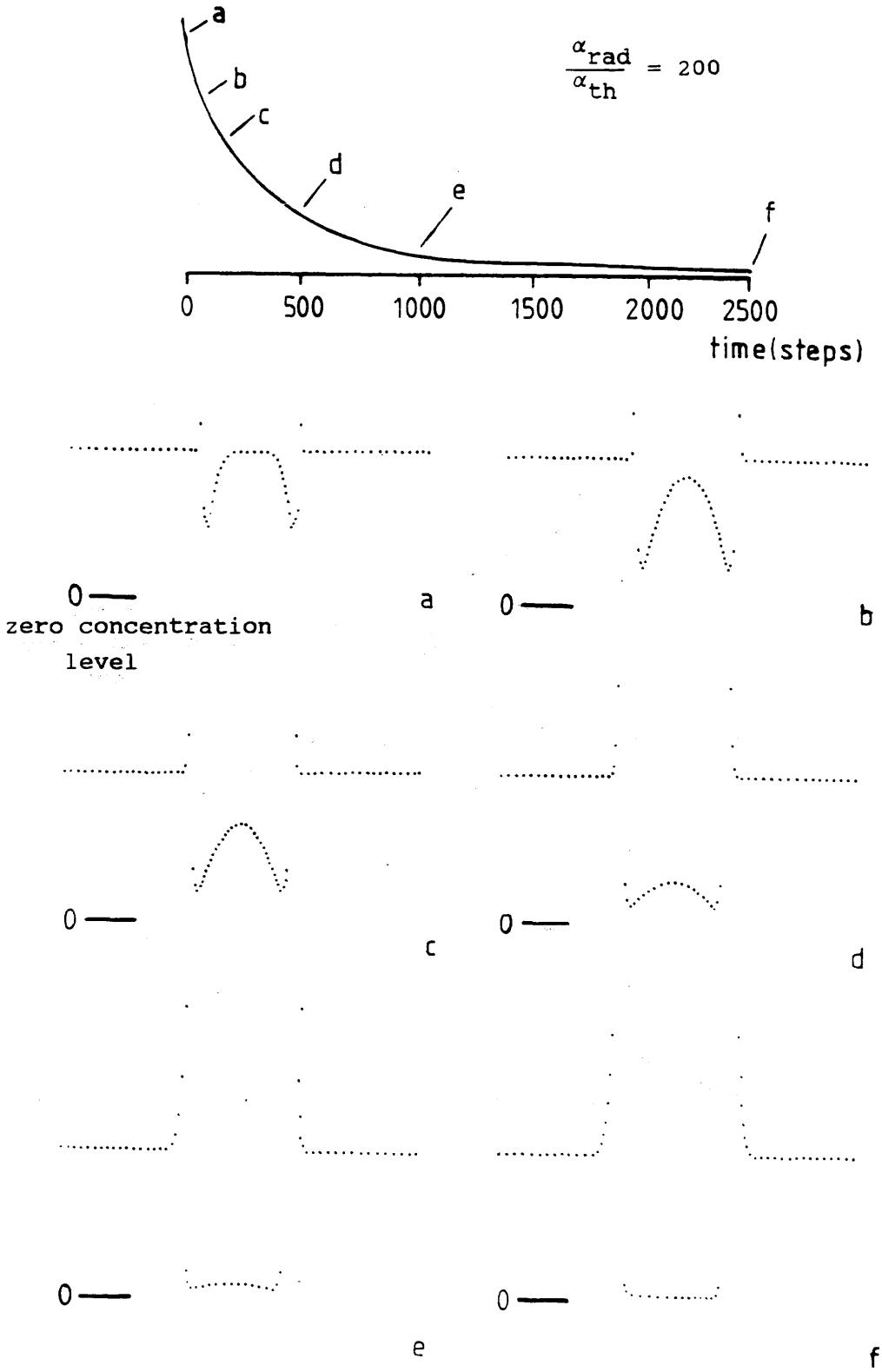

Figure 3.9 Theoretical depletion of material within the irradiated region of the specimen as a function of time for the one dimensional numerical solution to the diffusion equation (equation 3.14). The concentration profiles (a) to (f) show the spatial distribution of material within the sample. The points at which these profiles were calculated is indicated on the depletion curve above.

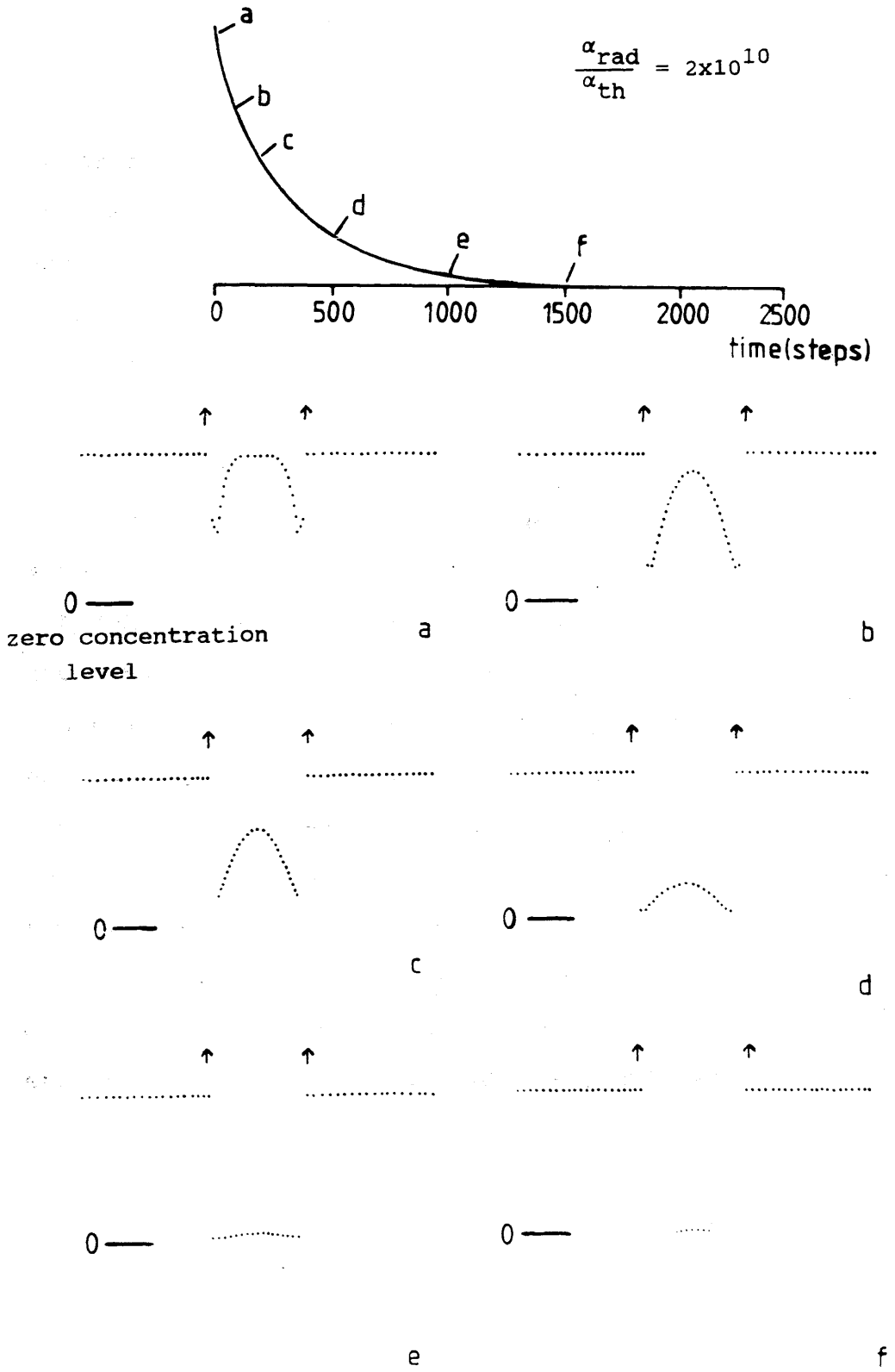

Figure 3.10 Theoretical depletion of material within the irradiated region of the specimen as a function of time for the one dimensional numerical solution to the diffusion equation (equation 3.14). The concentration profiles (a) to (f) show the spatial distribution of material within the sample. The points at which these profiles were calculated is indicated on the depletion curve above.

quasi-equilibrium level decreases as the difference between α_{rad} and α_{th} increases.

For large values of α_{rad}/α_{th} there is a very large build up of material at the boundary (illustrated by an arrow in the concentration profiles of figures 3.10). In reality, however, the displaced atoms will be in positions of high strain and hence have a lower energy barrier for diffusion in a region where the lattice vibrations are far more intense due to the energy deposited by the electron beam. Thus the atoms will disperse from the immediate peripheral areas at a rate higher than predicted by thermal diffusion alone.

Although the thermal diffusion coefficients are not accurately known at room temperature, the extrapolation of experimental self diffusion data for C in TiC (Sarian 1968) provides an approximate diffusion coefficient of $\sim 10^{-53} Å^2/s$. The radiation induced diffusion coefficient (calculated from equation 3.8) is of the order of 1 $Å^2/s$ for an electron dose rate of $3x10^5$ electrons/$Å^2$/s. For these values of diffusion coefficients, the thermal diffusion is effectively zero. However, as noted above, the effective temperature at the periphery of the irradiated region may be much higher than room temperature. Consequently D_{th} may be much higher than the literature suggests in the area immediately surrounding the probe. Nevertheless, it is unlikely to approach D_{rad}.

However, it should be noted that despite these limitations the model does provide a qualitative indication of the overall damage process since the depletion curves of figures 3.9 and 3.10 for $\alpha_{th} \ll \alpha_{rad}$ are consistent with the

experimental results.

Once the general format of the program output was finalised, it was possible to establish the relevance of the assumption of free-flow from the cylindrical surface in the analytical model of section 3.3. The 1-dimensional simulation program discussed here was modified by altering the boundary conditions to allow free flow from the edge of the irradiated region. To enable a direct comparison, a constant α_{rad} of 1.0 is assumed in the irradiated region for both the free-flow and bound conditions. Figure 3.11 compares the result for free flow of material from the edge of the irradiated region with those for a range of α_{rad}/α_{th} ratios when the irradiated region is bounded by material. As expected the largest deviation occurs at large values of α_{th} since there is a significant flow of material back into the irradiated region. For small α_{th}, the agreement after 100 steps of the program is better than 10% for $\alpha_{th}=10^{-11}$(table 3.1) but decreases for increasing time. Even at 500 steps, which corresponds to a 80 to 90% loss of material, consistent with the largest observed experimental loss, the deviation between the free-flow and restricted flow (for $\alpha_{th}=10^{-11}$) is less than 20%. Qualitatively, the solutions are of the form of a free boundary solution sitting on a quasi-equilibrium level. Therefore, for low values of the quasi-equilibrium level (at eg. $\alpha_{th}\sim10^{-11}$), there is only a minor perturbation on the free-flow solutions until the depletion nears the equilibrium condition.

In conclusion, the deviation introduced into the free-flow analytical solution when the irradiated material

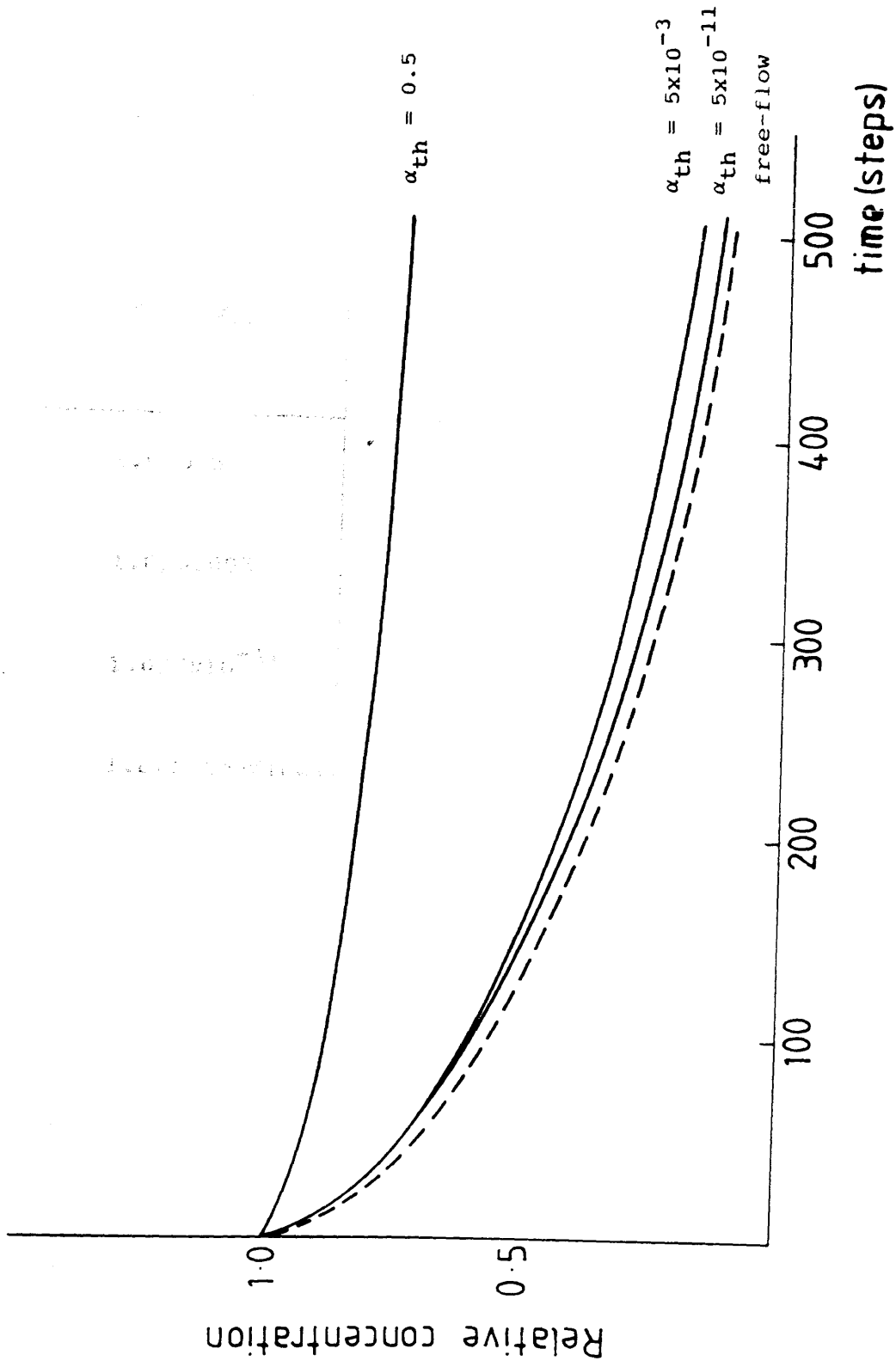

Figure 3.11 Theoretical depletion of material within the irradiated region of the specimen as a function of time for values of α_{th} ranging between 0.5 and $5x10^{-11}$ and a constant α_{rad} of 1.0. Also shown for comparison is the predicted depletion for free flow from the edge of a sample for α_{rad}=1.0.

α_{rad}/α_{th}	concentration at 100 steps	concentration at 500 steps
1.0/0.5	0.908	0.759
1.0/0.005	0.624	0.316
$1.0/5x10^{-11}$	0.608	0.14
1.0(free-flow)	0.559	0.12

Table 3.1 Comparison of the theoretical depletion of material within the irradiated region of the specimen for various values of α_{rad}/α_{th} and free-flow from the edge of the sample at 100 steps and 500 steps through the program. The diameter of the irradiated specimen was 50 displacement distances.

is bounded by specimen is small provided there is a significant difference between the diffusion coefficients of the two processes and the data is not extracted too close to the quasi-equilibrium level.

A further modification was carried out to the program to investigate the effect of probe repositioning errors which were significant in several of the experimental data sets. This was achieved by displacing the position of the irradiated region (corresponding to the probe position) so that it was over the build up of material at one periphery of the initial irradiated region (shown schematically in figure 3.12a). The results are presented in figure 3.12 which shows the theoretical depletion curve and the corresponding concentration profiles for an irradiated region of the specimen where probe repositioning errors have occurred. As expected, figures 3.12 b,c and d show that some of the material from the excess concentration initially flows back into the irradiated region. There is also a large increase in the relative concentration caused by detection of the excess material in the peripheral region. However, the theoretical depletion curve shows that the concentration falls back towards the expected value when the probe is replaced at the original position. In this way, figure 3.12 can be used to justify the procedures adopted when processing the experimental data, namely points which lie above the general trend are considered anomalous and that their effect on subsequent data points can be generally ignored.

In conclusion, the 1-dimensional numerical model provides a useful check on the validity of the approximate boundary

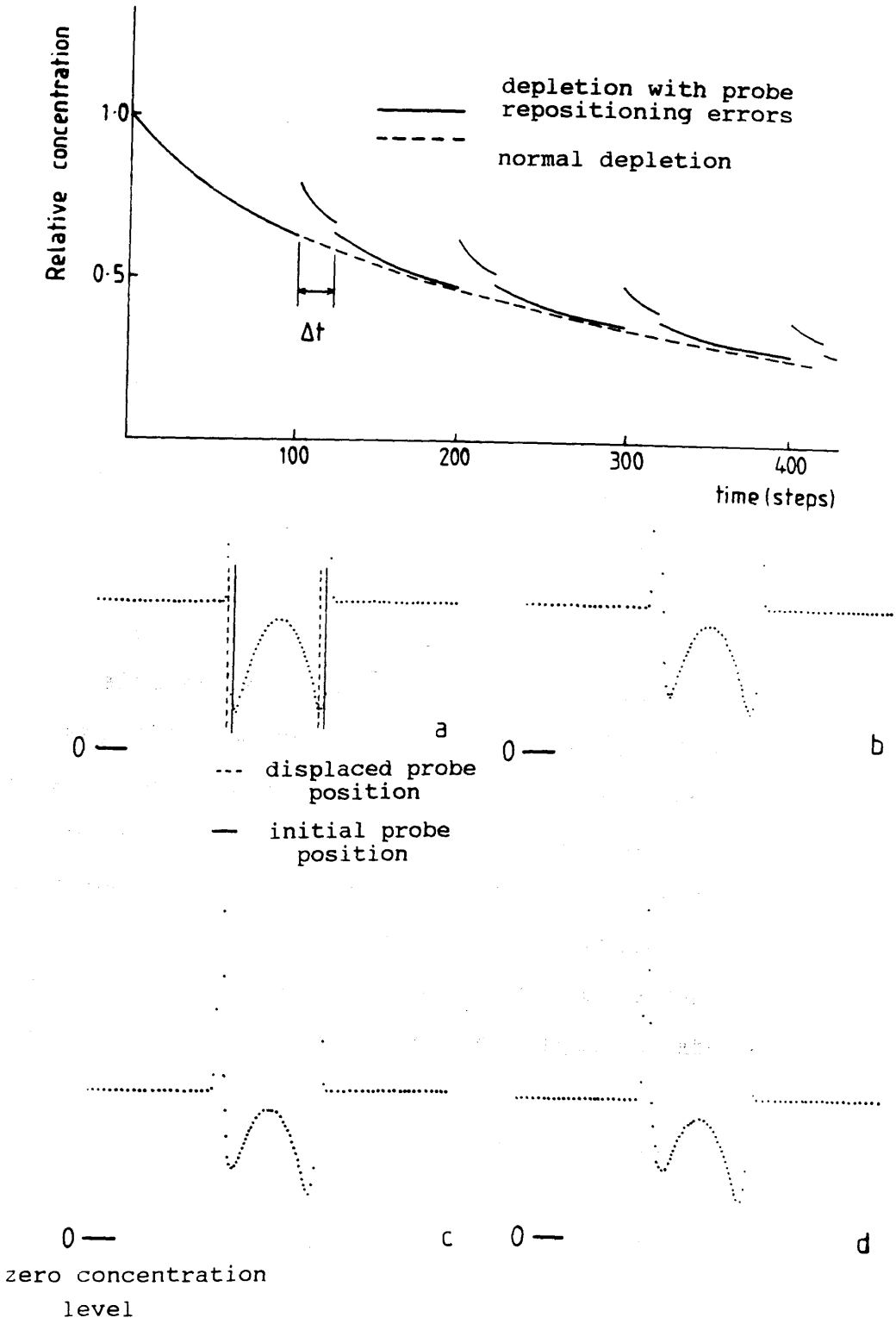

Figure 3.12 Theoretical depletion of material within the irradiated region of the specimen as a function of time for a probe repositioning error with $\alpha_{rad}=1$ and $\alpha_{th}=5\times10^{-3}$. The concentration profiles were extracted before the probe repositioning error (b) and immediately after (c) to (e).

conditions of the analytical solution. It also allows us to check on the overall effect of the probe repositioning errors and confirms the procedures adopted in the experimental analysis of chapter 7.

3.6 CONCLUSIONS

In this chapter, we have presented, contrasted and discussed in detail two possible damage mechanisms; forward knock-on displacement and radiation induced diffusion. These models have considered two possible extremes of the displacement process; displacement of the atom through the sample in a forward direction and random displacements in the sample which are considered to be isotropic due to the "cage effect" of the crystal structure. In reality, however, the damage mechanism is likely to lie somewhere between these two extremes, where the momentum transfer will be forward biased but will have random components in the plane of the specimen. In the presence of the crystal lattice this will lead to a forward bias in the displacement of the atoms which can only be displaced in directions that pass between the larger Ti atoms resulting in a strong channeling effect. An estimate of the relative contribution of each of these damage mechanisms considered here and the way in which the models can be applied to experimental data will be discussed in greater detail in chapters 6 and 7.

CHAPTER 4 INSTRUMENTATION

4.1 INTRODUCTION

All experiments described in this thesis were carried out using an extended VG HB5 scanning transmission electron microscope (STEM). This chapter describes the microscope, the detectors employed in EELS and imaging and the standard operating conditions used to acquire the data presented in this thesis. The majority of the EELS data discussed in this thesis were acquired and stored for subsequent analysis using a Toltec Data Processing System. Towards the end of the work, EELS acquisition was switched to the LINK AN10000 on which all digital images were acquired using the Electron Signal Processing (ESP) program.

Samples with large areas of uniform thickness are essential, as low dose experiments involve defocussing the probe over relatively large areas of the specimen. Consequently, two methods of sample preparation are discussed in the final section of this chapter, namely the deposition of crushed material on a holey carbon support film and preparation from bulk by mechanical polishing followed by ion beam thinning. Some experimental results that compare the relative merits of the two techniques are discussed.

4.2 THE VG HB5 STEM

In a STEM, a demagnified image of the electron source is formed on the specimen by a pre-specimen electron-optical configuration. This image, known as the probe, can be

scanned in a raster across the specimen to form an image or be held stationary for microanalysis. The magnification of the STEM depends solely on the size of the specimen area scanned, the resolution available being dependent on such factors as the size of the probe, the signal examined and specimen thickness. The various signals which arise from the interaction of the incident electron beam with the specimen can be used to form spectra or images by the available detectors. Figure 4.1 shows a schematic diagram of the extended HB5 microscope column at Glasgow University. Details of the source and the various stages of the electron optical system are described separately in this section. The electron detection systems used to collect both the bright and dark field images and EEL spectra are described in the final parts of the section together with a description of the microscope operating conditions used throughout this work.

4.2.1 The Electron Source

Microanalysis with high spatial resolution requires both a small probe size to enable analysis of small volumes of specimen and a high probe current to enable adequate statistical accuracy in the detected signal in an acceptable period of time. These conditions are best satisfied using a field emission gun, detailed by Crewe (1971), which produces a high brightness of the order of 10^9 A/cm^2/sr ie a high probe current contained within a small probe.

The electron gun in the HB5 consists of a single crystal tungsten cathode welded onto a tungsten filament. By

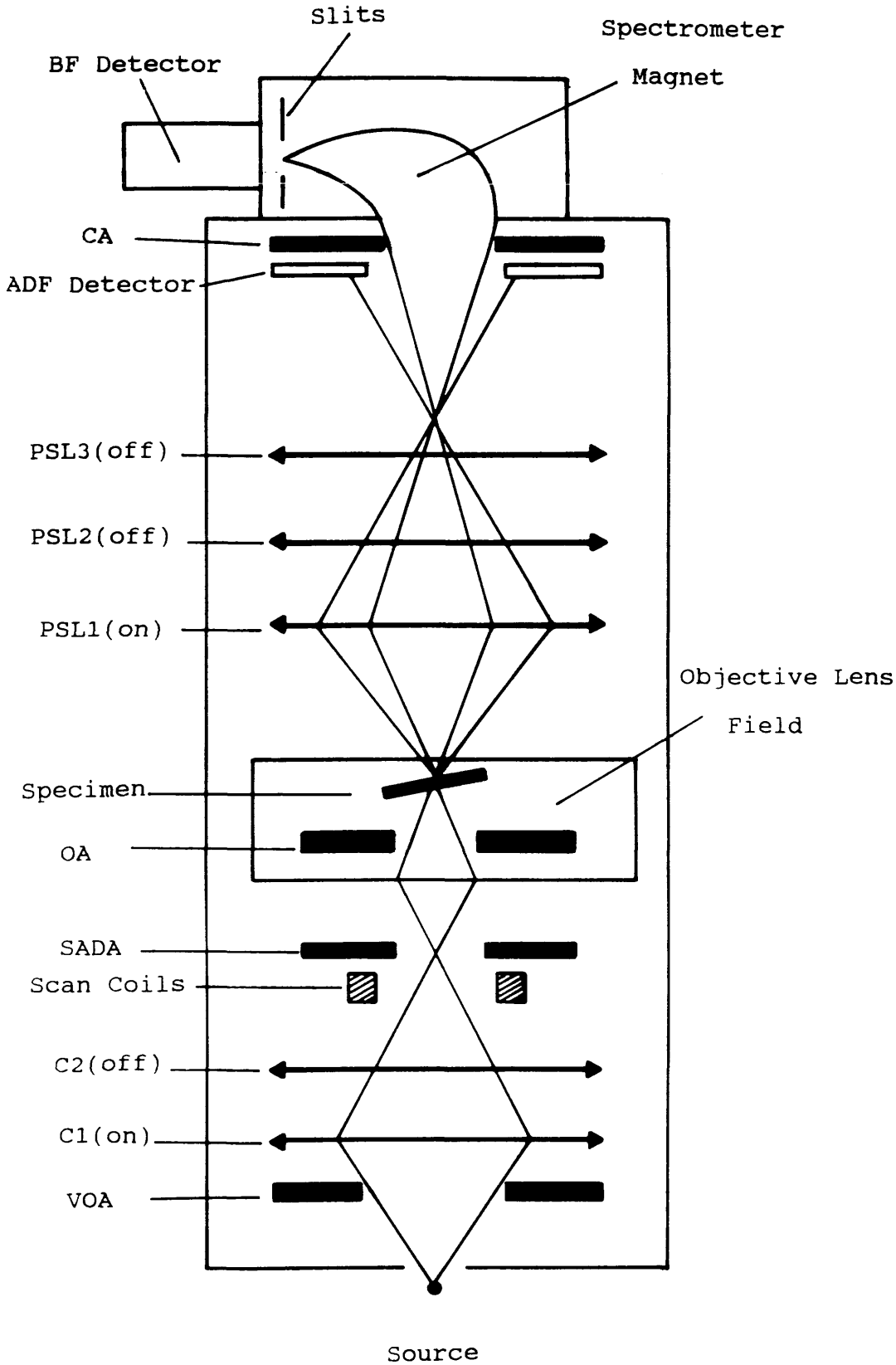

Figure 4.1. Schematic diagram of the extended VG HB5 STEM at Glasgow University.

chemically etching the tip material to a point radius of ~500Å, an extraction voltage of 3 to 4kV is sufficient to strip electrons from the cathode surface. A second anode is then used to accelerate the electrons up to an energy of 100keV. The presence of such a high field at the tip surface (~10^8V/cm) requires a very good vacuum around the tip to prevent vacuum arcing. In the HB5, this is achieved by separating the gun chamber from the relatively large volume of the column of the microscope using a differential pumping aperture which enables a vacuum of ~ 4 x 10^{-11} mbar to be maintained at the gun whilst the rest of the column is in the range 10^{-9} to 10^{-8}mbar. Even under such stringent vacuum conditions, surface contamination can build up on the tungsten cathode causing a change in the emission properties of the tip. This results in a decay of emission current, typically a drop of 10% in 500s, as the work function of the tip material increases. These contaminants are removed from the tip using a procedure known as "flashing" the tip which involves passing a short, high current pulse through the tip support filament at intervals of typically 30 minutes. To achieve a reasonably constant current density on the specimen during radiation damage studies it may be necessary to flash the tip more frequently, depending on the vacuum conditions.

4.2.2 Pre-Specimen Optics

Two condenser lenses are available on the HB5 providing great flexibility for probe forming conditions. However, for EELS microanalysis use of condenser lens C1 only provided the most suitable probe size and current for

radiation damage experiments. In image mode, the excitation of C1 is adjusted to form an intermediate image of the source in the same plane as the selected area diffraction aperture (SADA). Since the specimen is located within the objective lens field the pre-specimen field can be used to form a demagnified image of this intermediate image on the specimen (known as the probe).

The convergence angle, α, of the electron probe is defined by the excitation of the pre-specimen field of the objective lens and the objective aperture (OA) selected. However, Wardell (1982) observed that during microanalysis, stray electrons scattered from the objective aperture blade can lead to a spurious signal in the spectrum. To reduce this contribution a virtual objective aperture (VOA), situated immediately after the source in a plane approximately conjugate to the OA (figure 4.1), is used to define the angular extent of the probe. Stray scattering is further reduced by inserting a small SADA in line with the optic axis. Crozier (1985) measured values of α for several real and virtual objective apertures at a constant excitation of the objective lens using convergent beam diffraction techniques. Details of the convergence angles used in this work will be given in section 4.2.6.

To reduce channeling effects, which may complicate the interpretation of the radiation damage experiments, the specimen was held in a $\pm 30^{\circ}$ beryllium double tilt cartridge, manufactured by VG Microscopes, so enabling the selection of suitable specimen orientation. Contamination problems were reduced by baking the specimen and cartridge which were then left in the microscope vacuum overnight. This enabled specimen and cartridge to attain thermal

equilibrium with the objective lens surroundings, so minimising specimen drift rates.

4.2.3 Post-Specimen Optics

The Glasgow HB5 STEM has been extended to include three post-specimen lenses (PSLs) which, together with the post-specimen field of the objective lens, allow a focussed image of the specimen to be formed on the object plane of the spectrometer. The PSL configuration is selected to match the angular distribution of the transmitted electrons to the detectors used in a particular experiment. For example, to optimise collection efficiency, PSL1 was selected for EELS microanalysis because of the large total compression available in the post specimen optics. The collection semi-angle (β) defines the angle subtended by the spectrometer at the specimen and is limited by both the collector aperture (CA), situated immediately before the spectrometer, and the PSL configuration selected. As discussed in chapter 2, calculation of the theoretical cross-sections requires knowledge of β and these have been measured by Crozier (1985) for the available post-specimen lens configurations. The values used in this work are summarised in section 4.2.6.

4.2.4 The Electron Spectrometer

As discussed above, the post-specimen optics form an image of the specimen in the object plane of the electron spectrometer. The spectrometer magnet deflects these electrons through an angle which is dependent on the

electron energy thus forming an energy loss spectrum. This spectrum can be recorded serially by allowing the scan coils, which are situated after the spectrometer magnet, to scan the spectrum across the slit in front of an electron detector. The spectrometer dispersion plane is tilted with respect to the plane of the slit and so the whole spectrum cannot be focussed at one time. This effect is minimised by focussing the spectrum at the midpoint of the energy region to be scanned.

In the VG Mk1 sector magnet used on the HB5, second order aberrations are dominant and so the resolution is proportional to the square of the collection semi-angle, β (Egerton 1984a). A large collection angle was selected for radiation damage studies in order to maximise the collection efficiency and improve the statistical accuracy. Under these conditions the resolution of the EEL spectra, defined as the full width half maxima of the zero loss peak collected without a specimen, was ~ 2 to 3eV.

4.2.5 Electron Detectors

This work used two of the electron detectors available on the HB5: the annular dark field (ADF) detector and the bright field (BF) detector, which is also used in the collection of EEL spectra. The electron detectors consist of a scintillator coupled to a photomultiplier tube. An electron, on striking the scintillator produces a burst of photons some of which are detected by the photocathode of the photomultiplier producing photoelectrons. The small resultant current is then amplified by the photomultiplier tube and subsequent pre-amplifiers. The signal from the

bright field detector is treated in three different ways; the current signal from the photomultiplier can be used to modulate the signal sent to a cathode ray tube producing a bright field image or passed to the EELS acquisition system where the signal is analysed using two different counting techniques as described in section 4.3.1. The angular range of electrons recorded by the BF detector is, as stated previously, limited by the size of the collector aperture and the PSL configuration. The ADF detector, however, sits just below the CA (figure 4.1) and collects electrons scattered through larger angles in an angular range determined by the size of the inner and outer diameters of the detector (4 and 25mm respectively) and the PSL excitation. It should be noted, however, that although the outer angles subtended by the ADF detector can be limited by distortions these should not be significant for the PSL excitations considered in this work.

4.2.6 Data Acquisition Conditions

This section describes the microscope configuration used throughout all the experiments involving EELS and imaging detailed in this thesis. The z-lift specimen stage facility, available on the HB5 STEM at Glasgow, allows the probe to be focussed on the specimen by varying the specimen height in the objective lens field. Thus the objective lens can be operated at a constant excitation chosen to give suitable optical properties (Buggy 1985). Combined with the fixed position of the intermediate image on the SADA plane, this ensures that the post-specimen lens configuration remains constant throughout all the

experiments ie. a standard microscope configuration may be defined.

Condenser lens C1 was used in conjunction with a 100μm VOA to define a probe convergence angle, α, of 11 mrad at the chosen objective lens excitation (course 18, medium 12, fine 15 (Buggy 1985)). A 25μm SADA was inserted as a spray aperture. The lower dose spectra were acquired by defocussing the condenser lens C1 as discussed in section 6.2.2. Particular care is required whilst aligning the microscope to ensure minimum condenser astigmatism so that radial symmetry is retained when the probe is defocussed. This pre-specimen optical configuration was used in the acquisition of both the ADF images and the EEL spectra.

The ADF digital images were recorded using PSL3 only, at a constant excitation (coarse -2, fine 7.85) corresponding to a total post-specimen angular compression of -2. In conjunction with a 500μm collector aperture this defined a collection semi-angle, β, of 3.1 mrad at the specimen giving rise to high contrast in the BF images and high signal and contrast in the ADF image. As the bright field detector can record either a BF image or an EEL spectra, only ADF images were acquired during spectral analysis to avoid resetting the parameters after each acquisition. As will be discussed later in this thesis the ADF images were recorded with zero black level.

PSL1 was selected for EELS microanalysis at a constant excitation (coarse -6, fine 4.82) corresponding to a total post specimen angular compression of -17. For a 500μm collector aperture, this defined a collection semi-angle, β, of 27 mrad. To record high spatial resolution EEL spectra, the probe was held stationary on the specimen by

entering "computer mode" which disables the analogue scan of the HB5. The values of α and β for the standard microscope operating conditions used in this work are summarised in table 4.1.

Joy (1980) found that when using EELS partial cross-sections to extract quantitative data from a spectra, a correction to the spectrometer collection angle (β) is required for the effects of a convergent probe, since the cross-section calculations in chapter 2 assume parallel illumination. However, Crozier (1985) found that, for β = 27mrad, the correction was negligible provided that the probe convergence angle was less than 15 mrad. This was always the case here and so no probe convergence corrections were necessary.

4.3 THE COMPUTER ACQUISITION SYSTEM

4.3.1 The Toltec Minicomputer

EEL spectra were recorded and processed using a Toltec minicomputer system with a GEMS framestore configured to act as a multiscalar analyser. The system is described in detail by Craven and Buggy (1984), but a brief description of the important points is given here. The computer controls the spectrometer scan coils enabling the spectrum to be collected sequentially. Data are acquired from each channel or energy window (typically 1eV wide) for a period known as the dwell time which is set from the menu before acquisition. By scanning the spectrum from high to low energy loss any distortion due to decay tails in the scintillator from the zero loss peak is minimised. The

aperture type	aperture size	probe convergence semi-angle (α)
VOA	100μm	11.0 mrad

PSL used	collector aperture size	collection semi-angle (β)
PSL1	500μm	26.8 mrad
PSL3	500μm	3.1 mrad

Table 4.1 Values of the probe convergence semi-angle and the collection semi-angle for the standard settings of the objective lens used in this work.

spectra were recorded over a single scan to maximise the energy resolution but it should be borne in mind that this can result in artifacts in the spectra due to fluctuations in the tip current.

To count over the dynamic range present (~10^9 to 10^4 electrons/s in the experiments discussed in this thesis) the EELS acquisition system depends on two independent but simultaneous counting techniques. A pulse counter, which allows single electrons to be counted but saturates at the high count rates such as those in the zero loss peak, is used to analyse high energy losses. This signal is known as the pulse signal. An analogue to digital conversion system based on a voltage to frequency converter is used for low energy losses (typically up to 150eV) but, because of dark current effects, is unsuitable for detecting the low count rates found at higher energy losses. This signal is known as the current signal. As stated previously, the signals are collected simultaneously and stored on disc for further analysis in which they can be merged together to form the EEL spectra as discussed in chapter 5.

The software for configuring the GEMS as a multiscalar analyser and acquiring EEL spectra was written by Toltec Computers Ltd. The acquisition parameters are set from an EELS menu by the user and are described in detail by Crozier (1985). The values used for this work are summarised in table 4.2. Further analysis and spectral manipulation programs have been written and incorporated into the Toltec software by previous users Buggy (1985), Crozier (1985) and Steele (1987). Relevant details of these will be given in chapter 5.

Beam Voltage	100keV	
Count limit	max number of counts in any channel	10^6
Time limit	for radiation experiments	20s
Number of channels		1024
Channel width		1eV
Start energy	energy loss of first channel in the spectrum	-100eV
Zero loss offset	energy of the undeflected beam	-546eV
Rest energy	energy which passes through the slit when no spectrum is being recorded	2000eV
Scan direction	scanned from high to low energy	
Base dwell	dwell time	20ms

Table 4.2 Values for the main parameters in the EELS acquisition as used in this work.

4.3.2 The Link Analytical AN10000

In addition to the TOLTEC acquisition system a number of the later EELS experiments described in this thesis were carried out using a Link Analytical AN10000. An EELS interface was designed and built at Glasgow University to control the EELS spectrometer from the AN10000. The interface reads both the current and pulse signals from the spectrometer, storing one of them in an intermediate memory, as there is only one input channel on the AN10000. All spectra were transferred to the TOLTEC or a UNIX computer since the AN10000 analysis software had not yet been fully developed. The acquisition parameters are set from the EELS menu as described for the TOLTEC in the previous section.

The Link Analytical AN10000 was used primarily to collect digital images using an "Electron Signal Processing" program (ESP). The program can acquire digital images from both the bright and annular dark field detectors by digitally controlling the position of the the electron beam on the specimen. Images were acquired in arrays of 256x256 pixels, with each pixel measured to 8 bit precision. The optimum dwell time of the beam for each pixel was 51μs. The ESP program stores the images in a memory buffer which can then be accessed from the image processing program DIGIPAD and saved for future processing. A description of the image processing techniques is given in chapter 6.

4.4 SPECIMEN PREPARATION

To obtain the low doses required to follow the radiation

damage processes it is necessary to defocus the electron probe over relatively large areas of the specimen (~$1.5 \times 10^4 Å^2$). Consequently, the preparation of samples possessing large uniform areas which are electron transparent (at 100keV incident electron energies) is an important consideration in the work presented in this thesis. The following sections detail two specimen preparation techniques, namely the deposition of crushed material on a holey carbon support film and ion-beam thinning from bulk, and present results from preliminary experiments which can be used to determine the relative merits of each technique.

The TiC and TiN materials were supplied in bulk form by Dr C.G.Chatfield at Sandvik Hard Materials, Sweden. The material had large grain sizes ~500μm and so could be treated as essentially single crystal specimens for electron microscopy. Four different materials were supplied, together with their bulk analysis results as detailed in table 4.3. The bulk analysis was carried out at Sandvik using a standard combustion technique to an accuracy of 0.02% for the N and C where the Ti is determined as the remainder of the TiC or TiN material.

4.4.1 Crushed material on a holey carbon support film

Crushed specimens of TiC and TiN were mounted on holey carbon support films as described in appendix 1. Figure 4.2(a) shows a bright field image of a typical sample prepared in this way, indicating the extent of the electron transparent area overhanging a hole in the carbon support film.

specimen	composition from bulk analysis
A	$TiC_{0.98}$
B	$TiN_{0.59}$
C	$TiN_{0.8}$
D	$TiN_{0.83}$

Table 4.3 Bulk analysis results of the TiC and TiN samples received from Dr. C.G.Chatfield.

Figure 4.2(a). BF image of a TiN sample prepared by crushing the material using a mortar and pestle and then depositing on a holey carbon support film.

Figure 4.2(b). ADF image of a TiN specimen prepared in a similar manner to that shown in (a).

	experimentally calculated concentrations	expectected bulk concentrations
C/Ti	0.79 ± 0.08	0.98
C/Ti	0.86 ± 0.04	0.98
C/Ti	0.91 ± 0.04	0.98
N/Ti	0.59 ± 0.03	0.8
N/Ti	0.75 ± 0.04	0.83

Table 4.4 A comparison of the C/Ti and N/Ti ratios measured by EELS analysis and bulk analysis results for specimens prepared by crushing the material. The experimental EELS results were calculated from radiation damage experiments using the standard Egerton method described in chapter 5 where the results were extrapolated to zero dose to calculate the initial C and N content.

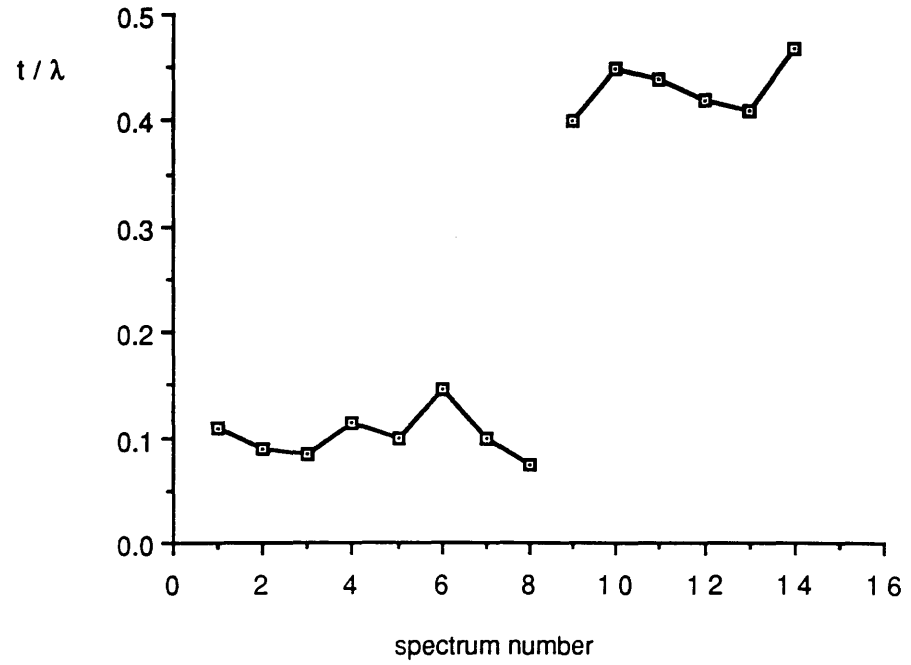

Figure 4.3. t/λ values for a defocus to focus experiment which show the rapid increase in relative thickness when the probe is focussed onto the centre of the specimen.

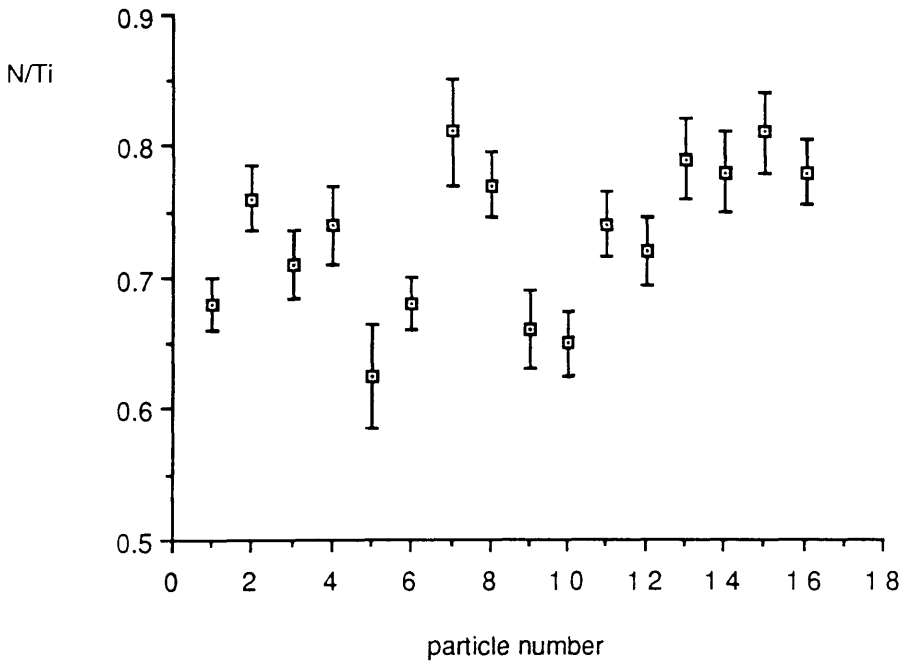

Figure 4.4. N/Ti ratios acquired from a number of particles prepared by crushing and depositing on a holey C support film. The N/Ti ratio was measured at a low dose which causes insignificant mass loss, and was calculated using the hydrogenic cross-section program SIGMAL2.

where the radiation damage is insignificant. Figure 4.4. shows the distribution of N/Ti ratios calculated using the Egerton fit technique with the theoretical cross-section SIGMAL2 (discussed in chapter 5) for the range of particles examined. There was no correlation between the specimen thickness and the composition for the particles investigated. As before the elemental ratios were found to vary about an average value (N/Ti = 0.73±0.02) slightly lower than that expected from the bulk analysis results (N/Ti =0.83)

One possible explanation for these lower than expected N/Ti ratios may be inaccuracies in the theoretical cross-sections used in the calculations. Malis and Titchmarsh (1985, 1986) predicted that both theoretical cross-sections, SIGMALR and SIGMAL2, may underestimate the Ti L-edge by as much as 30%, resulting in a lower than expected elemental ratio. From the experimental data presented in figure 4.4 it is difficult to say whether there is a real effect of lower than expected N content in the areas analysed or whether this is an artifact of the EEL cross-sections used. However, subsequent experiments on ion beam thinned samples revealed elemental ratios that were much closer to the expected bulk results for both TiC and TiN samples using the SIGMAL2 program. Therefore, it would appear likely that the lower than expected N/Ti ratios observed here are an artifact of the specimen preparation where the material is preferentially broken in areas of low N content, possibly because these areas are more brittle.

It should be noted that the standard deviation of the data in figure 4.4 (σ_{n-1}=0.06) was a factor of 2 greater

than the errors resulting from the analysis techniques. This suggests the existence of a real variation in the particle compositions that cannot simply be attributed to fluctuations in concentration due to noise. Therefore, there is an added problem of a variation in the specimen composition when analysing these particles.

In conclusion, although preparing samples by crushing the material is quick and convenient and provides samples suitable for standard EELS microanalysis, the random orientations and rapid changes in the specimen thickness over areas comparable with a defocussed probe make analysis of the radiation damage experiments very difficult. The lower N/Ti ratios also suggests that the samples are preferentially broken at areas with a lower N content which may or may not affect the radiation damage studies to be carried out in this project. Consequently, all subsequent radiation damage experiments described in this thesis were carried out on samples prepared from bulk by ion-beam thinning as described in the next section.

4.4.2 Ion Beam Thinning

An alternative method of preparing samples for TEM and STEM microanalysis involves mechanically thinning the samples to ~50μm and then ion-beam thinning to electron transparency using argon (Ar) ions (eg SiO, Bravman 1984 and various semiconductor materials, Chew and Cullis 1987). As part of this project we have used these references as a starting point to develop the optimum thinning conditions for the ceramic materials TiC and TiN which are discussed in the following pages.

A brief description of the salient features involved in the mechanical thinning of TiC and TiN is given here. However, for a more detailed description the reader is referred to appendix 2. Due to the very slow ion-etching rates of these ceramic materials, it is essential to prepare as thin a sample as possible by mechanical means to reduce the ion-beam thinning times. The material is cut into thin (~1mm) slices using a slow rotation diamond saw to prevent fracture. The specimen is then mounted on a glass slide and polished to a thickness of ~50μm using 600 grit silicon carbide paper. A 3mm disc, suitable for mounting in the microscope specimen holder, is cut from the thinned material using an ultrasonic drill. A copper washer is then mounted onto the disc, using epoxy resin, to provide support before removing it from the glass slide. The specimen is further thinned to ~20μm using a dimple grinder, which has the advantage of providing support at the edges of the specimen whilst forming thin regions at the centre of the disc.

The final thinning to electron transparency is carried out on an Ion-Tech FAB306A ion-beam thinner which bombards the sample with Ar ions causing sputtering from the surfaces of the sample. The specimen chamber is held at a base pressure of 10^{-6}torr to prevent ionisation of any contaminants which may damage the specimen surface. The specimen is placed between two tantalum plates, to provide good thermal contact, in a specimen holder which is rotated at 1 rev/s about a vertical axis as shown in the schematic diagram of figure 4.5. Two beams of Ar ions, which are incident from opposing faces, remove the material by sputtering until a hole is formed in the centre of the

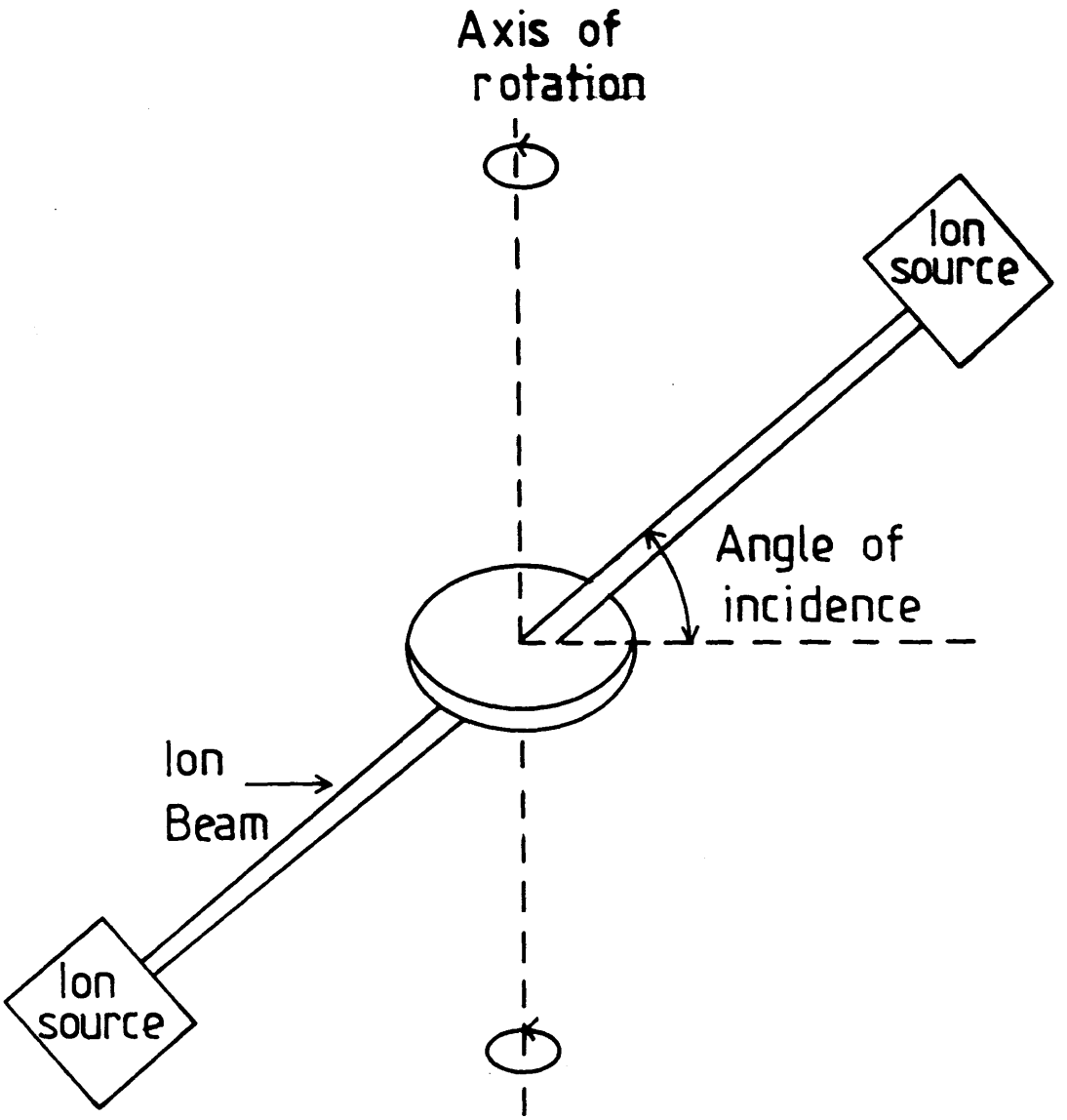

Figure 4.5. Schematic representation of the ion-beam thinner used to prepare specimens that were examined as part of this project.

sample. The ion beam is formed by pumping Ar gas through a needle valve into the ion sources, which are designed to form a saddle field when a potential difference of up to 10kV is applied to the gun. The characteristics of the ion guns are described in detail by Chew and Cullis (1987), but in general, the focussing of the ion beam is controlled by the voltage applied to the gun and the flow of Ar through the gun. As saddle field ion sources are symmetric the ion current at the specimen can be monitored by means of an electrically isolated plate mounted in the path of the ion beam emitted from the rear of the gun. A beam steering unit allows careful alignment of the focussed beam onto the centre of the specimen and is particularly important for dimpled samples where the thickness increases rapidly from the centre of the dimpled area. The beam is centred on the specimen by replacing the specimen with a thin glass slide which fluoresces under the ion beam. The angle of incidence of the beams is an important parameter because it controls the optimum sputtering rates and the extent of thin areas produced around the hole. The beam induced damage is reduced by cooling the sample using a liquid nitrogen "cold finger" and by keeping the angle of incidence to a minimum during thinning. (Chew and Cullis 1987, Howitt 1984).

Initially, the TiC and TiN samples were prepared as described above using 6keV ions with 20μA ion current per gun at an incident angle of 14^{o}, following a private communication with Chatfield (1988). Despite reducing the angle of incidence towards the end of the thinning period to 12^{0} (the minimum possible) only very limited thin regions, unsuitable for EELS microanalysis, were produced.

By reducing the ion beam energies to 5keV whilst

retaining an ion current of 20μA per gun, a reasonable number of thin areas were produced in both the TiC and TiN samples. Because of the long ion beam thinning times involved (>30 hours), the angle of incidence was initially set to 14^{o} and reduced to glancing angles (12^{o}) on perforation of the sample. The final thinning process at glancing angles is carried out using 4keV ions with 10μA per gun to reduce the radiation damage to the surface layer of the specimen.

During initial radiation damage experiments on these samples, anomalies in the measurement of elemental composition in both the TiN and the TiC samples were noted. Firstly, a lower than expected N/Ti ratio was measured at low doses where the radiation damage was minimal. Secondly, a significantly higher C/Ti ratio was measured on the ion-beam thinned TiC samples than was expected from the bulk analysis results. Subsequent experiments established that this excess C was not due to beam induced contamination. However, the monotonic decrease in the C/Ti ratio with increasing specimen thickness, shown in figure 4.6, suggests that there is a uniform layer of carbon on the specimen surface. The most likely source of the excess C is the epoxy resin used in the specimen preparation which may polymerise during a specimen bake depositing a layer of C on the specimen surface. In later experiments to reduce this possible source of C on the specimen surface the specimens were baked in air at $150^{o}C$ before ion beam thinning to remove any contaminants from the glue. This was found to significantly reduce the excess C on the sample but not to eradicate it completely.

Another artifact introduced by ion-beam thinning of TiC

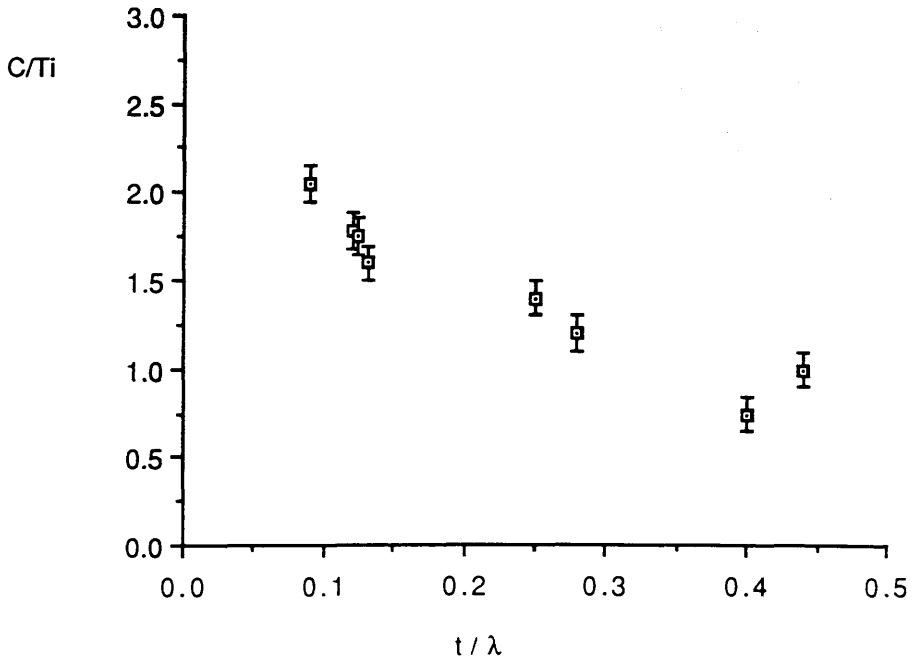

Figure 4.6. C/Ti ratios acquired from a series of radiation damage experiments (extrapolated to zero dose to show the initial C content) as a function of t/λ.

and TiN is shown in figure 4.7, where the surface of the specimen is seen to be very badly ridged. As the ridges run in the same direction throughout an essentially single crystal sample, this would appear to be a crystalographic effect. Therefore, although these specimens are suitable for standard EELS analysis, their topography was on the same scale as the defocussed probe (~130Å) and so they presented similar difficulties for low dose experiments as specimens prepared from crushed material.

In an attempt to reduce the structural damage on the specimen surface, the Ar ion energies were reduced to 4keV for the entire thinning process (with 10μA per gun to retain a focussed ion probe). The initial thinning was carried out at 14^{o} with a reduction to glancing angles as soon as specimen perforation occurred. These conditions were found to eradicate the ridging effects and to provide much smoother specimen surfaces, together with an elemental composition closer to the predicted bulk composition for both the TiC and TiN samples. As a result of shadowing effects (Howitt 1984), where irregularities in the specimen surface cause preferential etching, it was found to be necessary to thin at the lower ion energies throughout the thinning process and not just during the final thinning process. The micrograph in figure 4.8 shows the improved quality of the samples prepared under these ion beam thinning conditions.

In conclusion, the work described here has shown that by pre-baking the specimen and ion beam thinning at lower ion energies, artifacts induced by the ion-beam thinning specimen preparation technique are reduced. This work has shown that, with suitable care and attention, ion beam

Figure 4.7(a). ADF image of a TiC sample prepared by ion-beam thinning using 5keV Ar ions and 20μA ion current per gun.

Figure 4.7(b). ADF image of a TiN sample prepared by ion-beam thinning using 5keV Ar ions and 20μA ion current per gun.

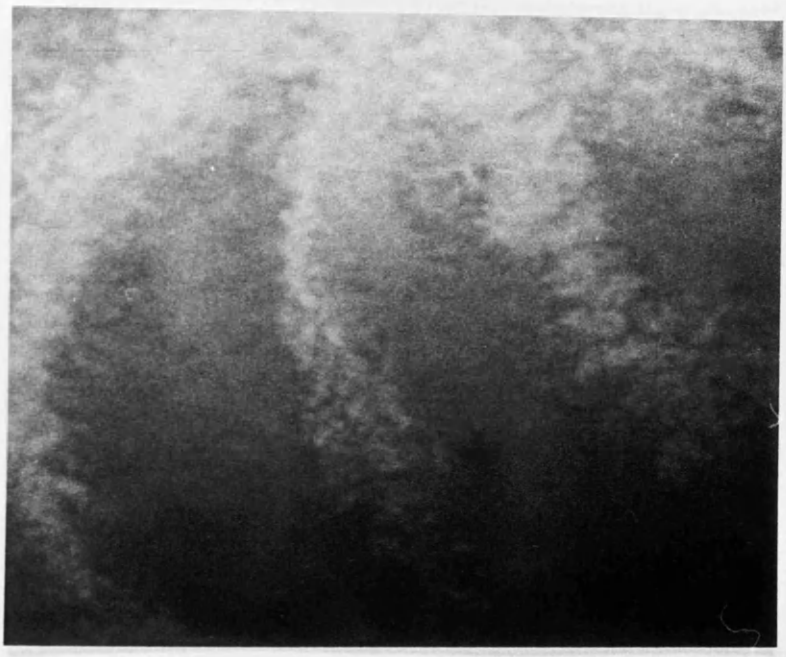

Figure 4.8. ADF image of a TiN sample prepared by ion-beam thinning using 4keV Ar ions and 10μA ion current per gun.

thinning of brittle materials such as TiC and TiN can produce samples suitable for radiation damage studies.

CHAPTER 5 DATA ANALYSIS TECHNIQUES

5.1 INTRODUCTION

This chapter describes the procedures used for the extraction of quantitative information from EEL spectra. We begin with a discussion of the different processes which contribute to the EEL spectrum and the way in which, using the theory outlined in chapter 2, elemental concentrations can be determined.

As a result of the rapid mass loss observed in VC and TiN specimens at the high dose rates available in a focussed probe, the dose rate in the experiments described in this thesis was significantly reduced by using a defocussed probe. However, for the acquisition times considered in this work, this results in poor statistical accuracy, which in turn hinders the extraction of characteristic signals from the spectra. Three methods of signal extraction are examined here to determine which, if any, is the most reliable when applied to noisy data. We will show that analysis of the VC data produces similar results for all three techniques but that there is some doubt as to whether there is mass loss observed or that the results produced are simply a variation about a mean value. A more stringent test on the stabilities of each of the background fitting techniques is carried out on a series of TiN spectra where the proximity of the N and Ti characteristic edges necessitate small fitting windows.

In addition, each of the three techniques was applied to theoretical spectra, where the values of the fitting parameters were known, to see if any of the techniques

introduced a systematic shift in the calculation of A and r, the fitting parameters.

5.2. THE FORM OF AN EEL SPECTRUM

As discussed in section 4.3.1, all EEL spectra were acquired using two independent but simultaneous counting techniques; analogue (current spectrum) and digital (pulse spectrum). To obtain a single spectrum that is valid over the entire energy range of interest, a series of programs were developed for the Toltec minicomputer (Craven and Buggy 1984). These programs merge the pulse and analogue signals together at a suitable energy, simultaneously correcting a number of the artifacts inherent in the spectra that can be attributed to the collection system such as non-linearity in the analogue system at high counts.

The corrections for dead time in the pulse signal and dark current in the analogue signal are insignificant in the characteristic edges of interest in this thesis since the switch-over between the counting techniques occurs well away from any features of interest. However, where an estimate of the absolute number of atoms is required rather than the elemental ratio, the scaling factor between the pulse and analogue signal becomes an important parameter. In addition, any non-linearity in the zero-loss peak may be significant when measuring specimen thickness.

Figure 5.1 shows a VC spectrum in which the pulse and analogue signals have been merged and corrected. Several different processes contribute to the EEL spectrum and the importance of each depends on the energy range of interest.

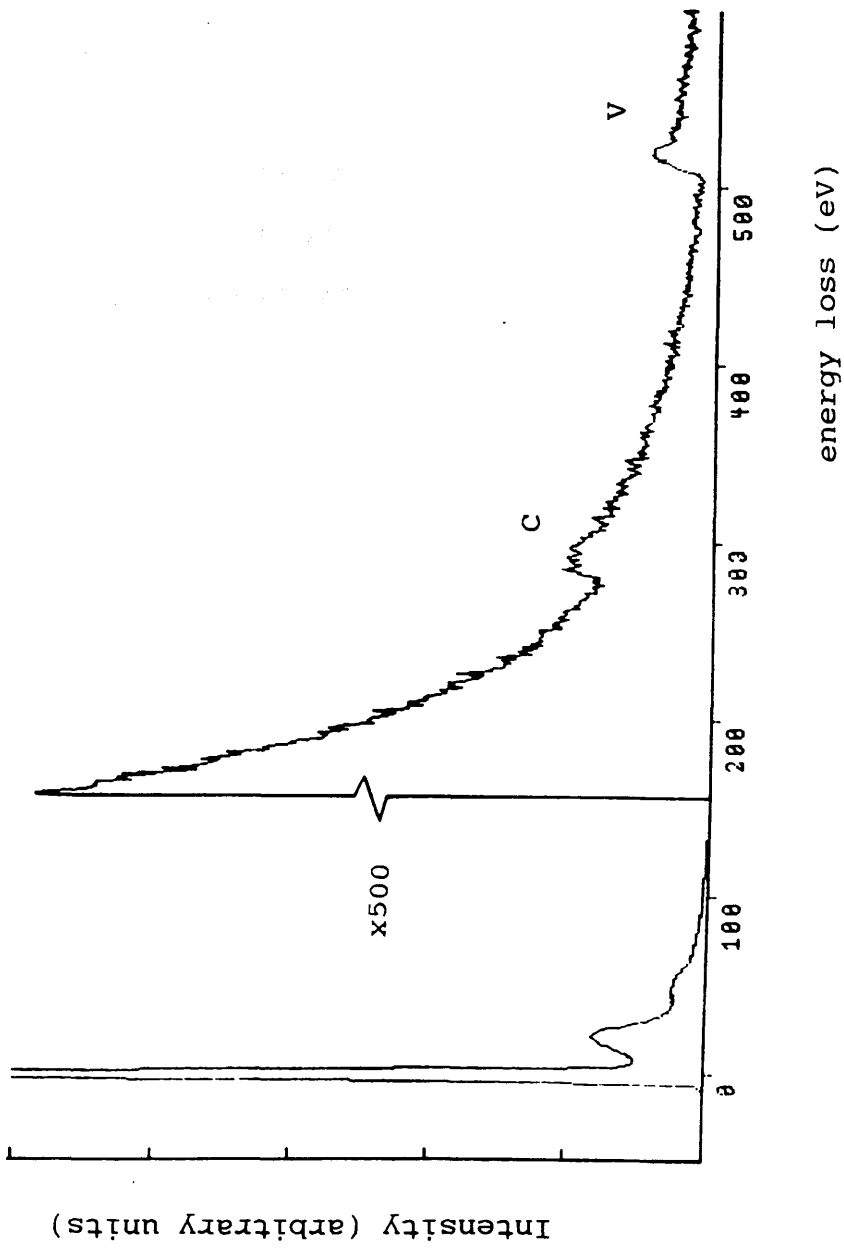

Figure 5.1. A typical VC electron energy loss spectrum showing the low loss region (analogue spectrum) and the characteristic C and V edges (digital spectrum).

In the low energy loss region (<100eV) counts detected in the zero loss peak can arise from three different processes: For a thin sample, the predominant contribution to the zero loss peak comes from electrons which have passed through the sample without undergoing any interaction. Also included in the zero loss peak are elastically scattered electrons which have not undergone any subsequent inelastic scattering and electrons which have transferred energy to the material in the form of phonons. The latter are included in the zero loss peak since the energy losses are less than the energy resolution of the spectrometer (~2 to 3eV).

At slightly higher energy losses (between ~5 and 30eV Egerton 1985), there are broad peaks in detected intensity which result from interactions with the valence electrons in the specimen causing plasmon excitations as discussed in section 2.5.2. For the VC, TiN and TiC materials of interest in this thesis, there is also a characteristic M edge from the transition element superimposed on the high energy side of the plasmon peaks. The characteristic M-edges are ~48 and ~53eV for Ti and V respectively. Therefore, for plasmon energies in the range 20 to 25eV found in VC, TiC and TiN the second plasmon excitation will be strongly affected by the characteristic M-edge from the transition elements Ti and V. The importance of the low energy loss region in the determination of specimen thickness was discussed in section 2.5.2.

Beyond the low loss region the spectrum consists of a monotonically decreasing "background" on which are superimposed signals characteristic of the elements present in the sample under investigation. These signals are formed

by excitation of the electrons within atomic inner shells by the incident electron beam. A significant contribution to the background arises from the tail of the low energy losses such as a plasmon excitations and to valence electron scattering. For many materials there is also a contribution to the background from the tails of preceding core loss edges of other elements or higher atomic shells of the same element. Consequently, the signal to background ratio depends strongly on the specimen thickness and the nature of other elements that are present in the sample but in general is much lower than that found in EDX spectra.

From the definition of the cross-section for electron energy loss in equation 2.1 the number of atoms per unit area of element a, n_a, is given by

$$n_a = \frac{S_a(\delta,\beta)}{\sigma_a(\delta,\beta)\ I_{11}(\delta)} \qquad 5.1$$

where $S_a(\delta,\beta)$ is the intensity of the characteristic signal obtained using a collection angle β and integrated over energy loss range E to E+δE, $I_{11}(\delta)$ is the low loss signal integrated over the same energy loss range, 0 to δ and $\sigma_a(\delta,\beta)$ is the relevant partial ionisation cross-section. $I_{11}(\delta)$ is used instead of the total number of incident electrons as it takes into consideration (to a first approximation) both elastic and multiple inelastic scattering (Egerton 1978).

When the integration window, δE, is the same for two edges, the relative concentration (C_{ab}) of elements a and b is given by

$$C_{ab} = \frac{S_a \, \sigma_b}{S_b \, \sigma_a} \qquad 5.2$$

It is this ratio, C_{ab}, which is most commonly used in EELS analysis since, to a first approximation, the relative contributions from multiple scattering in each of the characteristic edges cancel out if similar integration windows are selected.

The discussions in chapter 2 suggested that the available theoretical cross-sections for the K-shell or L-shell ionisations are more reliable than those for higher energy excitations. Consequently, quantitative EELS analysis is generally limited to light and medium elements which have characteristic K and L edges within the energy range 0 to 2keV that is scanned during EELS acquisition. Such constraints are, however, suitable for the analysis of TiN, TiC and VC. The accuracy with which the elemental concentration, C_{ab}, can be determined is limited by the extraction of the characteristic edges from the background. This process is discussed in the following sections.

5.3 EXTRACTION OF CHARACTERISTIC SIGNALS: BACKGROUND SUBTRACTION

In order to determine elemental concentrations using equation 5.2, the characteristic signal, S_a, must be extracted from the uninformative background signal. The most commonly used procedure is to fit a functional form before the edge and to extrapolate this to energies beneath the edge. The simplest and most commonly used background form is suggested by the linear decrease in intensity when

the spectrum is plotted on a log-log scale. Accordingly, the background Y(E), is usually fitted to a function of the form

$$Y(E) = AE^{-r} \qquad 5.3$$

where A and r are constants of the fitting region. However, r is only constant over a limited energy range which gives rise to inaccuracies if the background is extrapolated over a large range of energy loss.

The poor statistics that are inherent to spectra acquired during radiation damage experiments carried out at low doses exacerbate the problems of fitting the functional form of 5.3 to experimental data. Therefore, the following sections compare and contrast three background fitting techniques to see which, if any, offers an advantage in the presence of noise. There are several methods for calculating the background contribution, and in the following sections we consider two which calculate the functional form preceding the characteristic edge and a third which calculates the functional form both before and after the edge.

5.3.1 The Egerton Fit

The function AE^{-r} may be fitted to the region of the spectrum preceding an edge using a weighted least squares fit (Guest 1961,Barford 1967). Egerton noted that the least square procedure is simplified by making a log transformation so that equation 5.3 becomes

$$\ln(Y_i) = r\ln(E_i) + \ln(A) \qquad 5.4$$

where Y_i is the number of counts in the i^{th} channel with energy loss E_i. The solution of a least square equation for a straight line is well known.

Software to enable a weighted least square background fit according to Egerton has been written by Crozier (1985) for execution on the Toltec computer. A brief summary of the algorithm, known as the Egerton fit (EF), is given here with reference to a typical Vanadium edge as shown in figure 5.2. Most programs on the Toltec computer deal with energies relative to the energy loss marked by the position of a cursor, known as the "bug". A weighted least square fit is carried out in the pre-edge fitting region, w_1, to calculate the optimum values for the fitting parameters A and r in equation 5.4. The background curve described by these values of A and r is then extrapolated beneath the edge, over the energy range w_2 and subtracted from the spectrum to leave a stripped edge, S_a.

Egerton (1982) attributed the error with which the characteristic signal can be extracted from the background to a random error. This results from both the statistical fluctuations within the spectrum on the determination of A and r and the effect of these uncertainties in A and r on the extrapolation of the background beneath the characteristic edge. The error bars associated with the elemental concentrations quoted throughout this thesis have been evaluated by the EF program from these random errors, according to Egerton (1982). There is also a systematic error that is attributable to the deviation of the background from the inverse power law. However, this

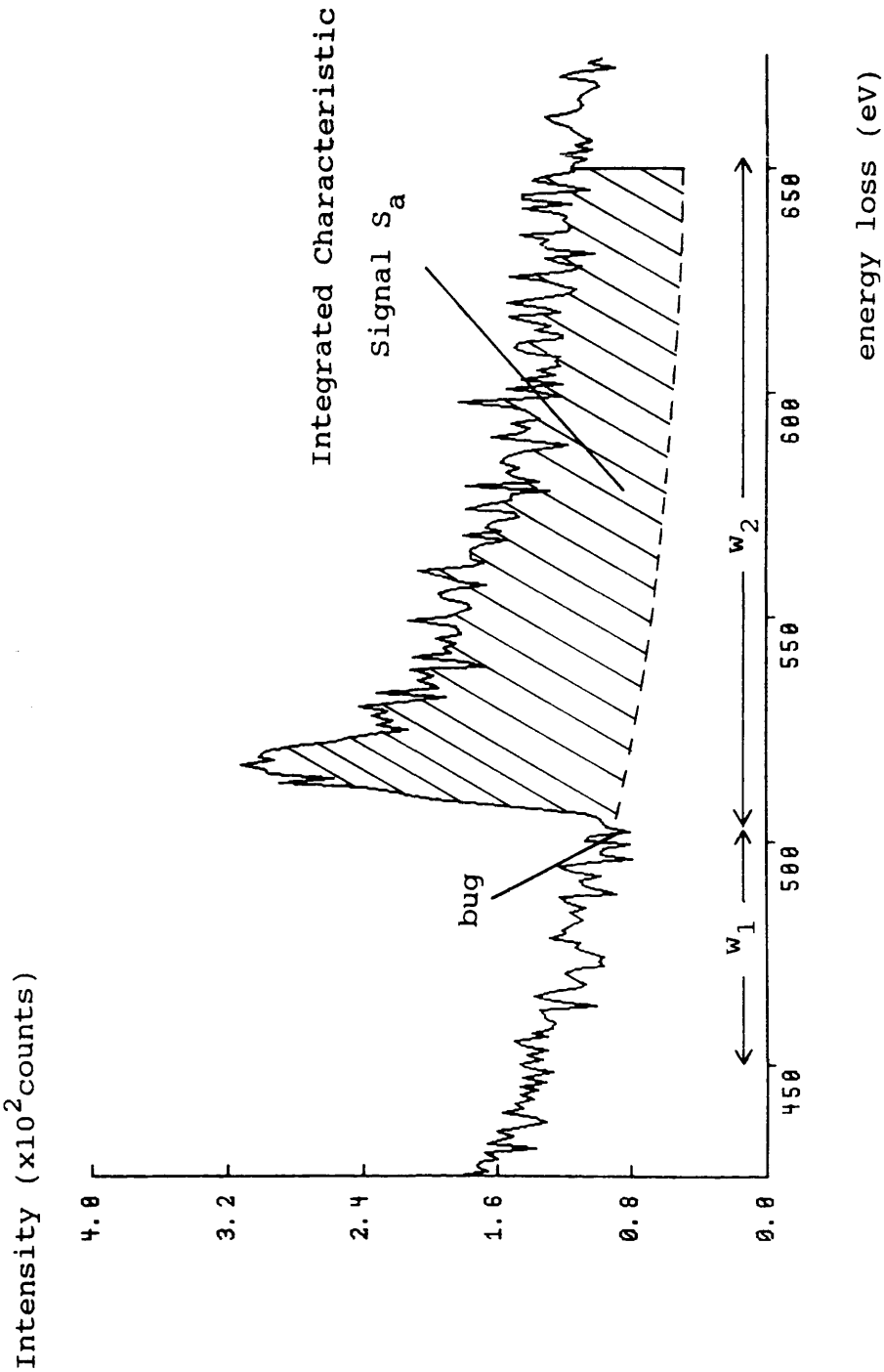

Figure 5.2. A V L-edge illustrating the fitting and extrapolation windows required for the EF and TF techniques.

systematic error is more difficult to quantify and in general is minimised by fitting over a region of the background unaffected by preceding edges, or in other words, by choosing an area of the background where the power law holds best.

5.3.2 The Trebbia Fit

Many authors have noted that the log transformation involved in the EF can introduce a bias in the result, particularly for noisy data (eg. Buggy(1985) and Pun(1985)). Trebbia (1988) developed a program, known as the Trebbia fit (TF), which fits the functional form AE^{-r} to the region before the characteristic edge using a maximum likelihood search. This involves minimising a function of the form

$$\chi^2 = \frac{1}{N_1-1} \sum_{i=0}^{N_1} \frac{(Y_i - AE_i^{-r})^2}{Y_i} \qquad 5.5$$

over a pre-edge fitting region, w_1, as defined in figure 5.2. where Y_i is the number of counts in the i^{th} channel and N_1 is the number of channels in the pre-edge fitting region. For a Poisson noise distribution the variance is equal to the number of counts in the channel, Y_i. As for the EF, the best estimate of the background and hence the characteristic signal is achieved by extrapolating beneath the characteristic edge over an energy range w_2. By evaluating the variances and covariances of A and r, the program estimates the variance and thus the error on the integrated signal, S_a.

As part of this project, the TF program was modified to run on an IBM mainframe. However, since there were no spectral display facilities on the IBM, the spectra were transferred as data files from the Toltec minicomputer, the start and finish energies being determined beforehand.

5.3.3 Background Fitting Incorporating Scaled Cross-Sections.

Regardless of the method used to fit the functional form, AE^{-r} to the pre-edge region, inaccuracies occur when the background is extrapolated over a large energy loss. This effect is particularly important in cases where the pre-edge fitting region is restricted by a preceding edge. The inaccuracies involved may be reduced by fitting a function both before and after the edge. Steele et al (1985) proposed such a technique which involved fitting a function of the form

$$F(E) = AE^{-r} + k\sigma(E) \qquad 5.6$$

where A and r are fitting constants as defined in the extrapolation techniques, $\sigma(E)$ is the energy differential cross-section which is zero before the edge onset and k is a scaling factor for the cross-section, acting as a third fitting parameter. Using this technique, the background shape is fitted to the experimental data both before and after the edge onset. The constant k is proportional to the number of scattering atoms which allows equation 5.2 to be rewritten as

$$C_{ab} = \frac{k_a}{k_b} \qquad 5.7$$

where k_a and k_b are the cross-section scaling factors associated with elements a and b. As the program yielded the required elemental ratios, Steele named the process the single stage fit (SSF). In practice, however, the process requires many preparatory steps before the SSF program can be executed and takes much longer to run than the simpler EF or TF techniques. The anticipated advantage of this technique lies in the improved accuracy of the background fits especially where the pre-edge fitting region is restricted.

Software designed to run the SSF routine on the Toltec computer was written by J.D.Steele and is described in detail in his PhD thesis (1987). The relevant fitting windows for the SSF are shown schematically in figure 5.3, where an additional offset (O_c) is required in the post-edge fitting region. This prevents fitting over the near-edge region where the theoretical cross-section is least accurate. The alignment offset, O_A, allows the theoretical cross-section to be aligned with the experimental edge. For each value of r, the program finds the minimum χ^2 in the pre-edge region by minimising a reduced chi-squared function of the form

$$\chi_1^2 = \frac{1}{N_1-1} \sum_{i=0}^{N_1} \frac{(Y_i - AE_i^{-r})^2}{Y_i} \qquad 5.8$$

where Y_i is the number of counts in the i^{th} channel, N_1 is

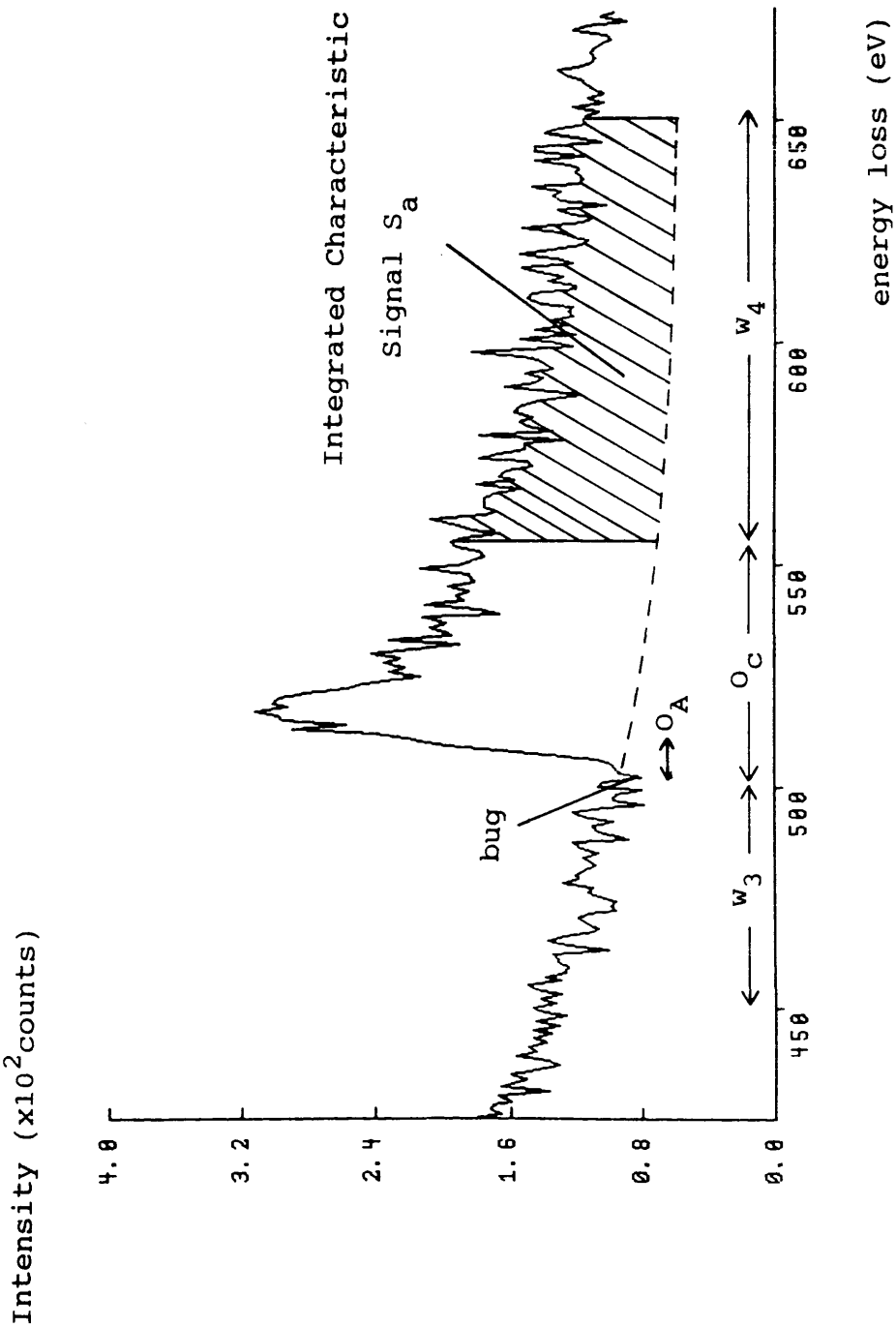

Figure 5.3. A V L-edge illustrating the pre-edge and post-edge fitting windows required for the SSF technique.

the number of channels in the pre-edge fitting region w_3. Since the same function is being minimised in the TF and the SSF one would expect the same value for χ^2 and the fitting parameters A and r. However, the SSF carries out the search for the minimum χ^2 by finding the optimum value of A for every value of r. Thus it searches the two parameter space along lines of equal r. The TF method searches all of the two parameter space and therefore depending on the precision of the different techniques they may not give exactly the same value of r for the minimum χ^2.

Having produced an optimum value of the parameter A for a given value of r, the program then fits over the post-edge region w_4 to find the optimum value of k by minimising another reduced chi-squared function of the form

$$\chi^2 = \frac{1}{N_2-1} \sum_{j=0}^{N_2} \left(\frac{Y_j - (AE_j^{-r} + k \frac{d\sigma}{dE_j})}{Y_j} \right) \qquad 5.9$$

where Y_j is the number of counts in the j^{th} channel, $d\sigma/dE_j$ is the energy differential cross-section, N_2 is the number of channels in the post-edge fitting region w_2 and the only variable in this expression is k.

In this way, a set of values of the three fitting parameters can be produced, with optimum values of A and k for each r. The program selects one value of r, with it's corresponding value for A and k, on the basis of minimising the total χ^2 defined by

$$\chi_T^2 = \chi_1^2 + \chi_2^2 \qquad 5.10$$

Initially, a wide range of r is chosen to ensure a minimum χ_T^2 within the range. Successively smaller ranges of r are chosen until the variation in χ_T^2 between two r values at the minimum is small, $\sim 10^{-3}$. Thus, obtaining a background fit and the corresponding k-value with the required accuracy often entails the program to be run 2 or 3 times for each characteristic edge.

One of the main disadvantages of the SSF technique as implemented by Steele (1987) is that it does not estimate the variances of the fitting parameters A, r and k since they are all interdependent. Consequently, the elemental ratios calculated from equation 5.7 are quoted without error bars throughout this thesis.

5.3.4 Theoretical Cross-Sections for the SSF

The SSF technique that was discussed in the previous section involves a direct comparison between the theoretical energy differential cross-section, $d\sigma/dE$, and the experimental edge. However, the latter is affected by factors such as multiple scattering and the finite energy resolution of the spectrometer, which are not allowed for in the theoretical cross-sections. Egerton (1985) suggested that the effects of multiple scattering may be removed from the experimental edges by deconvolution with the low loss region of the spectrum, provided chromatic aberrations are not significant. However, a simpler method has been adopted here, where the theoretical cross-section has been convoluted with the low-loss region of the spectrum. Paterson (1988) has written FORTRAN programs to convolute

the theoretical cross-sections SIGMAKR and SIGMAL2 with the low loss region of the spectrum. It should be noted that, before the low loss region is convoluted with the L-edge cross-sections, corrections are made for the spin orbit splitting of the L_2 and L_3 edges (Ahn and Rez 1985). The output from the convolution program is then suitable for use in the SSF program.

5.4. ANALYSIS OF VANADIUM CARBIDE PRECIPITATES.

The accurate analysis of data from initial experiments on VC precipitates, carried out with high spatial resolution, was hindered by the rapid loss of C at the high current densities available in the focussed probe (Duckworth 1985). To alleviate this problem, further experiments were carried out using a defocussed probe, which resulted in a lower accumulated dose incident on the specimen. These experiments were carried out to determine whether it was possible to extrapolate the C/V ratios to zero dose in a reliable manner and so measure the composition of the precipitates. A defocus to focus series, as defined in chapter 4, was collected from a VC precipitate on a Si extraction replica by Duckworth (1988) under the microscope operating conditions detailed in section 4.2.6.

As part of this project, these VC spectra were used to compare and contrast the reliability of the data extraction techniques outlined in the previous sections in the presence of noise. The VC spectra were particularly suitable as test spectra because the C and V edges at 280eV and 513eV respectively are well separated. This allows a range of fitting regions to be selected, which are not

restricted by the characteristic edges, in order to ascertain the optimum fitting windows for each technique.

5.4.1. Comparison of Fitting Techniques on the VC Data.

To analyse a series of VC spectra, a typical spectrum with no obvious artifacts was selected to establish the optimum fitting windows for each of the fitting techniques. The pre-edge window, w_1, was selected by examining the variation of the fitting parameter r with the magnitude of the pre-edge fitting window. Figure 5.4(a) shows the value of r as a function of the pre-edge fitting window for the EF, TF and SSF on a typical C edge. It should be noted that a post edge fitting window of 150eV and an offset of 60eV were selected for the SSF, the choice of which will be discussed in more detail later in this section. Figure 5.4(a) shows that only the SSF remains sensible over small fitting windows, the EF and TF proving unreliable at pre-edge fitting windows less than 50eV. This is not surprising since the SSF technique was developed specifically for situations such as these. For larger pre-edge fitting windows, the value of r decreases in all the fitting techniques because the fitting parameters are constant only over a limited energy range. The actual variations in r are dependent on the noise spread in the spectra and vary from spectrum to spectrum as will be discussed for the theoretical spectra in section 5.7. For the calculations described here, a 60eV pre-edge window was selected for both the C and V edges because it yielded a consistent value of r for each of the three fitting techniques which had not yet started to decrease. It should

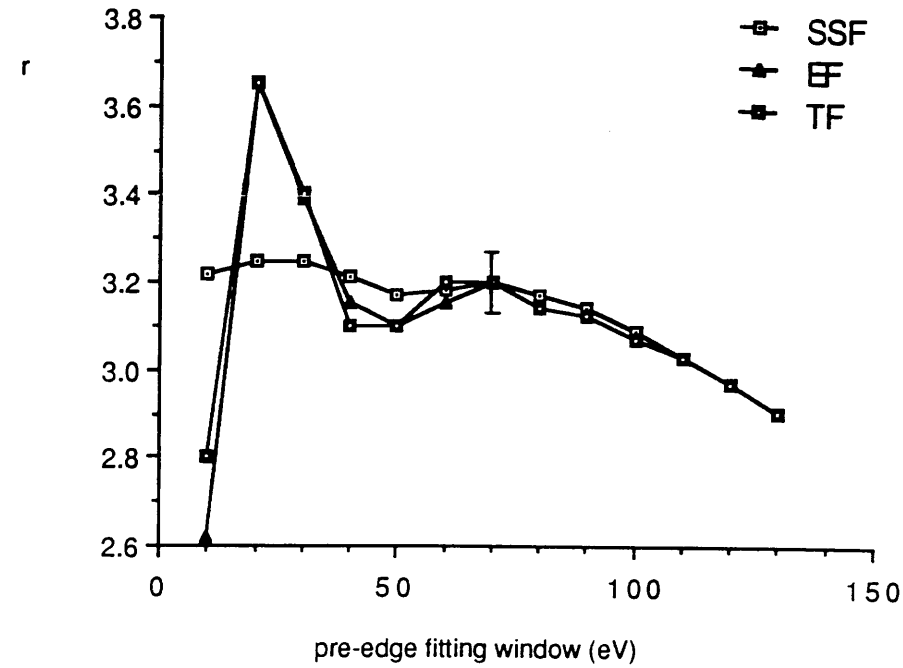

Figure 5.4(a). The variation of fitting parameter r with the magnitude of the pre-edge fitting window for the EF, TF and SSF techniques. A typical error bar is shown on the EF at a pre-edge fitting window of 60eV.

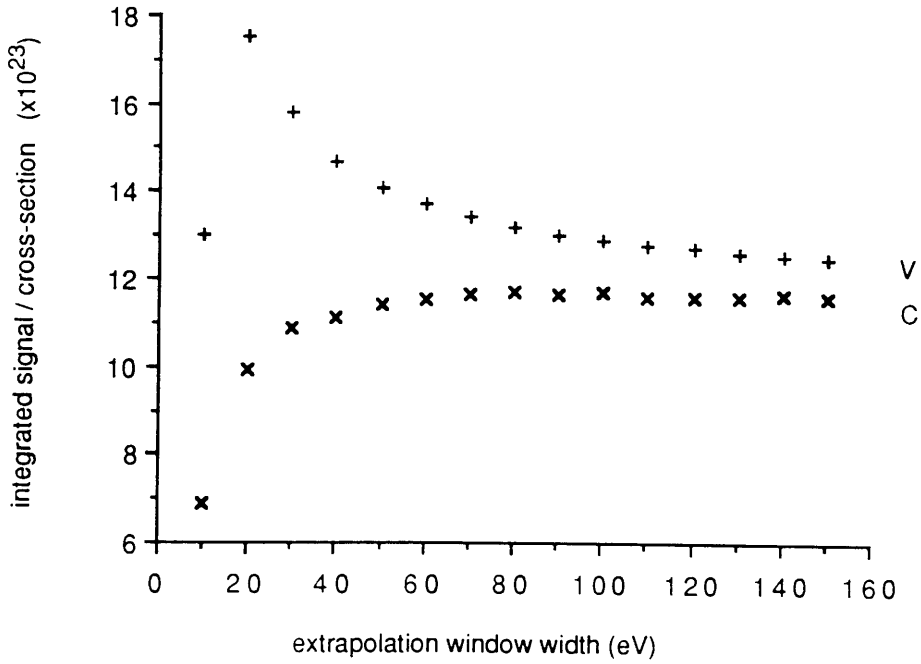

Figure 5.4(b). Variation in the ratio of the integrated signal to the cross-section for increasing extrapolation windows using the EF technique. The hydrogenic cross-section programs SIGMAKR and SIGMALR were used to calculate the ratio for the C and V edges respectively.

be noted that for the EF and TF, 60eV also corresponds to the minimum χ^2 for the C and V edges examined here. The variation in the χ^2 for the SSF is minimal and it is not possible to select an optimum pre-edge fitting window from this criterion alone.

To select the optimum extrapolation window for the EF and TF, the variation in the ratio of the extracted signal to that of the theoretical cross-section was examined as a function of extrapolation window width. The results for both the C and V edges are shown in figure 5.4b for a pre-edge fitting window of 60eV. The near edge effects are not significant in the C K-edge and so the ratio very quickly tends towards a constant level at window widths of ~70eV. However, "white line" transitions dominate the near edge structure of the V edge introducing a systematic error in the overestimation of the ratio which decreases when larger extrapolation windows are selected. Egerton (1982) noted that the error in the signal extraction is minimised when the extrapolation window, w_2, is comparable in size with the fitting window, w_1. Therefore, the choice of extrapolation window for the V L-edge is a compromise between the systematic error introduced by the inaccuracies in the near-edge structure and the background extrapolation error in the extracted signal. For the VC data, a 150eV extrapolation window was selected to minimise the effects of the near edge structure for both the C and V edges.

Using the SSF technique, the post edge fitting region is only limited by the energy range in which the values of the fitting parameters A and r can be expected to remain constant. Therefore, a post-edge fitting region of 150eV was selected for the C and V edges which also ensures a

degree of self consistency with the EF technique. The important parameter in this region is the offset, O_C, which excludes the near edge effects from the fit since it is in this region that the theoretical cross-sections are least accurate. By comparing the values of k (as defined in equation 5.6) obtained for various vales of O_C, the optimum value for the offset was found to be 60eV for both the C and V edges. This value was selected since, for $O_C \geq 60eV$, k decreases towards a constant value. This is consistent with figure 5.4c which shows the comparison of a C characteristic edge and the convoluted cross-section. It can be seen that for energies greater than 60eV from the edge onset, there is reasonable agreement between experiment and theory. Choosing the minimum value of O_C, consistent with the limiting constant value of k at large extrapolation windows, has the advantage of maximising the post-edge fitting region for the SSF. The alignment offset, O_A, is taken to be 3eV on the C edge and 5eV on the Ti edge to match the cross-section with the experimental edge. The selected fitting and extrapolation windows for each of the three background fitting techniques, which were identical for both the C and V edges, are summarised in figure 5.5.

Having established sensible fitting windows, the characteristic edges were extracted from the background signal using the EF, TF and SSF techniques with cross-section programs SIGMAKR and SIGMALR. The C/V ratios that were obtained are shown in figure 5.6 with the spectrum number plotted along the x axis for ease of reference. For the VC data presented here, the EF and the TF produce similar results and are plotted as a single entity. A typical error bar is drawn on the end points of

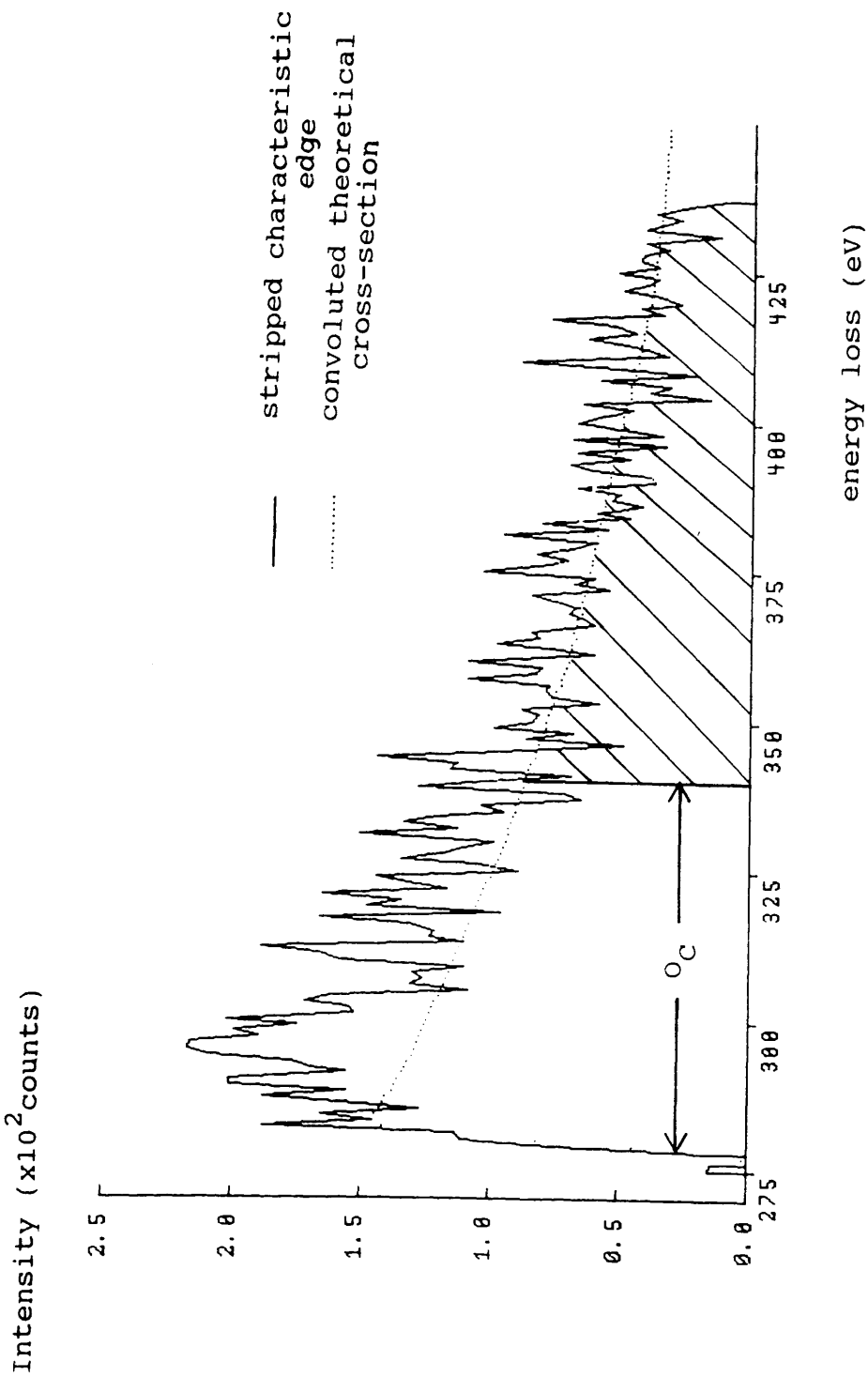

Figure 5.4(c). Comparison of a stripped C K-edge and a convoluted theoretical cross-section. This illustrates the agreement between the two at values greater than 60eV. The background was subtracted from beneath the C edge using the SSF technique.

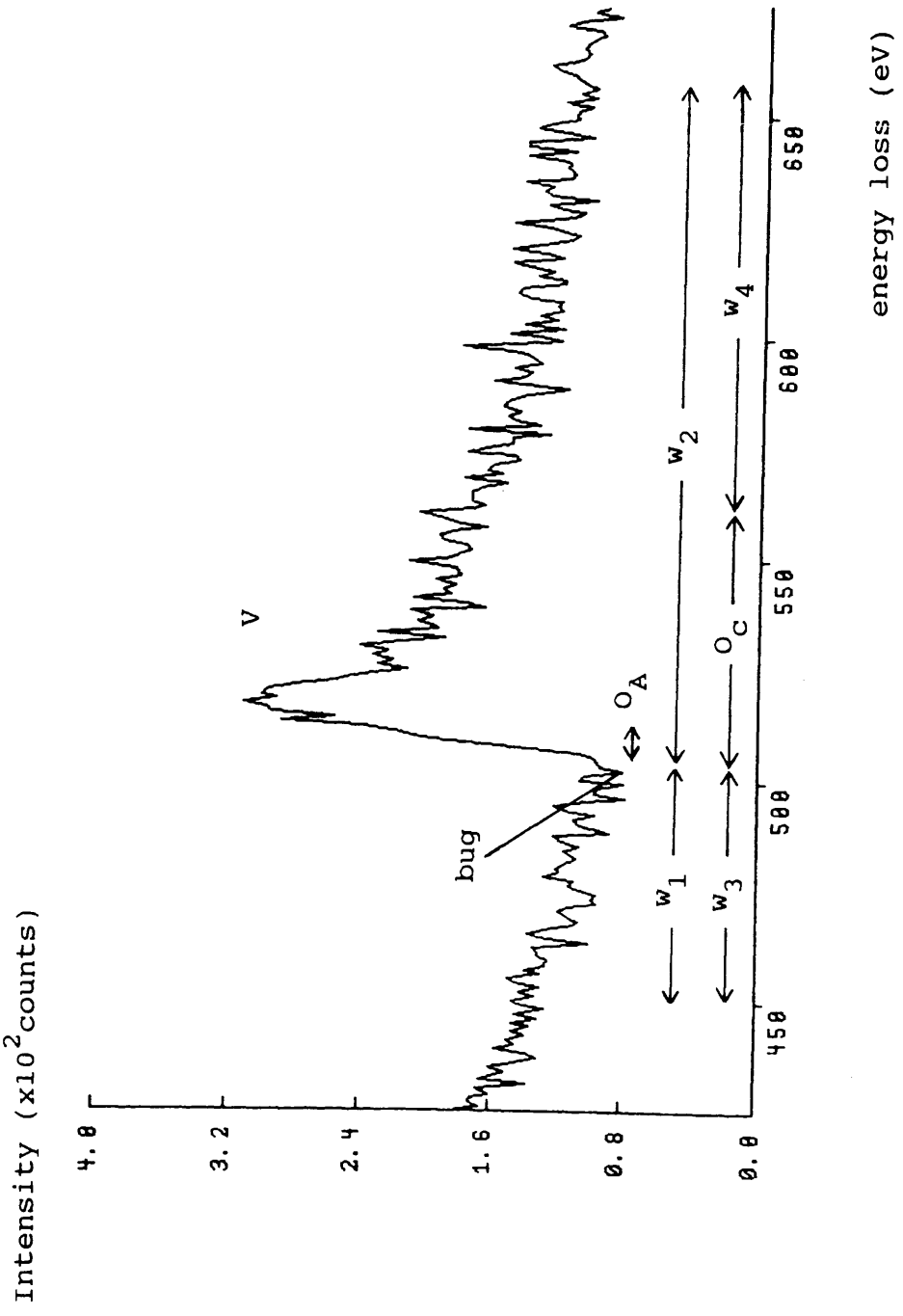

Figure 5.5. The selected fitting windows for the EF(TF) and SSF on both the C and V edges. For the EF(TF), w_1=60eV and w_2=150eV and for the SSF, w_3=60eV, w_4=90eV with an offset (O_C) of 60eV from the bug position. In the SSF, the alignment offset (O_A) was 3eV and 5eV for the C and V edges respectively.

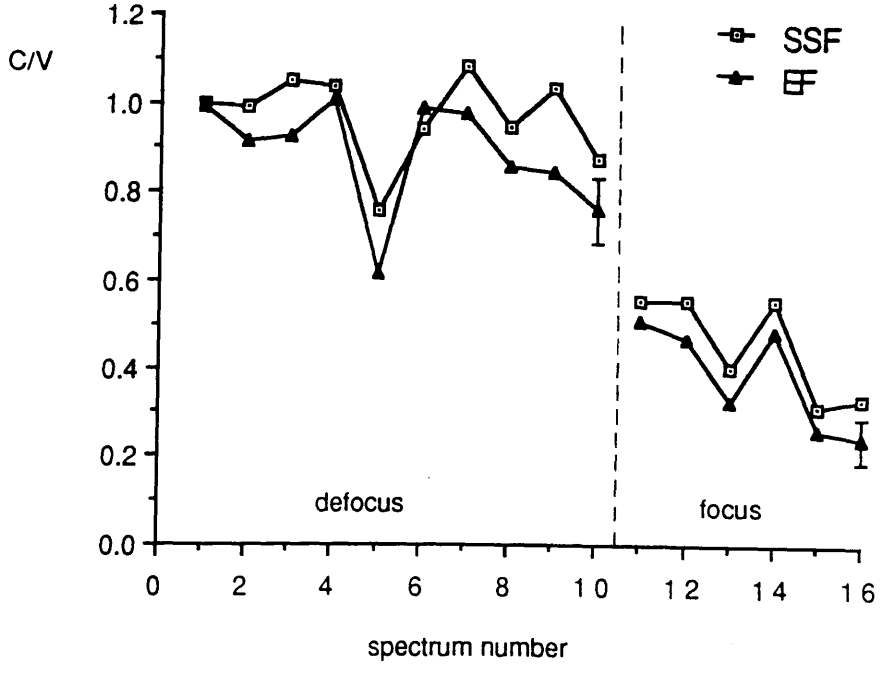

Figure 5.6. The C/V ratios evaluated using the EF(TF) and the SSF techniques with the fitting windows described in figure 5.5 and the hydrogenic cross-section programs SIGMAKR and SIGMALR. A typical error bar is shown on the EF but the SSF does not calculate an error. The dose per spectrum for the defocus spectra is ~7×10^6 electrons/Å^2 and for the focussed spectra ~280×10^6 electrons/Å^2.

the EF curves to indicate the magnitude of the error. As stated previously, the SSF does not calculate an error. It can be seen that there are significant fluctuations in this C/V ratio, however, the three techniques do produce similar results. Therefore, for this data set there does not appear to be a significant advantage in any one of the background fitting techniques. There is, however, a slight systematic shift between the C/V ratios obtained from the EF and SSF because the near edge structure is not included in the SSF calculations.

A significant part of the fluctuations in the C/V ratio can be attributed to noise in the spectra which produces fluctuations in the fitting parameter r as shown in figure 5.7 for (a) the C edge and (b) the V edge. Although the fluctuations in r for the C-edge are smaller than those for the V-edge their effect on the C/V ratio is larger due to the much lower signal to background ratio for the carbon edge.

For the defocussed probe spectra, where little or no loss of C is apparent from figure 5.6, the r values should remain constant since the background contributions remain constant (with the exception of a scaling factor to account for the decay in emission current of the field emission gun). Thus, the r values should represent a set of independent measurements where the mean is closer to the true value. This is consistent with the variations of r about a mean value for the defocussed probe spectra as shown in figure 5.7 (a) and (b). If the mean value for r is used in the background fitting, are the fluctuations in the C/V ratio reduced? An average value for r was calculated from those obtained for the defocussed probe spectra using

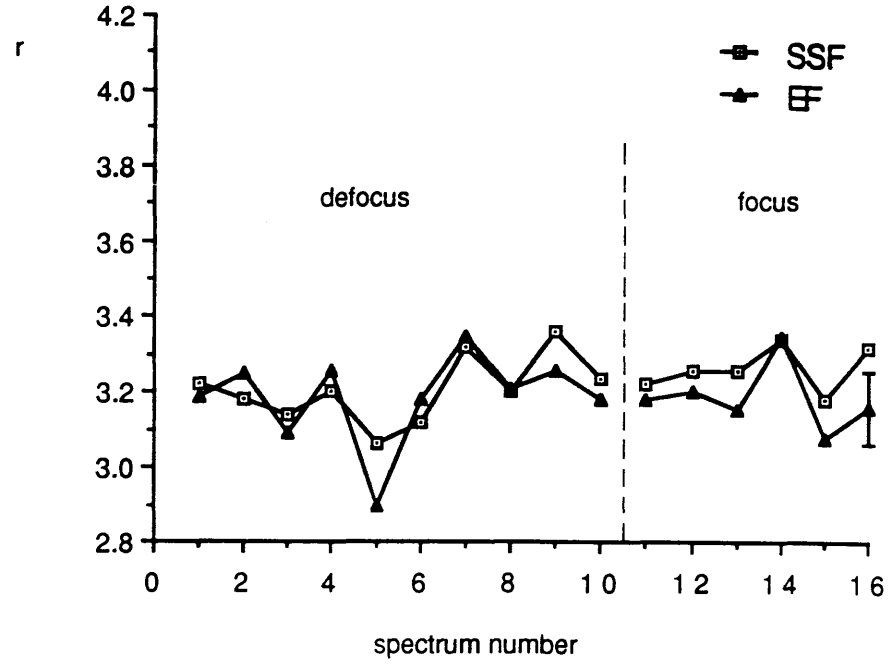

Figure 5.7(a). The r values for the background beneath the C K-edge using the EF(TF) and SSF techniques.

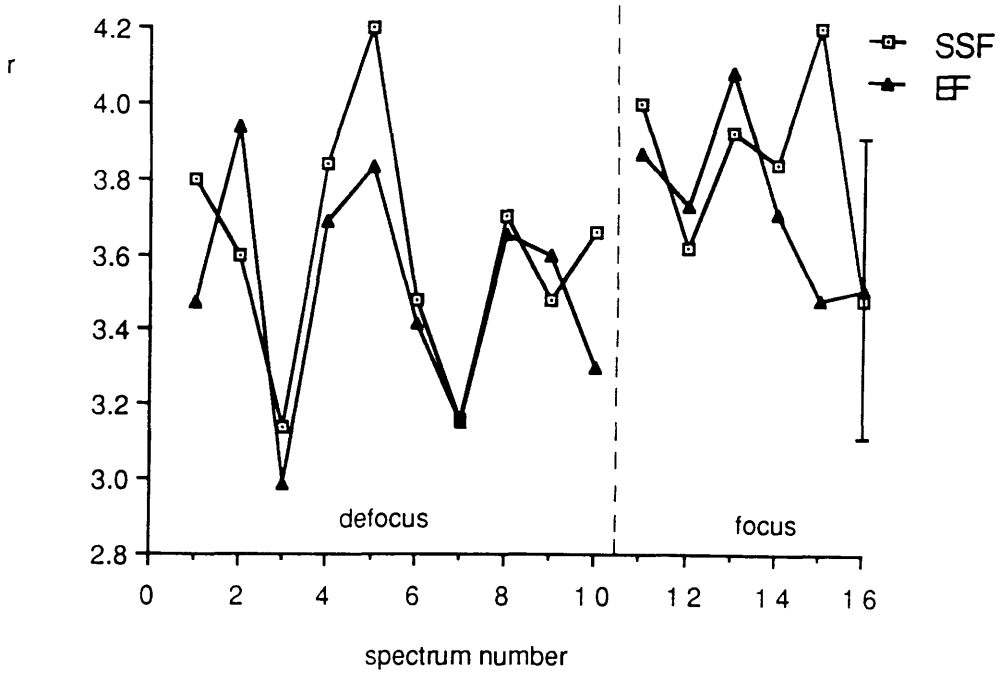

Figure 5.7(b). The r values for the background beneath the V L-edge using the EF(TF) and SSF techniques.

the SSF but excluding spectrum 5 which appears anomalous. (Closer inspection of this spectrum revealed no obvious artifacts in the spectrum to explain the low C/V ratio). The average value of r was then substituted in the SSF to re-evaluate the C/V ratios. This technique is known as the constrained single stage fit (CSSF). The C/V ratios calculated from the CSSF are presented in figure 5.8(a) for comparison with the SSF, where it can be seen that the fluctuations have been considerably reduced, especially the anomalous C/V ratio of spectrum 5. It should be noted that the CSSF has also introduced a slight decrease in the C/V ratios as a function of dose. This was not observed in the SSF but may have been concealed by the fluctuations in the C/V ratio.

Perhaps surprisingly, figure 5.7 suggests that the r values for the focussed probe, where a loss of C has been observed, are also consistent with this variation about an average value of r. The C/V ratio of the focussed probe spectra were recalculated, using this same average value of r and are also shown on figure 5.8(a). As a result of the rapidly dropping C/V ratio as a function of time in the focussed spectra, it is difficult to determine whether the fluctuations have been significantly reduced as they were for the defocussed spectra. However, it should be noted that for spectrum 14, which has an anomalous t/λ value (figure 5.8b) suggesting a probe repositioning error, the C/V ratio has not been reduced for the CSSF. This is not surprising since if the spectrum was collected from a previously unirradiated area then the higher C/V ratio is correct and not due to the presence of noise in the spectrum. Therefore, these analyses show that the CSSF

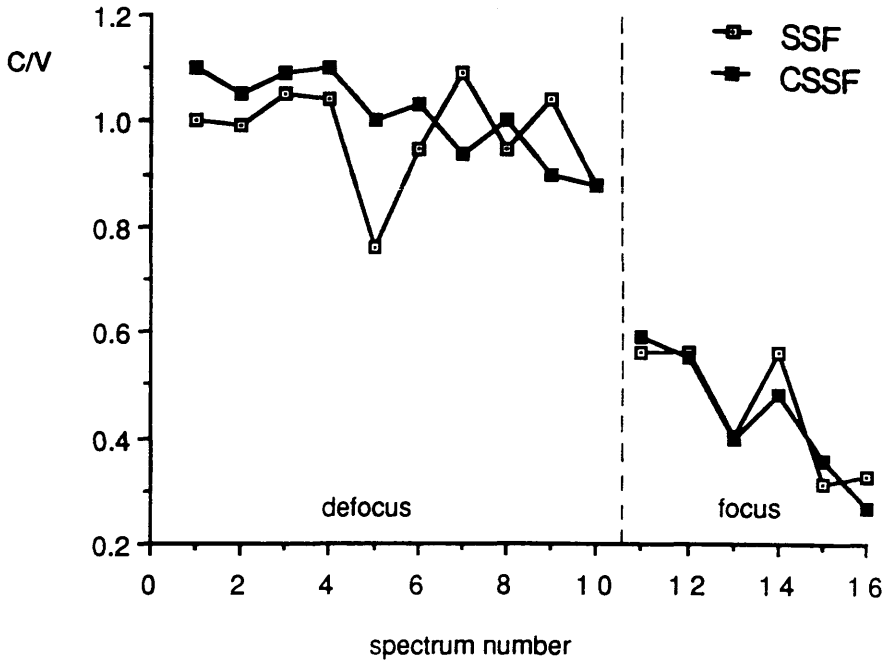

Figure 5.8(a). The C/V ratios of figure 5.6 re-evaluated using CSSF and shown in comparison to the SSF results.

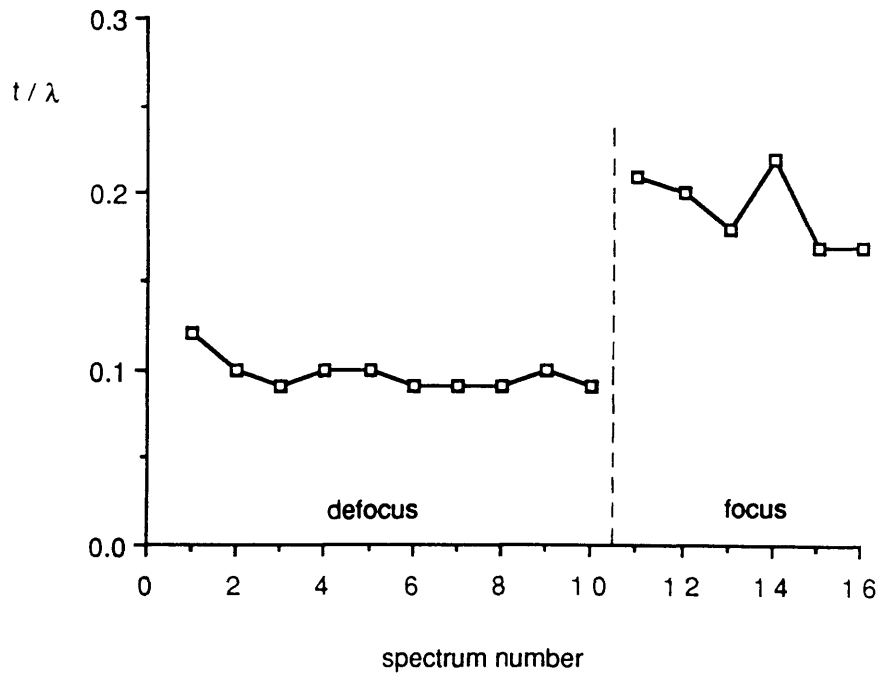

Figure 5.8(b). t/λ values for the data points shown in figure 5.8(a) which confirm that spectrum 14 was acquired from another area of the specimen.

reduces fluctuations in the C/V ratio which are due to the presence of noise in the spectra but not fluctuations occurring as a result of probe repositioning errors.

The large increase in relative thickness between the defocussed and focussed spectra in figure 5.8(b) is probably due to an increase in the average thickness of the extracted precipitate as the probe is focussed onto the centre of the particle. In addition, it was noted that the defocussed spectra contained a significant Si signal (from the extraction replica) which may have increased the total plasmon mean free path and thus decreased the apparent t/λ value for the defocussed probe. These irregularities in the specimen thickness may cause problems in the interpretation of the radiation damage information since (as will be shown later in the thesis) the rate of loss of C is dependent on the specimen thickness.

5.4.2 Determination of the C/V Ratio at Zero Dose

The ultimate aim of collecting spectra with a defocussed probe is to enable the C/V ratio to be calculated at zero dose and so measure the initial elemental concentration for a given sample. The values for C/V from the CSSF suggest that there might be a small loss of C (even with a defocussed probe) and so a number of methods of obtaining the best value of C/V for the defocussed probe were attempted. These were to (1) extrapolate to zero dose assuming a linear mass loss as a function of dose (2) take an average of the values assuming no mass loss and (3) sum the individual spectra and analyse, assuming no mass loss.

Table 5.1 shows the results obtained with these methods

	EF	SSF	CSSF
Extrapolate to zero dose using a linear fit.	1.02±0.06	0.97±0.05	1.06±0.05
Average	0.92±0.03	0.93±0.02	0.94±0.03
Sum of spectra	0.85±0.08	0.9	0.92

Table 5.1 The C/V ratio at zero dose. For the linear fit and the average value the errors are the standard error in the mean for the least square fit or the average. Where the low dose spectra are added together and the sum analysed the error is calculated from the EF technique. The SSF does not calculate an error.

with spectrum 5 again excluded due to its anomalous C/V ratio. As noted previously, the TF yields the same results for the C/V ratio as the EF and is not included in the table as a separate entity. For the linear fit, both the EF and the CSSF give a negative gradient showing a similar rate of mass loss, whereas the SSF has a zero gradient. Thus it is quite possible that there is a small mass loss even at these lower doses ($\sim 66 \times 10^{6}$ electrons/Å^{2} over 10 spectra). The rate of loss suggested is not incompatible with the rate apparent in subsequent experiments on TiC and TiN discussed in chapters 6 and 7. This work, therefore, suggests that the C/V ratio should, in future, be extrapolated to zero dose since there can be a significant mass loss even at the lower dose. However, for either assumption in table 5.1, the C/V ratio calculated from the EF, SSF and CSSF techniques remain internally self consistent. This confirms the conclusion of section 5.4.1 that no single background subtraction techniques has an advantage over another for the VC data analysed.

Although the VC data provided a useful initial analysis of radiation damage under electron beam irradiation, the dramatic changes in the average specimen thickness make the interpretation of the results difficult. Therefore, subsequent work was carried out on an ion-beam thinned TiN sample in an attempt to analyse a specimen of more uniform thickness. The analysis of TiN also provides a further, more stringent test on the accuracies of the various background fitting techniques since the proximity of the N and Ti edges restricts the fitting windows available.

5.5 ANALYSIS OF TITANIUM NITRIDE

A defocus to focus experiment was carried out on an ion beam thinned TiN sample using standard microscope operating conditions (section 4.2.6). The probe was initially defocussed to ~300Å diameter. It was subsequently focussed to ~130Å diameter and then fully focussed (~20Å). This corresponds to a range of dose rates between 0.7×10^5 and 130×10^5 electrons/Å^2/s. A typical TiN spectrum from this experiment is illustrated in figure 5.9, where it can be seen that the proximity of the N and Ti edges severely limits the extrapolation window on the N edge and the pre-edge fitting window on the Ti edge. The optimum fitting windows for the TiN spectra were selected in a similar manner to those of the VC data by examining a typical TiN spectrum with no obvious artifacts. As for the VC data the optimum pre-edge fitting window for each of the background fitting techniques was found to be 60eV for the N K-edge The maximum extrapolation window, w_2, available on the N edge is 50eV. It was shown earlier in this chapter that if the first order cancellation of multiple scattering is to be achieved to best effect using the EF technique, the extrapolation window must also be restricted to 50eV on the Ti edge. The effect of limiting the extrapolation window is greater on the Ti edge than on the N edge because of the presence of the Ti white lines which are not accounted for in the theoretical cross-sections and can be expected to introduce a systematic increase in the Ti content. For the SSF, the post-edge fitting window (w_4) is still restricted to 50 eV on the N edge again because of the proximity of the Ti edge. However, the post-edge fitting window for the

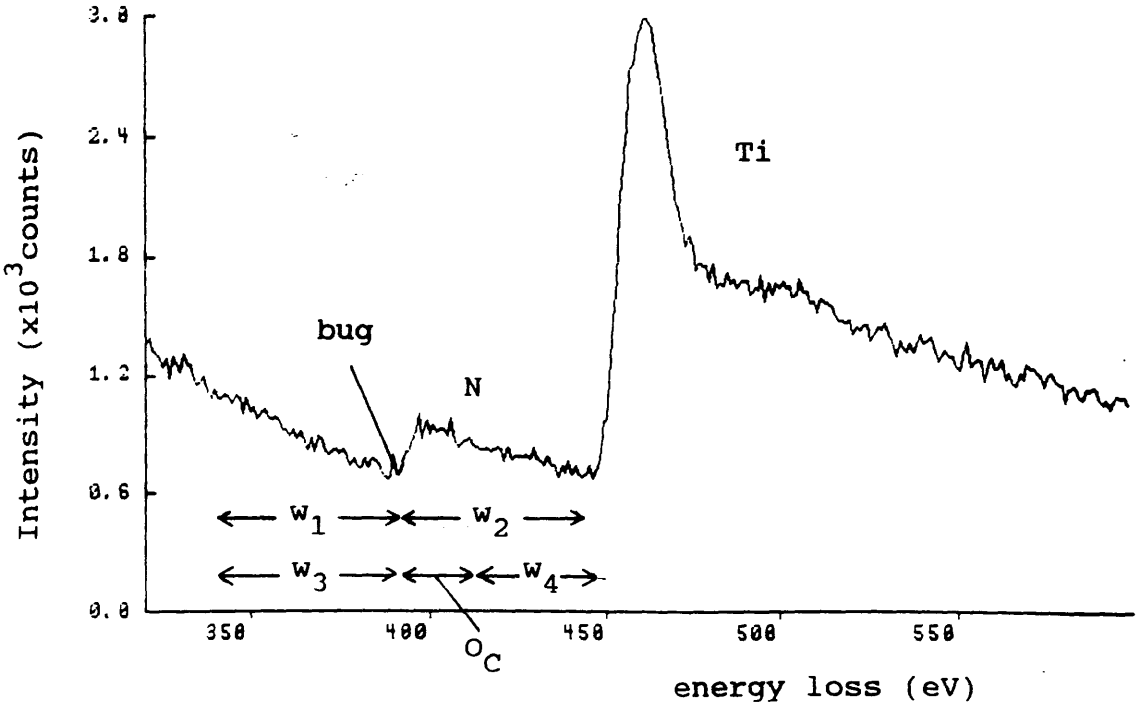

Figure 5.9(a) The selected fitting regions for the EF and SSF techniques on the N K-edge. For the EF, w_1=60eV, w_2=50eV and for the SSF, w_3=60eV, w_4=50eV with a 30eV offset from the bug position (O_C) and O_A=3eV.

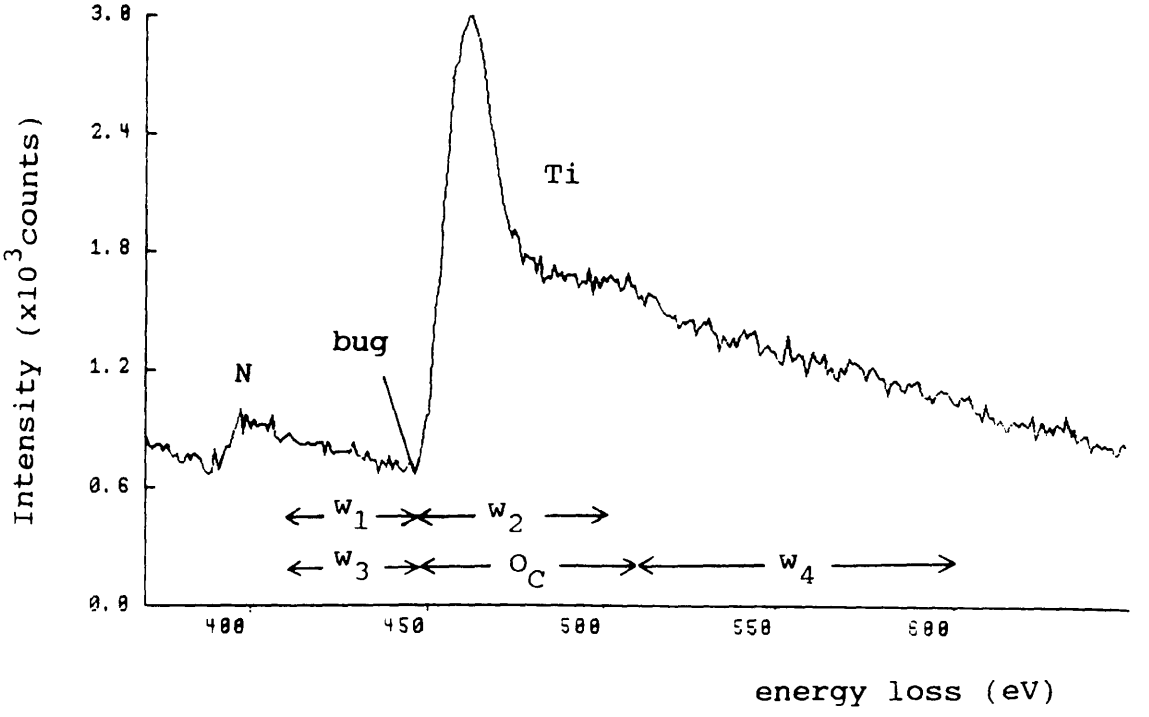

Figure 5.9(b) The selected fitting regions for the EF and SSF techniques on the Ti L-edge. For the EF, w_1=30eV and w_2=50eV and for the SSF, w_3=30eV, w_4=150eV with a 60eV offset from the bug position (O_C) and O_A=5eV.

Ti edge is not restricted to 50eV as in the EF since the effect of multiple scattering has already been taken into account with the use of a convoluted cross-section. The fitting windows selected for each of the techniques on the N and Ti edges are summarised in figure 5.9.

The N/Ti ratios that were obtained for each of the fitting techniques are shown in figure 5.10, where again the EF results are plotted as a representation of both the EF and TF results. As for the VC data, a typical error bar is shown on each line to indicate the magnitude of the errors on the EF. Again, one might expect a systematic difference between the SSF technique and the EF(TF) since the near edge structure is included in the fit of the latter and it is in this region that the theoretical cross-sections are least accurate. This systematic difference can be clearly seen in the figure and is much more pronounced in the TiN data compared to that of VC because of the restricted extrapolation windows available on the Ti edge.

The variations in r about an average value in figure 5.11 for each of the fitting procedures, would appear to justify the application of the constrained SSF detailed in section 5.4.1. Therefore, the N/Ti ratios were recalculated using the CSSF technique and are shown in figure 5.12(a) for comparison with the SSF results. The fluctuations in the N/Ti ratio have been slightly reduced but the effect is not as large as observed in the VC data. This is perhaps due to the improved statistics when analysing a thicker sample where the defocussed VC spectra have an average t/λ of 0.1 compared to an average t/λ of ~0.5 for the defocussed TiN spectra. As in the case of the VC data, the CSSF reduces

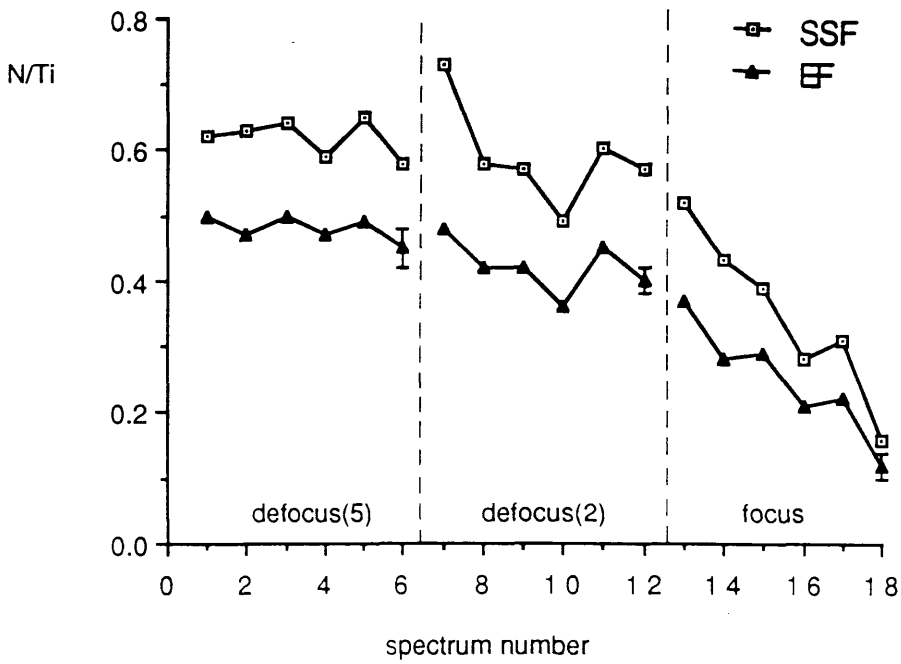

Figure 5.10. The N/Ti ratios evaluated using the EF and SSF with the fitting windows described in figure 5.9 and the hydrogenic cross-section programs SIGMAKR and SIGMALR. A typical error bar is shown on the EF but the SSF dose not calculate an error. The dose per spectrum for the defocus(#5) spectra is ~1.4×10^6 electrons/Å^2, for the defocus(#2) spectra is ~7×10^6 electrons/Å^2 and for the focussed spectra is ~270×10^6 electrons/Å^2.

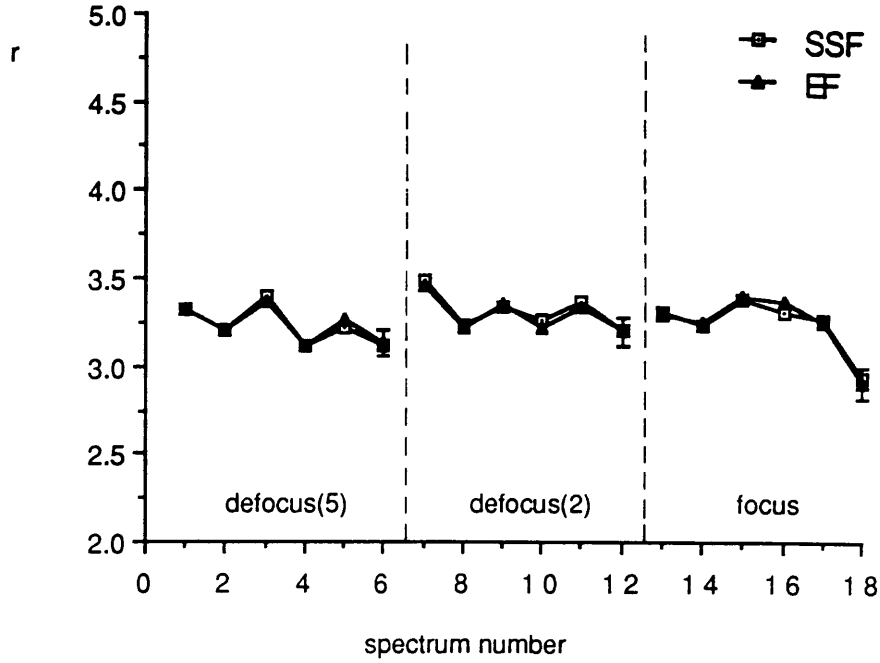

Figure 5.11(a) The r values for the background beneath the N K-edge using the EF and SSF techniques.

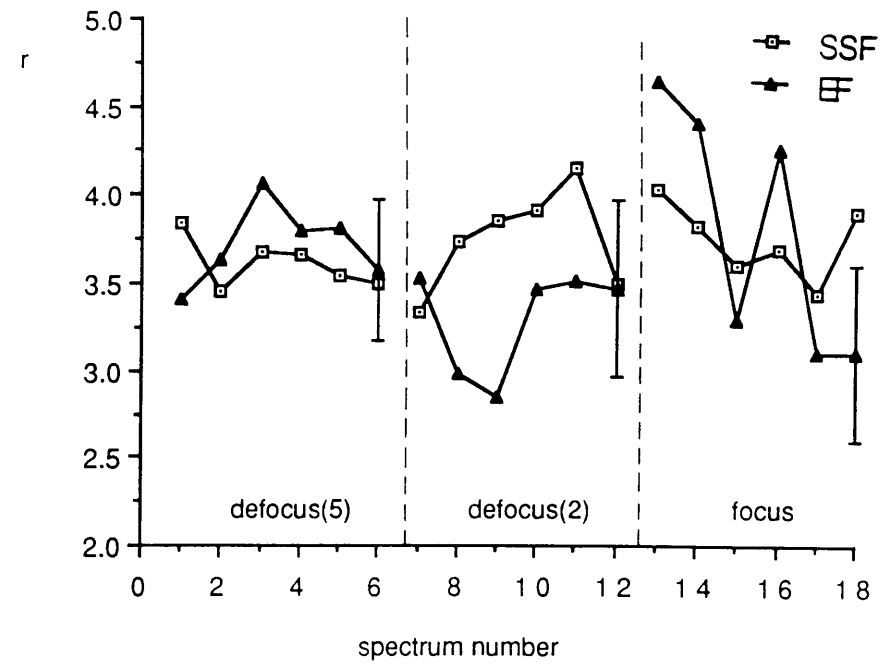

Figure 5.11(b) The r values for the background beneath the Ti L-edge using the EF and SSF techniques.

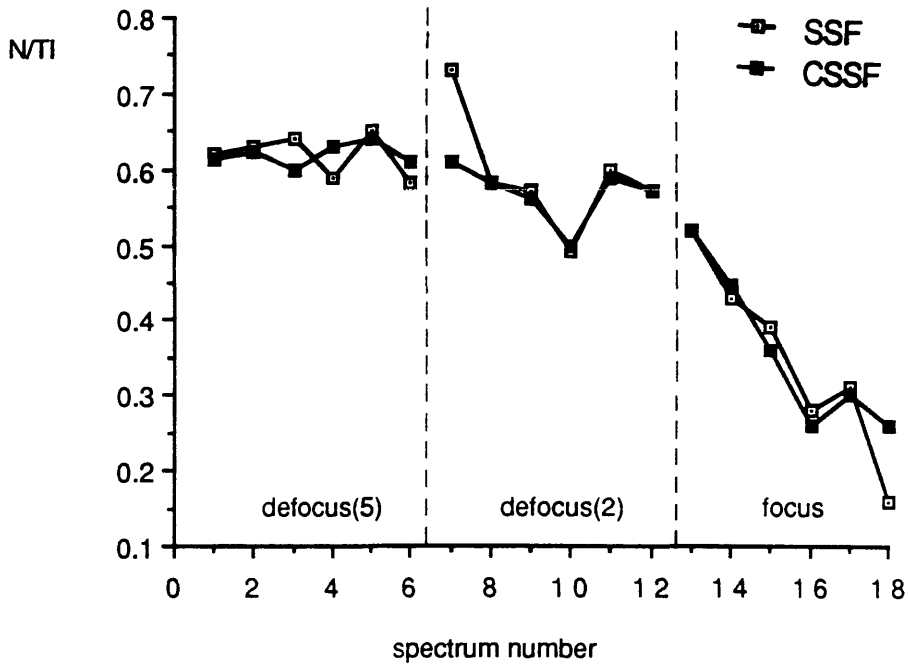

Figure 5.12(a). The N/Ti ratios of figure 5.10 re-evaluated using the CSSF and shown in comparison to the SSF.

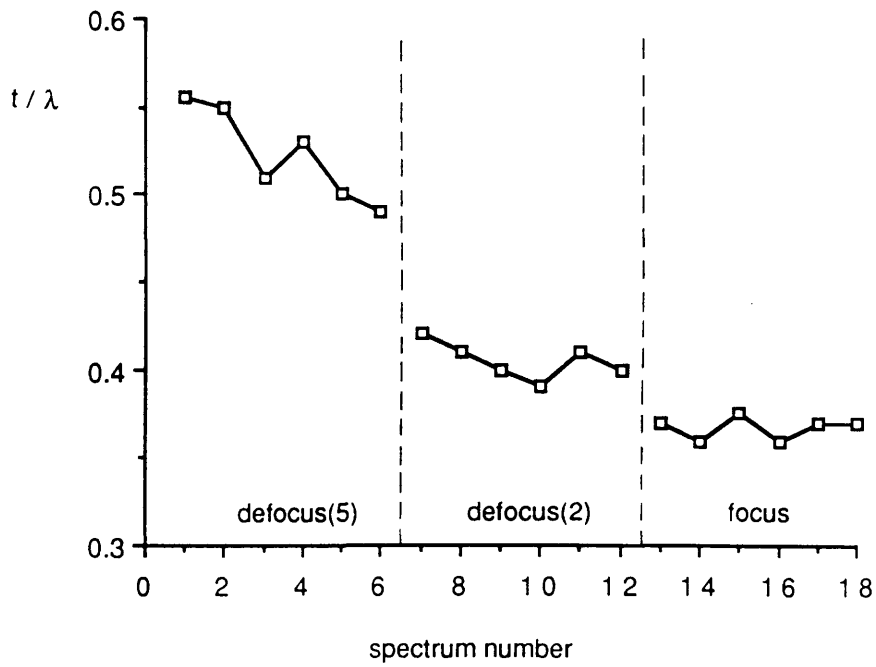

Figure 5.12(b). t/λ values for the data points shown in figure 5.12(a) which suggest that spectra 11 and 12 were collected from another region of the specimen.

the fluctuations in points which are apparently anomalous (eg spectrum 7) but not where the anomalous N/Ti ratio is the result of a probe repositioning error as in spectra 11 and 12 (indicated in the t/λ graph of figure 5.12b).

The decrease in t/λ seen in figure 5.12(b) is probably due to the poor specimen preparation techniques in the initial experiments. As was noted in chapter 4, the initial ion-beam thinning conditions produced a series of ridges and furrows in the specimen. As the probe was focussed, the average specimen thickness decreased because the centre of the area irradiated was in the centre of a "furrow". As in the VC data, the change in average thickness causes problems in the analysis of the radiation damage. Consequently, as discussed in chapter 4, the improvement of specimen preparation techniques was given high priority. For the VC data in figure 5.8, the decrease in t/λ for the focussed probe spectra corresponds to the loss of C from the sample. However, for TiN in figure 5.12, the most rapid change in t/λ does not correspond to the maximum rate of loss of N. Consequently, it is not clear whether the slow decrease in t/λ for a given probe size is due to mass loss in the specimen or a change in λ as the preferential loss of N alters the specimen density.

For the first 6 spectra, where there is no apparent loss of N, the N/Ti ratio at zero dose was calculated using the three techniques outlined in section 5.4.2 for the VC spectra. The results are shown in table 5.2 where the TF is again excluded due to its similarity to the results of the EF. As in the case of the N/Ti ratios shown in figure 5.10, there is a systematic shift between the N/Ti ratio at zero dose for the EF and the SSF techniques. However, the

	EF	SSF	CSSF
Extrapolate to zero dose using a linear fit.	0.50±0.03	0.64±0.02	0.61±0.02
Average	0.48±0.01	0.62±0.01	0.62±0.06
Sum of spectra	0.46±0.02	0.65	0.64

Table 5.2 The N/Ti ratio at zero dose. For the linear fit and the average value the error are the standard error in the mean for the least square fit or the average. Where the first 6 spectra are added together and the sum analysed the error is calculated from the EF technique. The SSF does not calculate an error.

results from the various methods of extrapolation to zero dose are consistent within the experimental errors for each of the EF and SSF techniques. This suggests that there is no loss of N from the material at the lowest dose, which is consistent with results discussed in later chapters for the specimen thicknesses and dose examined.

In conclusion, apart from the systematic shift in the N/Ti ratio between the EF and SSF, none of the background fitting techniques appears to have an advantage over the others for the data examined here even where the fitting windows on the TiN spectra are restricted.

5.6 EFFECT OF THE THEORETICAL CROSS SECTION ON THE RESULTS

In figure 5.10, the consistently lower values of the N/Ti that were obtained using the EF when compared to the SSF was attributed to inaccuracies in the cross-section values at the near edge onset (which are dominant when small integration windows are used, as in the case of TiN). By using a more accurate cross-section is it possible to significantly reduce this discrepancy? In the more recent hydrogenic cross-section program, SIGMAL2, Egerton (1985) has attempted to allow for the white line transitions that are present in the V and Ti edges. Figure 5.13 shows that, as expected, the hydrogenic cross-section programs, SIGMALR and SIGMAL2, differ most in the near edge region. However, it can also be seen that the integrated cross-sections SIGMALR and SIGMAL2 converge as the integration window is increased until only a small systematic difference exists for large windows.

The elemental ratios obtained from the EF(TF) and the SSF

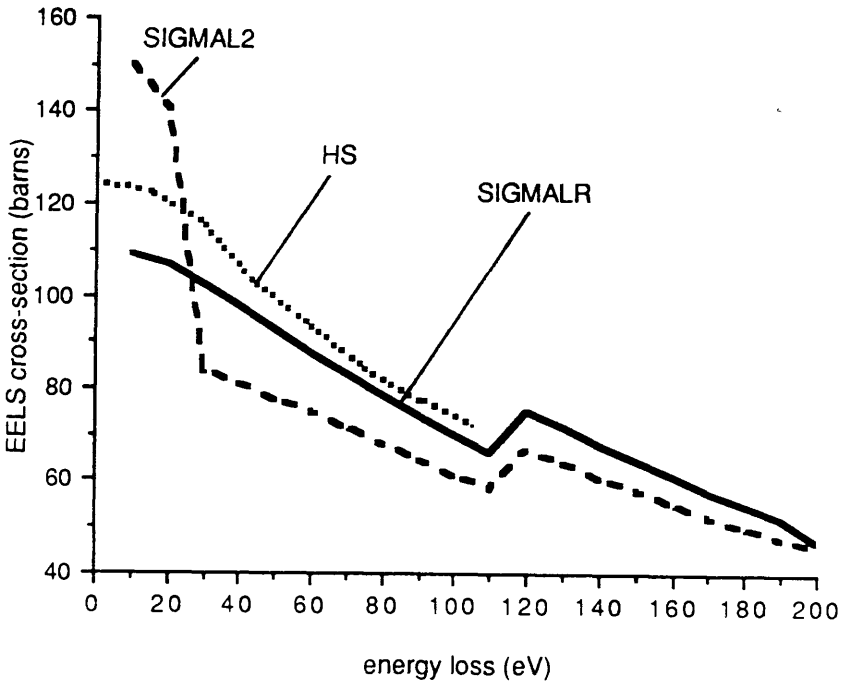

Figure 5.13. Comparison of the theoretical cross-sections for a V L-edge predicted by the hydrogenic SIGMALR, SIGMAL2 and Hartree Slater models. The V L-edge energy is 513eV.

techniques were recalculated using the SIGMAL2 cross-section over the fitting windows described in sections 5.4 and 5.5 for both the VC and TiN data and are plotted in figure 5.14. Figure 5.14(b) shows that the large discrepancy between the EF and the SSF for the TiN data has been reduced when a cross-section that attempts to allow for the near edge structure is used. There is only a small systematic shift in the C/V ratio of figure 5.14(a). This is because the VC results were calculated over a relatively large extrapolation windows where the inaccuracies at the edge onset are not significant. Recalculation of tables 5.1 and 5.2 using SIGMAL2 reduces the large systematic difference in the EF and SSF techniques as shown in table 5.3. This confirms that, within the experimental errors, the N/Ti ratio at zero dose is the same for all the fitting techniques and for both the assumption of mass loss or no mass loss. Moreover, the systematic difference between the assumption of mass loss and no mass loss for the VC data is maintained, suggesting that there is a real mass loss observed. However, the consistency between the different fitting techniques in the VC data for either the assumption of mass loss or no mass loss no longer holds within the experimental errors. The reason for this is not clear.

A further comparison was made using the Hartree-Slater (HS) cross-section discussed in section 2.4. This is also shown in figure 5.13 for the V L-edge. The energy range over which the HS cross-sections are valid (<100eV) is small and so these were not suitable for the large post edge fitting regions chosen for the SSF in the VC spectra. Therefore, the Hartree-Slater cross-sections were used only with the EF. This resulted in a systematic change by a

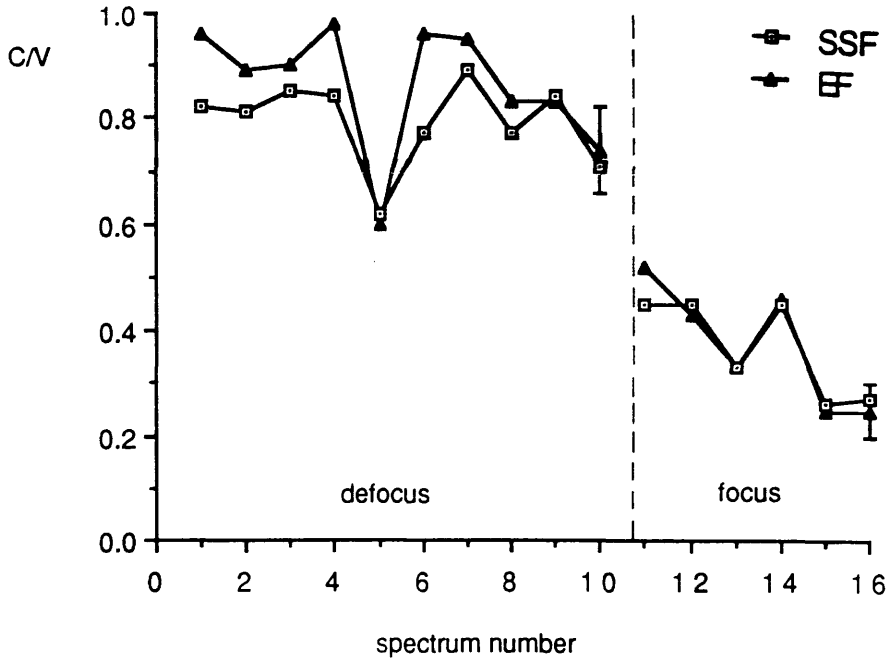

Figure 5.14(a). C/V ratios evaluated from the EF and SSF techniques using the SIGMAL2 cross-section program.

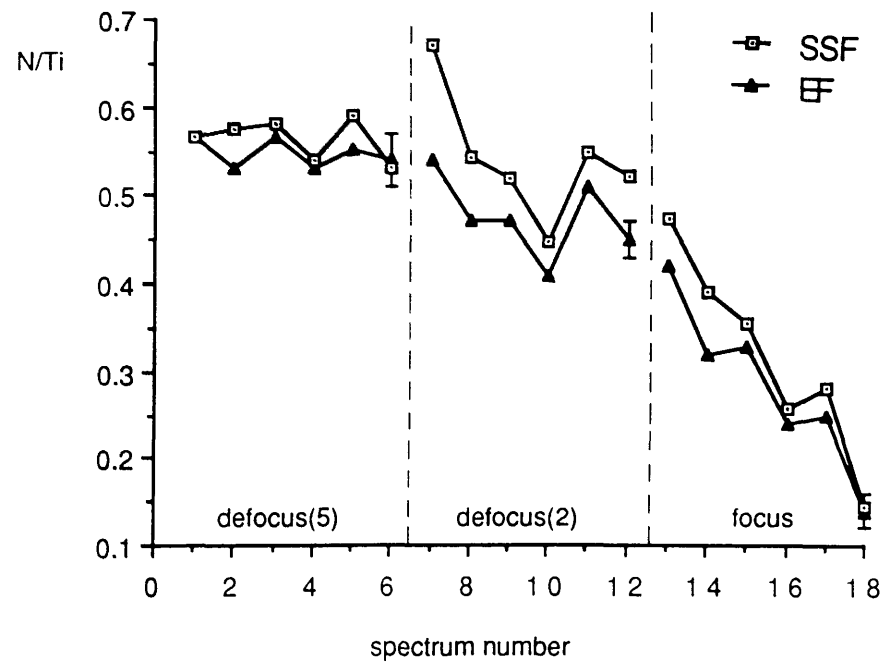

Figure 5.14(b). N/Ti ratios evaluated from the EF and SSF techniques using the SIGMAL2 cross-section program.

	EF	SSF	CSSF
VC			
Extrapolate to zero dose using a linear fit.	0.97±0.06	0.85±0.04	0.92±0.05
Average	0.87±0.03	0.81±0.02	0.82±0.03
Sum of spectra	0.8±0.08	0.78	0.8
TiN			
Extrapolate to zero dose using a linear fit.	0.56±0.03	0.58±0.02	0.56±0.02
Average	0.54±0.01	0.56±0.01	0.56±0.06
Sum of spectra	0.52±0.02	0.59	0.58

Table 5.3 The C/Ti and N/Ti ratios of tables 5.1 and 5.2 recalculated for the hydrogenic cross-section program SIGMAL2.

factor of 1.09 in the C/V ratio when compared to that obtained using the SIGMAL2 cross-section. A similar comparison on the TiN was not possible since the HS cross-section for Ti was not available during this work.

In conclusion, use of different cross-sections can result in a systematic shift in the elemental ratios calculated. However, for radiation damage studies it is the trends in the data which are of interest and therefore small systematic shifts in the C/V or N/Ti ratio are less important. It should be noted that in the later experiments described in chapters 6 and 7, because of the loss of Ti from the sample, it is the absolute number of C or N atoms/unit area which are of interest. In this case, the discrepancies between the L-edge cross-sections are unimportant. As a result of both the ease of use and the reduced discrepancy between the EF and SSF results for the TiN data, the more recent versions of the hydrogenic programs (SIGMA12) were used for all subsequent experiments.

5.7 THEORETICAL SPECTRA

Even where the systematic difference between the C/V and N/Ti ratios for the EF and SSF have been reduced by the use of a more accurate cross-section, it is still not possible to know which, if any, of the fitting techniques produces the most reliable answer. Because of the uncertainties that exist in the experimental data, it is preferable to use a theoretical background and characteristic edge for which the exact values of the fitting parameters A,r and k are known. The theoretical background was produced by assuming

a constant value of the fitting parameters A and r in the analytical expression of equation 5.3. A C-edge was added to this background by convoluting a theoretical C cross-section from the SIGMAK2 program with the low loss region of one of the VC spectra from section 5.4. There was no noise in the background signal and only a minimal noise contribution in the characteristic edge as a result of the convolution with the low loss region of an experimental spectrum. The background fitting routines were first tested on these spectra to check their susceptibility to the rounding errors introduced when the spectra are digitised. Figure 5.15 shows the results for the EF and TF for r=3.207 and a selection of values of A from $0.5x10^{10}$ to $100x10^{10}$, where the experimental VC spectra have an intermediate value for A of $3.4x10^{10}$. These values of A correspond to a range of 70 to $1.4x10^{4}$ counts at the C K-edge onset (-280ev) for r=3.207. In the absence of noise, the TF is more reliable for small fitting windows where there are fewest counts in the spectra. However, for increasing values of A, there is very little difference between the EF and TF especially at pre-edge fitting windows greater than 50eV.

To simulate experimental spectra, a Poisson noise distribution was introduced into the theoretical spectra using a random number generator. Figure 5.16 shows the values of r obtained from the EF, TF and SSF techniques on these "noisy" theoretical spectra for a range of values of A from 1 to $100x10^{10}$. Provided the fitting windows are greater than 50eV the EF, TF and SSF produce similar results for r. The values tend towards the true value of r (3.207) as the fitting window increases. It should be noted

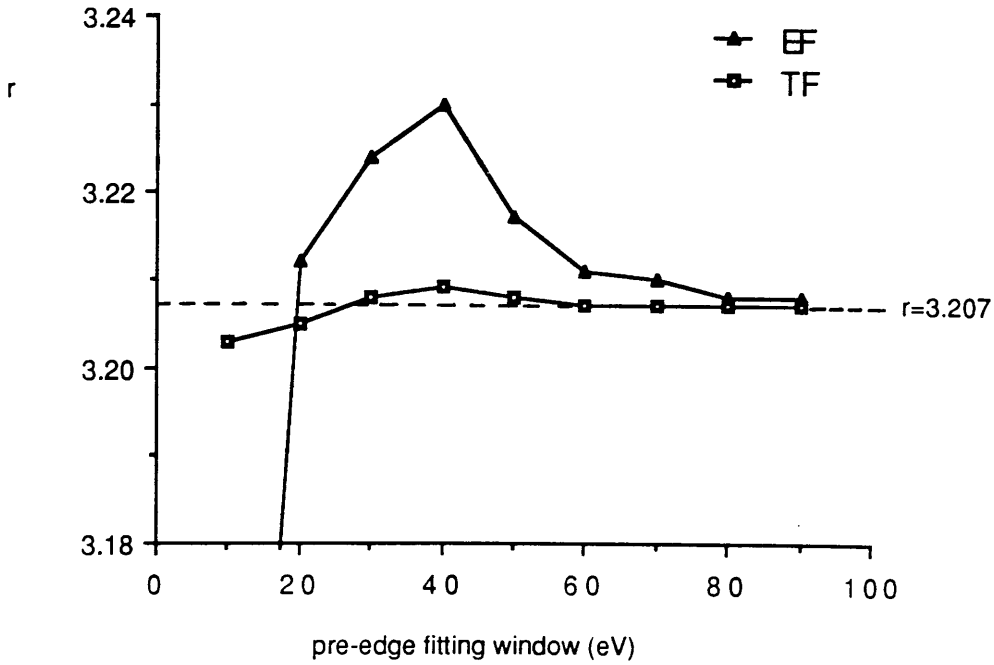

Figure 5.15(a). The values of the fitting parameter r for the background beneath a theoretical C K-edge (without noise) as a function of the pre-edge fitting window for the EF and TF techniques. $A=0.5x10^{10}$

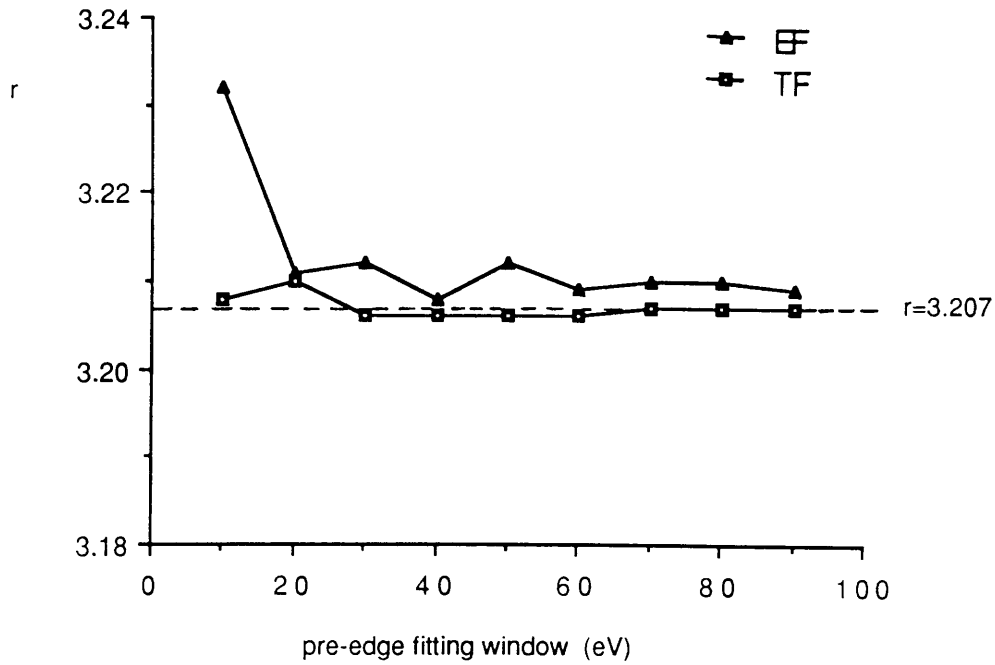

Figure 5.15(b). The values of the fitting parameter r for the background beneath a theoretical C K-edge (without noise) as a function of the pre-edge fitting window for the EF and TF techniques. $A=1x10^{10}$

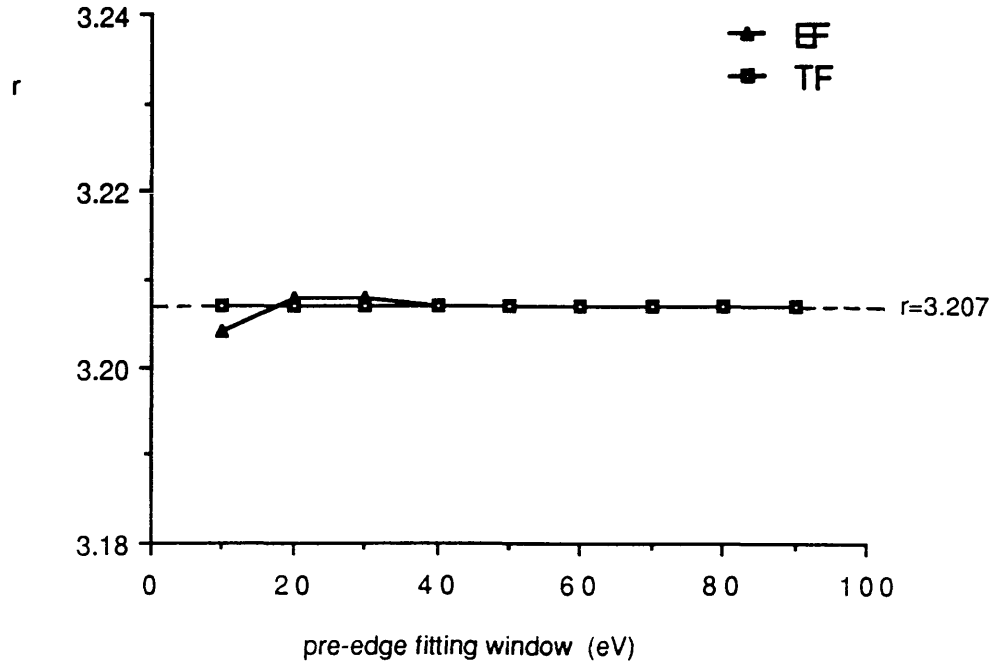

Figure 5.15(c). The values of the fitting parameter r for the background beneath a theoretical C K-edge (without noise) as a function of the pre-edge fitting window for the EF and TF techniques. $A=10x10^{10}$

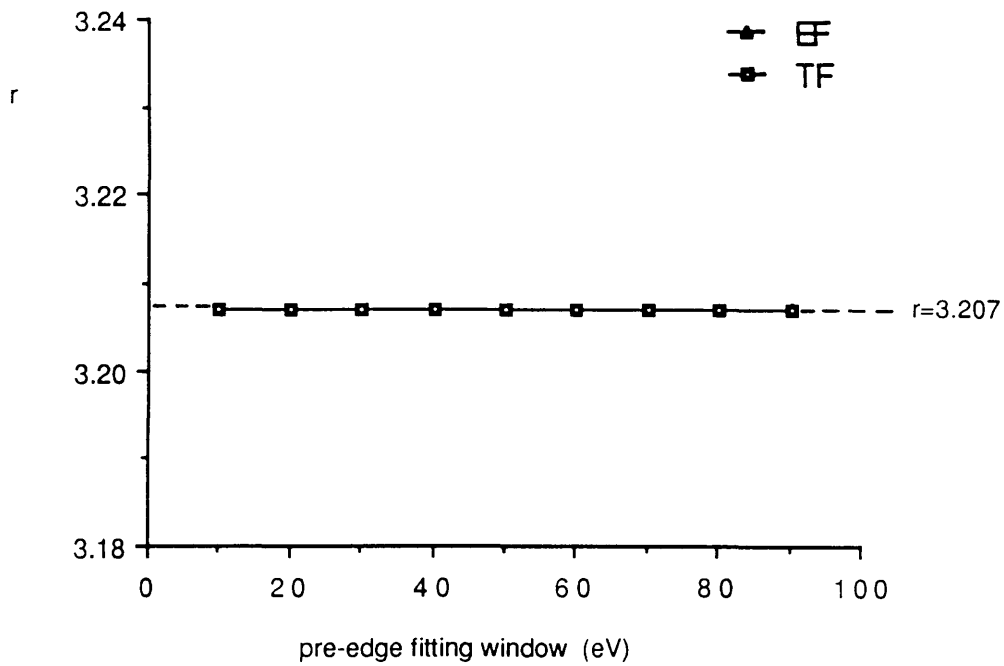

Figure 5.15(d). The values of the fitting parameter r for the background beneath a theoretical C K-edge (without noise) as a function of the pre-edge fitting window for the EF and TF techniques. $A=100x10^{10}$

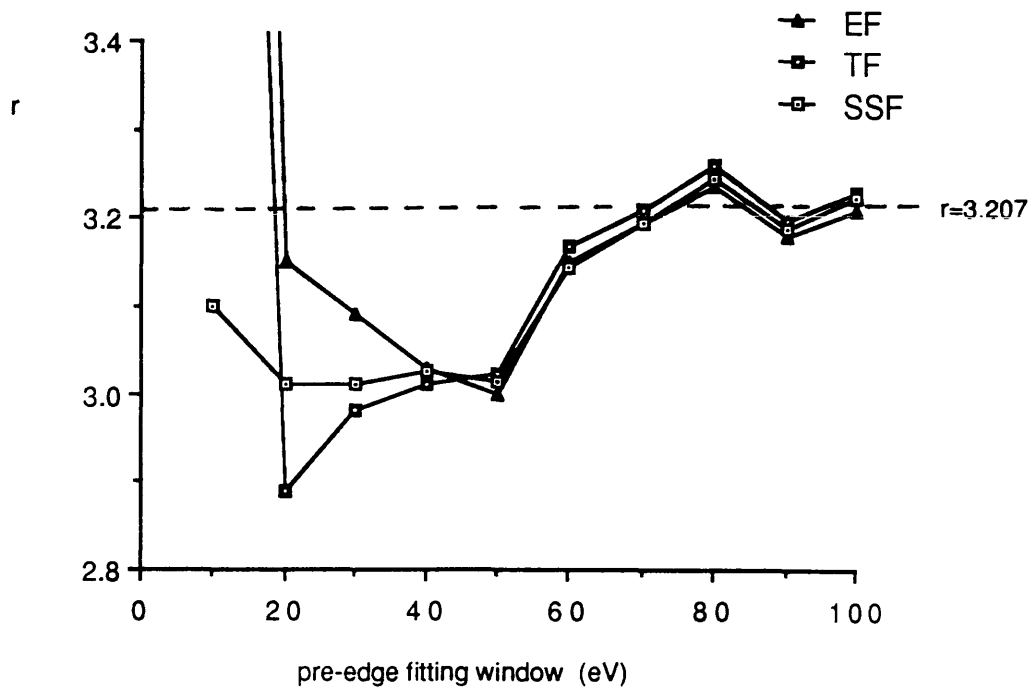

Figure 5.16(a). The r values for the background beneath a theoretical C K-edge (with Poisson noise) for the EF, TF and SSF techniques. $A=1x10^{10}$

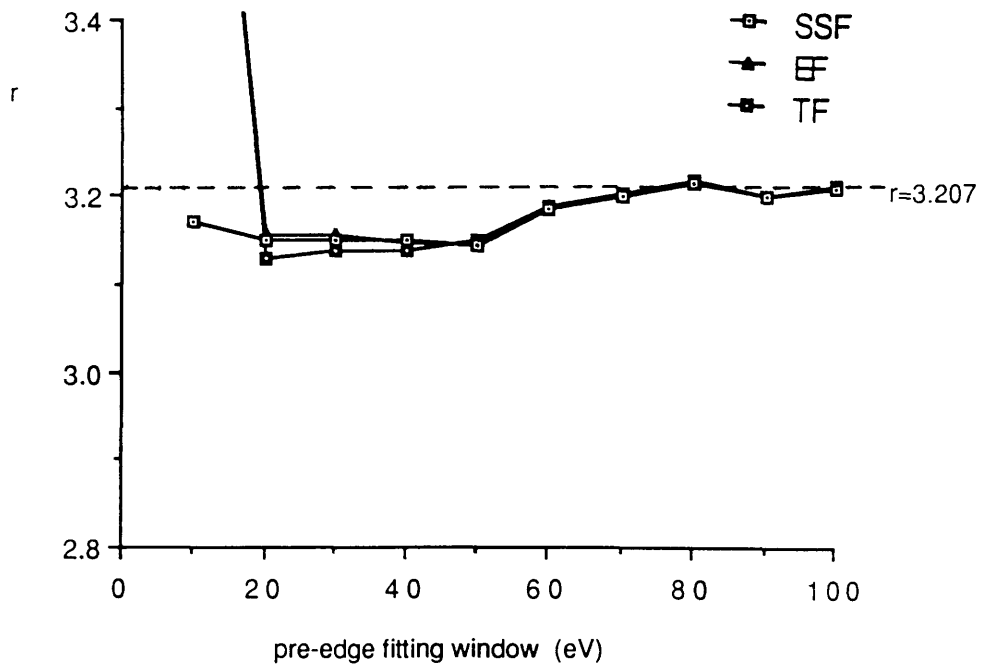

Figure 5.16(b). The r values for the background beneath a theoretical C K-edge (with Poisson noise) for the EF, TF and SSF techniques. $A=10x10^{10}$

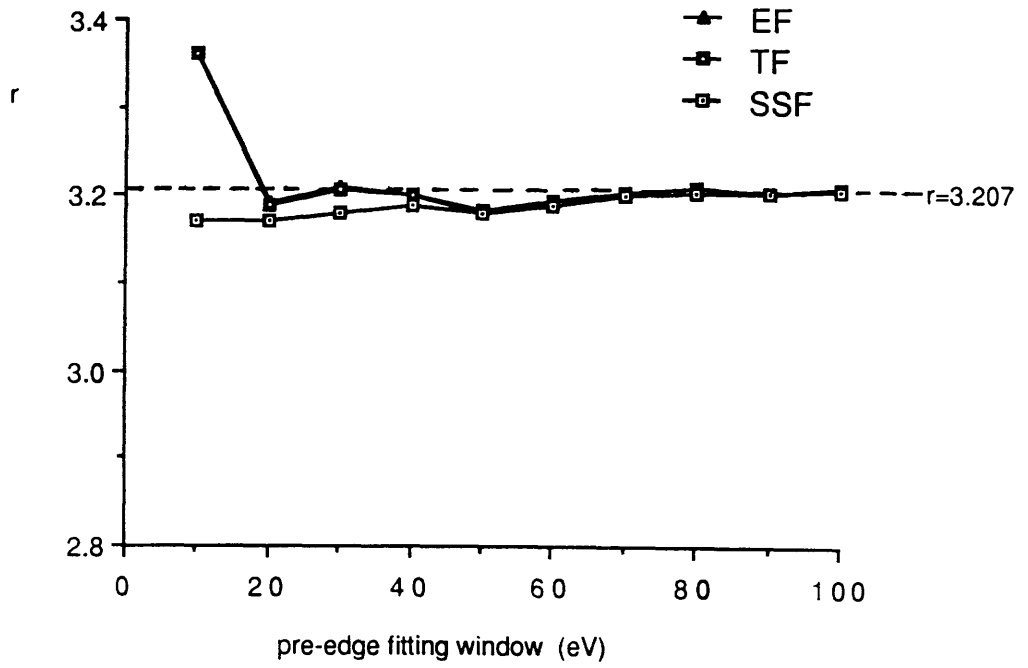

Figure 5.16(c). The r values for the background beneath a theoretical C K-edge (with Poisson noise) for the EF, TF and SSF techniques. $A=100x10^{10}$

that in the experimental data (figure 5.4a) the value of r started to decrease systematically for all three fitting techniques once the pre-edge fitting region was greater than 70eV. Therefore, it is advisable to take the smallest window for which figure 5.16 suggests that a reasonable value of r will be obtained.

By using different seeds for the random number generator, it was possible to examine different noise spreads on the theoretical spectra which had the same inherent values of A and r. Although the form of the fluctuations in r is dependent on the actual noise spread in an individual spectrum (ie the seed used in the random number generator), the EF, TF and SSF produce very similar results for fitting windows greater than 50eV, at intermediate values of A ($\sim 3.4 \times 10^{10}$). These values of A correspond to the experimental data discussed in this chapter.

To test whether the CSSF offers a real improvement, a series of 10 spectra were generated with the same values of A and r but a different noise content. The values of A and r chosen correspond to the experimental VC data. Figure 5.17(a) shows the values of r obtained using the EF and SSF. As for the experimental data of figure 5.7 and 5.11, the value of r appears to fluctuate about an average value. The average value for both the EF and SSF is 3.2±0.03, which agree with the true value of r (3.207) within the experimental errors. The CSSF was then applied to the series of spectra using an average value of r=3.2. The results are shown in figure 5.17(b) for the ratio of the integrated signal to the cross-section, k, for both the CSSF and the SSF. The average values of k and their standard errors are k=0.105±0.0008 for the CSSF and

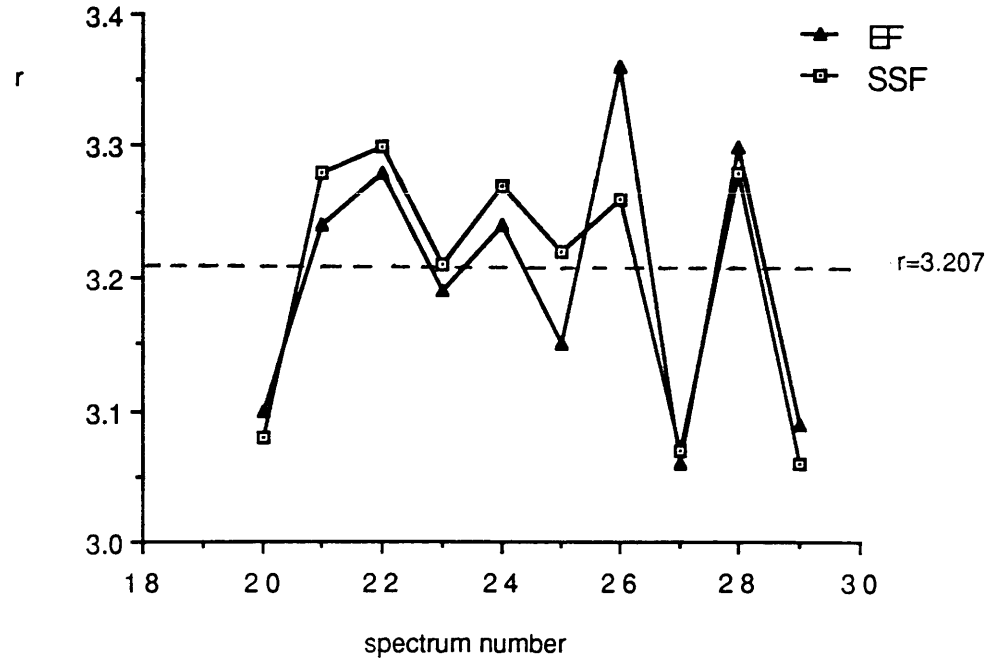

Figure 5.17(a). The variation in r for a series of theoretical spectra generated with different noise spreads but the same value of r for the EF and SSF techniques. For the EF w_1=60eV and w_2=150eV and for the SSF w_3=60eV, w_4=150eV with O_C=60eV.

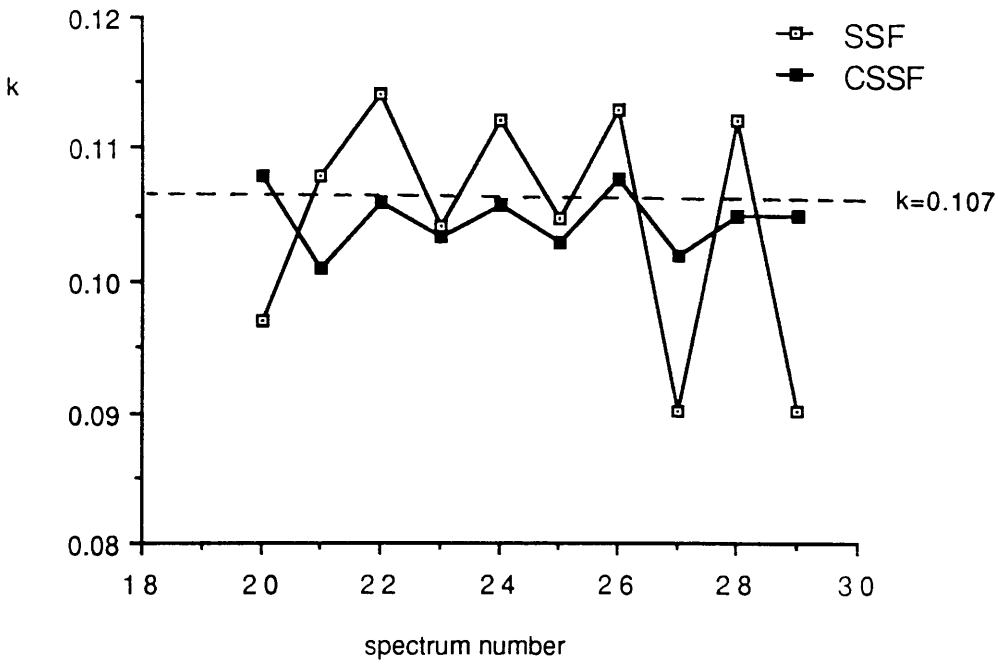

Figure 5.17(b). Comparison of the k values evaluated by the SSF and the CSSF for the data presented in figure 5.17(a).

k=0.104±0.003 for the SSF. Thus the average values agree within the standard error but the standard error is lower by a factor of ~4 for the CSSF. This reflects the reduction in the scatter of k values obtained using the CSSF. Therefore, the CSSF does appear to significantly reduce the fluctuations in the k value but the average value of k obtained from the CSSF is very sensitive to the choice of average value of r (eg. choosing the true value of r (3.207) produces a similar variation in the k value for the CSSF but around the correct value of k). It should be noted that, for the experimental data, the reduction in the fluctuations of k with the CSSF are not so significant. This suggests that in the experimental data, other artifacts such as tip emission fluctuations and the systematic change in r with energy loss are more significant than shot noise in introducing errors into the background fitting procedures.

In conclusion, provided the fitting windows are greater than 50eV, the EF, TF and SSF produce very similar results, all tending towards the true value. Only where rounding errors (occurring as a result of digitisation of the spectrum) are significant does the TF have a slight advantage over the EF and SSF. For noisy data, the CSSF, since it reduces the fluctuation in k, should make it easier to detect any small mass loss such as that observed in the VC data of figure 5.8. However, the average value of k achieved will be dependent on the average value of r substituted into the CSSF.

5.8 CONCLUSIONS

After a comparison of the available background fitting techniques on both experimental and theoretical data, the results are similar for the EF, TF and SSF background fitting techniques. For the restricted fitting windows available on the TiN spectra, the SSF, using the SIGMAL2 cross-section, offers a value of N/Ti consistently closer to the expected bulk values of $TiN_{0.59}$ than the EF and TF. However, use of a more accurate hydrogenic cross-section, SIGMAL2, significantly reduces the discrepancies between the EF and SSF in figure 5.10. Therefore, for the statistics available in the VC and TiN spectra examined here there is no advantage in any particular fitting technique provided the cross-sections SIGMAL2 are used throughout. Consequently, the faster, more convenient EF was used in conjunction with the SIGMAL2 cross-section for all subsequent data presented in this thesis.

As a final note, it should be pointed out that the data presented here has not been deconvoluted to remove the effects of multiple scattering from the characteristic edges. However, since this data was analysed, a deconvolution program became available on the UNIX computer allowing a check on the importance of deconvoluting the spectra. For the range of specimens examined ($t/\lambda \leq 0.5$) deconvoluting the spectrum was found to make less than a 5% difference to the C/V and N/Ti ratios. This suggests that the approximation discussed in section 5.2, where the relative contributions of multiple scattering to the characteristic edges are canceled out with the use of a similar extrapolation window on each edge, is valid for the

data presented here.

CHAPTER 6 DEVELOPMENT OF EXPERIMENTAL TECHNIQUES AND THEIR APPLICATION TO TiC

6.1 INTRODUCTION

In a study of the radiation damage processes we are interested in the rate of loss of material as a function of accumulated dose incident on the specimen. However, the rapid mass loss which occurs at the high dose rates that exist in a focussed electron probe make it very difficult to follow the damage process. To take into consideration this problem, the dose rate is reduced by defocussing the electron probe. The first section of this chapter describes the determination of the electron dose on the specimen which requires knowledge of the spatial current density distribution of the probe as a function of condenser defocus. Section 6.3 discusses experimental considerations that are applicable to the experiments described in this thesis and considers the relative contributions to the accumulated dose on the specimen from each of these techniques. Subsequent sections discuss experiments, to investigate the radiation damage process as a function of specimen thickness and dose rate in a TiC sample.

Digital annular dark field (ADF) images collected during the EELS experiments revealed mass loss, in the form of loss of intensity in the images, consistent with the area irradiated by the electron probe. The final section in this chapter discusses the extraction of information from these images which reveals the inhomogeneous nature of the damage process in both TiC and TiN.

6.2 DOSE MEASUREMENTS

6.2.1 Current Measurements

For a radiation damage experiment it is important to develop a consistent, repeatable technique for measuring the electron current density incident upon the specimen. This was achieved following a method described by Nicholson (1974) which involved connecting the real objective aperture (ROA) to ground via an electrometer and inserting the aperture into the path of the electron beam in a slightly off axis position to collect the total current incident upon the specimen. Using this approach, a correction for 39% back scattering from a molybdenum aperture in a phosphor bronze blade was made to the current readings. For a sequence of current measurements as in, for example, the measurement of dose during a radiation damage experiment, the continuous insertion of the ROA blade into the electron beam path is both time consuming and disruptive. Such a procedure can cause vibrations in the specimen stage and so exacerbate the problem of specimen drift. Therefore, in the experiments described in this thesis, the current on the ROA was calibrated to that measured from the virtual objective aperture (VOA) blade, which was connected to ground via a second electrometer. Since the VOA is already used as the probe defining aperture during EELS analysis, measurement of this current will not cause any disruption to the column alignment and specimen position during the acquisition of a series of EEL spectra. Although the current incident upon the VOA is that which is not used in forming the electron probe, the decay

in the measured current indicates the decay of emission from the tip. Therefore, provided that the microscope configuration remains stable throughout the acquisition of the data, the current incident upon the specimen can be measured by calibrating the current on the VOA and ROA at the end of each experimental session.

Since the dose rate experiments also involve the reduction of the tip bias voltage, calibrations were carried out between the ROA and the VOA for both the decay in tip emission as a function of time and tip bias voltage. A typical calibration curve is shown in figure 6.1. From this graph it is clear that the decrease in current on both the electrometers is linear as a function of both time and bias voltage over the range investigated. Calibration curves are characteristic of the tip used, and may change over large changes in extraction voltage. However, very little change is evident over a single experimental session where the column alignment remains as described in section 4.2.6.

6.2.2. Experimental Determination of Probe Size.

The dose rate at a radiation sensitive specimen should be sufficiently low as to enable the observation of the radiation damage trends. This can be achieved by reducing the condenser lens excitation producing a defocussed probe at the specimen. Consequently, in order to measure the current density incident upon the specimen, it is not only necessary to measure the total current incident upon the specimen but also the spatial distribution of this current. The probe size was estimated by measuring the extent to

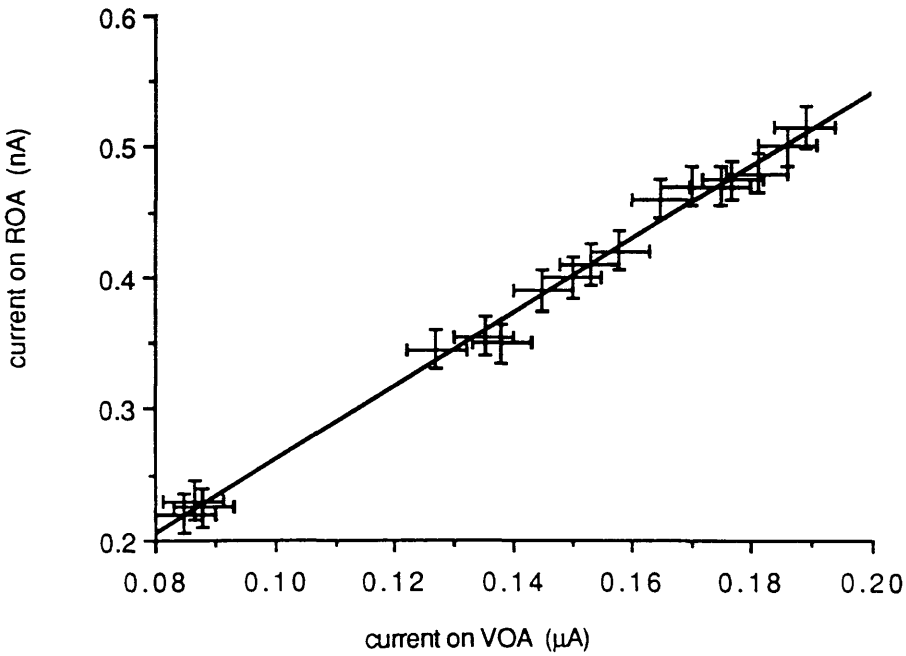

Figure 6.1. A typical calibration curve between the VOA and the ROA to measure the current incident upon the specimen. These current readings have not been corrected for the back scattering of electrons from the molybdenum aperture blade.

which the image of a sharp edge or point object was defocussed as a function of the condenser lens current.

A series of ADF images were collected from a sharp edge on an ion-beam thinned TiC specimen at increasing condenser defocus. Line profiles extracted from these images (figure 6.2) illustrate the loss of resolution as a function of increasing defocus and hence the probe size. It can be seen that the intensity fluctuations, due to the increasing thickness of the wedge shaped specimen and to irregularities in the specimen, hinder accurate determination of the beginning and end of the edge for the near focus images. Therefore, for the purpose of this experiment the beginning and end of the edge were defined to be the intersection of the tangent to the steepest part of the rise with the background intensity and the average level drawn through the intensity fluctuations on the specimen. This is illustrated in figure 6.2(a). For increasing defocus the detail in the specimen becomes less apparent making the average intensity on the specimen easier to define (6.2g). In measuring the width of the line profiles, w, the necessary corrections for the difference in area scanned on the AN10 and HB5 screens were made. The results are presented in figure 6.3 which shows a linear relationship between the measured probe size calculated from the line profiles and the condenser defocus. As expected, the estimation of the probe size at zero defocus is meaningless because of the finite size of the "sharp edge". As a result of spherical aberration and aperture diffraction effects, which affect the size of probe obtainable, theoretical considerations predict a probe of 20Å diameter for the 11mrad convergence angle used in this

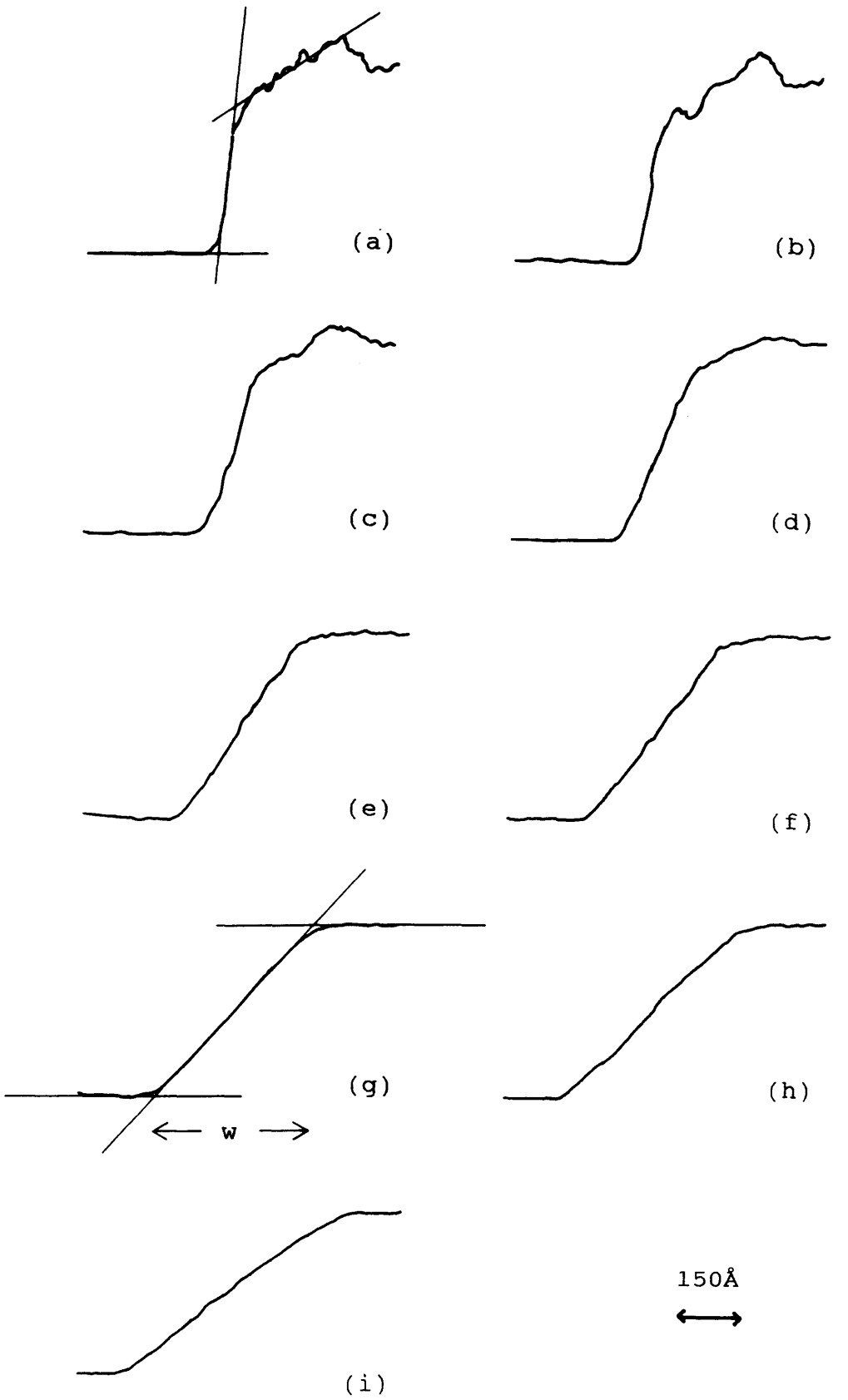

Figure 6.2. Line profiles extracted across an ADF image of a sharp edge at increasing condenser defocus.

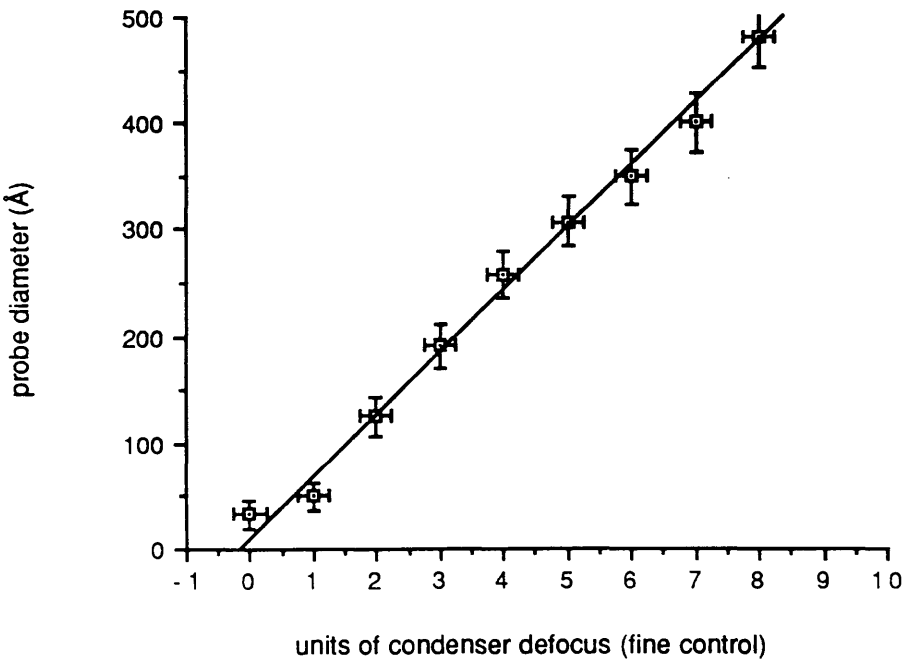

Figure 6.3. Probe diameter, estimated from the line profiles of figure 6.2, as a function of the condenser defocus.

work. However, figure 6.3 suggests that the diameter of the focussed probe under these conditions is (35±14)Å. The apparent disagreement between theory and experiment for the focussed probe measurements may be attributable to the convolution between the finite size of the edge and the probe which is dominant for small probes.

6.3 EXPERIMENTAL DETAILS

Before the beginning of each experiment, all apertures were removed, exposing the specimen to a high incident current at low magnifications. This procedure, known as "flooding" reduces the effect of contamination on the area of interest. The estimated dose administered to the sample during flooding ($\sim 2.5 \times 10^3$ electrons/Å^2) is a factor of 2600 less than that administered during the acquisition of one EEL spectra and so is not included in the accumulated dose calculations. The analysis was carried out on an area of sample possessing uniform thickness. In addition, strong diffraction conditions were avoided to reduce channeling effects which may increase the rate of radiation damage (Venables 1969, Phillip 1979). To measure the depletion rate of light elements from the material as a function of accumulated dose, a series of EEL spectra were acquired from the same specimen area. Consequently, it is important to be able to correct for specimen drift by accurately repositioning the specimen after the acquisition of each spectrum. The specimen drift was found to be in the range 20 to 50Å during the acquisition of an EEL spectrum. To overcome the lack of features visible in the image at high magnification (x2M) a focussed probe was used to burn a

hole in the specimen providing a feature which could be used to reposition the sample.

Initial experiments on VC data discussed in section 5.4. suggested that spectral acquisition be carried out for at least 20s to provide adequate statistics for reliable data extraction from the characteristic edges. At probe currents of ~0.7nA defocussing the probe by -2 units on the condenser fine control (~130±10Å) resulted in a current density at the specimen of ~3.3×10^5 electrons/Å^2/s. This current density was chosen because it resulted in a depletion rate that was easily observed (~50% loss recorded in 5 to 10 spectral acquisitions) for the specimen thicknesses examined in these experiments. The current was read from the VOA at the acquisition midpoint as described in section 6.2.1. After each spectrum was acquired the probe was refocussed to allow the specimen to be repositioned. A digital image was acquired with a focussed probe after every second spectrum to record any changes in the specimen occurring as a result of the radiation damage processes. The estimated dose administered during collection of each digital image was ~1×10^5 electrons/Å^2. This value is a factor of ~60 less than the dose administered during acquisition of an EEL spectra and therefore was not included in subsequent accumulated dose calculations.

These experimental conditions were used throughout the work presented in this thesis except in specific cases such as the collection of a series of spectra at a lower dose rate. The elemental ratios were calculated from the spectra using the background fitting techniques outlined in chapter 5 with the same fitting windows on the TiC spectra as

discussed for the VC spectra in chapter 5.

6.4. INITIAL RESULTS FROM A TiC SAMPLE.

6.4.1 Specimen Thickness Dependence.

Initial experiments were carried out on a $TiC_{0.98}$ sample prepared by ion beam thinning as described in chapter 4. To investigate the rate of loss of C as a function of the specimen thickness two series of spectra were collected at the same dose rate of 3.1×10^5 electrons/Å^2/s from different regions of the sample with varying thicknesses. The results are shown in figure 6.4 which shows the C depletion as a function of accumulated dose. As expected for EELS analysis of a uniform sample the intercepts at zero dose, which are a measure of the initial C content, are proportional to the specimen thickness at 5.5±0.2 and 3.5±0.2 C atoms/Å^2 for t/λ = 0.12 and 0.08 respectively. This suggests that a reasonable estimate of the rate of C depletion was calculated from the linear least squares fit applied to the data. The gradients were measured from this least square fit program to be $(3.8 \pm 0.5) \times 10^{-8}$ and $(4.0 \pm 0.5) \times 10^{-8}$ C atoms/electron for t/λ of 0.12 and 0.08 respectively. These results agree to within experimental error. This constant rate of loss of C atoms with respect to dose for increasing specimen thickness is consistent with the predictions of the knock-on displacement model discussed in chapter 3. As a further check, the fraction of C lost within the first 100s was (22±3)% at t/λ=0.12 compared to a (32±4)% loss over the same time period at t/λ=0.08. Again, within the experimental errors, the results are consistent with the

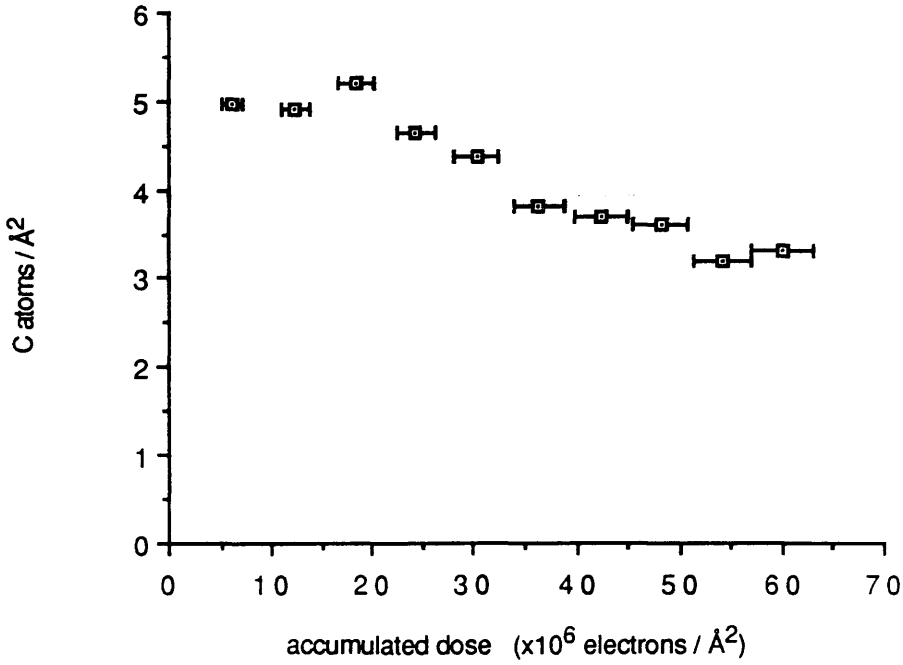

Figure 6.4(a). Loss of C from a TiC sample ($t/\lambda=0.12$) as a function of dose at a dose rate of 3.1×10^5 electrons/Å^2/s.

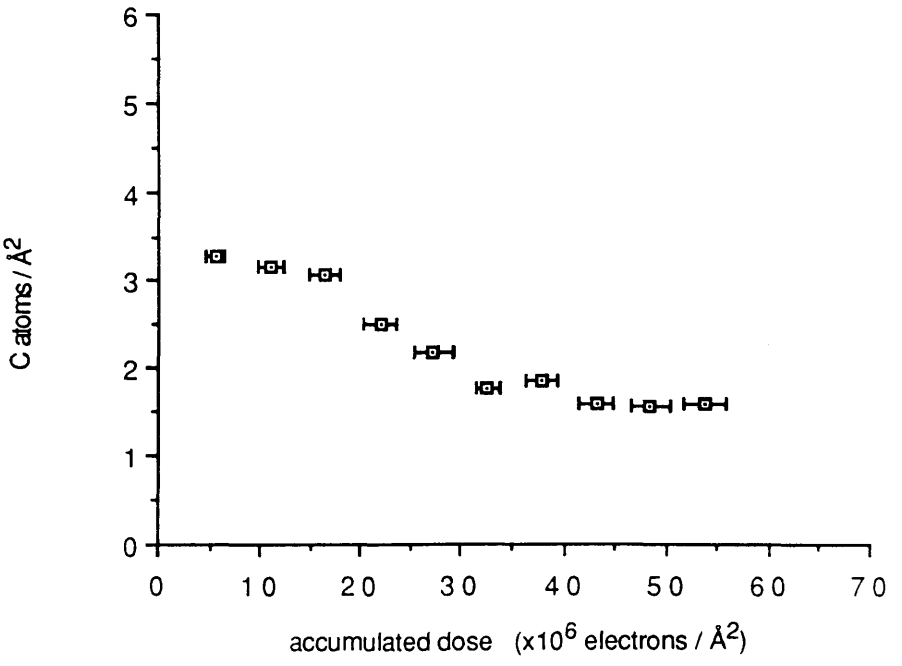

Figure 6.4(b). Loss of C from a TiC sample ($t/\lambda=0.08$) as a function of dose at a dose rate of 3.1×10^5 electrons/Å^2/s.

knock-on displacement model which predicted that fractional loss of C would be inversely proportional to the specimen thickness.

As the experimental data are consistent with the knock-on displacement model the rate of loss of C as a function of accumulated dose was substituted in equation 3.7 to calculate the displacement cross-section for C in TiC. Assuming a displacement distance of 3Å (corresponding to the C inter atomic spacing) and a total mean free path of 737Å in TiC (from equation 2.12), this yields a displacement cross-section of 21±5 and 23±5 barns for the two areas investigated in figure 6.4. (where 1 barn ≡ $10^{-8}Å^2$). These calculated cross-sections are considerably lower than theoretical displacement cross-sections calculated from equation 3.5 (184 barns for E_d=5eV) and correspond to a displacement energy of 14eV. However, the theoretical displacement cross-sections calculated from the McKinley-Feshbach approximation do not take into account the angular dependence of the displacement energy, E_d. As such they may overestimate the cross-section in a crystal structure where the displacement energy can be considerably greater than that of the "easy direction" assumed in the calculation, above, of a cross-section of 184 barns. This point will be discussed more fully in chapter 7.

6.4.2 Dose Rate Dependence

During initial experiments to burn a "positioning" hole in the sample it was noted that the dose rate, as well as the accumulated dose was important in the ability to burn a hole in the specimen. Investigations into this phenomenon

have previously been carried out in various forms of TiO (Berger 1987b). In order to establish whether radiation damage in general and the loss of the light element in particular from a TiC sample was dose or dose rate dependent, a further series of spectra were collected at a reduced dose rate. The lower dose rate series were collected from a neighbouring area to figure 6.4(a) to ensure a degree of self consistency in the specimen thickness and orientation.

The dose rate was reduced by a factor of 2 by decreasing the tip bias until the tip emission was half the previous value. Each spectrum was collected for 40s instead of the standard 20s to maintain the same total dose on the specimen. The results are shown in figure 6.5 for the lower dose rate (1.6×10^5 electrons/Å^2/s) and can be compared to the rate of loss at the higher dose rate in figure 6.4(a). It should be noted that the specimen thickness is the same for both the higher and lower dose rate experiments at $t/\lambda=0.12$. From a linear least squares fit to the C depletion curve of figure 6.5 the rate of loss of C is $(1.92 \pm 0.3) \times 10^{-8}$ at the lower dose rate compared to $(3.84 \pm 0.5) \times 10^{-8}$ C atoms/electron for the higher dose rate experiment of figure 6.4(a). Therefore, at the higher dose rate a factor of 2 more C atoms are lost per incident electron suggesting that there may be a dose rate effect in TiC. However, the lower dose rate experiment was carried out after the higher dose rate experiment but without reflooding the area. The experiment was also carried out over a longer period of time and therefore although beam induced contamination was not visible on the ADF images it is possible that there may have been an extra contribution

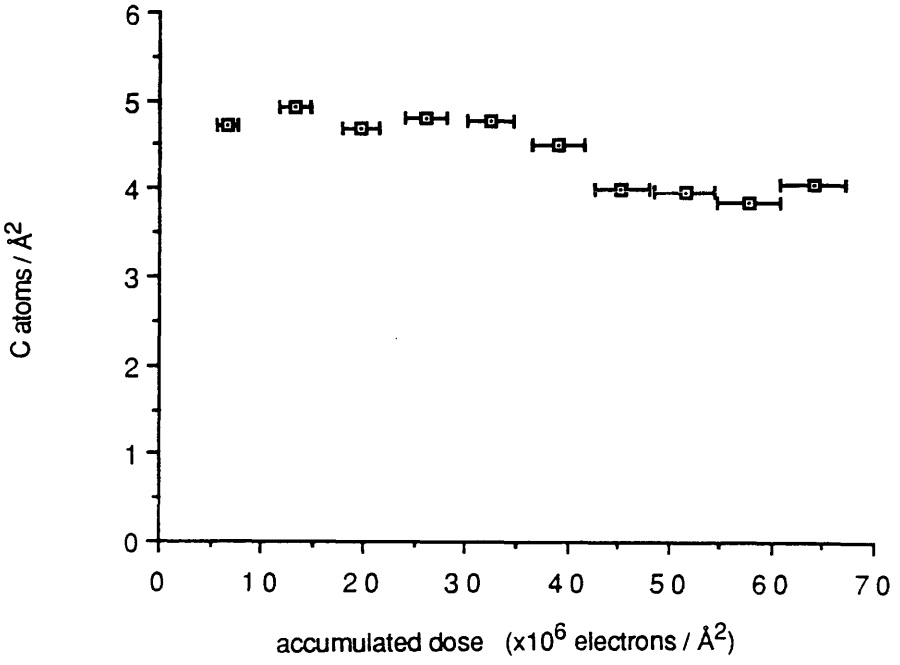

Figure 6.5. Loss of C as a function of dose for the lower dose rate experiment (dose rate=1.6×10^5electrons/Å^2 /s) for an area of the specimen with $t/\lambda=0.12$.

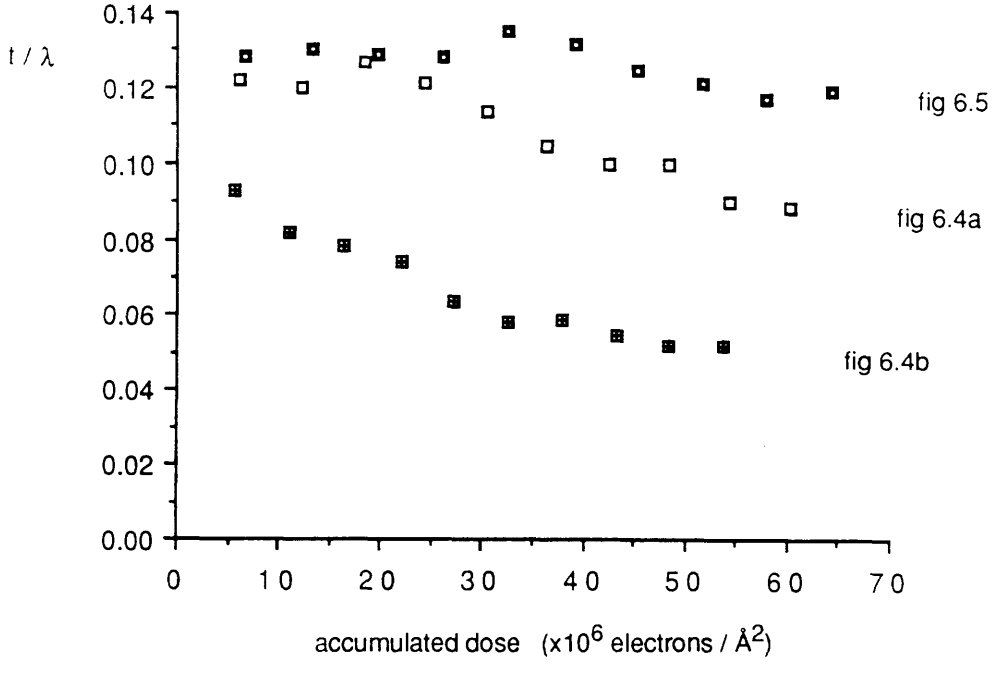

Figure 6.6. t/λ values as a function of dose for the areas of the TiC sample investigated in figures 6.4(a), 6.4(b) and 6.5.

to the C signal from the presence of contamination. Consequently, it is possible that the rate of loss of C in figure 6.5 has been reduced by a slow gain in the C signal from contamination sources. The inability to separate the contribution to the C characteristic edge from the C in the bulk of the sample and beam induced contamination yields inconclusive results from the TiC samples.

6.4.3 Loss of Ti

The t/λ graphs shown in figure 6.6 for each of the areas previously examined suggest a significant decrease in the relative specimen thickness for the higher dose rate experiments of figure 6.4. The loss of C alone is unlikely to account for a 40 to 50% decrease in t/λ and therefore the absolute number of Ti atoms as a function of accumulated dose were examined. The results are shown in figures 6.7. where it can be seen that there is an appreciable decrease in the Ti signal from the areas of the sample irradiated at the higher dose rate. Figure 6.7(a) also shows a threshold dose below which there is no significant loss of Ti from the sample, although neither of the three areas examined showed a threshold for the C depletion. For the lower dose rate experiment shown in figure 6.7(c) there is no loss of Ti observed within the limitations of noise in the data. It should be noted that the knock-on displacement model predicts that the Ti atoms cannot be displaced from the bulk of the sample since the binding energy of Ti in TiC (20eV) is greater than the energy transferred from an incident electron (5eV) or from an excited C atom (12.8eV). One possible explanation for

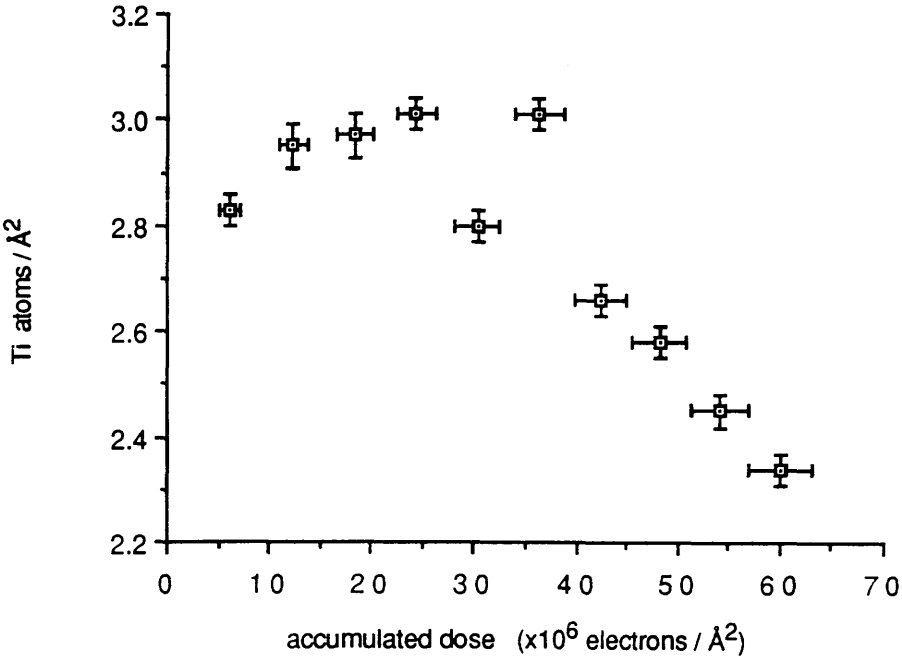

Figure 6.7(a). Loss of Ti as a function of dose for the area of the TiC sample investigated in figure 6.4(a).

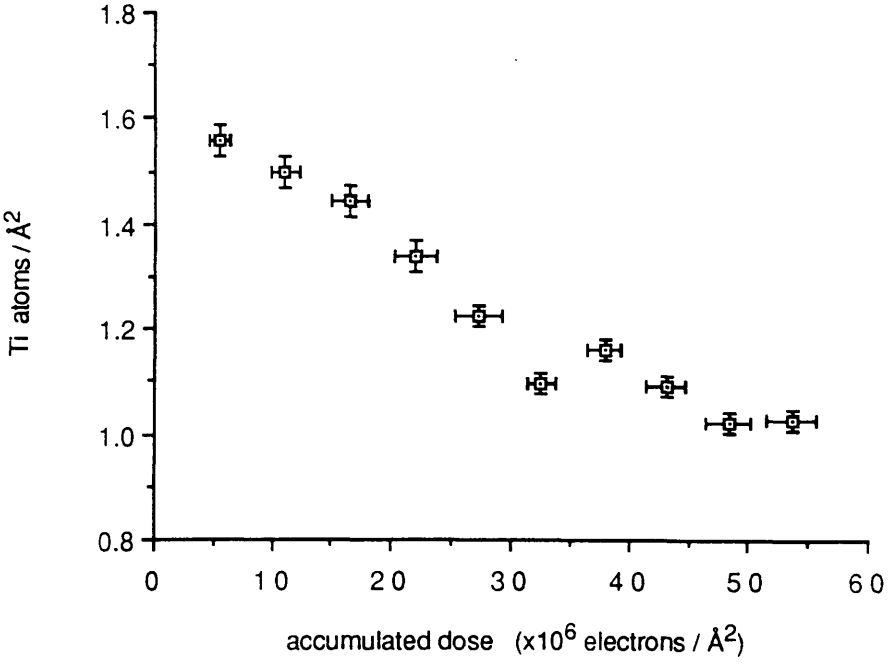

Figure 6.7(b). Loss of Ti as a function of dose for the area of the TiC sample investigated in figure 6.4(b).

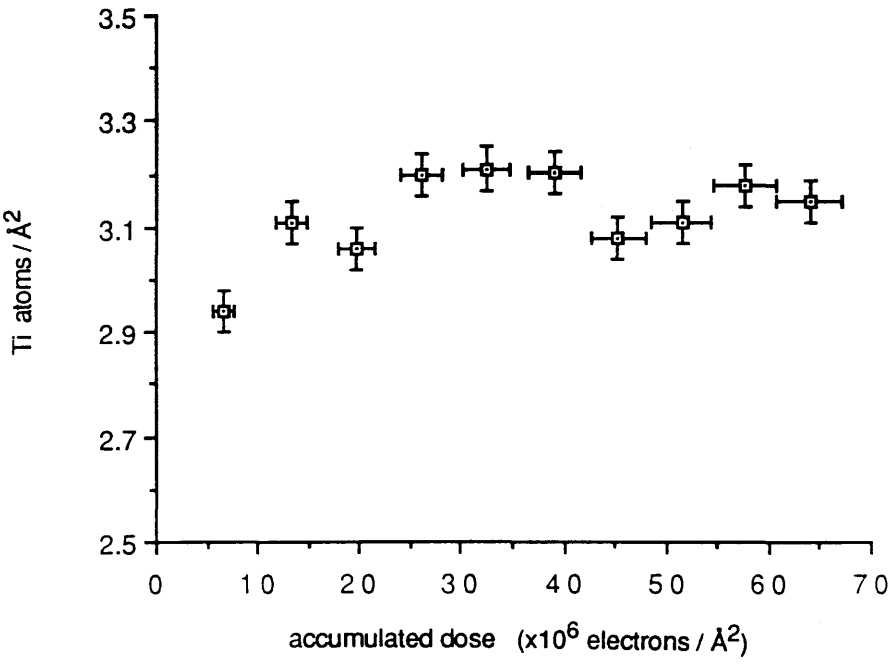

Figure 6.7(c). Loss of Ti as a function of dose for the area of the TiC sample investigated in figure 6.5.

the loss of Ti may be the presence of defects in the sample, around which the binding energies have been significantly reduced. This preferential loss of material from selected regions of the specimen is consistent with the results from the imaging techniques discussed in the next section. Another possible explanation for the loss of Ti may be sputtering from the specimen surface as a result of the reduced binding energies. The surface binding energies of the C and Ti atoms may be reduced by a factor of 4 to 5 compared to the binding energies in the bulk (Bradley 1988) enabling both the C and Ti to be sputtered from the specimen surface. Loss of both C and Ti from the specimen surface may result in the surface receding and a subsequent decrease in the specimen thickness as observed in figure 6.6.

In conclusion, the loss of Ti at the higher dose rates suggests that the Ti loss mechanism may be dose rate dependent. However, the preferential loss of material in selected regions of the specimen suggests that other factors, such as defects in the specimen, may also play a significant role in the loss of Ti. Further experiments are required to clarify the situation and the loss of Ti is discussed in more detail in section 7.5.3.

6.5 IMAGE ANALYSIS

Signals that are collected from electrons scattered through high angles only result in detected intensities that are predominantly attributable to elastic scattering and so display a strong dependence on atomic number, Z. Crewe et al (1970,1975) demonstrated such "Z-contrast"

imaging on the STEM using an annular dark field (ADF) detector, which intercepts a significant fraction of the total elastic scattering signal thus producing an image with strong Z contrast. Early work on this technique (Crewe 1970,1975 and Isaacson 1979) concentrated on the imaging of heavy atoms in light element matrices. In these experiments, where a large fraction of the total elastic scattering was collected, the scattering intensity on the ADF detector is, to a first approximation, proportional to $Z^{4/3}$ (Lenz 1954). At larger angles however, the scattering intensity tends towards that of unscreened Rutherford scattering and is proportional to Z^2. For the crystalline materials of interest in this thesis the image contrast is dominated by diffraction effects at low angles (Donald and Craven 1979), which may hinder Z contrast analysis. Provided the inner acceptance angle of the annular detector is large enough to omit low order diffraction signals the signal detected at larger angles becomes incoherent and the Z dependency can be recovered in high angle ADF images. This technique has been applied in chemical mapping investigations (Isaacson, 1976), grain boundary segregation in CuBi (Donald and Craven 1979), grain boundary segregation in Si (Pennycook 1989a) and semiconductor multilayers (Pennycook 1989b and McGibbon 1989).

Digital images acquired during EELS analysis revealed radiation damage in the form of mass loss from the sample which was evident as a decrease in the intensity of the ADF images in the irradiated areas. In view of the chemical mapping techniques outlined in the above references, an attempt was made to correlate the observed change in intensity of the ADF images with the mass loss recorded by

EELS analysis.

The images were carefully aligned, using the hole burned as a specimen positioning feature during EELS analysis. Although the images were collected with zero black level there may also be a background or dark current contribution from the DC offset in the amplifier of the ADF detector. This was calculated by acquiring an image with the tip switched off and was then subtracted from each image. The decay in intensity of the images due to the emission properties of the tip was normalised using the number of counts in an undamaged area of the image. The series of images shown in figure 6.8 represent a time sequence over ~200s of the radiation damage process in TiC and its effect on the irradiated area of the specimen. The apparent holes in the series of images are areas which have been preferentially thinned by the radiation damage process. In these, the intensity has decreased to ~70% of the original value at the end of the image sequence. It should be noted however, that at the current densities available in the focussed probe ($\sim 1.25 \times 10^{7}$ electrons/Å^{2}/s) it is possible to burn a hole in the sample over an extended period. By subtracting subsequent images, a clearer picture of the changes in the irradiated area as the damage progresses is obtained as shown schematically in figure 6.9(a). Note that if a preferentially thinned area appears in one image it will not be present in the next difference image unless more damage has occurred in that area. The damage appears to be inhomogeneous, with preferential damage occurring in small selected regions of the irradiated area even with a defocussed probe. This suggests that certain areas of the sample are more susceptible to radiation damage perhaps due

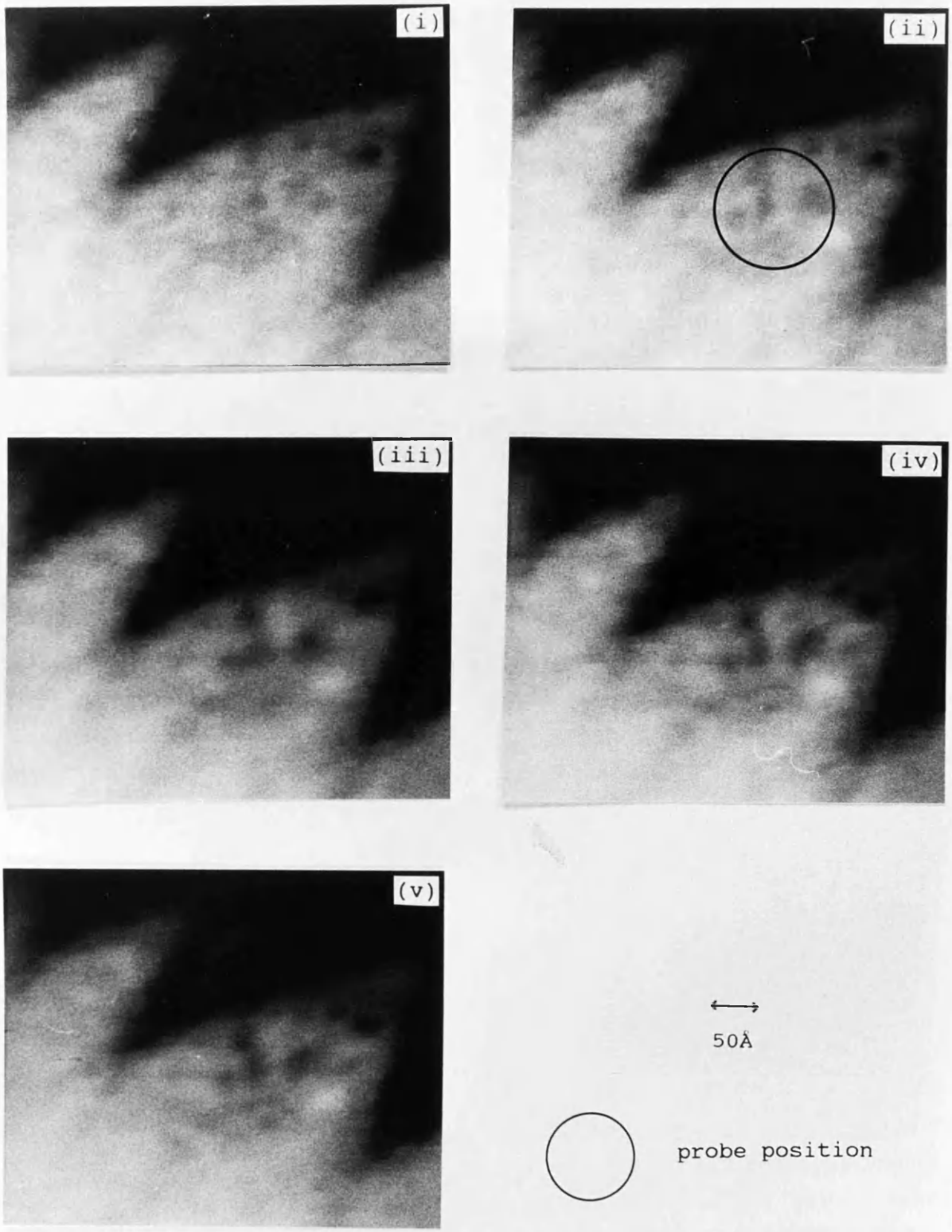

Figure 6.8 Series of ADF images to show the radiation damage process for the EELS data presented in figure 6.4(a). Image (i) was collected after the second EEL spectrum, image (ii) after the fourth EEL spectrum etc.

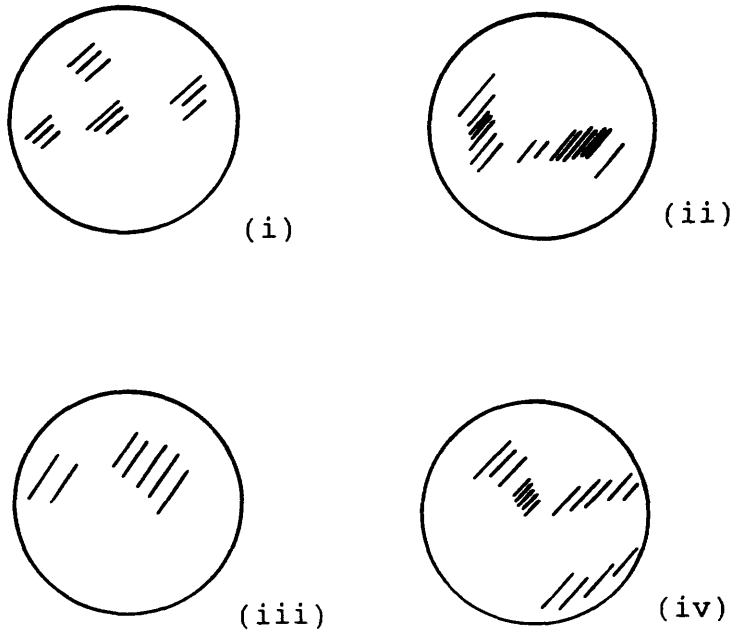

Figure 6.9(a). Sequence of difference images for the ADF images shown in figure 6.8. Image (i) is the difference between the first and second images of figure 6.8, image (ii) is the difference between the second and third images etc. The shading indicates the areas of change between each image in the series where the closer together the shading the larger the change in the image. The almost solid shading corresponds to the areas of preferential damage shown in figure 6.8.

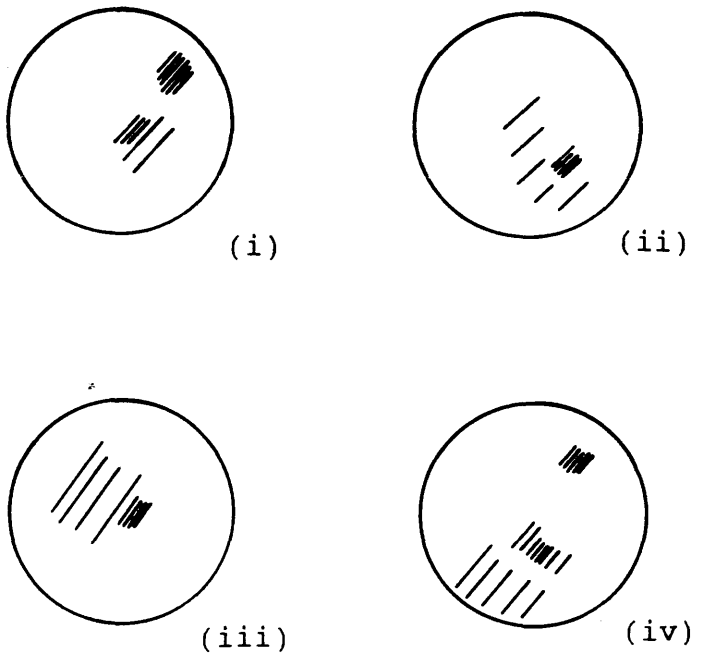

Figure 6.9(b) Sequence of difference images for the ADF images of the radiation damage process corresponding to the EELS data presented in figure 6.4(b).

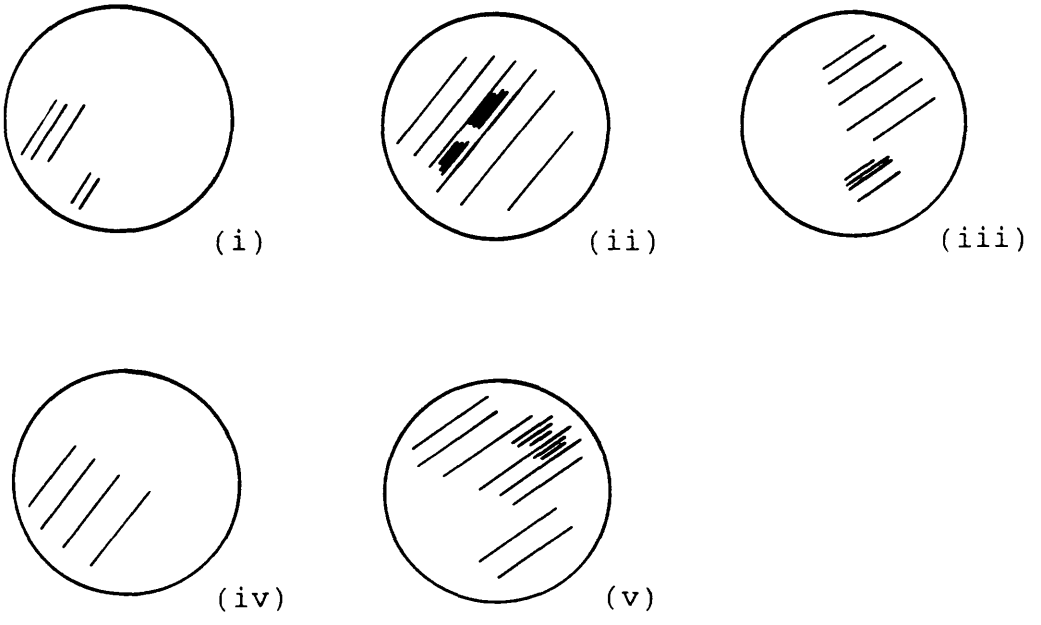

Figure 6.9(c) Sequence of difference images for the ADF images of the radiation damage process corresponding to the EELS data presented in figure 6.5.

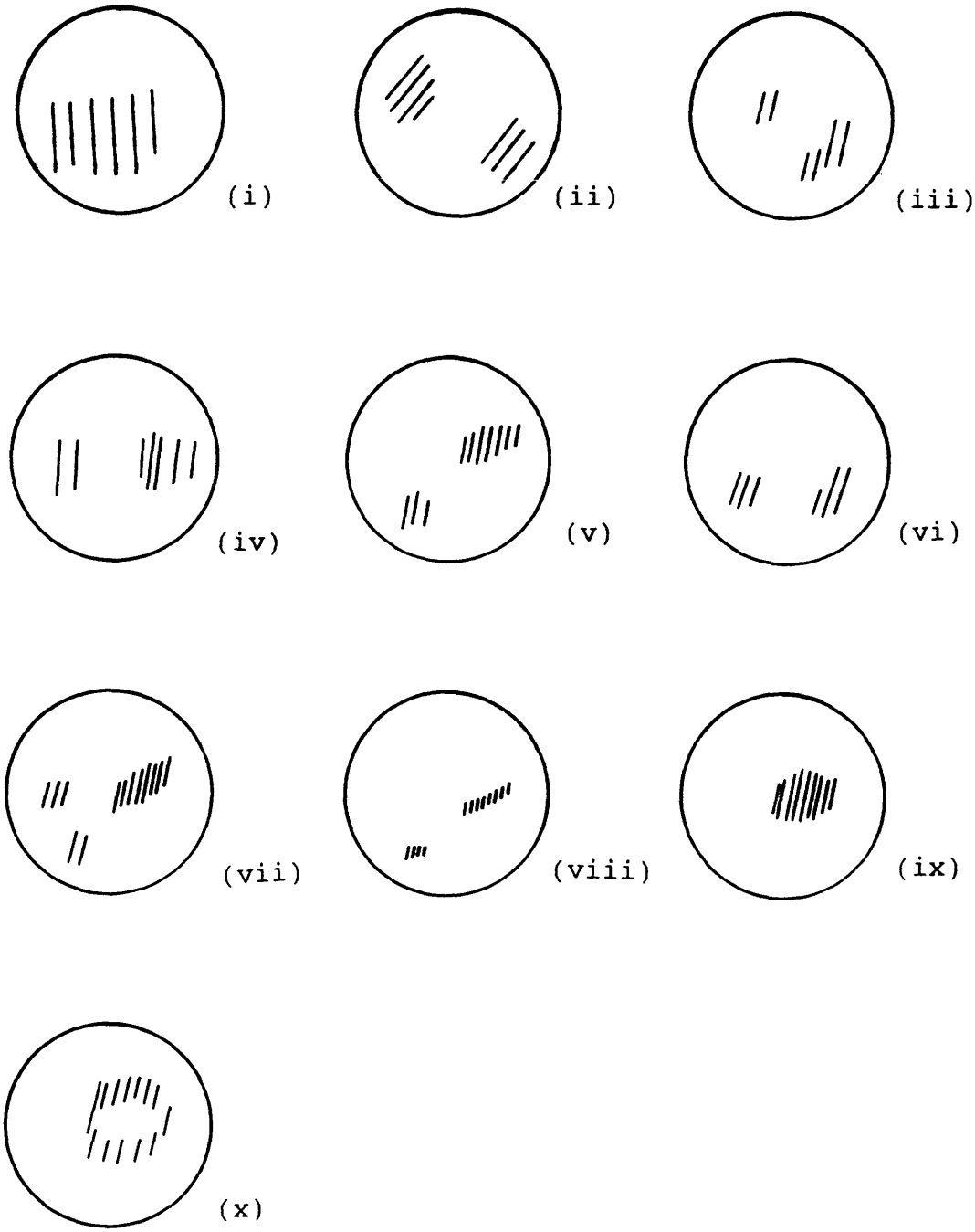

Figure 6.9(d) Sequence of difference images for the ADF images of the radiation damage process in the TiN samples corresponding to the N and Ti depletion curves of figures 7.11(a) and 7.15(a).

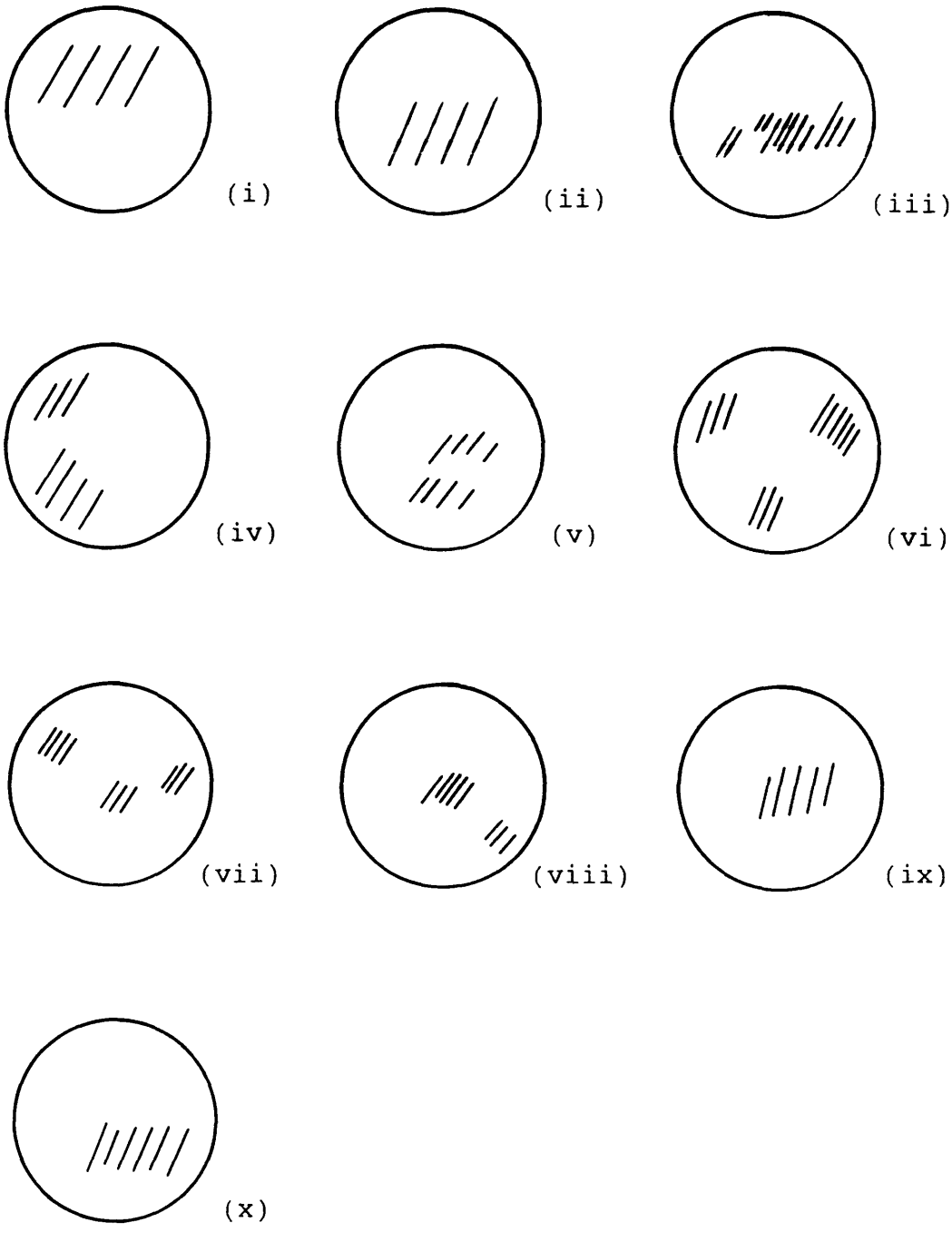

Figure 6.9(e) Sequence of difference images for the ADF images of the radiation damage process in the TiN samples corresponding to the N and Ti depletion curves of figures 7.11(b) and 7.15(b). The orientation of this sample was significantly closer to a strong diffraction condition than 6.9(d).

to defects in the sample or to the effects of the crystal structure. This is consistent with a report from Bulloch (1989) who noted that, during irradiation in a STEM, crystalline silicon developed an array of holes despite rastering the probe across the specimen to reduce the dose. The holes evolved in the crystalline silicon irrespective of specimen orientation but were absent in amorphous silicon. Figures 6.9(b) and 6.9(c) illustrate a similar time sequence of the radiation damage process for the remaining two TiC data sets discussed in section 6.4. To investigate the radiation damage processes at higher doses a series of 20 EEL spectra, corresponding to 11 ADF images, were collected from two different areas of a TiN sample. The difference images are shown in figures 6.9 (d) and (e). The corresponding EELS data is presented in section 7.5.2. It should be noted that the second series of TiN images were collected from an area significantly closer to a strong diffraction condition. As illustrated in figure 6.9 the damage occurs in a similar manner for all 5 areas examined, with preferentially damaged areas in both the low dose rate (figure 6.9c) and the higher dose rate experiments. However, the spatial distribution of the preferential damage within the defocussed probe is not the same for the areas of specimen examined in these experiments. This suggests that the preferential damage is not a result of an inhomogeneous current distribution within the defocussed probe but to factors dependent on the area of specimen irradiated.

If the Ti is lost from these preferentially thinned regions, one might expect to see a build up of Ti at the edges of these damaged areas as reported by Berger et al

(1987a and b) for Al in Al_2O_3 and Ti in TiO resulting in increased intensity in the ADF images. To within the accuracy of the alignment and normalisation of the images, there is no indication of a build up of Ti around the damaged regions. This suggests that the Ti is lost from the irradiated region by a forward knock-on process and insignificant quantities of Ti build up at the periphery at these specimen thicknesses. The loss of Ti from the sample is discussed in further detail in section 7.5.3 for the TiN materials.

On subtraction of the final image from the first image in a damage sequence the overall shape of the damaged region was consistent with the estimated size of the defocussed probe (diameter ~ 130Å) as illustrated in figure 6.10. In this way, a change in intensity is recorded on the ADF image that corresponds to the region of the sample irradiated by the electron probe. In an attempt to correlate this change in signal on the ADF image with the mass loss recorded by EELS analysis we must first consider the signal incident upon the ADF detector for the experimental conditions employed here. The inner acceptance angle of the ADF detector (θ_{in}) was estimated to be ~13 mrad by calculating the distance of the spectrometer image plane from that of the ADF detector using the angle subtended at the collector aperture of 3.1mrad measured by Crozier (1985). This value of θ_{in} is significantly smaller than the values of 65 to 85 mrads used in the above references. Assuming the angular distribution varies linearly with position on the ADF detector (valid for small post-specimen lens compressions, Buggy 1985) the outer angle subtended by the ADF detector (θ_{out}) is ~96mrads.

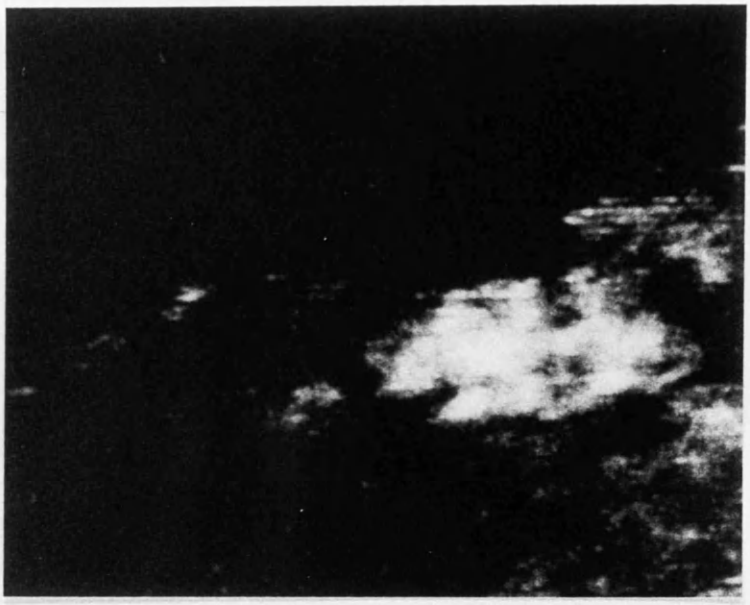

Figure 6.10. ADF image to show the extent of the radiation damage within the area irradiated by the electron probe. This was calculated by subtracting the first and last images of the damage sequence corresponding to the EELS data presented in figure 6.5

As discussed previously, the scattering intensity considered in this experiment is likely to lie between the two approximations of total elastic scattering, proportional to $Z^{4/3}$, and Rutherford scattering, proportional to Z^2, which dominates at higher scattering angles. However, for the angles subtended by the ADF detector in this experiment (13 to 96mrad) the scattering intensity will be significantly closer to the approximation of total elastic scattering. As a first approximation the scattering considered in these experiments was assumed to be incoherent providing strong diffraction conditions are avoided. Consequently, the scattering intensity in the ADF image is equal to the sum of the individual intensities (Isaacson 1979) and the elastic scattering from a TiC sample is proportional to

$$N_C Z_C^{4/3} + N_{Ti} Z_{Ti}^{4/3} \qquad 6.1$$

where N_C and N_{Ti} are the number of C and Ti atoms respectively and Z_C and Z_{Ti} are the atomic numbers of C and Ti respectively. An estimate of the theoretical ADF intensity was calculated from the EELS results presented in section 6.4 for the TiC spectra. The absolute number of C and Ti atoms in the volume irradiated were extracted from the depletion curves of figures 6.4 and 6.5 by multiplying the number of atoms/unit area by the probe size. To take into consideration the small fluctuations present in the data, which are probably due to probe repositioning errors, the C and Ti content were extrapolated from the best fit to the depletion curves as discussed in section 6.4.1. This is a reasonable estimate for the comparison of the EELS and

ADF digital images because an identical area is integrated on the image regardless of any repositioning errors which occur during the EELS analysis. In a similar manner the theoretical intensities for the TiN samples were calculated from equation 6.1 by substituting the EELS data for the N and Ti depletion curves presented in figures 7.11 and 7.15 of chapter 7.

The area irradiated by the probe was estimated from the digital images by subtracting the first and last images of a sequence, as discussed above. The total intensity within this area was calculated for the sequence of images using an integration program on the AN10000 computer.

Figures 6.11 (a) to (e) show the resulting graphs of the intensity integrated from the ADF images as a function of the theoretical intensity calculated from the EELS data substituted in equation 6.1. The graphs are drawn with suppressed zeros to show the trends more clearly and the intercept is indicated on each figure for completeness. There is a linear correlation between the experimentally determined scattering intensities and those predicted from equation 6.1 for the range of intensities examined in these experiments. However, there appears to be a large variation in the gradients measured from figure 6.11 for the 5 areas under investigation. For example, the low dose spectra (figure 6.11c) which do not lose Ti under the electron probe as discussed in 6.4, show a much smaller change in predicted theoretical intensity (~6%). This is not surprising since the Ti, being the heavier element, plays the dominant role in the calculation of the theoretical intensity in equation 6.1. However, this area also records one of the highest percentage changes in intensity measured

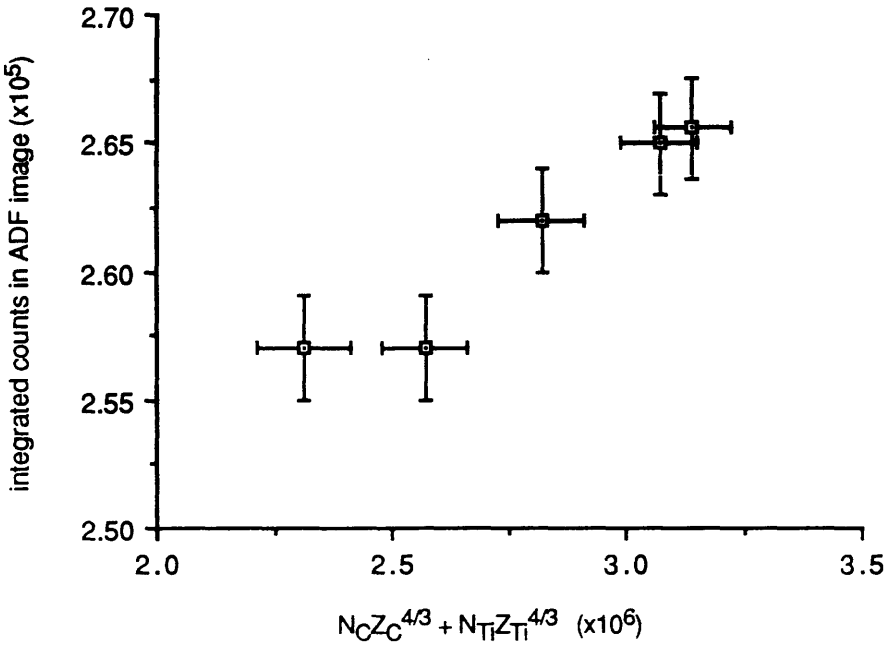

Figure 6.11(a). Intensity integrated from the ADF images as a function of the theoretical ADF intensity (calculated from equation 6.1) for the EELS data presented in figure 6.4(a). The linear fit to the data points is given by $y = (0.012\pm0.002)x + (2.3\pm0.1)\times10^5$

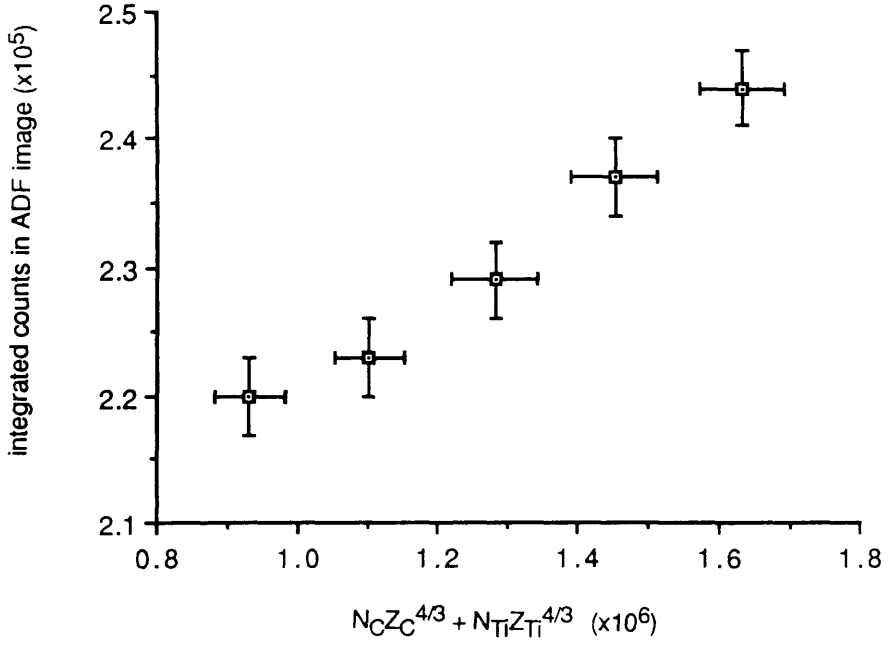

Figure 6.11(b). Intensity integrated from the ADF images as a function of the theoretical ADF intensity (calculated from equation 6.1) for the EELS data presented in figure 6.4(b). The linear fit to the data points is given by $y = (0.04\pm0.003)x + (1.9\pm0.1)\times10^5$

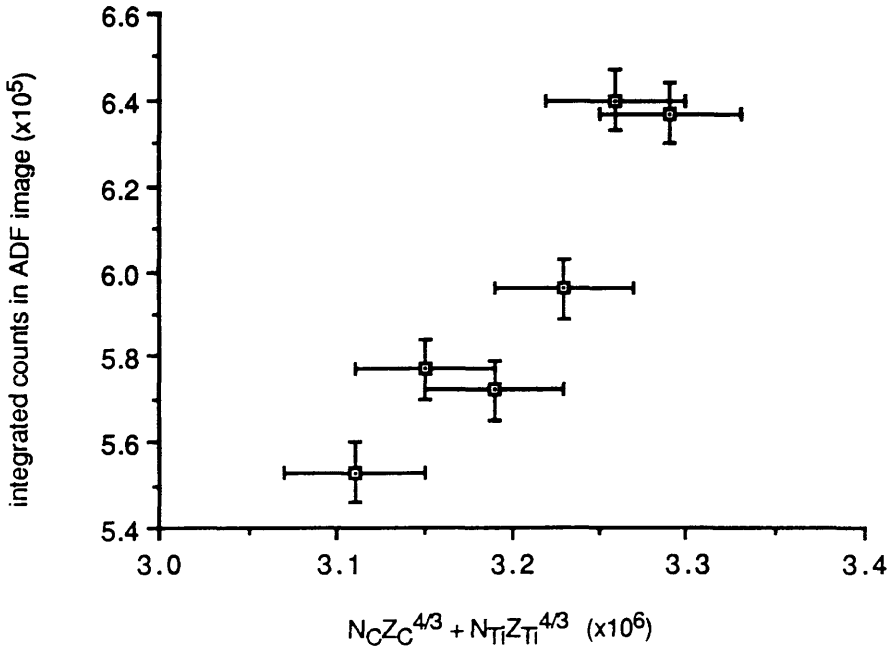

Figure 6.11(c). Intensity integrated from the ADF images as a function of the theoretical ADF intensity (calculated from equation 6.1) for the EELS data presented in figure 6.5. The linear fit to the data points is given by $y = (0.5\pm0.1)x - (9.8\pm3)x10^5$

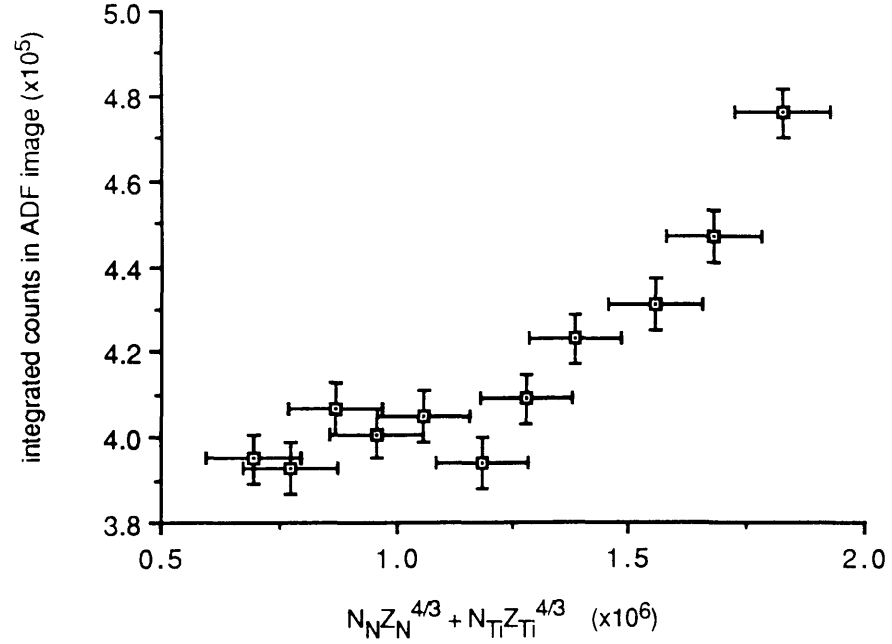

Figure 6.11(d). Intensity integrated from the ADF images as a function of the theoretical ADF intensity (calculated from equation 6.1) for the EELS data presented in figure 7.11(a). The linear fit to the data points is given by $y = (0.06\pm0.01)x + (3.4\pm0.2)x10^5$

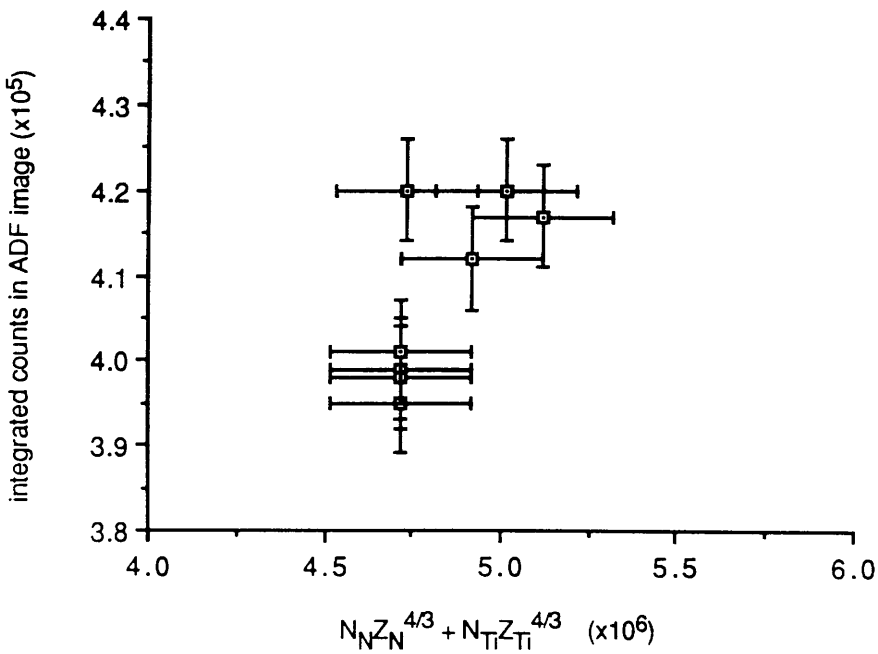

Figure 6.11(e). Intensity integrated from the ADF images as a function of the theoretical ADF intensity (calculated from equation 6.1) for the EELS data presented in figure 7.11(b). The linear fit to the data points is given by $y = (0.05\pm0.02)x + (1.9\pm0.9)x10^5$

from the digital images (~15%). Figure 6.11 also shows a large variation in the intercepts measured at zero theoretical intensity ($N_C Z_C^{4/3} + N_{Ti} Z_{Ti}^{4/3}$) which is a measure of the dark current present in the ADF detector. This may be because the dark current measurements were made retrospectively therefore introducing an error in the intercept where there was a large change in the gain of the ADF detector. Not surprisingly the linear relationship between the ADF intensity and the predicted change in intensity from the mass loss is somewhat dubious for the stronger diffraction conditions of figure 6.11(e) as reflected in the error on the intercept.

The collection of quantitative ADF images was not part of the original aim of the radiation damage experiments. Therefore, the gain on the ADF detector was not set at a constant value throughout the five experiments discussed above which will result in discrepancies in the signal level integrated from the ADF images. Howie (1979) showed that the diffraction effects from crystalline samples are attenuated by atomic thermal vibrations at higher angles. Provided low order diffraction conditions are avoided, Treacy (1982) found an inner angle of ~70 mrad was sufficient to exclude the effect of orientation on the ADF images. Consequently, at ~13mrad, even if strong diffractions conditions are avoided, the intensity on the ADF images may be affected by the exact orientation of the specimen and this was not consistent for the five areas investigated. Avoiding strong diffraction conditions also reduces electron channeling effects in the crystal which could influence the image contrast (Pennycook 1986). Treacy (1988) noted that the strain around a specimen defect may

give rise to an increase or decrease in the observed ADF intensity. The range of gradients obtained from figures 6.11 may be attributable to any or all of these effects and so future experiments should strive to keep the imaging conditions consistent throughout a series of experiments.

6.6 CONCLUSIONS

Initial experiments on a TiC sample are consistent with the predictions of the forward knock-on displacement model of chapter 3. However, the problem of beam induced contamination reduces the significance of the TiC results, since the contamination may contribute to the C characteristic edge. To extend this work over a wider range of specimen thicknesses and to verify the dose rate effect observed in TiC further experiments were carried out on TiN samples to avoid the complications of an unknown contribution to the characteristic edge of interest. In TiN even if contamination is a significant problem it can still be separated from the N signal, provided the contamination is not so severe it reduces the N signal to background ratio for EELS analysis.

Analysis of the ADF images has shown that there is a linear correlation between the mass loss recorded by EELS analysis and the change in image intensity of the ADF images. Provided the acquisition conditions of the ADF images are held constant throughout the experiments (ie the ADF photomultiplier gain and the specimen orientation) and the inner angle subtended by the ADF detector is increased to exclude low order diffracted beams, the experiments reported here suggest that some information can be

extracted from analysis of the ADF images. Incoherent high angle ADF imaging has proved successful in high resolution imaging of semiconductor materials where there is strong contrast between multilayers of different composition, yielding quantitative results consistent with EDX techniques (Martin 1990). However, in its present form ADF imaging is unlikely to compare with quantitative EELS analysis for the study of preferential loss of the light element under electron irradiation but the digital images do provide useful information on the inhomogeneous nature of the damage process.

CHAPTER 7 ANALYSIS OF TiN SAMPLES

7.1 INTRODUCTION

In this chapter we extend the range of thicknesses examined on an ion-beam thinned TiN specimen. Two independent sets of experiments are considered in section 7.2 to examine the rate of loss of N with respect to accumulated dose for increasing specimen thickness. The data is considered in relation to the radiation damage mechanisms discussed in chapter 3, and the cross-section for displacement of N in TiN is calculated from each of the damage mechanisms. Other factors which may affect the apparent rate of loss of N from TiN such as dose rate and specimen orientation are considered in the final section.

7.2 EXPERIMENTAL RESULTS

In an experiment to examine the effect of specimen thickness on the rate of loss of N, eight areas of a TiN sample which possessed different sample thicknesses were investigated. At each thickness, a series of spectra was collected to investigate the loss of N with respect to accumulated dose. All spectra were collected from the same ion-beam thinned $TiN_{0.59}$ sample at a dose rate of 3.1×10^5 electrons/Å^2/s. The experiments and analysis procedures were carried out in a similar manner to the TiC experiments described in chapter 6 with the analysis conditions described for TiN spectra in chapter 5. The N depletion curves are shown in figure 7.1 (a) to (h), arranged in order of increasing thickness. The later graphs have a

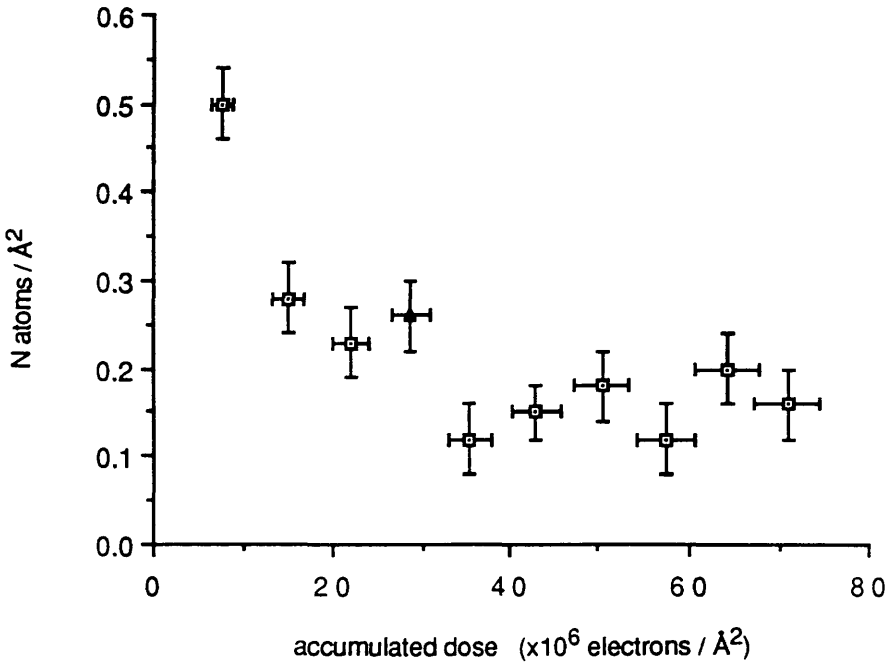

Figure 7.1(a). Loss of N from a TiN specimen ($t/\lambda=0.03$) as a function of dose at a dose rate of 3.4×10^5 electrons/Å^2/s

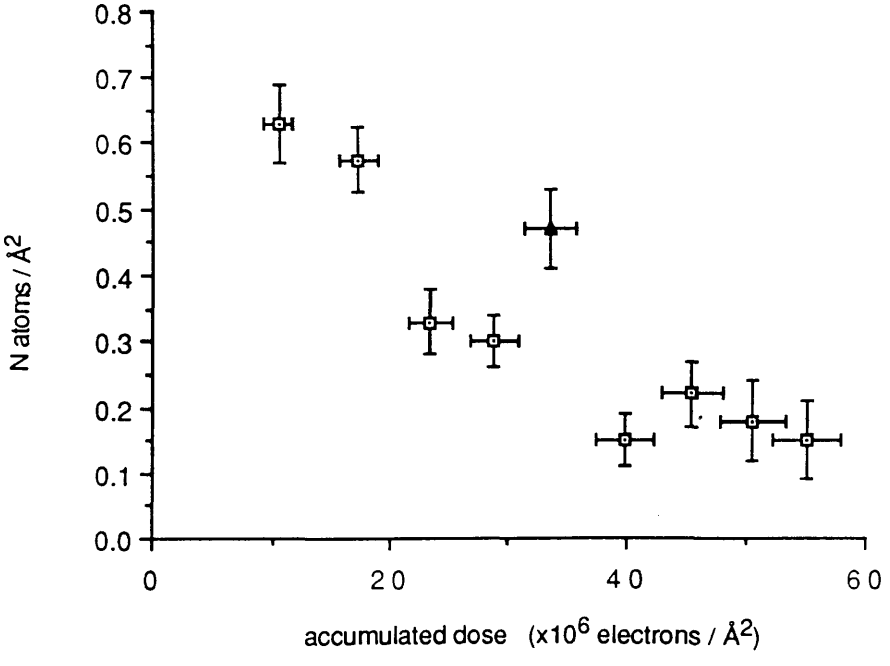

Figure 7.1(b). Loss of N from a TiN specimen ($t/\lambda=0.04$) as a function of dose at a dose rate of 3.4×10^5 electrons/Å^2/s

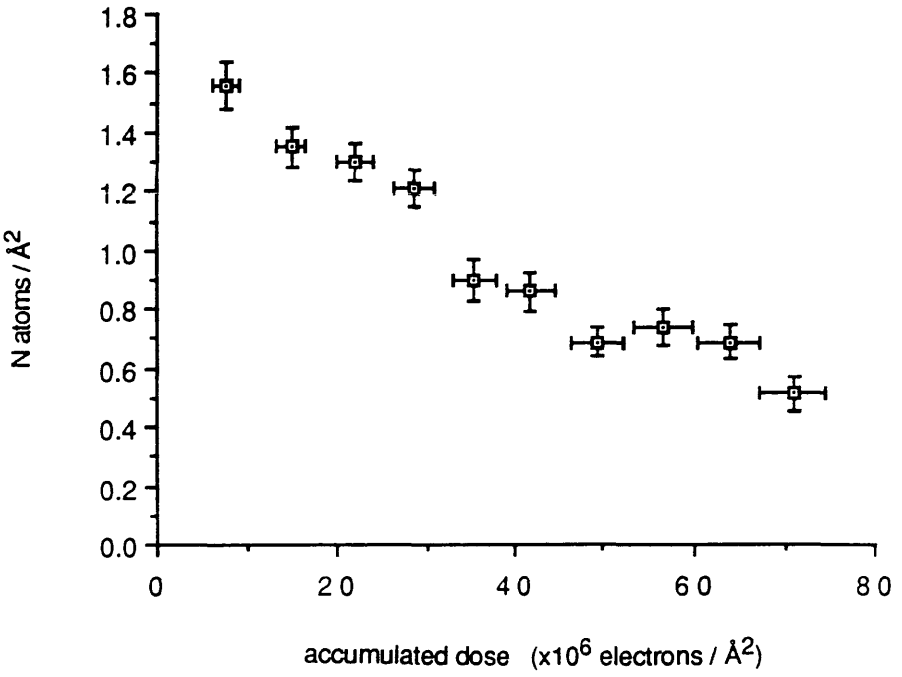

Figure 7.1(c). Loss of N from a TiN specimen ($t/\lambda=0.07$) as a function of dose at a dose rate of 3.4×10^5 electrons/Å^2/s

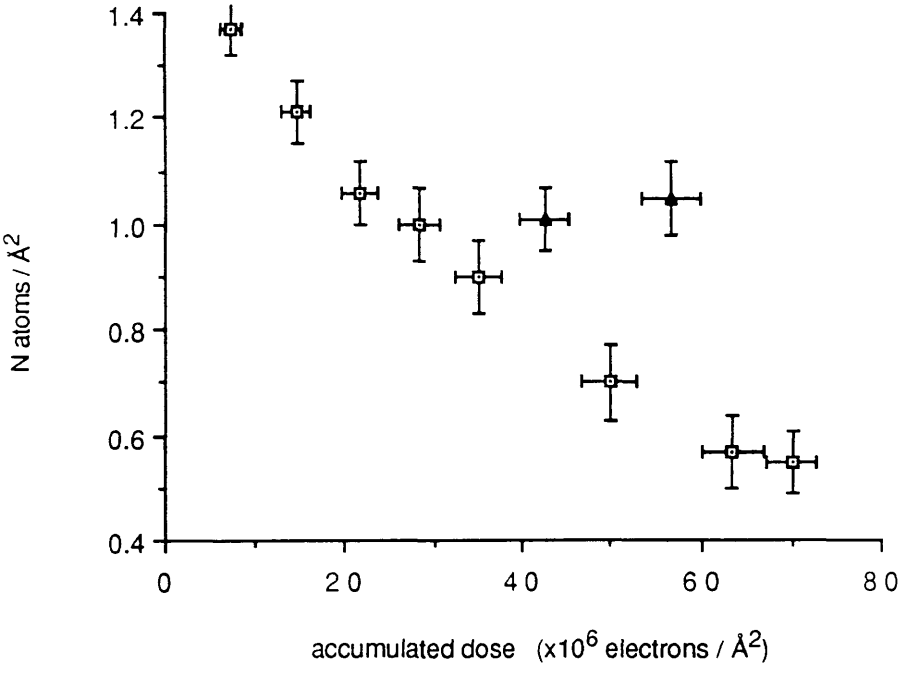

Figure 7.1(d). Loss of N from a TiN specimen ($t/\lambda=0.07$) as a function of dose at a dose rate of 3.4×10^5 electrons/Å^2/s

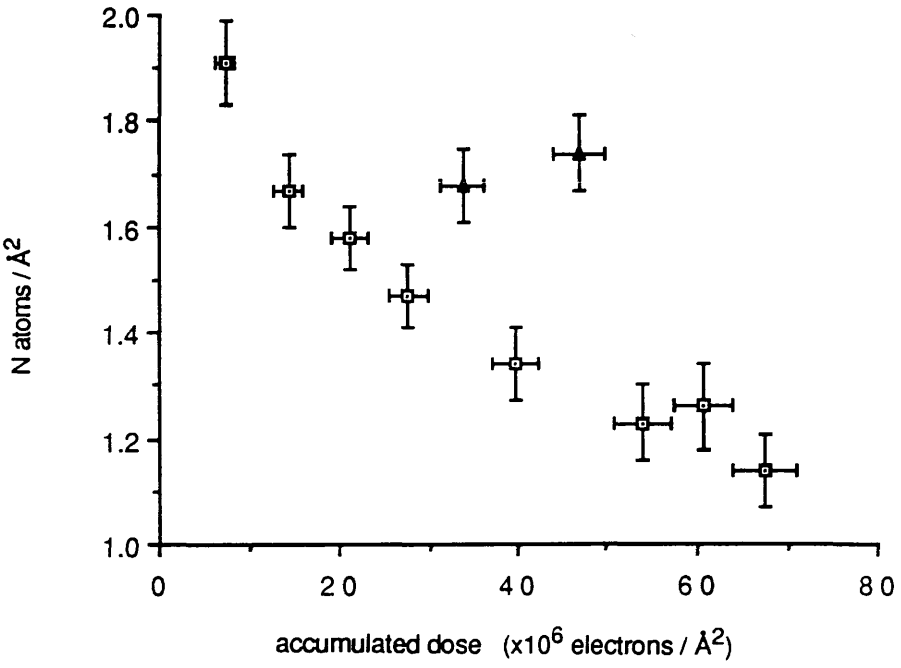

Figure 7.1(e). Loss of N from a TiN specimen ($t/\lambda=0.09$) as a function of dose at a dose rate of 3.4×10^5 electrons/Å^2/s

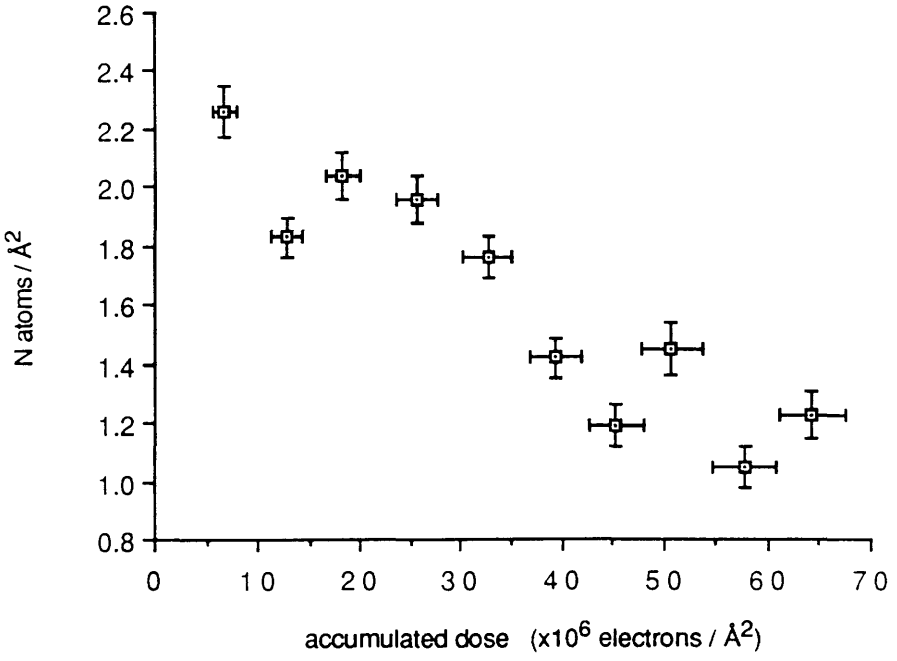

Figure 7.1(f). Loss of N from a TiN specimen ($t/\lambda=0.11$) as a function of dose at a dose rate of 3.4×10^5 electrons/Å^2/s

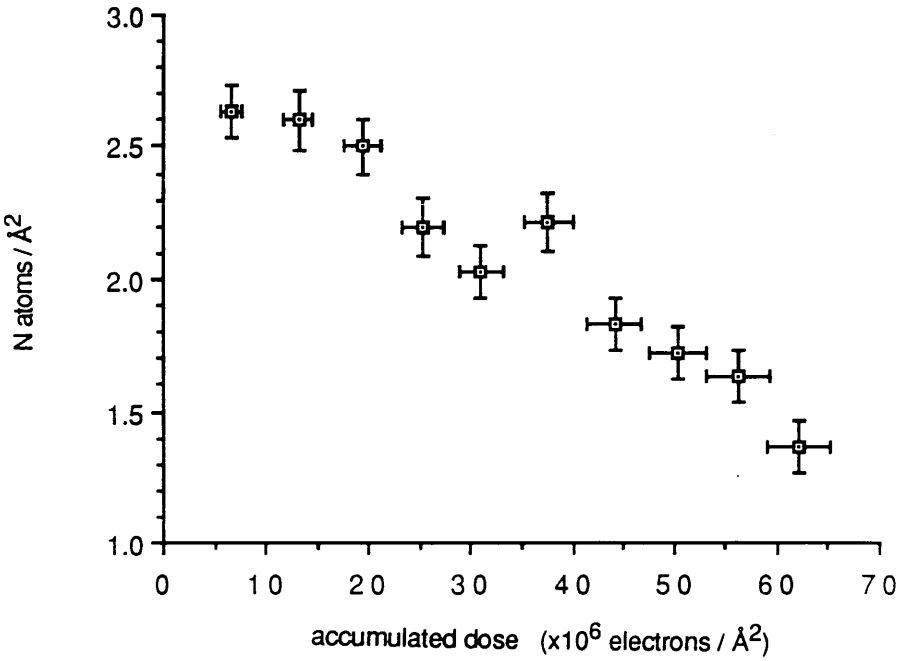

Figure 7.1(g). Loss of N from a TiN specimen (t/λ=0.13) as a function of dose at a dose rate of 3.4×10^5 electrons/Å^2/s

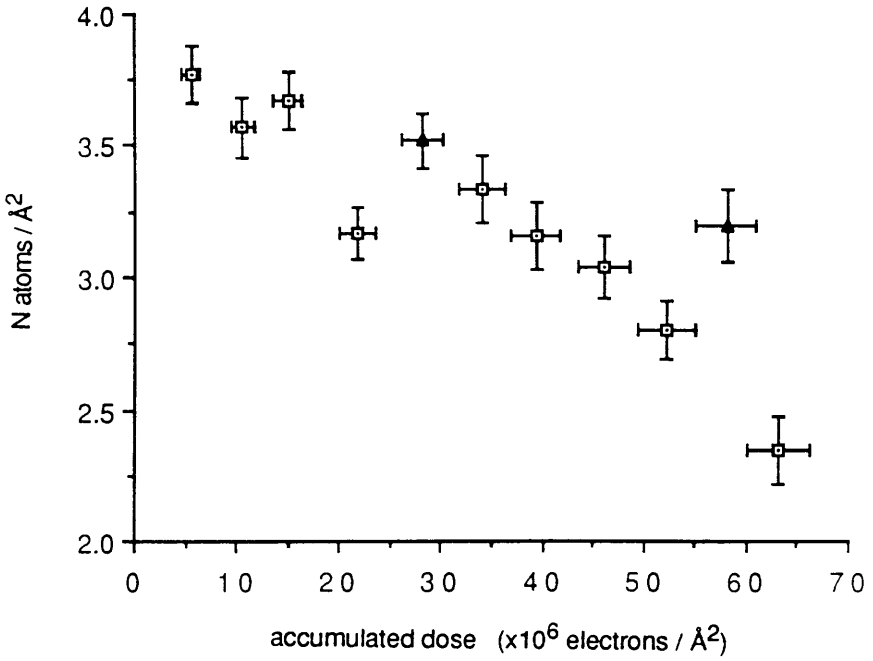

Figure 7.1(h). Loss of N from a TiN specimen (t/λ=0.17) as a function of dose at a dose rate of 3.4×10^5 electrons/Å^2/s

suppressed zero to show the details in the depletion curves more clearly. As the specimen thickness increases, the statistics in the EEL spectra are improved allowing more accurate extraction of the characteristic N signal. Consequently, the effect of noise in the N depletion curves becomes less significant and so the trends in the later graphs of figure 7.1. are more apparent.

The anomalous data points in the depletion curves, previously accredited to probe repositioning errors in chapter 4, occur much more frequently and are more severe for this data set. This can be attributed to instabilities in the high tension (HT) supply which caused a problem on the day these spectra were collected. Fluctuations in the HT cause the image to jump in and out of focus so exacerbating the probe repositioning errors. As a result of the improved specimen preparation techniques employed, the anomalous data points do not necessarily correspond to anomalous t/λ values as they did in the VC results of chapter 5. Consequently, the attribution of anomalous data points in the N depletion curves to probe repositioning errors was determined from the N/Ti ratio. Data points which had a higher N/Ti ratio than neighbouring points are probably caused by the collection of spectra from a partially damaged area of the specimen and correspond to a probe repositioning error. These points are plotted as ▲ on figure 7.1. Points which look anomalous but have a lower N/Ti ratio cannot definitely be accredited to probe repositioning errors and there is no justification for excluding them from data fitting calculations.

A further data set was collected from a second $TiN_{0.59}$ sample to investigate the reproducibility of the

experiment, extend the range of thicknesses examined and to increase the total dose given to the thicker regions of material. The results are presented in figure 7.2 (a) to (f) in order of increasing thickness. As a result of the improved statistical accuracy in the EEL spectra of thicker samples and, in addition, the correction of the HT instability problem of the previous data set, the depletion curves in figure 7.2 possess a greater statistical accuracy than those in figure 7.1. However, at increased specimen thicknesses the advantage of improved statistics is outweighed by the problems of burning a positioning hole and the decrease of image contrast from the specimen. Consequently, smaller probe repositioning errors occur more frequently and the data sets of figure 7.2(e) and 7.2(f) have more "scatter" in the data points than those in other figures.

The discussion in chapter 3 indicated that it is not possible to decide from the individual depletion curves of figures 7.1 and 7.2 alone which, if either, of the two damage mechanisms is responsible for the observed loss of N. It is necessary to compare the rate of loss of N with respect to the accumulated dose as a function of specimen thickness. To do this, the gradients of figures 7.1 and 7.2 were calculated using a linear least squares fit program. Points considered to be anomalous (again plotted as ▲) were excluded from the calculation of the gradient. For the thinnest specimen regions (figure 7.1 a, b and 7.2a), the depletion of N is very rapid and the limited extent of the region in which the N loss is linearly dependent on dose can be seen. As the specimen thickness increases, the increase in the extent of this linear depletion region,

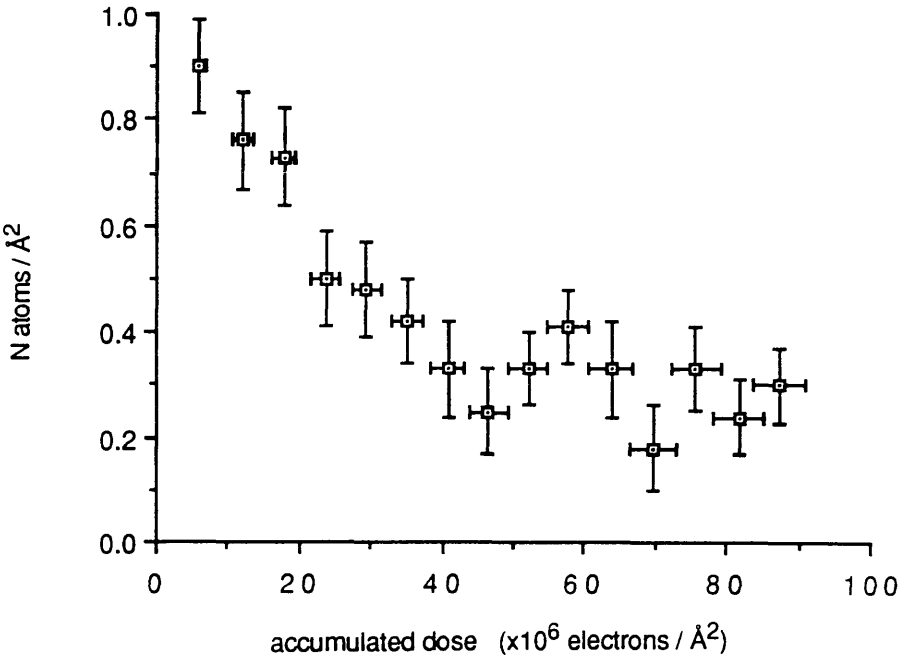

Figure 7.2(a). Loss of N from a TiN specimen (t/λ=0.07) as a function of dose at a dose rate of 3.4×10^5electrons/Å^2/s

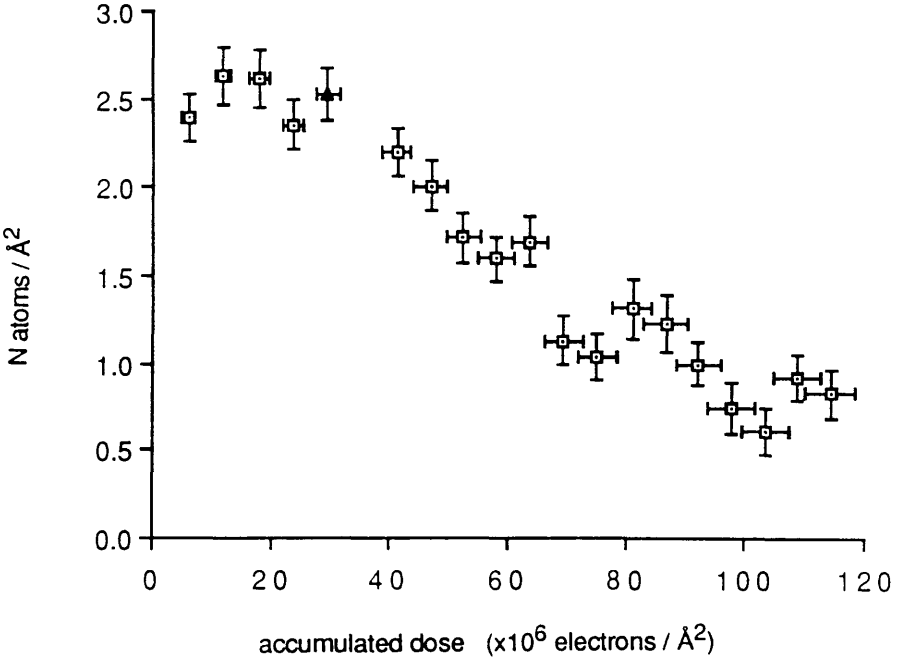

Figure 7.2(b). Loss of N from a TiN specimen (t/λ=0.15) as a function of dose at a dose rate of 3.4×10^5electrons/Å^2/s

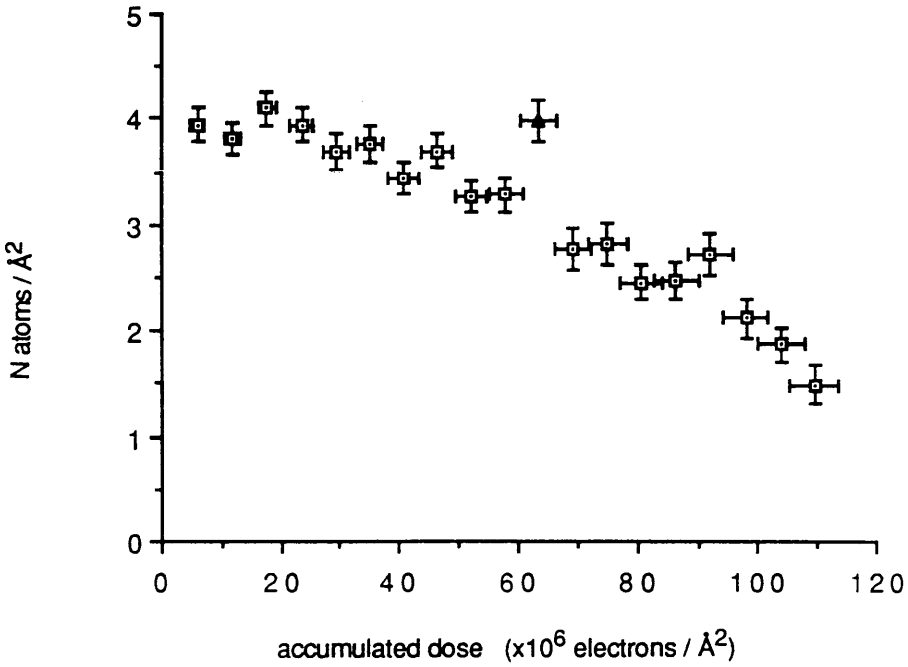

Figure 7.2(c). Loss of N from a TiN specimen ($t/\lambda=0.22$) as a function of dose at a dose rate of 3.4×10^5 electrons/Å^2/s

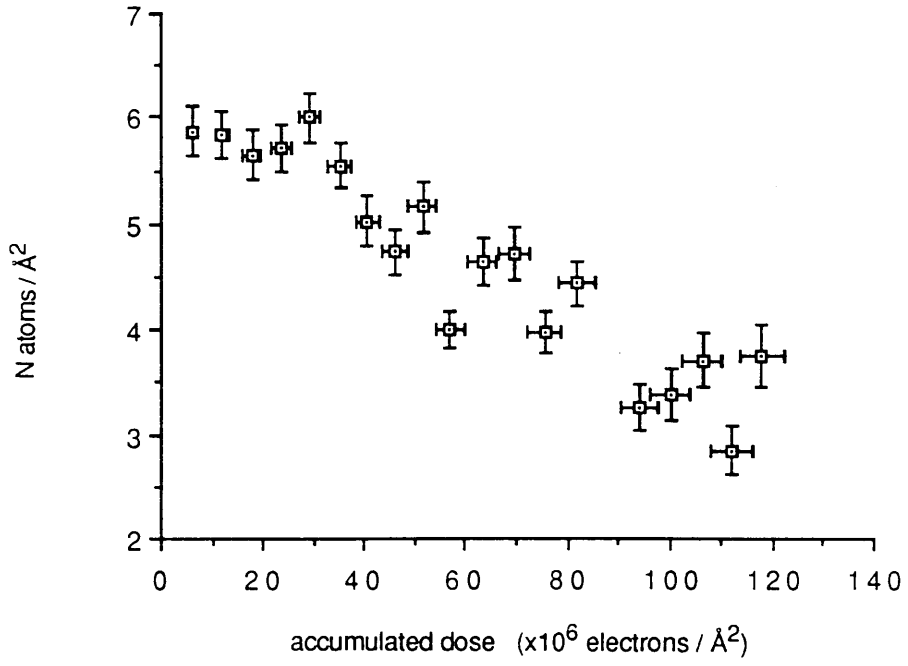

Figure 7.2(d). Loss of N from a TiN specimen ($t/\lambda=0.3$) as a function of dose at a dose rate of 3.4×10^5 electrons/Å^2/s

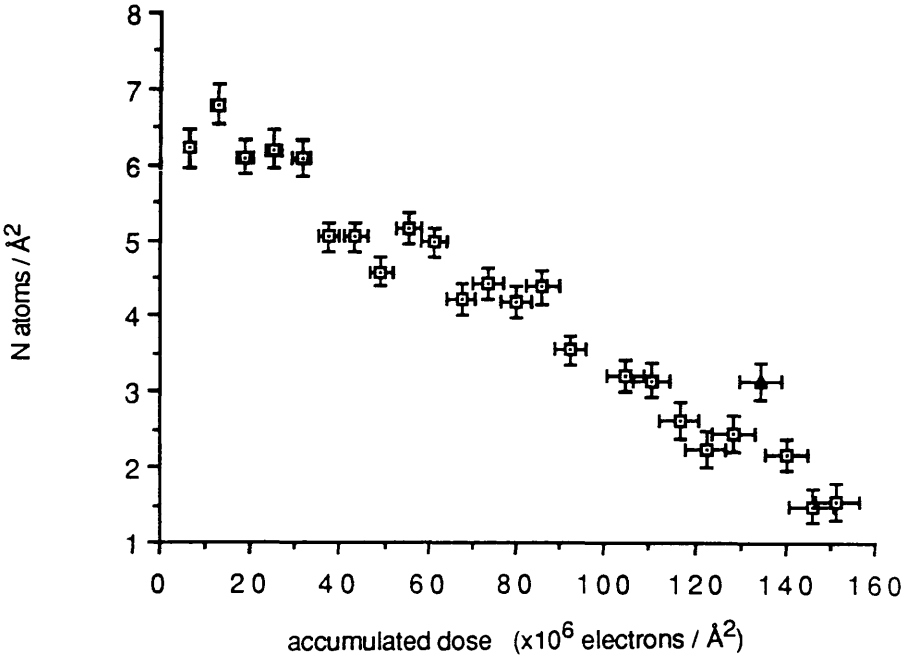

Figure 7.2(e). Loss of N from a TiN specimen ($t/\lambda=0.33$) as a function of dose at a dose rate of 3.4×10^5 electrons/Å^2/s

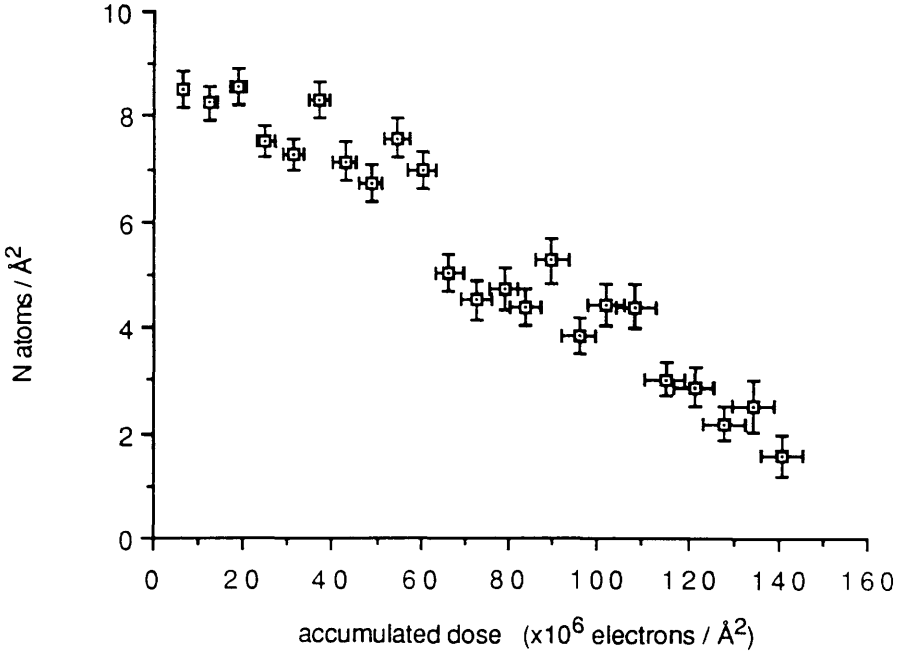

Figure 7.2(f). Loss of N from a TiN specimen ($t/\lambda=0.4$) as a function of dose at a dose rate of 3.4×10^5 electrons/Å^2/s

observed in figure 7.1, is consistent with the predictions of the knock-on displacement model. Consequently, the initial gradients were calculated over an increasing number of dose units for increasing specimen thickness, as summarised in table 7.1. This maximises the accuracy of the least squares fit by increasing the number of data points.

Figure 7.3 shows the intercepts of these fits, which correspond to the N content at zero dose, as a function of t/λ for both data sets. The linear relationship for each of the data sets is consistent with the proportionality between the N content and the relative specimen thickness for EELS analysis of a uniform sample. Although both data sets have similar gradients, the intercepts on the t/λ axis are different (0.004±0.003 and 0.03±0.005 for the first and second data sets respectively). The measurement of a positive, non-zero t/λ at zero N content is consistent with the layer of C present on the surface of the specimen, as discussed in chapter 4.4.2. It should be noted, however, that the layer of C is not a constant thickness on either of the data sets. Therefore, the thickness and hence the t/λ value for the C layer is estimated from the average C K-edge signal over the sample. Assuming a carbon density of 2300 kg/m^3, the thickness of the C layer was calculated from the average K-edge signal to be (2.9±0.8)Å and (20.0±3.8)Å for each of the data sets. The error is the standard error in the mean. From equation 2.12 the mean free path, λ, for C is 949Å resulting in a value of t/λ of 0.003±0.001 on the first data set compared to an intercept on the t/λ axis of 0.004±0.003. For the second data set a t/λ of 0.021±0.004 was measured for the C layer compared to an intercept of t/λ = 0.030±0.005 on figure 7.3. The

thickness	number data points fitted over
$t/\lambda < 0.05$	4
$0.05 < t/\lambda < 0.1$	7
$0.1 < t/\lambda < 0.15$	10
$0.15 < t/\lambda < 0.2$	14
$0.2 < t/\lambda < 0.25$	17
$0.25 < t/\lambda < 0.3$	20
$0.3 < t/\lambda < 0.35$	24
$0.35 < t/\lambda < 0.4$	27

Table 7.1 The number of data point used in the linear least squares fit program. In each case any anomalous points due to probe repositioning errors were excluded.

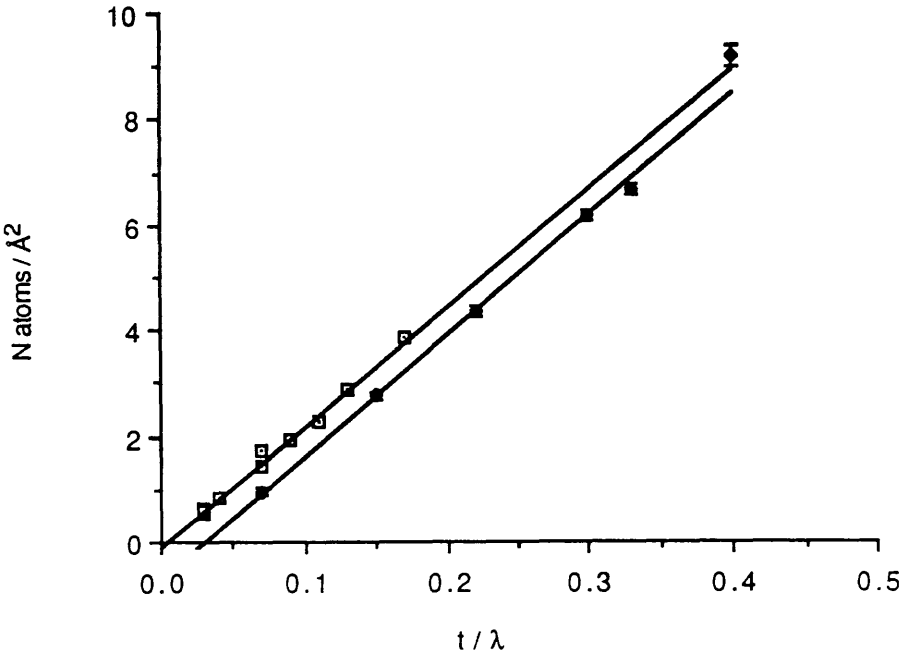

Figure 7.3. The N content, extrapolated to zero dose, for each of the data sets presented in figures 7.1 and 7.2 as a function of t/λ. The magnitude of the error bars on the N content are too small to plot on the graph.

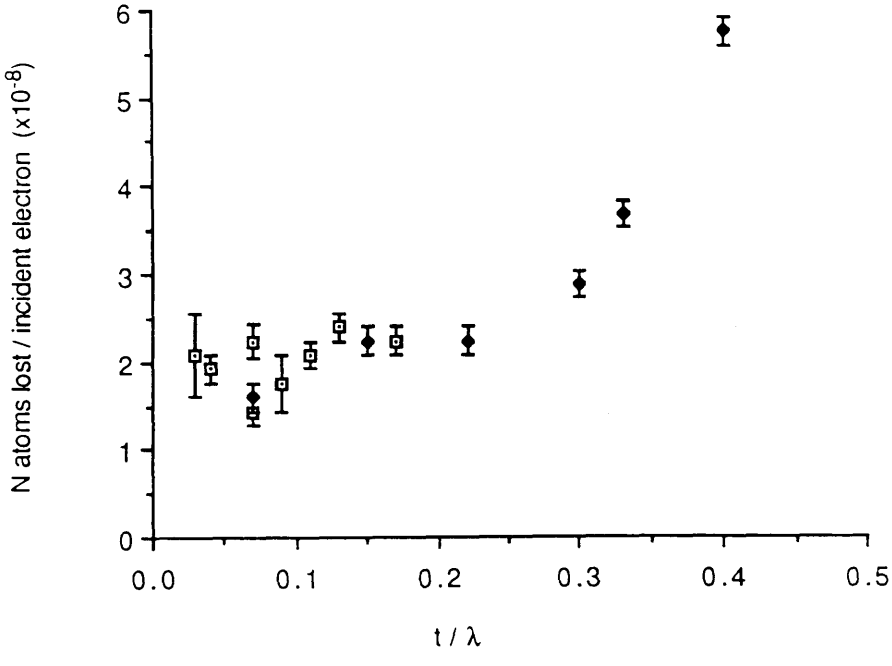

Figure 7.4. The gradients extracted from the N depletion curves of figures 7.1 and 7.2 plotted as a function of t/λ. The gradient is a measure of the number of N atoms lost per incident electron.

positive, non-zero intercepts on figure 7.3 show reasonable agreement with the thickness of the C layer as measured by an independent technique.

It was noted that during the acquisition of a series of EEL spectra, the C signal decreased by as much as 50% for an accumulated dose of 120×10^{6} electrons/Å^{2}. This suggests that the surface layer of C is also subject to radiation damage as the C atoms on the specimen surface are displaced by the electron beam. This result is useful in that it confirms that the C signal is an artifact of the specimen preparation (chapter 4) and is not attributable to beam induced contamination, since one would expect the C signal to increase if the contamination was significant.

The gradients extracted from figures 7.1 and 7.2 by the above method are shown as a function of relative specimen thickness in figure 7.4. The errors were obtained from the least squares fit to the data. Figure 7.4 shows that, despite the greater thickness of the C layer in the second data set, the loss of N with respect to the dose is consistent over the common thickness range of the two data sets. The initial gradients are constant to within the calculated errors for t/λ up to 0.27, with an average value of $(2.0 \pm 0.1) \times 10^{-8}$ N atoms/electron. The constant rate of loss of N with respect to dose for increasing specimen thickness is consistent with the dominant loss mechanism occurring at the surface of the specimen. However, at $t/\lambda >$ 0.27 (~200Å) the loss of N with respect to dose is no longer constant but increases with specimen thickness. The increasing rate of N loss with specimen thickness suggests that loss through the cylindrical surface of the irradiated volume becomes more significant as the thickness increases.

7.3 DISCUSSION OF THE EXPERIMENTAL RESULTS

The knock-on displacement model predicted a constant rate of loss of N with respect to accumulated dose for increasing specimen thickness. This is consistent with the results of figure 7.4 for $t/\lambda < 0.27$, suggesting that the knock-on displacement damage model is a good description of the damage process where the predominant loss is from the surface of the material. However, the increase in the rate of loss of N with specimen thickness for $t/\lambda > 0.27$ suggests that the knock-on damage mechanism cannot fully explain the observed behaviour and that other damage mechanisms play a significant role at greater specimen thicknesses. The observed increase in the loss of N in figure 7.4 at $t/\lambda > 0.27$ is consistent with the radiation induced diffusion model discussed in chapter 3 where the loss of N from the edge of the irradiated volume plays an important part.

The damage mechanism thought to be responsible for the loss of N in TiN is based on a knock-on model but one in which, because of the presence of the crystal structure, displacements of the N atoms may take place in any direction. This results in a component of the atom motion which is essentially a random walk process, analogous to diffusion. The process is shown schematically in figure 7.5. On receiving energy from an incident electron, the N atom will only be displaced from its lattice site if the direction of motion causes it to pass between the larger Ti atoms. Therefore, in general, the N atoms will collide with the stationary Ti atoms, dissipating energy in the process. The incident energy received by the N atom from the

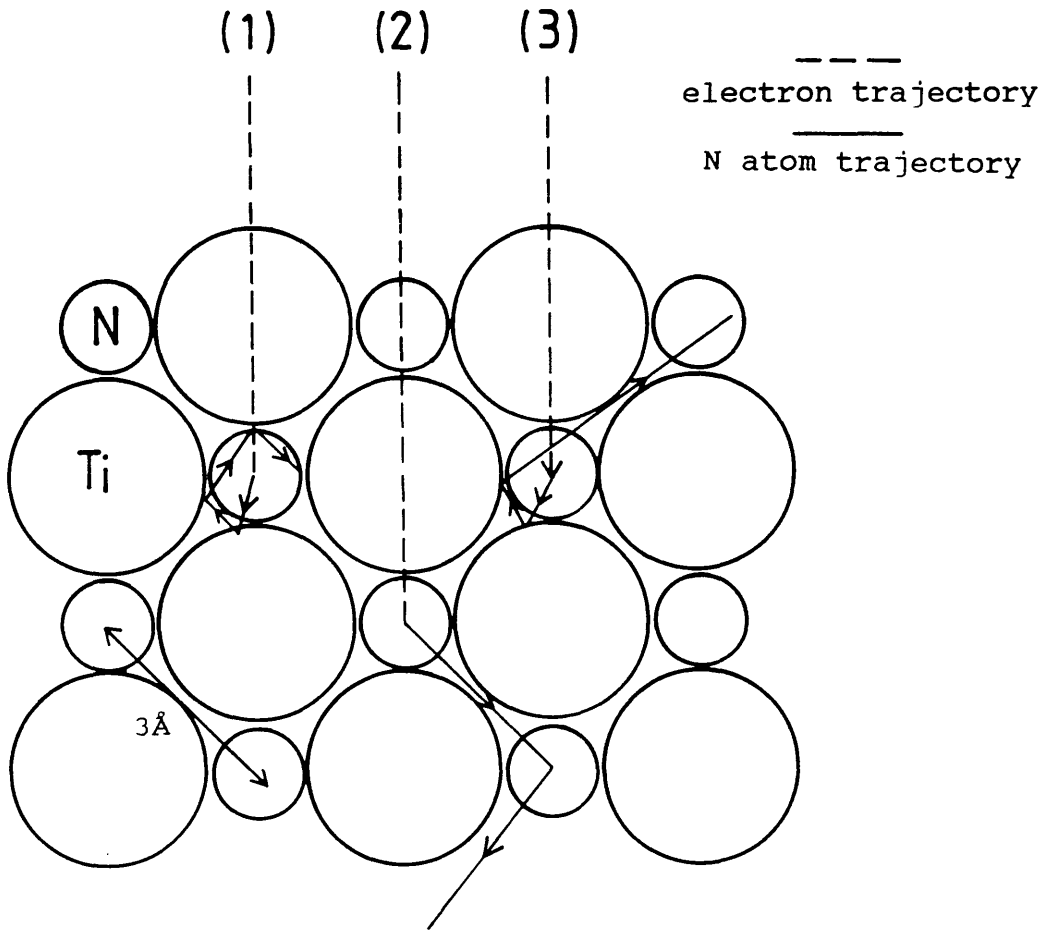

Figure 7.5. Schematic diagram of the random knock-on displacement mechanism which leads to the radiation induced diffusion model. In collision (1) the N atom dissipates its energy in collisions with the surrounding Ti atoms. Collision (2) results in a forward displacement of the N atom whereas collision (3) may result in a random displacement if the N atom retains sufficient energy to overcome the binding energy despite numerous collisions.

electron (≤17eV from equation 3.6) will be dissipated over a number of collisions with the Ti atoms as the energy transferred by a N atom to a Ti atom is less than 12eV from non-relativistic energy-momentum considerations. Therefore, there is a finite possibility that the N atoms will still have sufficient energy to overcome the 5eV binding energy after a number of collisions with the surrounding Ti atoms. In this event, the displacement of the N atom from its lattice site will not necessarily be in the forward direction. Thus the atoms can be displaced in a random walk process analogous to diffusion. However, because of the dissipation of energy by the excited N atom in collisions with the surrounding Ti atoms, the displacements will be forward biased as it is more energetically favourable for the atom to overcome the binding energies when travelling in a forward direction. The process can be represented by a random knock-on process analogous to diffusion which is shown schematically in figure 7.6. The diffusion coefficient is dependent on the fraction of displacements which occur in any given direction ie. the factor f in equation 3.8. Thus $f\sigma_D$ represents the effective cross-section for displacement in a particular direction. For 3-dimensional diffusion, with no bias, the fraction of atoms going in either the x,y or z direction is equal and therefore $f_x=f_y=f_z(\leq 1/6)$. In the forward knock-on displacement model, the atoms are displaced in the forward direction resulting in a non-zero value of $f_z^+(\leq 1,)$ whilst the fraction of N atoms displaced in any other direction is zero. For biased 3 dimensional diffusion, the fraction of atoms displaced in the forward z direction (f_z^+) will be greater than the fraction of atoms displaced in the

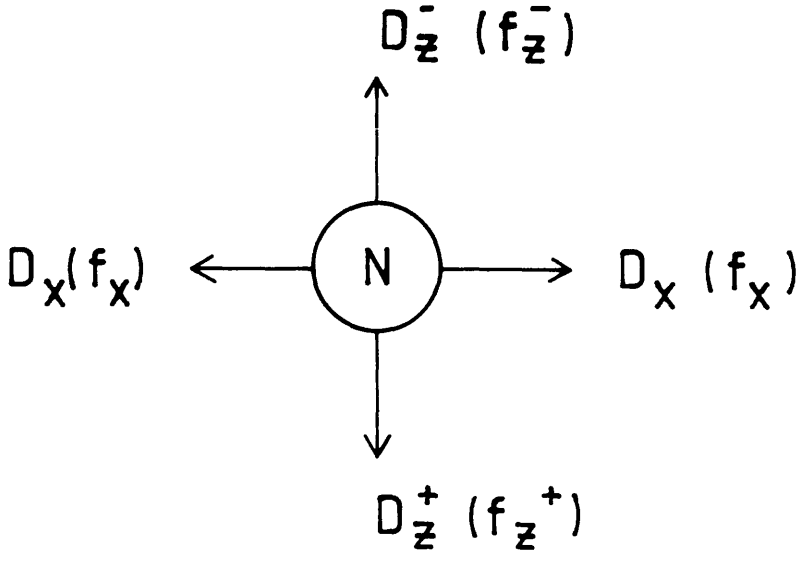

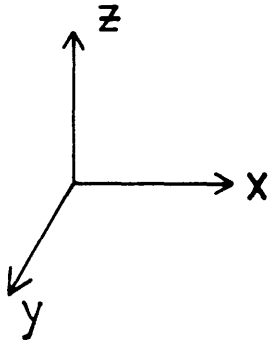

Isotropic, 3 dimensional diffusion model

(with no bias)

$$f_x = f_y = f_z \quad (\leq 1/6)$$

Forward knock-on displacement model

$$f_x = f_y = f_z^- = 0 \quad \text{and} \quad f_z^+ \leq 1$$

Forward biased 3 dimensional diffusion model

$$f_z^+ > f_z^- \qquad (f_z^+ > f_x \text{ and } f_y)$$

Figure 7.6. Schematic diagram to show the fraction of atoms which are displaced in the x,y or z direction for a forward knock-on mechanism, an isotropic radiation induced diffusion mechanism and a forward biased radiation induced diffusion mechanism.

negative z direction (f_z^-). Consequently, the forward knock-on mechanism will be an important feature only when the difference $f_z^+ - f_z^-$ is the same order of magnitude as the average value of f.

From these considerations, the mechanism can vary from random diffusion to forward biased diffusion which is analogous to the motion of carriers in a semiconductor under the action of both diffusion and an applied electric field, to a forward knock-on displacement model. For thinner samples, the damage mechanism is dominated by forward knock-on displacement as the N atom is more likely to be knocked out of the specimen surface before it has moved any lateral distance in the plane of the sample. At increasing specimen thicknesses, the N atoms become more likely to be displaced out of the edge of the irradiated region in a random walk process, particularly where the specimen thickness is greater than the radius of the irradiated region.

To compare the predictions of the two models, it is necessary to calculate the average "gradient" for the exponential decay of the N depletion curves predicted by the radiation induced diffusion model. The results were shown in figure 3.7 for a range of specimen thicknesses. Provided diffusion from the edge of the irradiated volume does not significantly alter the N concentration profiles at the edge of the irradiated region thus reducing the effective surface area for the knock-on displacement model, the loss mechanisms will not influence each other. Therefore, to a first approximation, the overall loss mechanism can be attributed to the addition of the forward knock-on displacement and the radiation induced diffusion

models. Figure 7.7 shows the addition of the gradients calculated for each of the damage mechanisms in chapter 3. In the presence of experimental error, any residual curvature in the diffusion model at $n \leq 50$ could easily be mistaken for a straight line. Assuming a constant value of the gradient for lower values of n, the intersection of the two extremes of the curves in figure 7.7 occurs at n=55. This corresponds to a relative thickness of $t/\lambda = 0.23$ in TiN which has a displacement distance of 3Å. This is in reasonable agreement with the observed "change over point" between the mechanisms measured experimentally in figure 7.4. of $t/\lambda = 0.27$.

It should be noted that the range of specimen thickness over which one mechanism becomes dominant will be dependent on the geometry of the irradiated region. For a probe diameter of 130Å, as in the data examined above, the surface area used in the forward knock-on displacement calculations (corresponding to a circular surface area of diameter 130Å) is 1.33×10^4 Å^2. At $t/\lambda = 0.27$ (200Å) and a probe diameter of 130Å, the surface area of the cylinder considered for the 3-dimensional diffusion model (excluding the top and bottom surfaces) is 8.2×10^4 Å^2. Therefore, the cross-over between the mechanisms occurs when the areas are of a similar order of magnitude but the knock-on displacement model dominates until the cylindrical surface area is approximately 6 times that of the area of the free surfaces. This is not surprising considering the random nature of the displacements in the plane of the specimen. At a probe radius of 22 displacement distances a N atom requires a factor of ~7 times more displacements in the x,y plane to be removed from the probe area compared to forward

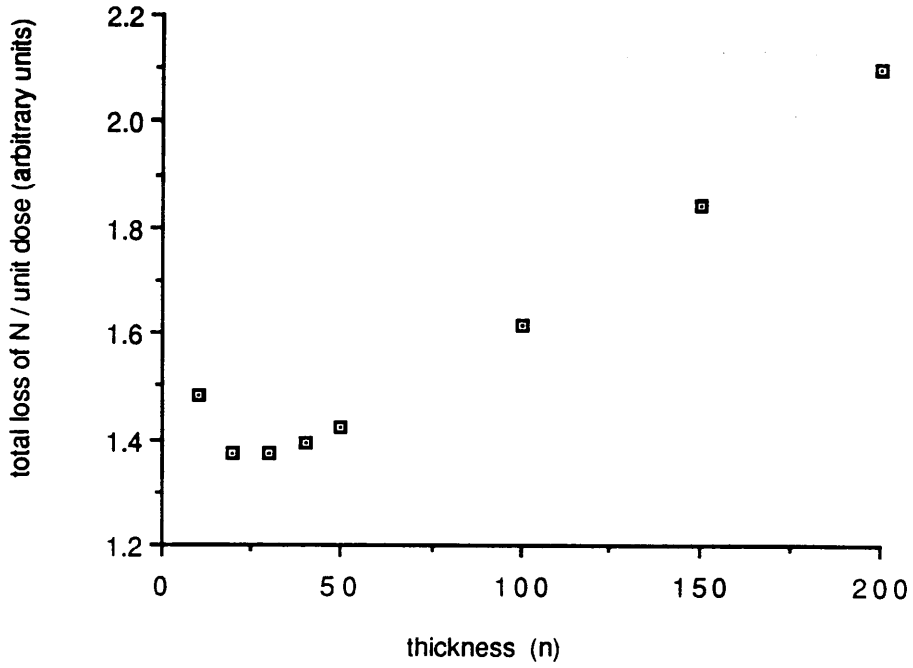

Figure 7.7 The addition of the theoretical gradients for forward knock-on diffusion and radiation induced diffusion shown in figure 3.6. To a first approximation this gives a measure of the total loss of material from the sample as a function of specimen thickness,n.

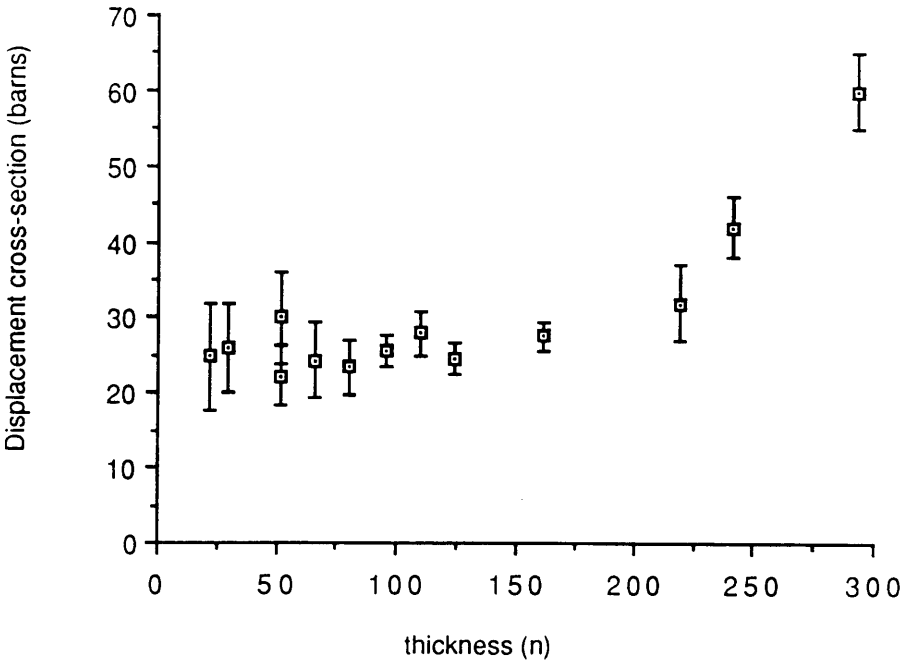

Figure 7.8. Displacement cross-section, calculated from the forward knock-on displacement model, as a function of specimen thickness, n.

displacements through the specimen thickness (n=67).

Although the proposed 3 dimensional diffusion model is only a first estimate (because of inaccuracies in the boundary conditions) it appears to give a reasonable qualitative explanation of the observed loss of N with increasing specimen thickness in figure 7.4. However, further work is required to explore the process in more detail.

7.4 CALCULATION OF CROSS-SECTIONS

The forward knock-on displacement mechanism is characterised by a displacement cross-section σ_D. This can be calculated from the comparison of the experimental and theoretical N depletion curves as described in section 3.2.3. The displacement distance was assumed to be 3Å, corresponding to the inter-atomic spacing between the N planes (figure 7.5). The specimen thicknesses were calculated from the t/λ values using a total mean free path of 730Å, calculated from equation 2.12. This allows us to calculate the specimen thickness in terms of the displacement distance, ie the factor n in equation 3.7. The results are shown in figure 7.8 where, as expected, the cross-sections calculated for $t/\lambda > 0.27$ appear anomalous since the experimental results were found to deviate from the knock-on displacement model at these thicknesses. The errors on σ_D are considerable, especially for small t/λ where the error on the least square fit to the N depletion curves is at a maximum. There is also considerable error in the calculation of the specimen thickness because of the systematic error in the calculation of λ from equation

2.12. Allowing for this uncertainty in the thickness the knock-on displacement cross-section evaluated from the experimental results of figures 7.1 and 7.2 lies in the range 18 to 27 barns, with an average value of 22.5 barns.

The knock-on cross-section evaluated from the McKinley-Feshbach calculations of equation 3.5 yield a cross-section of 200 barns for TiN assuming a displacement energy of 5eV (Sarian and Venables). As was shown in figure 3.2, the theoretical displacement cross-section is strongly dependent on the displacement energy, E_d. For example, for E_d in the range 3 to 7eV, the cross-section varies from 407 to 114 barns for TiN. However, the experimentally calculated average displacement cross-section of 22.5 barns corresponds to an E_d of 13eV for N in TiN which is outwith the expected range. The lower than predicted cross-sections, consistent with the data presented for TiC in chapter 6, may be attributable to a strong angular dependence on the N displacement that was not allowed for in the theoretical calculations of McKinley-Feshbach. Therefore, the experimentally calculated cross-sections, while being lower than the predicted theoretical values, are perhaps a better estimate of the true cross-section for atoms constrained in a crystal structure as such atoms would have a reduced probability for atomic displacement. This is consistent with the knock-on damage mechanism observed in metal crystals where the displacement energy and thus the displacement cross-sections were found to be strongly dependent on the crystal orientation (Vajda 1977).

The discussions in section 7.3 suggested that the variable of particular interest is $f\sigma$, where f is the fraction of atoms displaced in a particular direction. For

the forward knock-on displacement model f was assumed to be unity. However, the experimental results presented above suggest that for $f\sigma$ equal to 22.5 barns, the value of f is of the order of 1/9 to yield an average displacement cross-section of 200 barns over the random specimen orientations considered in these experiments. Consequently the orientation dependence of the cross-section may be represented by a variation in the factor f with specimen orientation where a larger proportion of atoms are displaced along the "easy directions" in the crystal (eg the <110> direction in a FCC lattice such as TiN).

Medlin, in a private communication, suggested incorporating the role of vacancies into the knock-on displacement model. In this case, the N atoms are only displaced if a vacancy exists in a neighbouring site ie. the displacement energy to an occupied site is assumed to be much higher than that to a vacant site. This would also cause a reduction of the observed cross-section relative to that predicted theoretically. It is possible to predict the initial number of vacancies present in the material from the bulk composition and thus make an estimate of the effect on the measured cross-sections. However, the magnitude of the cross-sections measured in the TiC and TiN data are similar, whereas the initial vacancy fraction varies by a factor of 20. This suggests that the vacancy fraction is not an important feature of the forward knock-on displacement model.

The final three data points of figure 7.8 were found to be anomalous when analysed by the direct knock-on displacement model. This is consistent with the increased rate of loss associated with the loss from the edge of the

irradiated cylindrical volume at higher values of specimen thickness. Consequently, to calculate the cross-section for the displacement of N in TiN at these thicknesses, it is necessary to use the radiation induced diffusion model. As in the case of the knock-on displacement model, the value of the cross-section (which is contained in the units of dose $d=f\sigma it$ in the theoretical model) can be estimated by comparing the theoretical and experimental depletion curves. The overall loss of N is the sum of the loss from the free surfaces and the edge of the irradiated cylindrical volume. Consequently, the difference in the rate of loss between two specimens of different thickness, t_1 and t_2, is a measure of the loss from the sides of a cylinder of height Δt, where $\Delta t= t_2-t_1$. This corresponds to 2-dimensional diffusion from the edge of the irradiated cylinder because the loss of material from the front surface is independent of thickness. The theoretical N depletion curve was obtained by multiplying the relevant 2-dimensional fractional depletion curve (with $n_r=22$) by the number of atoms in thickness Δt. Following the discussion in section 3.4, an estimate of the gradient of this theoretical N depletion curve was made using a least squares fit program. The rate of loss of N from a cylinder of height Δt was calculated from the experimental data by subtracting the rates of loss from specimens of thickness t_1 and t_2. This corresponds to the difference between the gradients of the data sets in figure 7.2(f) and 7.2(d). For a difference in gradient of $(2.88\pm0.36)\times10^{-8}$ N atoms/electron from the later data points of figure 7.4 $f\sigma$ has a value of (77±11) barns. This corresponds to a displacement cross-section, σ, of (230±33) barns for f=1/3

and of (460±67) barns for f=1/6. The calculation of a cross-section greater than the theoretical displacement cross-section of 200 barns for TiN from equation 3.5 is probably due to the simple treatment of the model proposed. However, other mechanisms such as radiolysis may also contribute to the diffusion like component of the motion increasing the apparent cross-section.

In conclusion, calculating a larger $f\sigma$ from the diffusion model than from the forward knock-on displacement model may suggest that the loss of material from the edge of the irradiated region is the dominant loss mechanism at these thicknesses. However, further experiments at various specimen geometries are required to investigate the relationship between loss from the specimen surface and loss from the edge of the cylindrically irradiated volume.

7.5 FURTHER CONSIDERATIONS

The relationship between the rate of loss of N with respect to accumulated dose as a function of specimen thickness is very difficult to measure experimentally as this can only be achieved when all other factors are held constant. It should be stressed that the experimental procedures designed to minimise the effect of such factors which may influence the rate of loss of N from TiN are very exacting. Consequently, the following sections discuss such factors as dose rate effects, channeling effects, loss of Ti from the sample and a quasi-equilibrium N level beyond which no further N is lost. We investigate the consequences of these effects for the rate of loss of N and estimate their importance in regard to the interpretation of the

data already presented.

7.5.1 Dose Rate Effect

Although Thomas (1985) reported that there was no dose rate effect observed in TiC, initial experiments presented in chapter 6 indicated that the rate at which the dose is applied to the sample may be an important consideration in the loss of C from TiC. To investigate a possible dose rate effect in the TiN samples, two dose rate experiments were carried out on different regions of the specimen by acquiring two series of spectra at dose rates differing by a factor of 2. As before, the two series of spectra for each dose rate experiment were acquired from adjoining areas of the specimen to maintain a degree of self consistency in the specimen thickness and orientation. The results are shown in figure 7.9 (a) and (b) for both the lower dose rate (1.6×10^5 electrons/Å^2/s) experiments. The corresponding higher dose rate (3.4×10^5 electrons/Å^2/s) experiments were shown previously in figure 7.1(a) and (d) respectively. It should be noted that the total accumulated dose was reduced by a factor of 2 for the first of the lower dose rate experiments (figure 7.9a), although the dose rate is the same for both experiments shown in figure 7.9. The initial gradients were calculated from the N depletion curves as described in section 7.2. The first two data points of figure 7.9 (b) are anomalous, perhaps due to a shift in the area of TiN examined, and as such are excluded from the calculation of the gradient. The initial gradients are $(1.9 \pm 0.3) \times 10^{-8}$ and $(2.0 \pm 0.2) \times 10^{-8}$ N atoms/electron for the low dose rate experiments compared

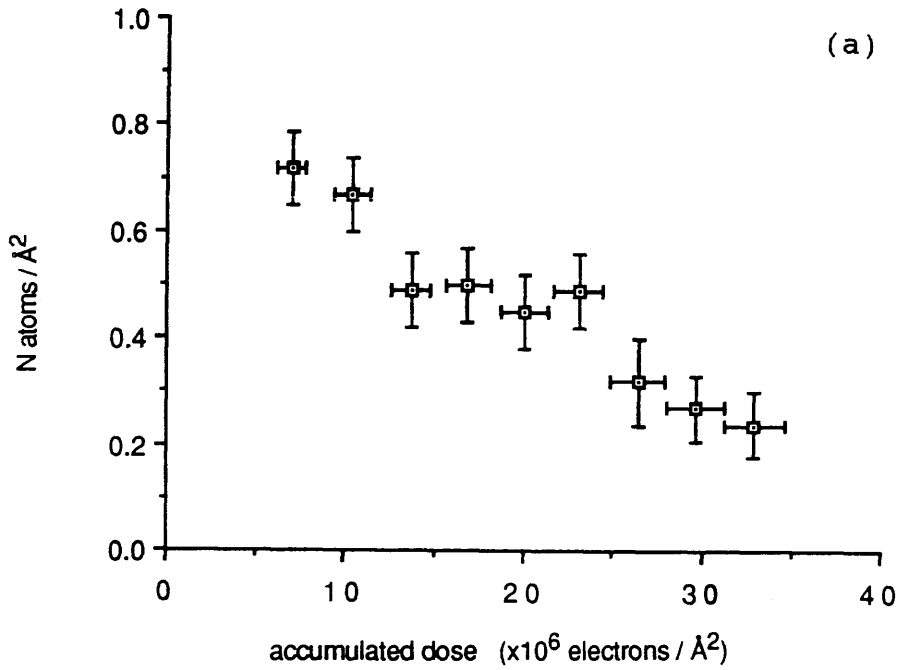

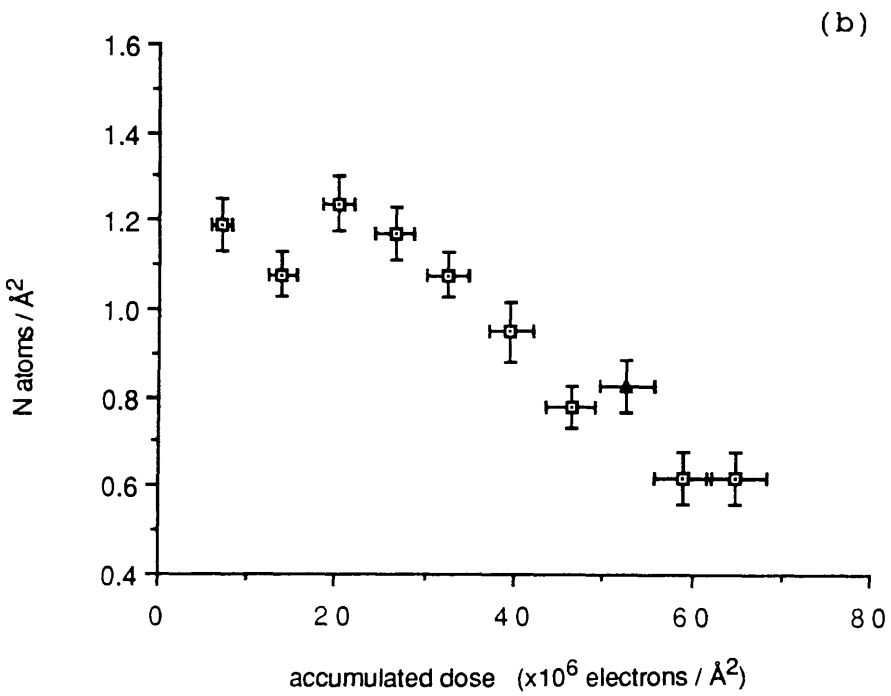

Figure 7.9. Loss of N from a TiN specimen of thickness (a) $t/\lambda=0.03$ and (b) $t/\lambda=0.07$ as a function of dose at a lower dose rate of 1.6×10^5 electrons/Å^2/s. The corresponding higher dose rate experiments were shown in figures 7.1(a) and (d) respectively.

to gradients of $(2.1\pm0.5)\times10^{-8}$ and $(2.2\pm0.2)\times10^{-8}$ N atoms/electron for the corresponding higher dose rate experiments. Therefore, to within the experimental error, the rate of loss of N with respect to dose is the same for both the higher and lower dose rate experiments, all of which are consistent with the average gradient of $(2.0\pm0.1)\times10^{-8}$N atoms/electron in figure 7.4. This suggests that the rate at which the dose is applied does not significantly affect the amount of N lost from the specimen ie. there is no dose rate effect at these dose rates.

Although these results were carried out in a controlled manner, where most of the factors could be held constant, there is only a change in dose rate of a factor of 2. Further information on the dose rate effect was contained in a defocus to focus experiment, the results of which are shown in figure 7.10. The figure shows the N depletion from a series of EEL spectra acquired from the same area of the sample where the probe was initially defocussed to (190±10)Å diameter. It was subsequently defocussed to (130±10)Å and then to (65±10)Å probe diameters. This corresponds to a range of dose rates from 1.9×10^{5} to 14×10^{5} electrons/Å^{2}/s at the largest and smallest probe diameters respectively. Despite the uncertainties in the results due to a change in the irradiated volume as the probe is focussed and also to possible probe repositioning errors, the N depletion does not show any sudden changes in gradient as might be expected for a dose rate effect. Moreover, the gradual decrease in the gradient, observed in figure 7.10, is consistent with the decreasing rate of N loss predicted by both the knock-on displacement and radiation induced diffusion models. Within the limits of

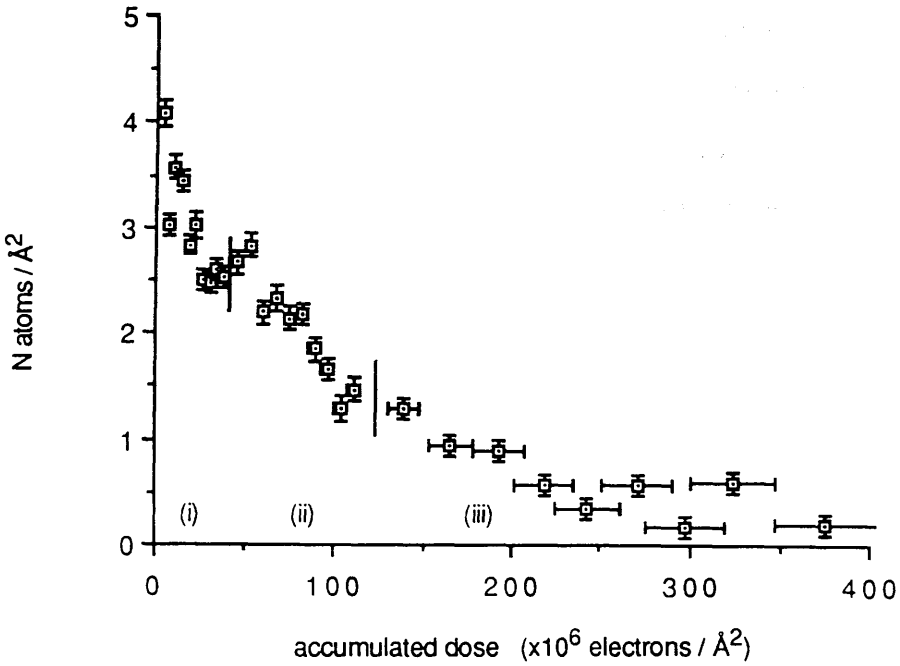

Figure 7.10. Loss of N from a TiN specimen ($t/\lambda=0.17$) as a function of dose for a defocus to focus experiment. This corresponds to a dose rate of 1.9×10^5 electrons/Å^2/s in area (i), 3.4×10^5electrons/Å^2/s in area (ii) and 14×10^5 electrons/Å^2/s in area (iii).

the experiment, there are clearly no major dose rate effects for an increase in dose rate of a factor of 7.

For the knock-on displacement interaction, which is responsible for the displacement of the atom from its lattice site, there is unlikely to be a dose rate effect unless an atom remains in an excited state sufficiently long for a second collision with the electron beam. From the inverse Debye frequency, the lifetime of the excited atom vibrating in the crystal structure is approximately 10^{-13} s. At the dose rates examined here of $1.9x10^5$, $3.4x10^5$ and $14x10^5$ electrons/Å^2/s the time between collisions with the incident electrons, within a cross-sectional area of 9Å^2 (corresponding to a unit cell in TiN), is of the order of 10^{-7}s. Consequently, there is a very high probability that the "excited" atom will have lost its energy by phonon excitation before another incident electron can induce a second collision. Even in the case of a focussed probe, the time between collisions with an electron is of the order of 10^{-8}s. This suggests that the hole burning process at the high current densities available in a focussed probe cannot be explained by the knock-on damage mechanism since a dose rate effect was observed in the ability to burn a positioning hole in the sample (Berger 1987b). In conclusion, for the specimen geometries and the dose rates examined here, where knock-on displacement is the dominant mechanism, no significant variation with dose rate was observed.

7.5.2 Channeling Effects

The EEL spectra investigated in the previous sections

were collected from areas of the sample which avoided strong diffraction conditions. This was carried out to ensure that any changes in the rate of loss of N were primarily attributable to changes in the specimen thickness and not induced by channeling effects in the radiation damage process. There are two sources that can contribute to channeling effects in these crystalline materials. The first is that associated with strong diffraction conditions where there is a large concentration of electrons incident on the atom centres, increasing the probability of a scattering event. Secondly, as a result of the orientation dependence of the knock-on displacements, there are selected specimen orientations where it is easier to displace the N atoms due to the reduced binding energy in for example the <110> direction in a face centred cubic structure such as TiN (figure 7.5).

To investigate the effect of the sample orientation on the rate of N loss, two series of spectra were collected at different orientations. One was taken from an area avoiding strong diffraction conditions, as in the previous experiments, and the other from an area close to a low order symmetry point. The exact diffraction conditions are not known but the first region of specimen examined was on an area of the specimen with no bend contours whilst the second, stronger diffraction conditions were recorded from an area of the specimen between two bend contours, close to a pole. These experiments were carried out using a third $TiN_{0.59}$ sample, which had been prepared in a similar manner by ion beam thinning. This had the added advantage of enabling further confirmation of the results obtained from the first two TiN samples. The results are shown in figure

7.11 (a) and (b). The relative thicknesses of the two samples were $t/\lambda = 0.07$ and $t/\lambda = 0.17$. Both of these lie within the constant rate of loss region of figure 7.4. Therefore, although the spectra were collected from areas with different relative thicknesses, the initial loss of N with respect to dose should be equivalent for the two areas under observation (from thickness considerations alone). The initial gradient of figure 7.11(a), which was collected from the region of the specimen avoiding strong diffraction conditions, is $(1.9\pm0.1)\times10^{-8}$N atoms/electron, which lies within the expected range of gradients in figure 7.4. However, for the series of spectra collected at strong diffraction conditions, figure 7.11(b), the initial gradient is $(4.0\pm1.2)\times10^{-8}$N atoms/electron which is not consistent with the loss of N from the other areas studied in figure 7.4. The rate of loss of N at the stronger diffraction condition is at least twice as fast as those observed from the other specimen areas suggesting that channeling effects can become very significant. This justifies the selection of specimen orientations made in the previous TiN experiments, where strong diffraction conditions were avoided, as the increased rate of N loss due to channeling effects would mask any relationship between the rate of loss of N and the relative specimen thickness.

7.5.3 Loss of Ti

Loss of Ti was observed in 2 of the 3 areas examined on the TiC sample in section 6.4.3. Therefore, to investigate the loss of Ti from the TiN sample and its effect on the

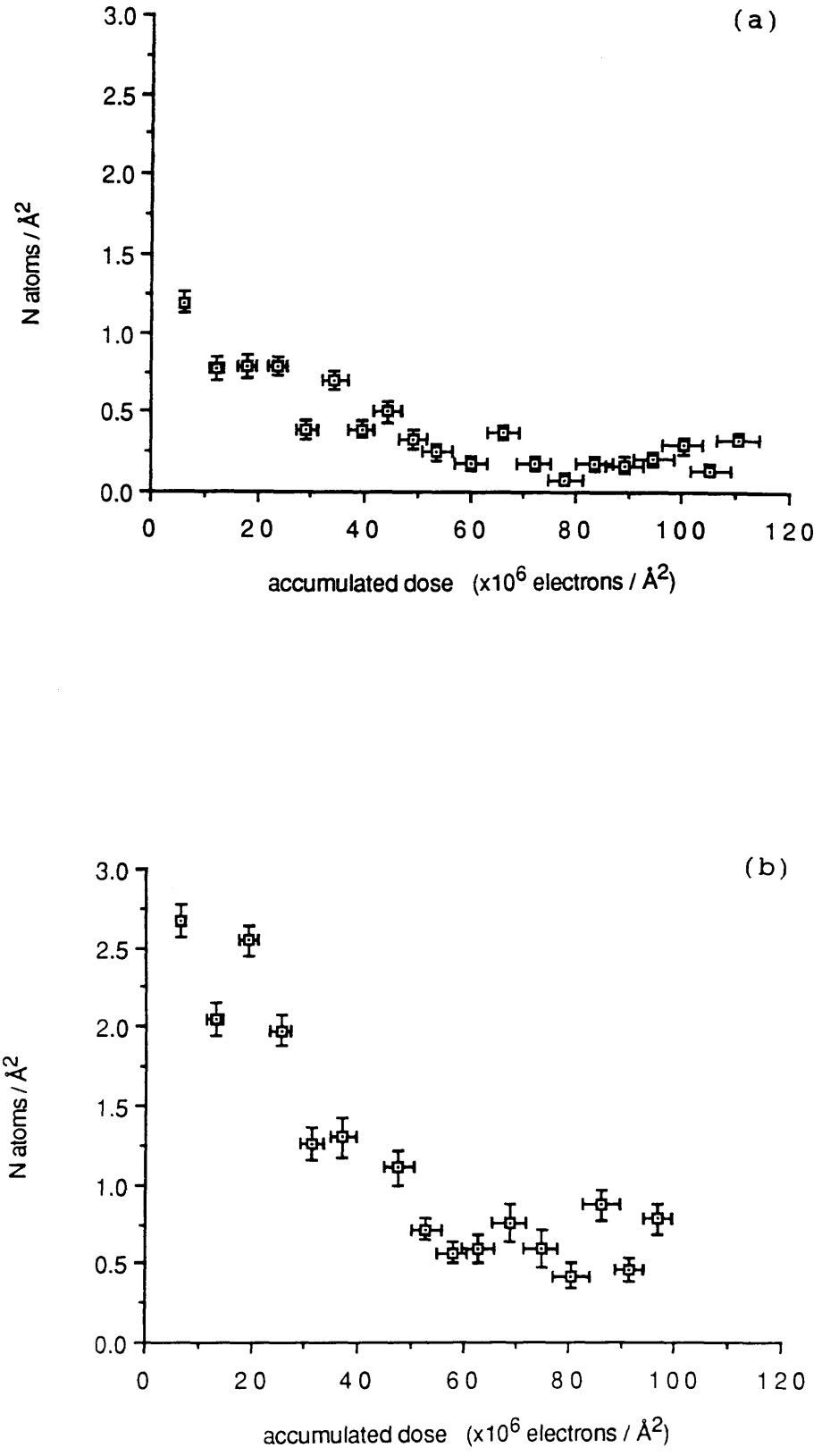

Figure 7.11. Loss of N as a function of dose for (a) an area of the sample avoiding strong diffraction conditions ($t/\lambda=0.07$) and (b) an area of the specimen significantly closer to a low order symmetry point ($t/\lambda=0.17$).

rate of loss of N, the TiN spectra discussed in the previous section were re-examined. Figures 7.12, 7.13, 7.14 and 7.15 show the number of Ti atoms/Å^2 as a function of electron dose for each of the specimen areas examined in the previous sections. The corresponding N depletion graphs are indicated on the figures for ease of reference. For the thinnest areas of TiN examined, the error on the Ti signal is too small to plot on the depletion graphs. From the Ti depletion graphs it can be seen that there is a significantly larger variation in the Ti content than can be attributed to the random errors calculated by the Egerton background fit to the EEL spectra. This suggests that for these Ti edges the random error underestimates the error in the signal extraction. The systematic error in the background fit is much more significant for the Ti edge in TiN because it sits on the top of the preceding N K-edge whose near edge structure may perturb the AE^{-r} background fit. There was some evidence of changes in the near edge structure of the N K-edge during electron irradiation which may explain the large fluctuations in the Ti depletion curves.

Although there is an apparent loss of Ti observed in several of the irradiated areas (eg 7.13a), it is often very difficult to determine whether there is a gradient significantly different from zero because of the noise level in the experimental data. Therefore, the following policy was adopted to decide whether there was a real loss of Ti from a particular area. A linear least-squares fit was carried out on the Ti data to establish the gradient and its error, which, in this case, is equivalent to the standard deviation. A statistical t test was performed on

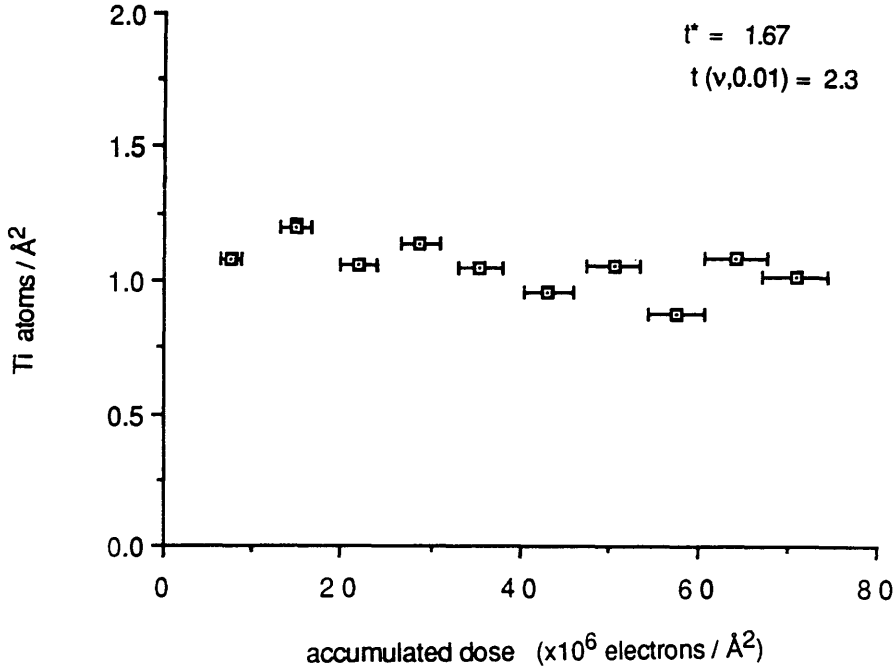

Figure 7.12(a). Loss of Ti as a function of dose for the area of the TiN sample investigated in figure 7.1(a).

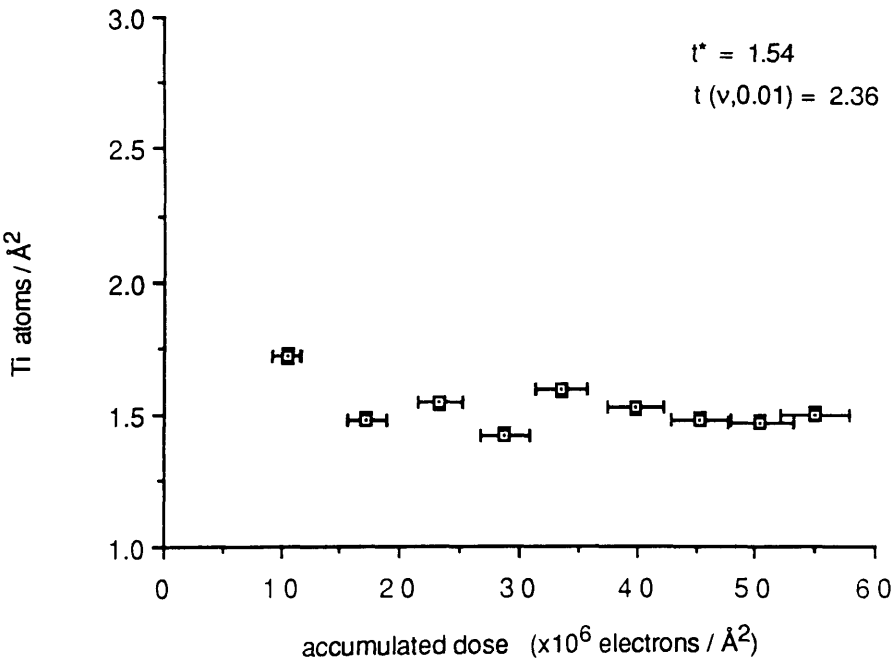

Figure 7.12(b). Loss of Ti as a function of dose for the area of the TiN sample investigated in figure 7.1(b).

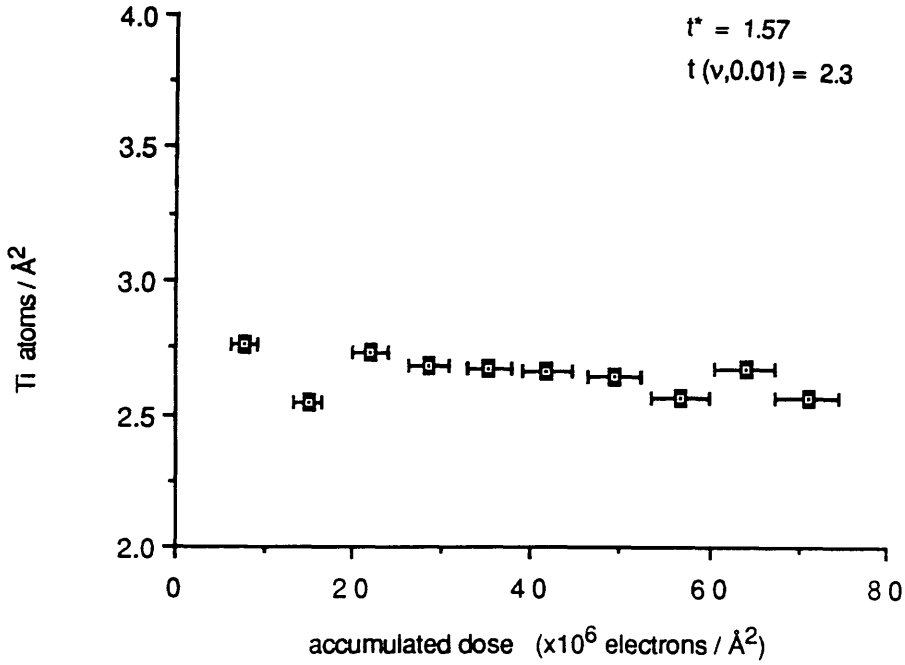

Figure 7.12(c). Loss of Ti as a function of dose for the area of the TiN sample investigated in figure 7.1(c).

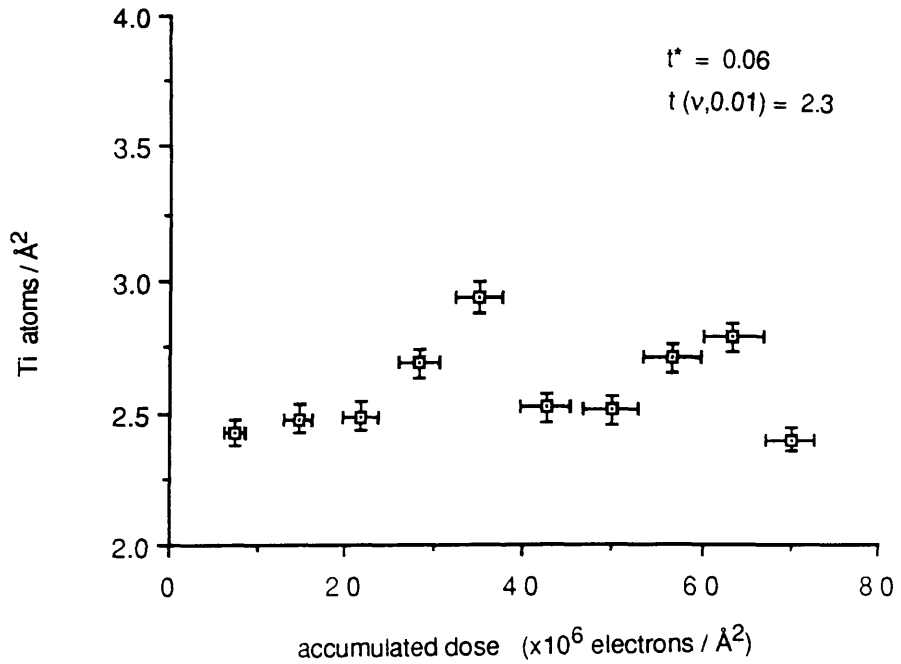

Figure 7.12(d). Loss of Ti as a function of dose for the area of the TiN sample investigated in figure 7.1(d).

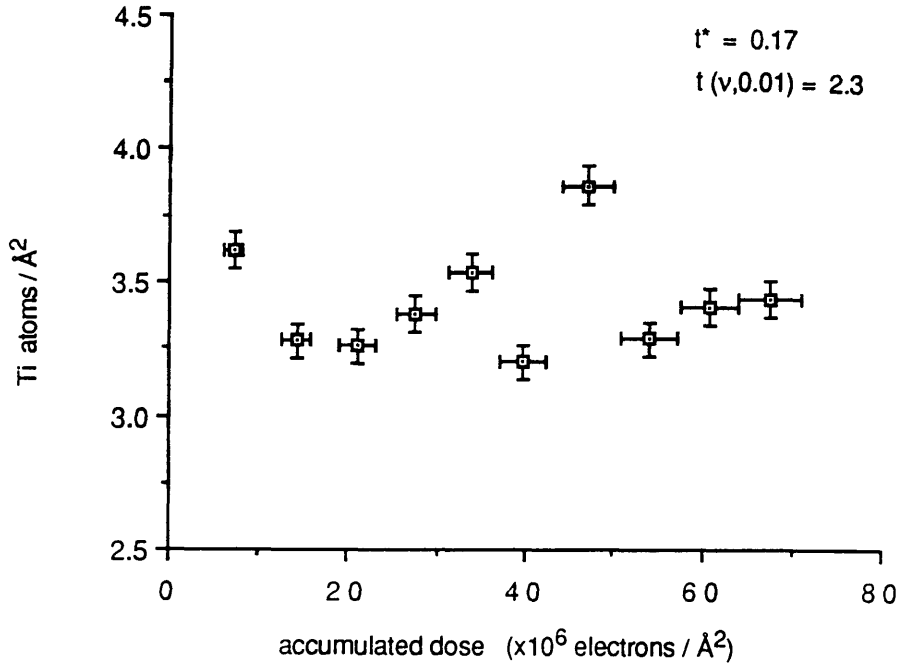

Figure 7.12(e). Loss of Ti as a function of dose for the area of the TiN sample investigated in figure 7.1(e).

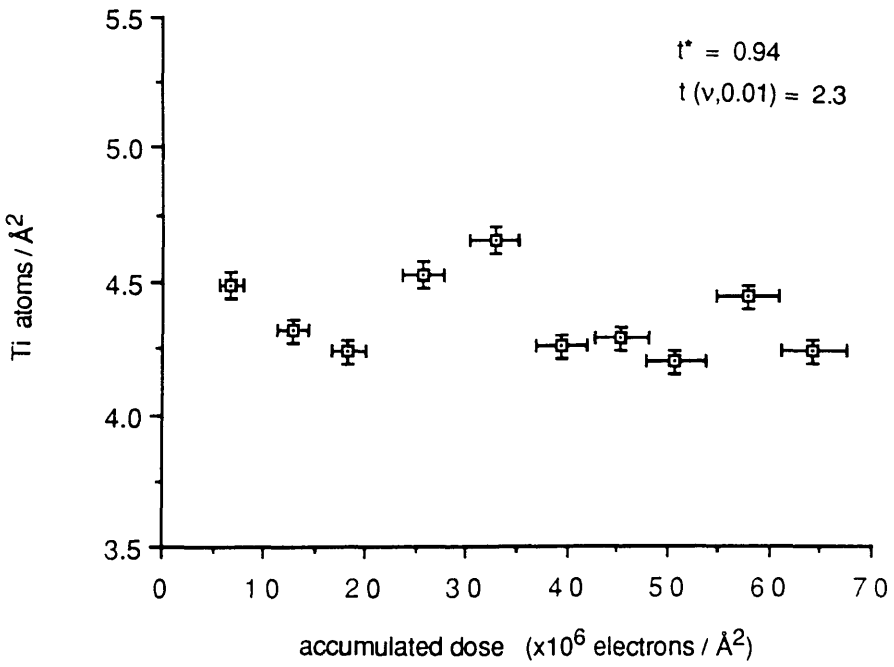

Figure 7.12(f). Loss of Ti as a function of dose for the area of the TiN sample investigated in figure 7.1(f).

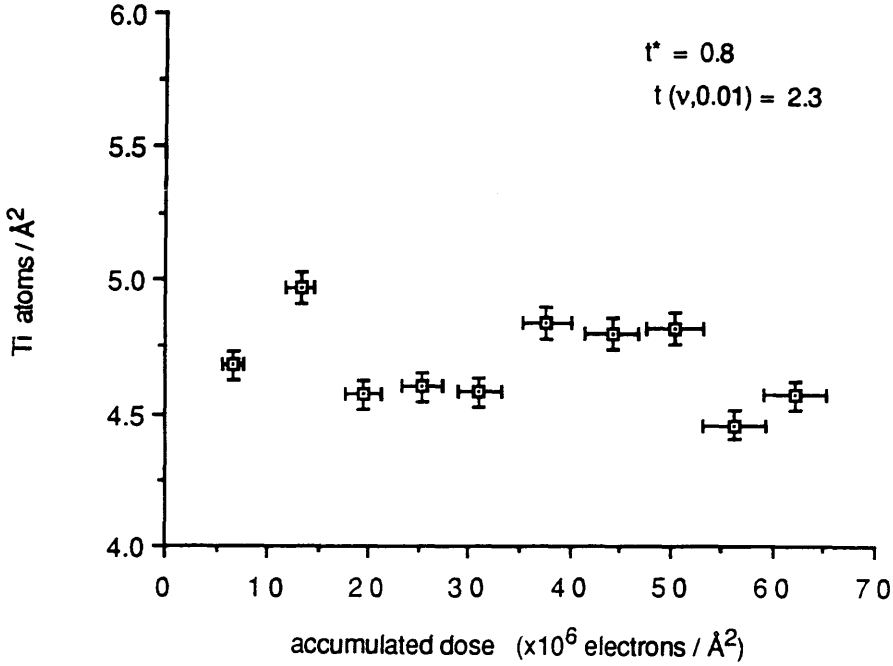

Figure 7.12(g). Loss of Ti as a function of dose for the area of the TiN sample investigated in figure 7.1(g).

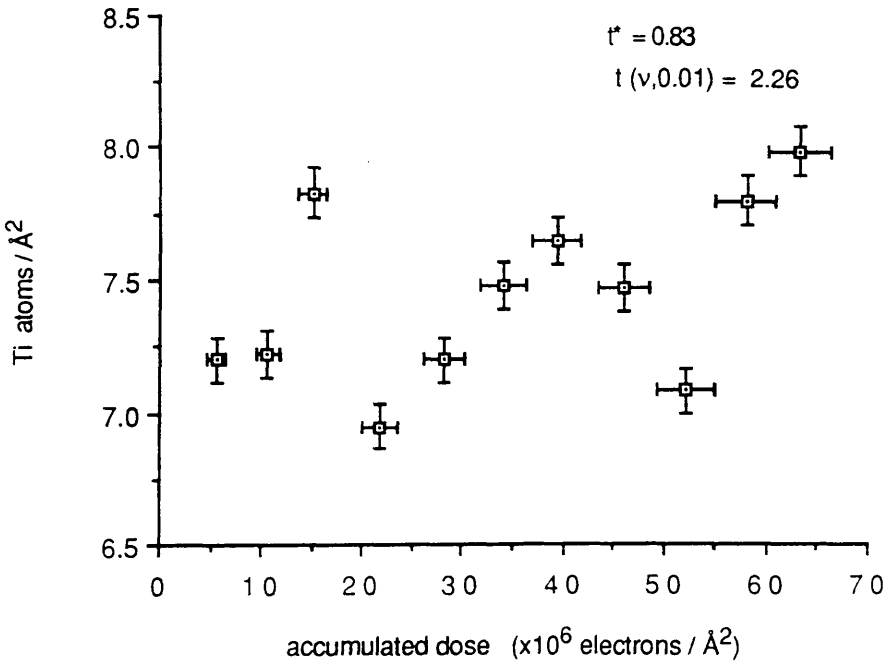

Figure 7.12(h). Loss of Ti as a function of dose for the area of the TiN sample investigated in figure 7.1(h).

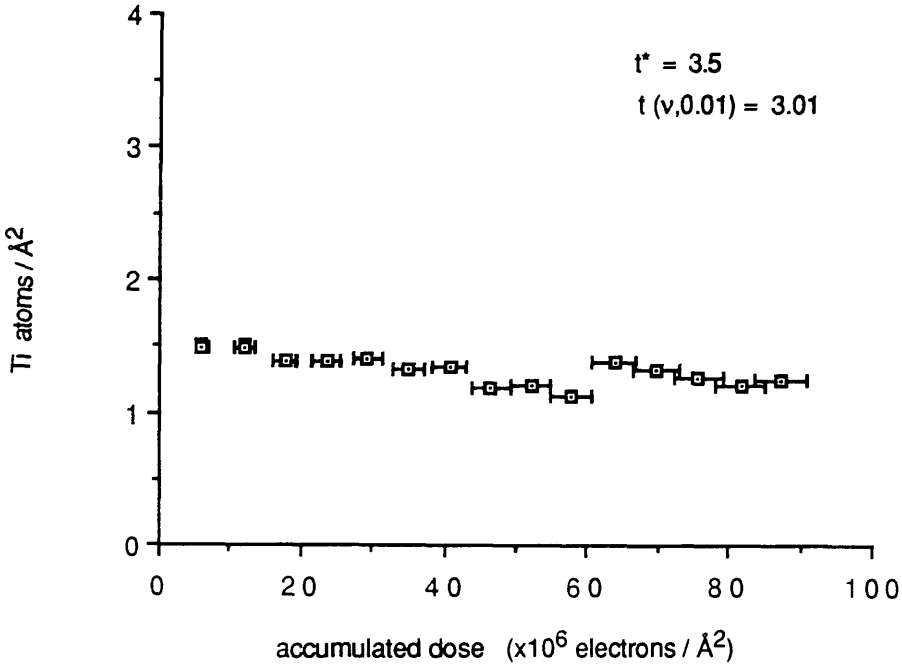

Figure 7.13(a). Loss of Ti as a function of dose for the area of the TiN sample investigated in figure 7.2(a).

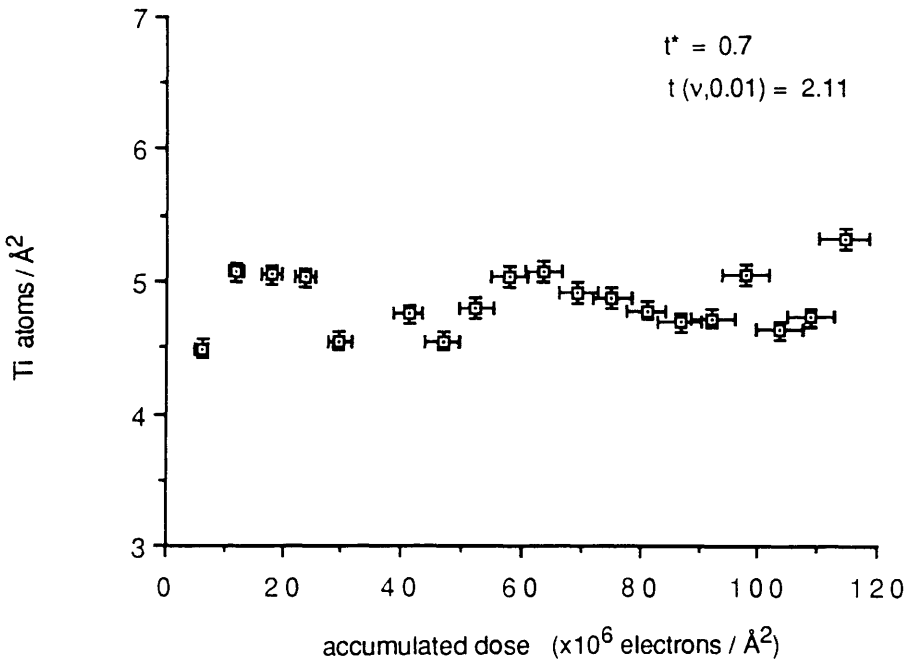

Figure 7.13(b). Loss of Ti as a function of dose for the area of the TiN sample investigated in figure 7.2(b).

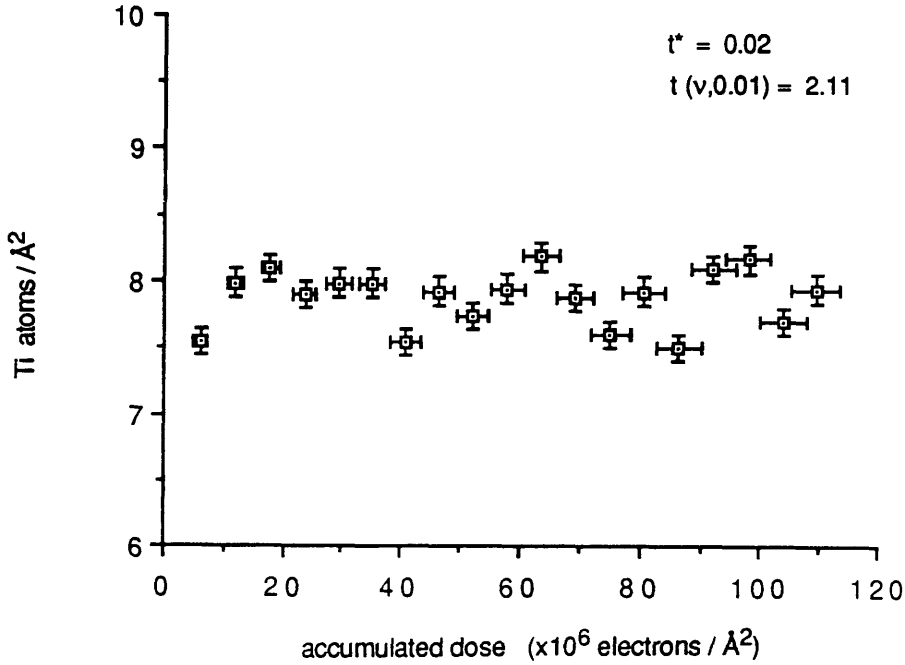

Figure 7.13(c). Loss of Ti as a function of dose for the area of the TiN sample investigated in figure 7.2(c).

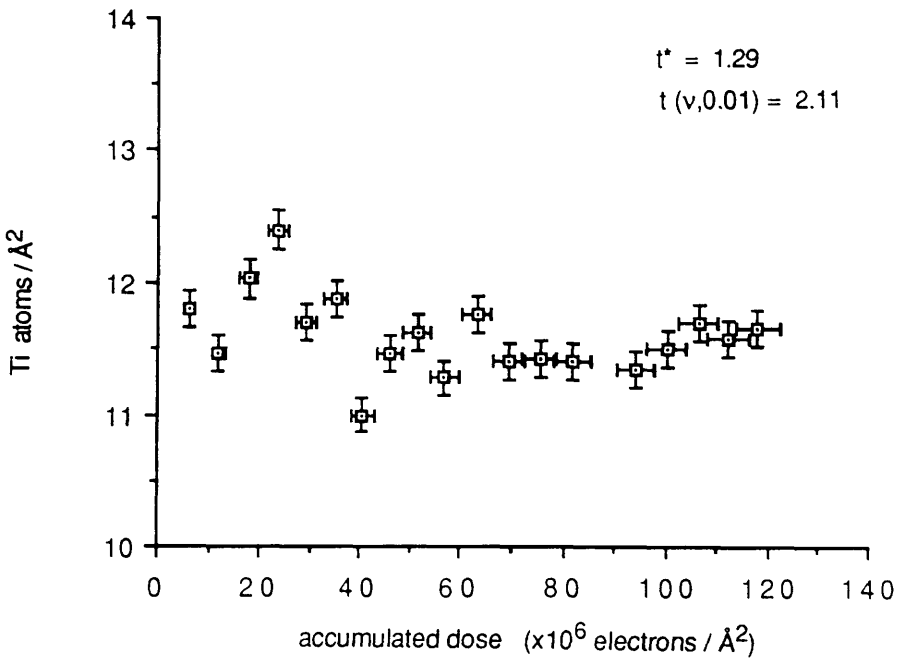

Figure 7.13(d). Loss of Ti as a function of dose for the area of the TiN sample investigated in figure 7.2(d).

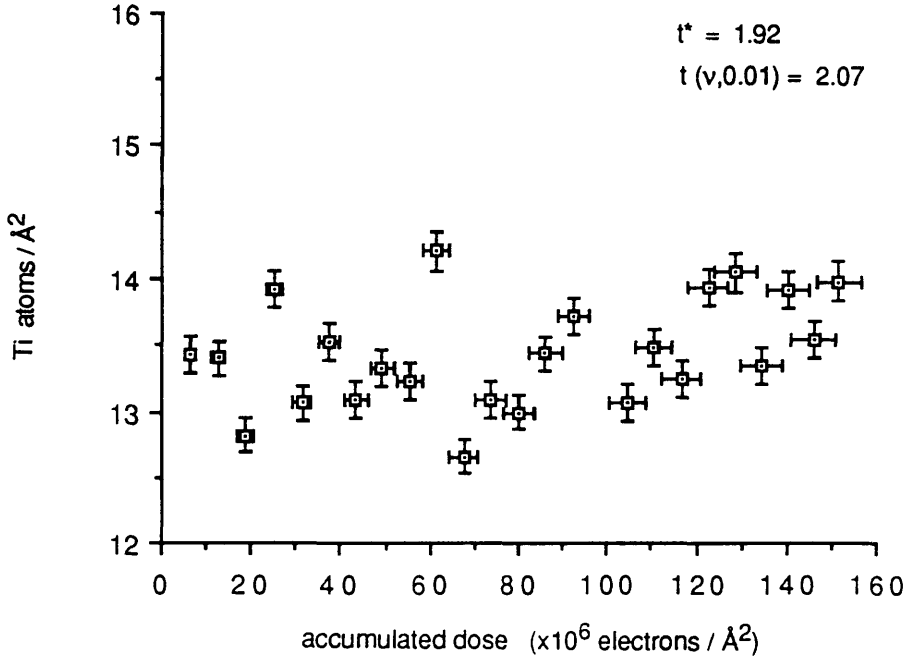

Figure 7.13(e). Loss of Ti as a function of dose for the area of the TiN sample investigated in figure 7.2(e).

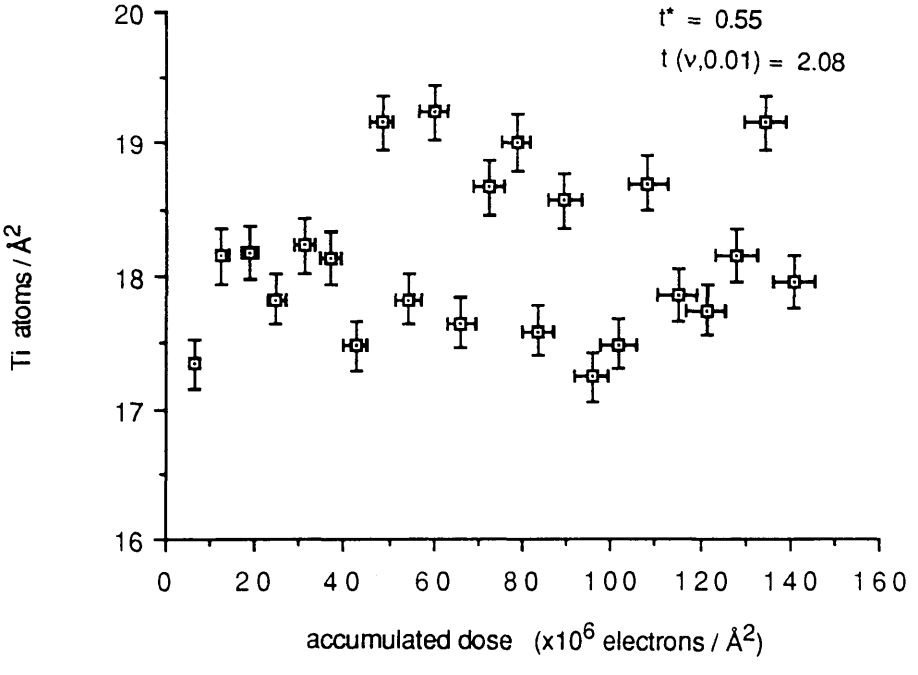

Figure 7.13(f). Loss of Ti as a function of dose for the area of the TiN sample investigated in figure 7.2(f).

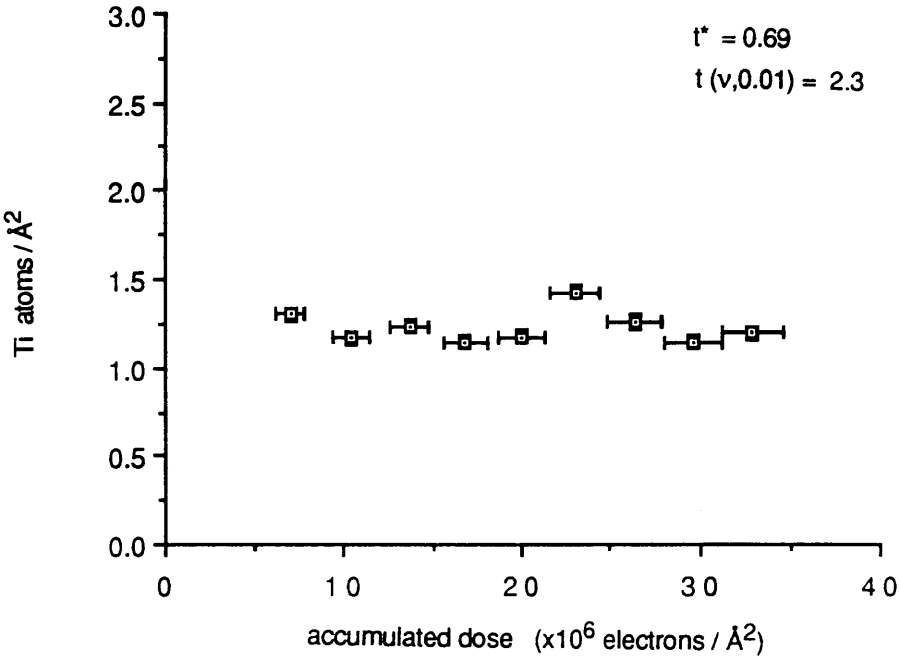

Figure 7.14(a). Loss of Ti as a function of dose for the area of the TiN sample investigated in figure 7.9(a).

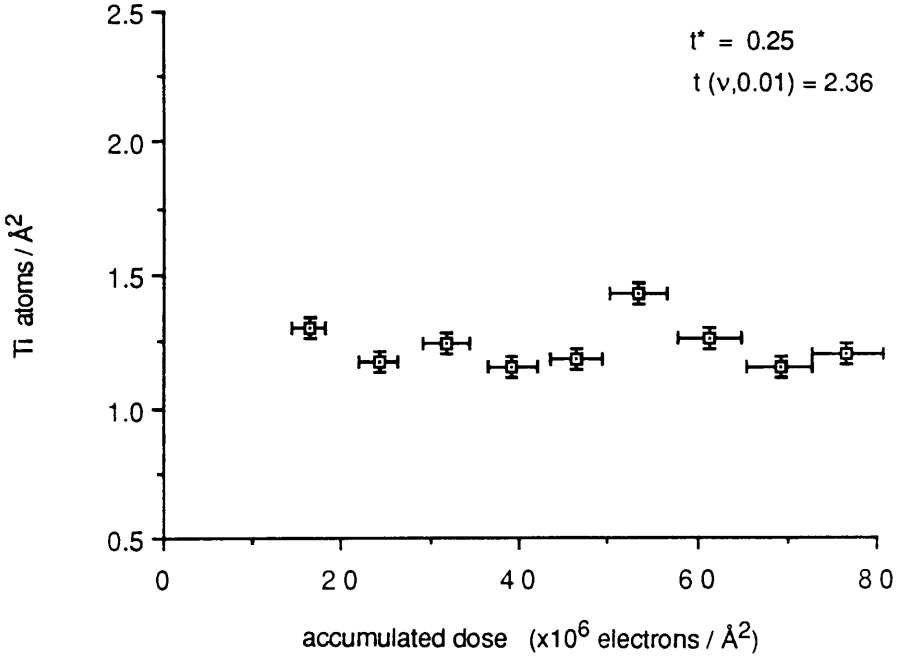

Figure 7.14(b). Loss of Ti as a function of dose for the area of the TiN sample investigated in figure 7.9(b).

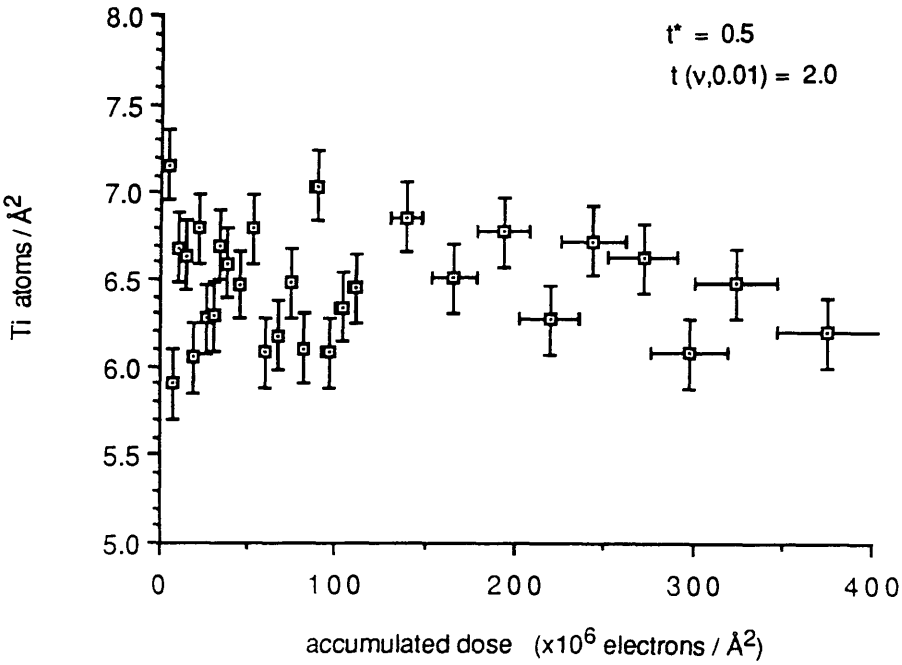

Figure 7.14(c). Loss of Ti as a function of dose for the area of the TiN sample investigated in figure 7.10.

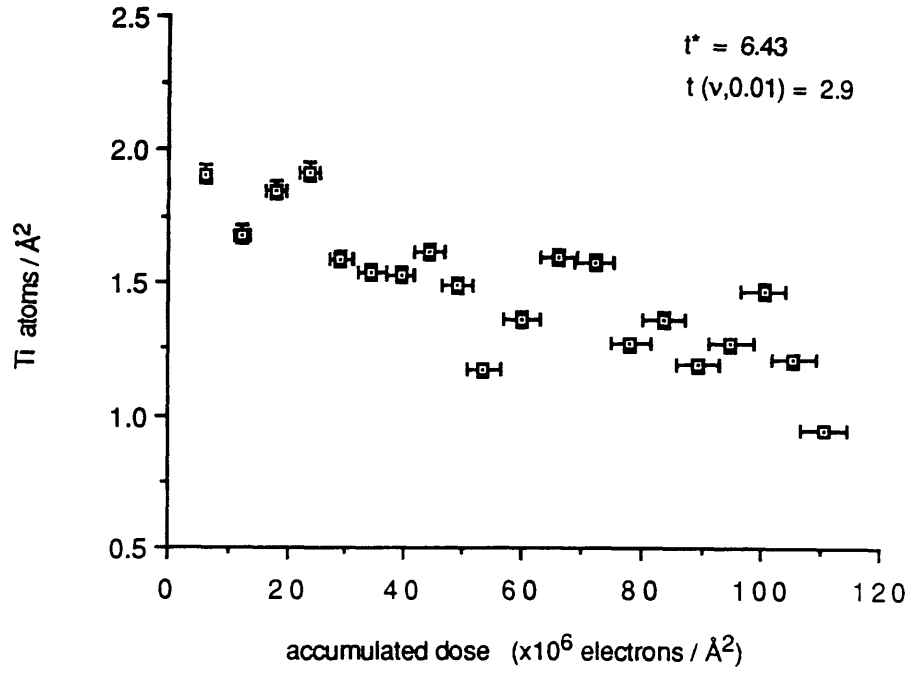

Figure 7.15(a). Loss of Ti as a function of dose for the area of the TiN sample investigated in figure 7.11(a).

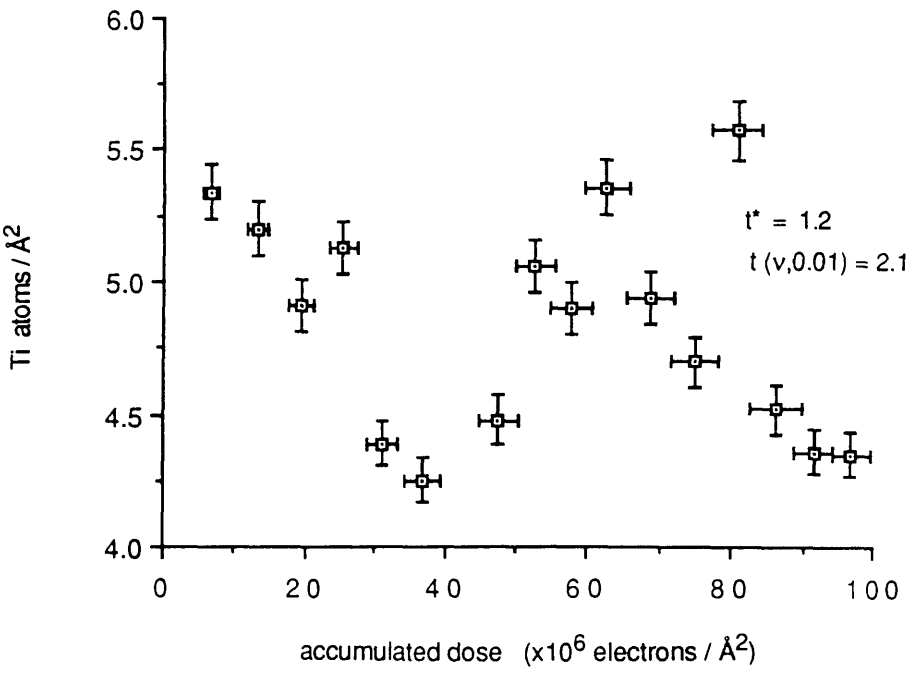

Figure 7.15(b). Loss of Ti as a function of dose for the area of the TiN sample investigated in figure 7.11(b).

these gradients to determine within a 99% certainty whether the gradient was non-zero. The gradient is defined to be non-zero if

$$t^* > t(\upsilon,0.01)$$

where t^* = measured gradient/standard deviation of gradient

and $t(\upsilon,0.01)$ is the critical value of the students t distribution for υ degrees of freedom at 99% certainty.

The values of t^* and $t(\upsilon,0.01)$ are shown in each of the graphs of figures 7.12 to 7.15. From the above criterion Ti is only lost from the areas irradiated in figures 7.13a and 7.15a. Although a significant Ti loss is only noted in thinner regions of the specimen, suggesting a surface loss mechanism, it should be noted that Ti is not lost from all the thinnest regions. This suggests that other factors, dependent on the area of the sample investigated, are also an important feature of the Ti loss mechanism.

The knock-on model predicts that the Ti cannot be lost from a TiC or TiN sample bombarded with 100keV electrons as the binding energy of the Ti atoms is of the order of 20eV compared to a maximum transferable energy of only 5eV in a collision of an electron with a Ti atom. The transfer of energy from the incident electron to the Ti atom via the N atom yields a maximum transferable energy of only 12eV. Therefore this mechanism cannot be responsible for the loss of Ti observed in some regions of the specimen. However, the image analysis of section 6.5 suggests that the radiation damage is inhomogeneous, with regions of preferential mass loss within the irradiated area. In these

preferentially damaged areas, the Ti atoms must have been displaced, as the loss of the light elements C and N alone could not explain the change in intensity observed in the ADF images. This is possibly because the radiation damage proceeds at a greater rate in regions of the sample around defects, where the displacement of the Ti becomes energetically possible due to reduced binding energies.

Where a loss of Ti is observed, the percentage of Ti lost is significantly lower than the percentage of N lost from the same region. The loss of Ti observed in figure 7.13(a) is only (7±3)% compared to a (49±9)% loss of N. Similarly figure 7.15(a) loses only (10±2)% of the Ti signal compared to (48±10)% of the N signal. Consequently, even if the loss of N is enhanced by the presence of specimen defects this is unlikely to affect the overall rate of loss of N because the N around the defect will be lost very rapidly and will contribute an insignificant amount to the total loss of N. Therefore, the N depletion observed can be primarily attributed to the loss of N from the whole irradiated area of the sample. This is verified in the N depletion curves of section 7.2 and 7.5 where the areas which lose Ti show a rate of loss of N which is consistent with the average rate of loss of N for $t/\lambda \leq 0.27$ in figure 7.4.

In conclusion, although the presence of specimen defects in the irradiated region may enhance the loss of Ti, they are unlikely to significantly increase the rate of loss of N from the sample unless they cover an extensive area. Therefore, the possible loss of Ti observed in several of the irradiated regions is unlikely to affect the relationship between the loss of N and the relative specimen thickness shown in figure 7.4.

7.5.4 Quasi Equilibrium Level.

In the thinner samples of figures 7.1 and 7.2 it was noted that the rate of depletion of N decreases at higher doses, leveling off to a non-zero N concentration. However, because of the limited number of data points in each of the series of spectra, the effect was only observed in the thinnest samples, where the statistics were poor. Thus, it is very difficult to comment on the form the N loss takes at higher doses. The data presented in figure 7.11(a) is an extension of the N depletion curves of figures 7.1 and 7.2 with extra data points allowing the observation of the exact N depletion at higher doses. From figure 7.11(a) it can be seen that the N content falls to a constant level, where, despite an increase in the accumulated dose, there is no further loss of N from the sample. Assuming a similar quasi-equilibrium N concentration for the thinner samples in figure 7.1 and 7.2, the fraction of N remaining in the sample at higher accumulated doses was investigated.

Table 7.2 shows the fraction of N remaining at the quasi-equilibrium level for a range of specimen thicknesses. For a given dose rate (3.4×10^5 electrons/Å^2/s) the fraction of N at the quasi-equilibrium level is constant with an average concentration of (21.5±1.6)%, where the error is the standard error in the mean. The knock-on displacement model, thought to be applicable for $t/\lambda \leq 0.27$, does not predict a quasi-equilibrium concentration and in fact predicts that the N will be lost at a decreasing rate to zero N concentration. However, once the rate of loss of N has been reduced to a low level thermal diffusion or even radiation induced diffusion (if

t/λ	dose rate $x10^5$ electrons/$Å^2$	percentage of N at quasi-equilibrium level
0.03	3.4	25±6
0.04	3.4	20±3
0.07	3.4	18±3
0.07	3.4	23±2
0.17	14	10±2

Table 7.2 Fraction of N left at the quasi-equilibrium level for specimens of various thicknesses.

there is a probe repositioning error) may cause diffusion of N back into the irradiated region. Such an influx of N into the irradiated region will balance any loss of N at the specimen surface resulting in a quasi-equilibrium N content. Since the mechanism which re-introduces N back into the irradiated region is diffusion controlled, one might expect the fraction of N flowing into the irradiated region to be constant over a range of specimen thicknesses. Consequently, for a given dose rate, the equilibrium condition will occur at the same fractional loss of N for various specimen thicknesses. This is consistent the quasi-equilibrium N concentrations shown in table 7.2.

For an increase in the dose rate (14×10^5 electrons/Å^2/s), the fraction of N remaining at the quasi-equilibrium level is only 10% compared to an average of 21.5% at the lower dose rate. Although the specimen thickness examined was higher for the higher dose rate experiment, all the specimen thicknesses considered here lie within the constant rate of loss of figure 7.4 and therefore should have a similar rate of loss of N. A lower quasi-equilibrium level at increased dose rates is consistent with an increase in the loss process within the irradiated region where the mechanisms responsible for the flow of N back into the irradiated region remain constant, and therefore the equilibrium flow of N in or out of the irradiated region occurs at a lower N concentration. This result was predicted by the 1-dimensional numerical solution to the diffusion problem where an increase in the ratio of the radiation and thermal diffusion coefficients resulted in a lower quasi-equilibrium concentration.

At orientations closer to a symmetry position, as in

figure 7.11(b), although there is an increase in the rate of loss of N, the experimental results suggest that the quasi-equilibrium level remains constant at a N concentration of (22±2)%. This is perhaps surprising, since the effective radiation diffusion coefficient has been increased in this region because of channeling effects. However, as a result of the massive loss of N, the crystal structure of the material may have been disordered, decreasing the effect of channeling and allowing the loss mechanism to return to that observed in the weaker diffraction conditions. Further experiments are required to clarify this observation.

It should be noted that for thicker specimens, where 3-dimensional diffusion becomes the dominant loss mechanism, the build up of N at the periphery of the irradiated region will exacerbate the probe repositioning errors. Consequently the quasi-equilibrium N concentration may appear higher than expected with a larger scatter in the data points unless very accurate probe repositioning is performed.

In conclusion, although the quasi-equilibrium N concentration was not predicted by the knock-on displacement model, it is unlikely to effect the results of section 7.2 because the gradients of the N depletion curves were extracted in conditions well away from that of the equilibrium.

7.6 CONCLUSIONS

The experimental results considered in the first section of this chapter established that for $t/\lambda < 0.27$ the rate of

loss of N from TiN is constant, which is consistent with the predictions of the forward knock-on model. The application of this model to the experimental data yielded a cross-section for the displacement of N in TiN which was significantly lower than that predicted by the theoretical displacement cross-sections (equation 3.5). This suggests that the crystal lattice introduces a strong orientation effect into the cross-section and is consistent with the knock-on displacement damage experiments carried out on crystalline metals (Vajda 1977). The orientation effect was confirmed in the channeling experiments of section 7.5. which revealed a significant increase in the rate of loss of N at a stronger diffraction condition.

The increase in the rate of loss of N at higher specimen thicknesses is consistent with the increasing contribution of loss of material from the edge of the cylindrically irradiated volume. Consequently, the simple forward knock-on model is insufficient to explain the observed rate of loss of material for $t/\lambda \geq 0.27$. An isotropic 3-dimensional diffusion model was found to qualitatively explain both the constant loss at smaller t/λ and the increase in the rate of loss, proportional to the specimen thickness, at greater values of t/λ. It should be noted, however, that the increase in the rate of loss of material by the isotropic diffusion model is not as steep as the increase observed in the experimental data of figure 7.4 suggesting that this model is not sufficient to explain the experimentally observed N losses. From energy transfer considerations, the damage mechanism is likely to lie somewhere between the two extremes of forward knock-on displacement and isotropic radiation induced diffusion

considered here. Further work is required to both extend the theoretical model to a forward biased diffusion model and to examine a wider range of specimen geometries in order to determine the relative contributions from loss of material at the specimen surfaces and the edges of the cylindrically irradiated volume.

Other effects on the rate of loss of N from TiN were considered in the final section but were not found to significantly affect the rate of loss of N with respect to dose provided sufficient care was taken (eg to extract the N depletion curves well away from the quasi-equilibrium condition). For the specimen geometries and the dose rates used in these experiments no dose rate effect was observed as expected from a simple knock-on displacement model.

CHAPTER 8 CONCLUSIONS AND FUTURE WORK

With the development of field emission guns and the resulting large current densities in the electron probe, radiation damage has become an important consideration in high resolution electron beam microanalysis. Previously, experimental limitations were set by the sample used and the electron optical configuration employed. However, with the gradual improvement in instrumentation and analysis techniques, the damage induced in the specimen on interaction with the incident electron beam will be the ultimate limit on the resolution and sensitivities achieved in the microscope for radiation sensitive specimens. The work presented in this thesis investigated such radiation damage processes in the ceramic materials TiC and TiN.

Initial experiments carried out on an ion beam thinned TiC sample investigated the rate of loss of C as a function of the specimen thickness and dose rate. The results, which were presented in chapter 6, were consistent with the prediction of the Howitt knock-on displacement mechanism where the rate of loss of C was found to be independent of the specimen thickness. This result suggests that, for the specimen thicknesses examined, the C atoms are predominantly lost from the specimen surface as a result of a forward shuffling process. In general, however, the results from the TiC sample were inconclusive because of the problems associated with beam induced contamination which can contribute to the C characteristic edge signal. Consequently, it was impossible to determine for example whether there was a real reduction in the rate of loss of C

with respect to dose at the lower dose rate or whether the loss of C was significantly reduced by a contribution to the C characteristic edge from contamination in the microscope.

Subsequent experiments were carried out on TiN samples, where the contamination could be directly monitored and its effects separated from the characteristic N signal. By extending the range of specimen thicknesses examined, the discussion in chapter 7 suggested that the forward knock-on displacement model was only applicable for $t/\lambda \leq 0.27$. For larger specimen thicknesses, the rate of loss of N was found to increase proportionately with specimen thickness, suggesting that the loss of N from the edge of the cylindrically irradiated volume must be taken into consideration. This is consistent with the radiation induced diffusion model considered in chapter 3 where the N atoms are displaced isotropically. This model was found to qualitatively explain the experimentally observed rate of loss of N as a function of specimen thickness. However, energy transfer considerations suggest that the diffusion process is more likely to be forward biased since the ejected atoms have more energy when travelling in this direction. Therefore, the damage mechanism is likely to lie somewhere between the two extreme situations considered in chapter 3, and further work is required to develop a model of a forward biased diffusion process.

The displacement cross-sections were calculated from the experimental data for $t/\lambda \leq 0.27$ using the forward knock-on displacement model to be on average 22.5±4.5 barns. For both the TiC and TiN experiments, this is considerably

lower than the predicted theoretical cross-section of 184 and 200 barns for C in TiC and N in TiN. However, the theoretical cross-section considered an atom which was free to be displaced in any direction (with a uniform displacement energy of 5eV) and so cannot be satisfactorily applied to an atom in a crystal lattice where the displacement energy is dependent on the orientation. Therefore, the experimentally calculated cross-section, while being lower than the predicted theoretical values, are perhaps a better estimate of the true cross-section for displacement of atoms constrained in a crystal lattice. A cross-section of 22.5 barns corresponds to a displacement energy of 13eV for the random orientations selected in these experiments. This suggests that the "average" 5eV displacement energy assumed for the TiC and TiN, from self diffusion considerations, underestimates the displacement energy in a weaker diffraction condition in which the C atom is displaced towards the much larger Ti atoms and is subsequently reflected back into its lattice site. It should be noted that the 5.4eV displacement energy measured by Venables (1969) in VC applies to the <110> direction, which for the face centred cubic structure of VC corresponds to a plane of C atoms. Therefore, the displacement of C atoms along the <110> direction is energetically favourable and so E_d=5.4eV represents the lower limit for the displacement energy of C along an "easy direction" within the VC lattice. The importance of orientation was confirmed in an experiment to check for channelling effects which showed that the rate of loss of N was increased by a factor of 2 when the specimen was

oriented closer to a strong diffraction condition. From the forward knock-on displacement model, this corresponded to a cross-section of 66 barns, with a reduction in the displacement energy to 9eV. As a result of the strong angular dependence of the displacement energies, care is required in the comparison of displacement cross-sections calculated from different experiments, which may explain some of the discrepancies in the literature. However, in general the radiation damage can be reduced by avoiding strong diffraction conditions, and for these experiments this was necessary to enable the investigation of other effects, such as thickness dependence.

Dose rate experiments on TiN confirmed that, at the specimen geometries investigated and dose rates employed, it is the total dose applied to the specimen and not the dose rate which is the important consideration in the knock-on damage process. This suggests that the dose rate effect observed in TiC was due to beam induced contamination slowing the rate of loss of C with respect to dose at the lower dose rate. It should be noted, however, that a dose rate effect was observed in the ability of the focussed probe to burn a positioning hole in the sample. This is consistent with observations in TiO, which has a similar conductivity to TiC and TiN, where an ionisation damage process was considered to be responsible for drilling holes with a focussed probe (Berger 1987). Therefore, further experiments with focussed probes are necessary to determine whether a different mechanism, such as that reported for electron beam hole drilling, comes into play at higher dose rates. The investigation of such

rapid mass loss requires the application of a parallel EELS recording system. This enables the EELS acquisition times to be significantly reduced, whilst maintaining sufficient statistical accuracy.

A loss of Ti was observed in some of the specimen areas examined on both the TiC and TiN samples. This was not expected, since energetic considerations predicted that a Ti atom cannot be displaced from the bulk of a TiC or TiN lattice by 100keV electrons. Loss of Ti was only observed in the thinner samples suggesting that the Ti is also involved in a knock-on displacement mechanism. However, the fact that Ti is not lost from all the thinner areas suggests that other factors, such as the presence of defects in the material, may significantly reduce the Ti binding energy and play a significant role in the displacement of Ti. Future experiments would aim to clarify this loss of Ti and the effect, if any, on the observed loss of the light elements. By selecting areas possessing a high density of defects, it should be possible to determine the importance of this effect on the rate of loss of the light element from the sample.

Analysis of annular dark field images acquired during EELS analysis of TiC and TiN, described in chapter 6, confirmed a linear correlation between the change in image intensity and the mass loss recorded by EELS analysis. The initial results suggested that the extraction of quantitative results should be possible from these images, provided that care is taken over the acquisition conditions used. One of the most useful features of this work was the information provided on the inhomogeneous nature of the

radiation damage process. More detailed ADF analysis may help to explain the loss of Ti in some of the sample areas examined, since the technique is very sensitive to changes in the relative concentrations of the heavier elements. However, this procedure is unlikely to compare with quantitative EELS analysis for the study of preferential mass loss from radiation sensitive materials.

A major consideration for radiation damage studies is the extraction of quantitative data from statistically poor EEL spectra. This results from the necessary reduction of the dose incident upon the specimen that is required to observe the damage process. Often, the accuracy with which quantitative data can be extracted from an EEL spectrum is limited by the accuracy of the background fitting routines. Chapter 5 compared and contrasted three such background fitting routines, namely the Egerton, Trebbia and single stage fits to see which, if any, has an advantage for the extraction of data in the presence of noise. For both the experimental and theoretical spectra considered in chapter 5, there was little evidence to suggest that any of the background fitting techniques were superior since the three methods produced very similar results. Therefore, the faster, more convenient Egerton fit was adopted to analyse the experimental data presented in this thesis. However, the comparison of these background fitting techniques served to highlight a problem of standardless EELS analysis. This is that the theoretical cross-sections considered in chapter 2 calculate only the probability of the atomic electron being ionised into the continuum. As such, they do not include the dominant white line

transitions that are present in transition elements such as Ti. This introduces a systematic shift between the extrapolation techniques of Egerton and Trebbia when compared to the single stage fitting technique because the near-edge structure is included in the first two named techniques techniques and it is in this region that the theoretical cross-sections are least accurate. Use of the hydrogenic cross-section SIGMAL2, which attempts to allow for the white line transitions, was found to significantly reduce the discrepancy between the Egerton/Trebbia fits and the single stage fitting technique. Although these considerations are important for the calculation of elemental ratios in TiC and TiN, they are insignificant in the measurement of the C and N displacement cross-section since the K shell cross-sections are considered to be more accurately determined (Rez 1984).

The marked reduction in the fluctuations achieved with the constrained single stage fit on the theoretical spectra in comparison with the experimental spectra in chapter 5 suggested that effects other than shot noise play a significant role in the noise introduced into the spectra. One possible source of additional noise is the short term fluctuation in the current emitted from the tip. Future experiments may consider extending this area of study further to introduce such effects into the theoretical spectra.

Perhaps the most significant single improvement in the extraction of quantitative data from these radiation damage experiments would be the application of a parallel EELS recording system. Parallel acquisition will allow an

equivalent statistical significance to be achieved with a much reduced dose incident on the specimen (Krivanek 1987). Consequently, by reducing spectrum acquisition times, high spatial resolution micro-analysis can be carried out on radiation sensitive specimens. This is seldom possible when serial EELS is used because the rapid mass loss precludes the extraction of reliable quantitative information.

An important consideration in radiation damage experiments, which involve defocussing the electron probe to reduce the dose on the specimen, is the preparation of electron transparent specimens with an adequate supply of uniform, thin areas. Chapter 4 considered two possible specimen preparation techniques; deposition of crushed material on a holey carbon support film and ion-beam thinning from bulk material. The crushed samples were found to be difficult to analyse because of the rapid variations in thickness and the random orientations of the particles. The lower than expected N/Ti ratios obtained from crushed material also highlighted a possible artifact in this specimen preparation technique where the material was preferentially cleaved at areas possessing a lower N content. Initially, preparation of electron transparent specimens by ion beam thinning was found to produce specimens with a rapid thickness variation over distances corresponding to the probe size and possible radiation damage by the argon ions. However, the radiation damage by ion-beam thinning was significantly reduced by lowering the energy of the argon ions and specimens with relatively large regions of uniform thickness and the expected N/Ti ratio were achieved, as discussed in chapter 4. Other

possible preparation techniques, such as electro-polishing (Hannink 1970) and sputtering of thin films (Tafto 1986), may be worth considering for future experiments to exclude possible radiation damage effects induced by the specimen preparation techniques themselves.

In conclusion, the work presented in this thesis has provided a sound base for future investigations in a STEM of materials such as TiC and TiN. This has involved the development of experimental techniques such as specimen preparation and experimental procedures using the STEM, spectrum analysis procedures and radiation damage models

Future experiments

The loss of C and N from TiC and TiN may be dependent on several variables such as specimen thickness, specimen orientation, the relative geometry of the irradiated volume and the dose rate. The experiments described in this thesis have investigated a small number of the possible combinations that are available during routine EELS analysis. Future experiments would aim to extend this investigation, especially into the effect of the specimen orientation and the relative specimen geometry, as this study was mainly limited to a probe diameter of 130Å, while at the same time striving to hold all other variables constant. As mentioned previously, a significant improvement on the statistical accuracy of the spectra collected during low dose radiation damage experiments can be achieved using a parallel EELS recording system. This would also allow the investigation of the damage process at

the higher dose rates available in the focussed probe, where the mass loss is too rapid to be followed using serial EELS acquisition.

APPENDIX 1 PREPARATION OF TiC AND TiN SAMPLES BY CRUSHING THE MATERIAL AND DEPOSITING ON A HOLEY C SUPPORT FILM

A holey formvar film was initially formed on a glass microscope slide using the apparatus illustrated in figure A1. The formvar/glycerine suspension was formed by adding 5ml of glycerin to a 1% solution of formvar in chloroform. The glycerine breaks down into small droplets in suspension and leads to the presence of holes in the formvar film. However, for the production of smooth formvar films it was found to be necessary to filter the suspension to remove any excess glycerine. The microscope slide was polished with a "Selvyt" cloth and placed in the tube as shown. After adding the suspension, the tap was opened allowing the solution to drain out of the tube, coating the glass slide in the process. The thickness of the film was determined by the speed at which the solution was drained, a slow rate of flow producing thicker films since there is more time for the film to form on the surface of the slide.

The formvar film was transferred to the desired Cu specimen grids by removing it from the glass slide. This was done by carefully running a moistened finger around the edge of the glass slide and floating the film off into a beaker of distilled water. The specimen grids were then placed on the floating film and picked up from the surface of the water using a microscope slide which had been coated in "Nesco" film. Once the film dried, each specimen was held in a jet of steam to evaporate the glycerin which produces the holes in the formvar film. The size and quantity of the holes formed was dependent on the time held in the steam, but a 30sec exposure was found to provide a

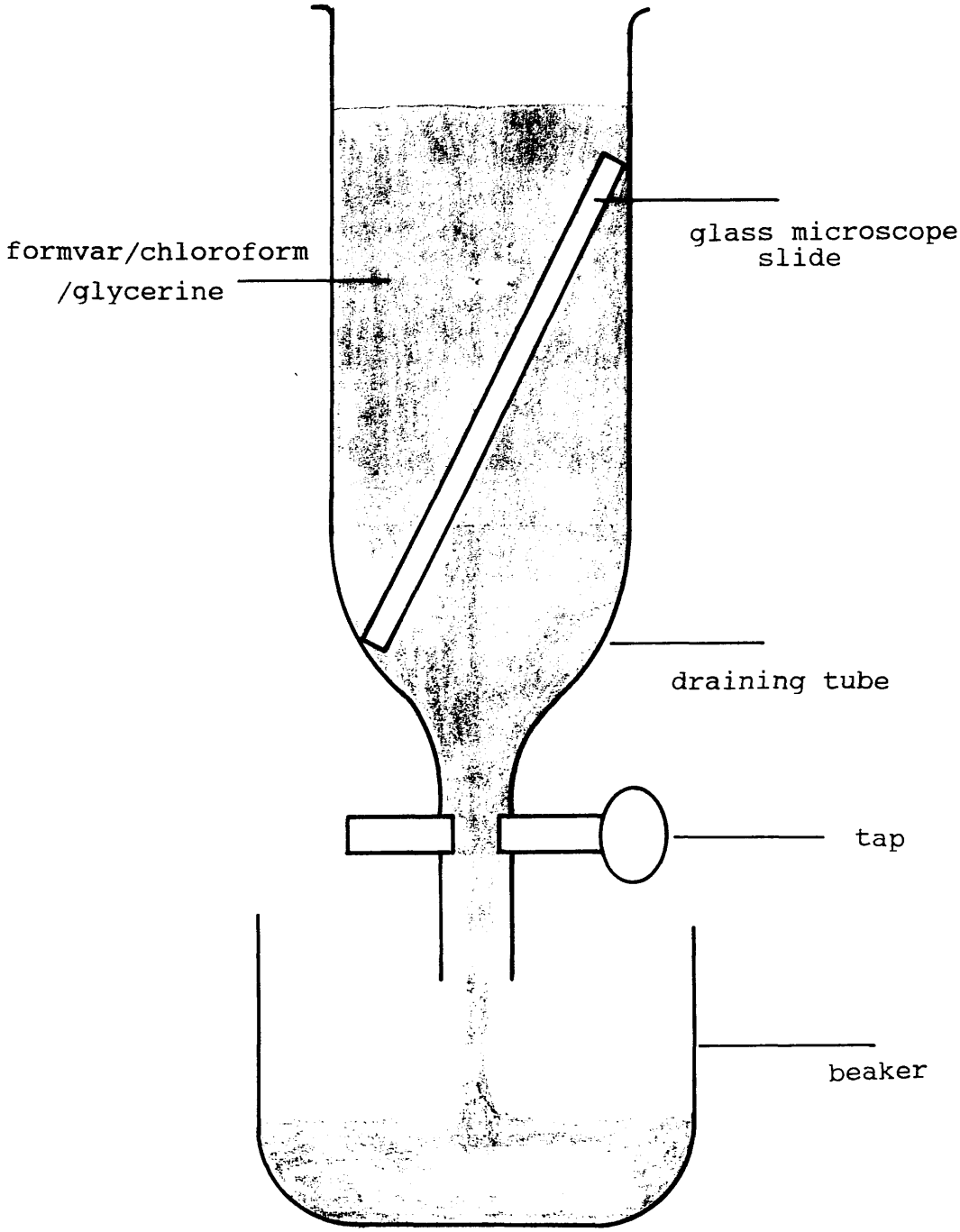

Figure A1. Apparatus for the preparation of holey formvar films.

plentiful supply of sufficiently large holes whilst retaining an adequate strength in the formvar film.

Since very thin carbon films can be produced, the holey formvar films were coated in carbon using an evaporator to a thickness of approximately 200Å. Use of a carbon film also reduces specimen charging effects under the electron beam. The formvar backing was then be removed by dissolving in chloroform.

The TiN and TiC specimens were crushed using an agate mortar and pestle and then mixed with isopropyl alcohol to form a suspension. After allowing the larger particles to settle to the bottom, a small quantity of the suspension was deposited on a holey carbon support film using a pipette. The alcohol evaporates leaving small particles of the material deposited on the film. Particular care is required when handling the specimen during evaporation of the alcohol since the C support film is particularly fragile at this point. As a results of the large number of particles, and provided they have been sufficiently crushed, there will be an adequate supply of thin areas over the holes in the support film that are suitable for EELS microanalysis.

APPENDIX 2 PRE ION-BEAM THINNING SPECIMEN PREPARATION

The ion etching rates for TiN and TiC are very slow, and so it is essential to prepare a very thin sample by mechanical means before ion-beam thinning the material. This was achieved by first cutting a 1mm slice from the bulk sample using a Bheuler Isomet low speed diamond saw. In order to cut brittle materials such as TiC and TiN, a maximum counter weight on the pivot arm was selected at a low saw speed to produce smooth specimen surfaces without fractures. The samples were then mounted on a glass slide using beeswax and polished on a Metalserve hand grinder using 600 grit silicon carbide paper with running water as the lubricant. The sample was thinned until a smooth, flat surface was obtained, which was then fine polished using 3 micron water based diamond paste on a cloth polishing wheel. The sample was then turned over and remounted on a clean glass slide and the hand grinding repeated until a smooth, parallel faced sample of ~50μm was obtained. Care was required in the final thinning stages since the specimen becomes very fragile at thicknesses less than 100μm, especially at the edges which start to recede if the thinning process has not been carried out evenly.

An ultrasonic drill with drilling tool of inner diameter 2.5mm and outer diameter 3.5mm was used to cut discs, suitable for mounting in the microscope specimen holder, from the sample using a 600 grit silicon carbide slurry. Care has to be taken not to cut across the grain boundary since this causes fractures during subsequent thinning procedures, especially during dimpling where pressure is applied to the sample. To make the samples more robust and

to avoid handling them in this fragile state, a copper washer, which had been hand ground to ~70μm, was glued on top of the discs using epoxy resin (Devcon 5-minute epoxy). The discs were then gently removed from the glass slide by dissolving the wax in warm organic solvents and floating the specimens off. Immersion in a cleaning agent also has the advantage of removing surface contaminants which might adversely affect the quality of the ion-beam thinning process.

A Gatan dimple grinder was used to dimple the sample ie. to create a concave impression in one of the faces of the discs. As a result, the outer perimeter of the disc remains thicker providing greater specimen strength during handling, while the centre can be thinned to ~20μm. The hardness of TiC and TiN required a maximum load and wheel speed to obtain thinning rates of ~1μm/min. A 15mm bronze wheel was used in conjunction with 3μm diamond paste to grind the sample to the required thickness. The dimpled surface was then polished with a plastic polishing wheel and 1μm diamond paste to obtain a smooth surface suitable for ion beam thinning. After each preparation stage the specimen was cleaned by immersion in warm acetone to remove surface contaminants thus reducing the build up of contamination throughout the specimen preparation. Before ion-beam thinning the specimens are heated to 150^{o}C in air to remove any possible contaminants from the epoxy resin.

REFERENCES

R.M.Allen (1989), in EMAG 1989 (Inst.Phys.Conf.Ser.No.98), 259

C.Allison, W.S.Williams, M.P.Hoffman (1984), Ultramicroscopy, **13**, 253

C.Allison, R.Stroller, E.Kenik (1988), J.Appl.Phys, **63(5)**, 1740

C.C.Ahn, P.Rez (1985), Ultramicroscopy, **17**, 105

C.C.Ahn, O.L.Krivanek (1988), EELS Atlas, available from HREM Facility, Centre for Solid State Science, Arizona State University, Tempe, AZ, USA

N.C.Barford (1967), Experimental Measurements: Precision, Error and Truth (Addison Wesley, London)

P.S.Bell, M.H.Lewis (1974), Phil Mag, **29**, 1175

J.Bentley (1982), 10^{th} International Congress on Electron Microscopy, Hamburg, 1, 585

S.D.Berger, I.G.Salisbury. R.H.Milne, D.Imeson, C.J.Humphreys (1987a), Phil Mag B, **55(4)**, 341

S.D.Berger, J.M.Macaulay. L.M.Brown (1987b), Phil.Mag.Lett, **56**(5), 179

P.R.Bevington (1969), Data reduction and Error Analysis for the Physical Sciences (M^{C}Graw-Hill), chapter 11

C.R.Bradley (1988), Calculations of Atomic Sputtering and Displacement Cross-sections, Argonne National Laboratory, report number 8848.

Bravman (1984), J.Electron Microscopy Technique, 1, 53

T.W.Buggy (1985), Phd Thesis, Glasgow University

Bulloch (1989), in EMAG 1989 (Inst.Phys.Conf.Ser.No.98), 267

C.Chatfield (1988), private communication

N.G.Chew, A.J.Cullis (1987), Ultramicroscopy 23, 175

V.E.Cosslet (1978), J.Microsc, 113, 113

J.Crank (1975), The Mathematics of Diffusion (Clarendon Press, Oxford) chapter 5

A.J.Craven, T.W.Buggy (1984), J.Microsc 136(2), 227

CRC (1988), Handbook of Chemistry and Physics, 68^{th}edition, D38-41 (CRC press)

A.V.Crewe, J.Wall, J.Langmore (1970), Proceedings 7th International Congress of Electron Microscopy, Grenoble

A.V.Crewe (1971), High Intensity Electron Sources and Scanning Electron microscopy in Electron Microscopy and Material Science, (ed) U.Valdre, 162

A.V.Crewe, J.P.Langmore, M.S.Isaacson (1975), in Physical Aspects of Electron Microscopy and Analysis (eds) B.Siegel and D.Beaman (Wiley and Sons 1975)

P.A.Crozier, J.N.Chapman, A.J.Craven, J.M.Titchmarsh (1984a), in introduction to Analytical Electron Microscopy 1984 (eds) D.Williams and D.C.Joy (Plenum)

P.A.Crozier (1984b), private communication with P.Rez.

P.A.Crozier (1985), Phd Thesis, Glasgow University

G.Das, D.Chaterjee, H.Lipsitt (1981), J.Mat.Sci, **16**, 3283

J.F.DeNatale, D.G.Howitt (1984), Nuclear Instruments and Methods, **B1**(1984), 489

R.W.Devenish, T.J.Bullough, P.S.Tuner, C.J.Humphreys (1989),in EMAG 1989 (Inst.Phys.Conf.Ser. N°98), 215

A.M.Donald, A.J.Craven (1979), Phil.Mag.A, **39**, 1

S.P.Duckworth, D.G.Howitt, A.J.Craven, T.N.Baker (1985), in EMAG 1985 (Inst.Phys.Conf.Ser.No78), 23

S.P.Duckworth (1988), private communication

R.F.Egerton (1975), Phil.Mag, **31**, 199

R.F.Egerton (1978), Ultramicroscopy, **3**, 242

R,F.Egerton (1979), Ultramicroscopy, **4**, 169

R.F.Egerton (1980), Scanning Electron Microscopy, **1**, 41

R.F.Egerton (1981a), Ultramicroscopy, **6**, 297

R.F.Egerton (1981b), Proceedings Electron Microscope Society of America (1981), (ed) G.W.Bailey, 198

R.F.Egerton (1982), Ultramicroscopy, **9**, 387

R.F.Egerton (1984a), in Quantitative Electron Microscopy, (eds) J.N.Chapman and A.J.Craven (SSUSP No25) p273

R.F.Egerton (1984b), Analytical Electron Microscopy, (eds) D.B.Williams and D.C.Joy (San Francisco Press 1984), 263

R.F.Egerton (1984c), Scanning Electron Microscopy (II), 505

R.F.Egerton (1985), Electron energy Loss Spectroscopy in the Electron Microscope, (Plenum Press 1985)

R.F.Egerton. P.A.Crozier, P.Rice (1987), Ultramicroscopy, **23**, 305

R.F.Egerton (1989), Ultramicroscopy, **28**, 215

Guest (1961), Numerical methods of Curve Fitting (Cambridge University Press 1961)

R.H.J.Hannink (1970), Metallography, **3**, 147

L.W.Hobbs (1979), Ultramicroscopy, **3**, 381

L.W.Hobbs (1984), in Quantitative Electron Microscopy (eds) J.N.Chapman and A.J.Craven (SUSSP No25)

A.Howie (1979), J.Microscopy, **117**, 11

D.J.Howitt (1984), J.Electron Microscopy Technique, 1, 405

D.J.Howitt, D.L.Medlin and T.M.Walker (1988), EMSA Bulletin 18:2, November 1988

C.J.Humphreys, I.G.Salisbury, S.D.Berger, R.S.Timsit and M.E.Mochel (1985), in EMAG 1985 (Inst.Phys.Conf.SerN^{O}78), 1

M.Inokuti (1971), Rev.Mod.Phys, **40**(3), 441

M.S.Isaacson, J.langmore, N.W.Parker, D.Kopf, M,Utlaut (1976), Ultramicroscopy, **1**, 359

M.S.Isaacson (1977), in Principals and Techniques of Electron Microscopy (ed) M.A.Hayat (Van Nostrand Rheinhold 1977)

M.Isaacson, M.Ohtsuki, M Utlaut (1979), in Introduction to Analytical Electron Microscopy, (eds) J.J Hren, J.I Goldstein and D.C.Joy (Plenum Press 1979)

M.Isaacson and A.Murray (1981), J.Vac.Sci.Technol, **19**, 1117

D.C.Joy, D.M.Maher, R.G.Farrow (1980), Microbeam Analysis 1980, 154

D.C.Joy (1982), Scanning Electron Microscopy, **137**, 505

A.S.Karim, M.E.Whitehead, M.H.Loretto, R.E.Smallman (1978), Acta.Metal, **26**, 975

E.Kohl (1990), Undergraduate project

O.L.Krivanek, C.C.Ahn and R.B.Keeney (1987), Ultramicroscopy, **22**, 103

R.D.Leapman, P.Rez, D.F.Mayer (1980), J.Chem.Phys, **72**(2), 1232

F.Lenz (1954), Z.Naturforsch, **9a**, 185

J.Liu, J.M.Cowley (1987), Proceedings Electron Microscope Society of America (1987), (ed) G.W.Bailey, (San Francisco Press), 176

A.J.McGibbon (1989), PhD Thesis, Glasgow University

M.J.Makin (1971), Electron Microscopy in Material Science, (ed) U.Valdre (Academic Press 1971)

T.Malis, J.M.Titchmarsh (1985),in EMAG 1985 (Inst.Phys. Conf.Ser.No78), 181

T.Malis, J.M.Titchmarsh (1986), private communication

J.L.Martin, J.N.Chapman, W.A.P.Nicholson, C.R.Stanley, A.H.Kean (1990), in proceedings of the XIIth International Congress for Electron Microscopy (San Francisco Press 1990), 1, 174

H.Massey, C.Mohr (1931), Proc.Roy.Soc (London), **A132**, 605

M.E.Mochel, C.J.Humphreys, J.A.Eades, J.M.Mochel, A.M.Petford (1983), Appl.Phys.lett, **42**(4), 392

J.Morillo, C.H.deNovion, J.Dural (1981), Rad Effects, **55**, 67

J.Morillo, C.H.deNovion, J.Dural (1983), Science of Hard Materials (ed) R.Wiswanadham (Plenum Press 1983)

Y.Murata, N.Yukawa, H.Mori, H.Fujita (1988), J.Less.Comm.Mets, **141**, 309

A.Murray, M.Isaacson, I.Adesida (1984), Appl.Phys.Lett, **45**(5), 589

R.S.Nelson (1975), Radiation Damage Processes (ed) C. Dupuy (Noordhoof, Leyden 1975)

W.A.P.Nicholson (1974), J.Microsc, **121**, 141

D.I.R.Norris (1975), Electron Microscopy in Materials Science (ed) E.Ruedle, Commission of the European Communities

O.S.Oen (1973), Oak Ridge national Laboratory, report number ORNL 4897

J.H.Paterson (1988), Phd Thesis, Glasgow University

S.J.Pennycook, S.D.Berger, R.J.Culbertson (1986), J.microscopy, **144**, 229

S.J.Pennycook (1989a), EMSA Bulletin 19:1, May 1989

S.J.Pennycook (1989b), Ultramicroscopy, **30**, 58

F.Philipp, B.Saile, H.Schmid and K.Urban (1979), Phys.Let, **73A(2)**, 123

L.A.Pipes (1958), Applied Mathematics for Engineers and Physicists (M^{C}Graw-Hill 1958)

T.Pun, J.R.Ellis and M.Eden (1985), J.Microsc, **137**, 93

P.Rez (1984), X-Ray.Spectrom, **13**(2), 55

Rutherford (1911), Phil.Mag, **21**, 669

I.G.Salisbury, R.S.Timsit, S.D.Berger and C.J.Humphreys (1984), Appl.Phys.Lett, **45**, 1289

S.Sarian (1968), J.Appl.Phys, **39**, 3305

V.Sarin (1983), Science of Hard Materials (ed) R.Wiswanadham (Plenum Press 1983)

F.Seitz, J.S.Koehler (1956), Displacement of Atoms During Irradiation Solid State Physics 1956(2), 305.

P.G.Shewman (1963), Diffusion in Solids (M^{C}Graw-Hill 1963)

Sklad (1984), Analytical Electron Microscopy (1984), 285

J.D.Steele, J.M.Titchmarsh, J.N.Chapman and J.H.Paterson (1985), Ultramicroscopy, **17**, 273

J.D.Steele (1987), Phd Thesis, Glasgow University

L.E.Thomas (1984),in Analytical Electron Microscopy 1984, (eds) D.B.Williams and D.C.Joy (San Francisco Press), 358

L.E.Thomas (1985), Ultramicroscopy, **18**, 173

M.M.Treacy (1982), J.Microsc.Spectrosc.Electron, **7**, 511

M.M.Treacy, J.M.Gibson, K.T.Short, S.B.Rice (1988), Ultramicroscopy, **26**, 133

P.Trebbia (1988), Ultramicroscopy, **24**, 399

P.Vajda (1977), Rev.Mod.Phys, **49**, 481

J.D.Venables, R.G.Lye (1969), Phil.Mag, **19**(159), 565

S.Vuorinen, A.Horsewell (1983), Science of Hard Materials (ed) R.Wiswanadham (Plenum Press 1983)

I.R.M.Wardell (1982), Ultramicroscopy **7**, 39

W.S.Williams, C.Allison, P.Mochel (1983), Science of Hard Materials (ed) R.Wiswanadham (Plenum Press 1983)

C.Zener (1930), Phys.Rev, **36**, 51

GLASGOW UNIVERSITY LIBRARY